EXTENDED PERFORMANCE TECHNOLOGY STUDY: 30–cm THRUSTER

J.R. Beattie

Hughes Research Laboratories
3011 Malibu Canyon Road
Malibu, CA 90265

JUNE 1983

NAS 3–21943
Final Report
26 June 1979 through 26 October 1982

NATIONAL AERONAUTICS AND SPACE ADMINISTRATION
Lewis Research Center
21000 Brookpark Road
Cleveland, OH 44135

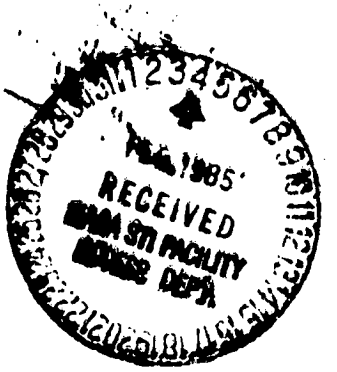

SUMMARY

The Extended Performance Technology Study was an investigation of advanced discharge chambers and thruster components that were designed to operate under conditions that result in an increase in the thrust and thrust-to-power ratio of the state-of-the-art J-series thruster. Achieving the extended-performance capability required a thruster design that would operate efficiently at beam currents as high as J_b = 5 A and at net-to-total accelerating-voltage ratios as low as R = 0.2. The performance goals were achieved using a ring-cusp-magnetic-confinement thruster design that demonstrated a baseline ion-production cost of only ε_i = 125 eV/ion, a beam current as high as J_b = 5.3 A, and an acceptable range of net-to-total accelerating-voltage ratios of $0.2 \leq R \leq 0.8$. When compared with the performance of the state-of-the-art J-series thruster, these performance levels represent nearly a factor-of-three increase in thrust, a factor-of-two increase in thrust-to-power ratio, and a 35% reduction in baseline ion-production cost.

The extended operating range and performance objectives translate into exacting requirements on the discharge chamber, ion-extraction assembly, hollow cathode, and propellant-flow electrical isolators. Therefore, the program was logically divided into four major elements or tasks that dealt with these critical technology areas.

In the first element, which consisted of three related tasks, several advanced discharge-chamber configurations and their variations were investigated. Each of the designs demonstrated performance that was comparable to that of the highly optimized J-series thruster, but the ring-cusp design was found to be far superior over the other two (a single-cusp and a multipole magnetic-confinement geometry). Extensive performance and plasma-diagnostic measurements were conducted using a laboratory model of the ring-cusp thruster, leading to a

preliminary description or model of the discharge plasma that is consistent with its high-performance characteristics. Our plasma-property measurements indicate that the ring-cusp-magnetic-confinement geometry effectively concentrates the ionization region near the ion-extraction assembly, resulting in a high probability that the ions produced in this volume will be extracted into the ion beam.

The investigation of a flexible-mount electrode-supporting structure that was developed under a previous NASA contract (NAS 3-21040), demonstrated that an advanced three-grid ion-extraction assembly could operate under high-beam-current extraction conditions (high power), while at the same time maintaining the ratio of net-to-total accelerating voltage as low as R = 0.2. The technology of three-grid-ion-extraction assemblies was further developed under this contract by performing a parametric analysis of the electrode-aperture displacement required to vector individual beamlets in a direction to minimize off-axis thrust losses.

A model of hollow-cathode lifetime that was also developed under NASA contract NAS 3-21040 was used to design a cathode that can operate under high-emission-current conditions for extended periods of time. Over 60,000 A-hr of operation were demonstrated with scaled versions of the high-performance cathode used in the state-of-the-art J-series thruster; our test results indicate that long lifetime can be expected at emission currents as high as J_E = 40 A. This will be possible as long as the diameter of the flow-restricting orifice is large enough to maintain the ratio of emission current to aperture diameter at about the same value as that of the J-series design.

A study of the breakdown-voltage characteristics of the state-of-the-art propellant-flow electrical isolator established the maximum conservative isolation voltage as 340 V per section. Our measurements further showed that the total breakdown voltage is directly proportional to the number of individual isolator sections. This finding enables a specified voltage standoff to be achieved simply by scaling the existing isolator design so

that the product of the number of sections and the section rating of 340 V provides a comfortable margin over the required value.

Other tasks included the design, fabrication, and testing of a simplified vaporizer power supply and a comprehensive investigation of the uncertainties in measuring thrust-loss factors. The power-supply simplifications incorporated multiplexing techniques to eliminate over 30% of the components required in the three vaporizer power supplies used in the power processor for the J-series thruster. The results of the uncertainty analysis indicated that the overall error in the thrust-loss factors, α and F_t, is less than 1.4%.

FOREWORD

The work described in this report was performed during a period of approximately three years at Hughes Research Laboratories (HRL). The technical effort was initially conducted in the High Voltage Technology Department, managed by Dr. H.J. King. In May 1981 this department was reorganized and became the Plasma Physics Department, managed by Dr. J. Hyman. The program was managed by Dr. J.R. Beattie of HRL and monitored initially by Mr. W.R. Kerslake, and later by Mr. V.K. Rawlin, both of NASA-Lewis Research Center (LeRC). Major technical contributions to this effort were made by:

J.R. Beattie	Program manager and principal investigator
S. Kami	Discharge-chamber design and fabrication
D.J. Hancock	Power-processor simplification
J.N. Matossian J.W. Ward	Computer analysis
W.D. Gosselin, R.L. Maheux, M.W. Sawins, and J.A. Tyrrell	Thruster and component fabrication, assembly, instrumentation, and technical assistance.

TABLE OF CONTENTS

APPENDICES

LIST OF ILLUSTRATIONS

SECTION 1

INTRODUCTION

By the beginning of the present program the 30-cm-diameter J-series thruster had reached a level of development that would enable confident application of prime-propulsion technology, and advanced studies had shown promise for extending the performance of the baseline design. The objective of this program was, therefore, to investigate discharge-chamber, ion-accelerator, and component designs that would produce significantly higher thrust and higher thrust-to-power ratio than could be achieved with the baseline 30-cm thruster.

A. PROGRAM GOALS

The work was performed under seven technical tasks. Tasks I, VIII, and IX required evaluation of advanced discharge-chamber and ion-extraction assemblies that would enable operation at increased thrust and increased thrust-to-power ratio. Task II required investigation of simplifications that would reduce the complexity and cost of the power processors required for the extended-performance thruster. Task III required lifetime evaluation of a high-emission-current (J_E = 40 A) hollow cathode. Task IV required measurements of the pressure-dependent electrical-breakdown voltage of individual sections of the state-of-the-art propellant-flow electrical isolator. Task X required calculations of the electrode compensation necessary to minimize the off-axis thrust loss of three-grid ion-extraction assemblies. Other work required under Task I included a detailed description of the technique used for determining the thrust-loss factors α and F_t, and an estimate of the uncertainties in the measurements.

B. PROGRAM ACCOMPLISHMENTS

Under Tasks I, VIII, and IX, three discharge chambers and two ion-extraction-assembly designs were investigated. The discharge-chamber designs included the ring-cusp, single-cusp, and multipole magnetic-confinement arrangements. The ion-extraction assemblies included a three-electrode arrangement that employs flexible mounts for supporting each grid and a two-electrode design that has the same aperture dimensions as the J-series ion-extraction assembly, but which uses flexible mounts for supporting the accelerator electrode. The performance of these discharge-chamber and ion-extraction designs was documented under the program. The ring-cusp configuration was found to give the best discharge-chamber performance, having a baseline ion-production cost of about ε_i = 125 eV/ion. The two-grid and three-grid ion-extraction assemblies were successfully operated at beam currents as high as J_b = 5 A, and the three-grid ion-extraction assembly was operated at net-to-total accelerating-voltage ratios in the range of $0.1 \leq R \leq 0.8$. A comprehensive analytical and experimental investigation into the uncertainties in the measured values of the thurst-loss factors α and F_t was completed, and the results showed that the uncertainty in these factors is less than 1.5%.

Under Task II, several power-processor simplifications were investigated. Of the various design simplifications that we identified, a multiplexed vaporizer power supply was selected for fabrication and testing with a J-series-equivalent thruster. The time-sharing device performed very well, and the simplified design results in a significant reduction ($\approx$ 70%) in parts count (and, therefore, lower cost and higher reliability) when compared with the three individual vaporizer power supplies required for the J-series thruster.

Work under Task III included the design of a high-emission-current (J_E = 40 A) hollow cathode. Three of these cathodes were tested for 500 hr each, accumulating 20,000 A-hr of operation per cathode. The lifetest results showed that the aperture wear is excessive unless the diameter of the flow-restricting orifice is $d_o > 1.27$ mm. Temperature measurements showed that the lifetime of the high-emission-current cathode (based on depletion of barium from the porous-tungsten insert) should be comparable to that of the J-series insert ($\geq$30,000 hr).

Under Task IV, the breakdown voltages of individual sections of a propellant-flow electrical isolator were measured as a function of flow rate and isolator-base temperature. The minimum breakdown voltage was found to be about 340 V per section, and the total breakdown voltage was found to scale linearly with the number of isolator sections.

Work under Task X resulted in design curves for use in determining the electrode-aperture displacement required to vector the beamlets emerging from three-grid ion-extraction assemblies. The parametric results cover a wide range of design variables, including electrode thickness, aperture diameter, and interelectrode spacing.

The work performed under the contract is described in detail in the following sections. The report also describes plasma-diagnostic measurements and analyses that were performed under Hughes funding, enabling the operation and plasma physics of the ring-cusp discharge chamber to be more fully documented.

SECTION 2

DISCHARGE-CHAMBER INVESTIGATION

The thrust produced by the state-of-the-art 30-cm-diameter thruster can be increased by increasing either the beam current, J_b, or the beam voltage, V_b; both of these approaches have been successfully demonstrated under previous extended-performance thruster investigations.[2-1,2-2] Increasing the thrust by simply increasing the beam current is not without limitations, however, since the power consumed in ionizing the propellant scales as $\varepsilon_i J_b$. Therefore, a reduction in the ion-production cost, ε_i, is necessary to minimize the power consumption and thermal impact of extended-performance thruster operation.

An increase in the thrust-to-power ratio of the state-of-the-art thruster will accompany any reduction in ion-production cost, ε_i. An additional increase can be realized by reducing the beam power, $J_b V_b$, through reductions in the beam voltage, V_b (or specific impulse, I_{sp}). The sensitivity of thrust-to-power ratio to these variables is illustrated in Figure 2-1. In order to operate near the maximum on these curves requires a relatively low specific impulse. However, there is a lower bound on I_{sp} which (for a given beam current) is set by the perveance of the ion-extraction assembly and the minimum permissible value of the net-to-total accelerating-voltage ratio, R. The perveance is primarily limited by the span-to-gap ratio of the electrodes, which we believe to be near the maximum for the state-of-the-art ion-optics design. The net-to-total accelerating-voltage ratio is limited to about $R \approx 0.6$ for two-grid ion-extraction assemblies, but it can be reduced to as low as $R \approx 0.1$ by the addition of a third (decelerator) electrode to the present two-grid arrangement. The performance gains that could be achieved by reducing the ion-production cost, ε_i, and the net-to-total accelerating-voltage ratio, R, are illustrated in Figure 2-2, where the performance

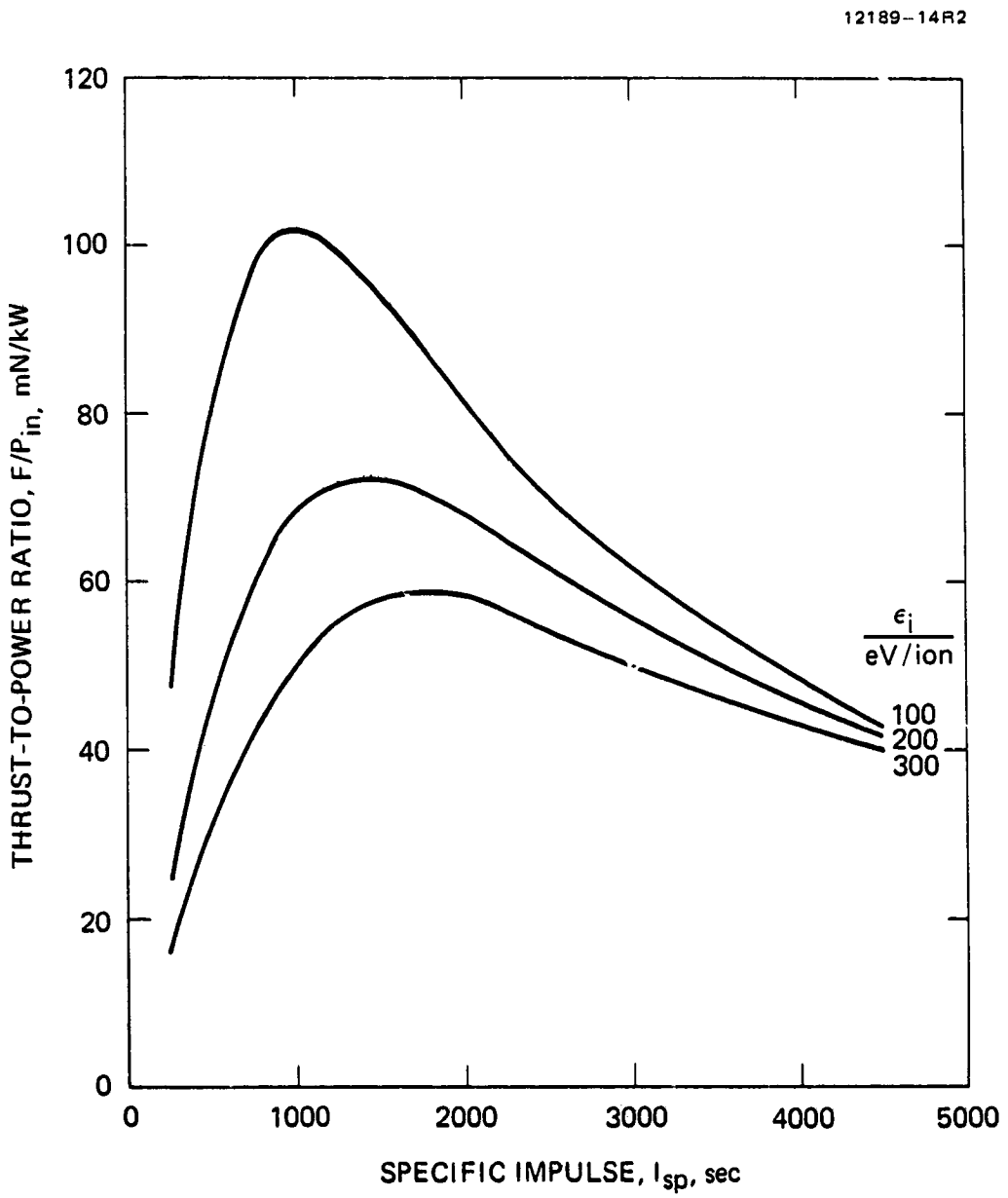

Figure 2-1. Variation of thrust-to-power ratio with specific impulse for an electrostatic ion thruster. Calculations represent the idealized case, where fixed-power, thrust, and un-ionized propellant losses have been neglected.

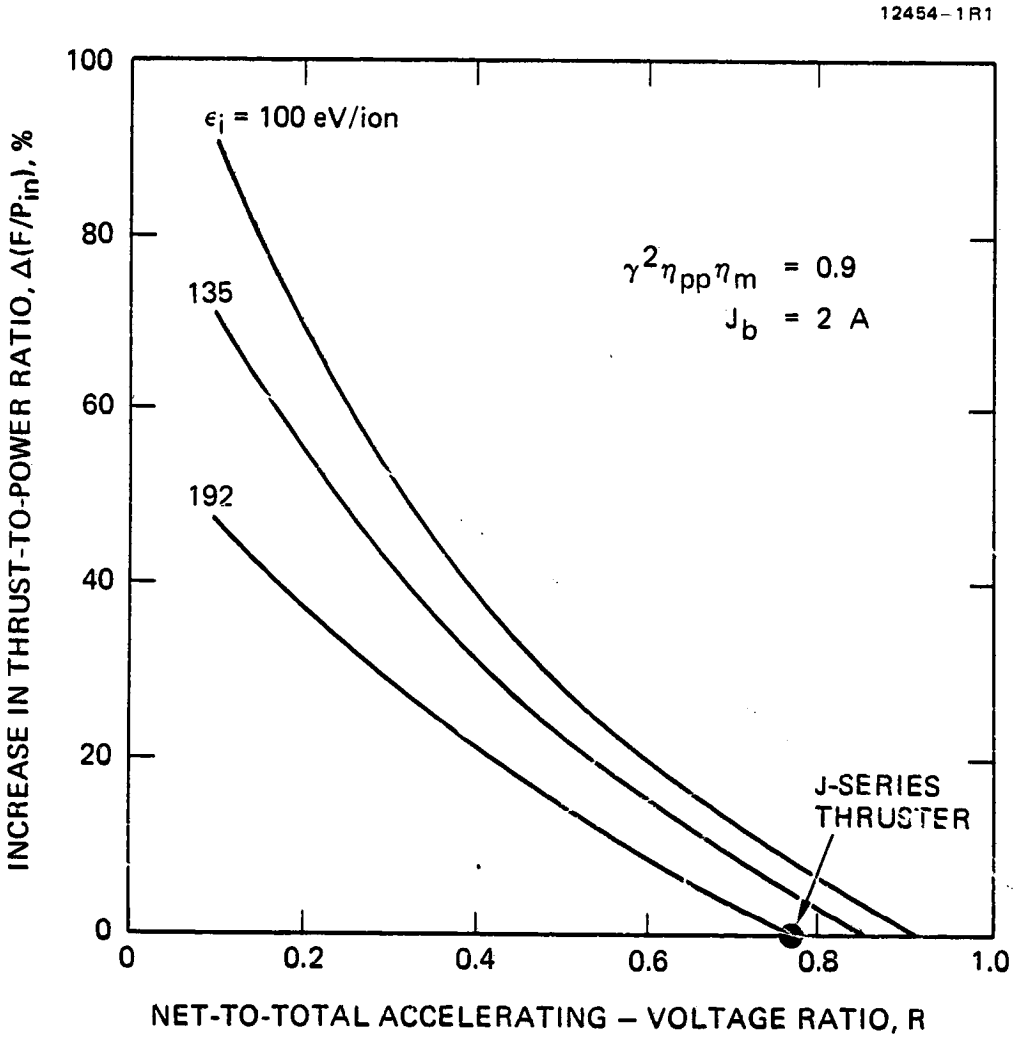

Figure 2-2. Performance gains that could be achieved by reducing the specific discharge power, ϵ_i, and net-to-total accelerating-voltage ratio, R, of the state-of-the-art 30-cm thruster. In performing these calculations, we have neglected fixed-power losses (vaporizers, keepers, etc.) and we have used the thrust-loss factor, γ, propellant-utilization efficiency, η_m, and power processor efficiency, η_{pp} indicated in the figure.

gain is expressed as an increase in thrust-to-power ratio over that of the J-series thruster. Figure 2-2 indicates that a 60% increase in the performance of the baseline thruster can be achieved by lowering the ion-production cost to ε_i = 135 eV/ion and by reducing the net-to-total accelerating-voltage ratio to R = 0.2.

Achieving the desired performance improvements of increased thrust and increased thrust-to-power ratio required a discharge chamber that could produce a sufficiently dense plasma with minimum power consumption, and an ion-extraction assembly that could efficiently extract the beam current at minimum net-to-total accelerating-voltage ratio. These requirements were demonstrated using the advanced-technology ring-cusp discharge chamber described below, and the advanced-technology three-grid ion-extraction assembly described in Section 3.

A. RING-CUSP DISCHARGE CHAMBER

Figure 2-3 illustrates the high-performance, laboratory-model ring-cusp discharge chamber that we fabricated and tested under this program. The design is based on the ring-cusp magnetic-confinement configuration developed at NASA-Lewis Research Center.[2-3] The entire cylindrical sidewall and circular endwall are maintained at anode potential and were fabricated from commercially available iron pipe and sheet stock. The cathode and cathode magnet are electrically isolated from each other and from the endwall and (in the laboratory-model thruster) can be independently moved during thruster operation using the cathode and magnet gear-drive arrangement that we also designed and fabricated.* The main propellant flow is introduced into the discharge chamber through a plenum which is electrically isolated from the endwall. A photograph showing the interior of the laboratory-model ring-cusp discharge chamber is presented in Figure 2-4.

*Details of the gear-drive arrangement are provided in Section 2-B.

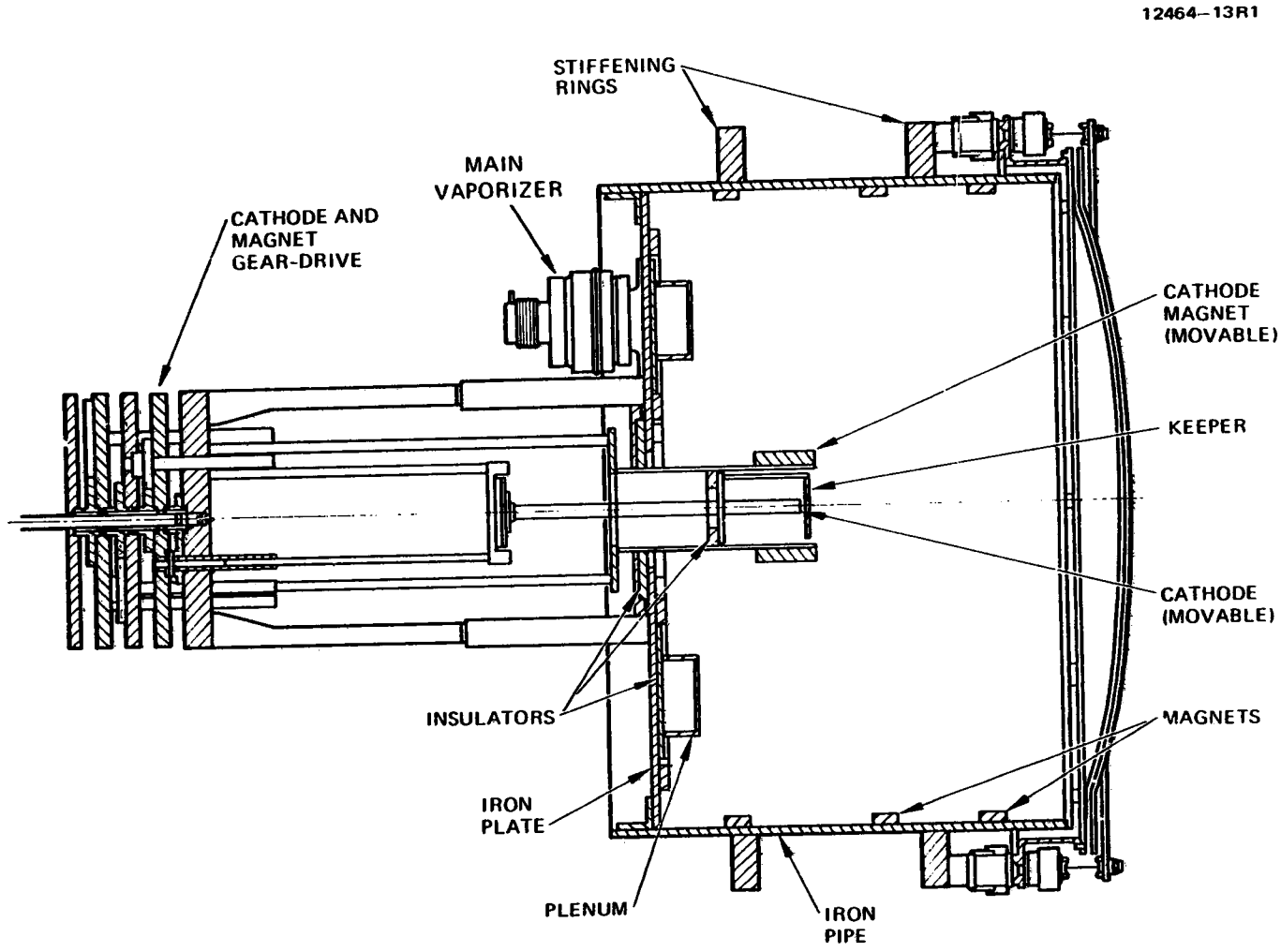

Figure 2-3. Laboratory-model ring-cusp thruster with movable cathode/cathode-magnet arrangement. (Cathode vaporizer not shown.)

M14386

12189-31

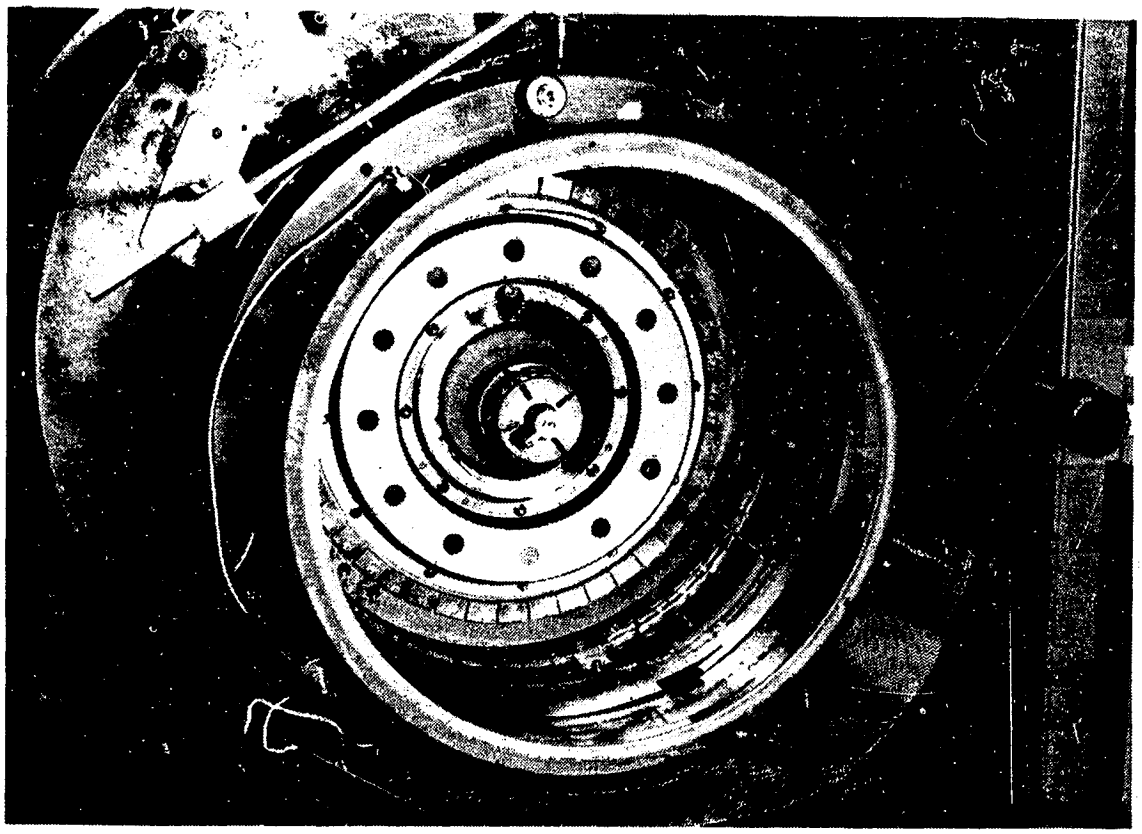

Figure 2-4. Photograph of the laboratory-model ring-cusp discharge chamber.

High-field-strength samarium cobalt ($SmCo_5$) magnets are used to produce the cusp fields along the boundary, and an array of Alnico-V magnets surrounds the cathode. The resultant confining magnetic field has the divergent-cusp shape evident in the iron-filings map of Figure 2-5. The $SmCo_5$ magnets are held in place by the strong forces of attraction between them and the soft-iron boundary; the magnetic-field strength at the surface of the magnets is approximately 2,400 G.

The electrically isolated magnet covers (shown in the photograph of Figure 2-4 and the schematic of Figure 2-6) allow the anode-current distribution to be determined, and they provide thermal protection for the magnets which have relatively low electrical conductivity and a maximum temperature rating of 325°C. A black-oxide coating on the exterior of the discharge chamber also aids in keeping the magnets cool by enhancing the radiative transfer to the surroundings. With this arrangement, steady-state testing at discharge powers up to 750 W is possible, while maintaining the magnets ≈65°C below their maximum temperature rating.

We measured the radial and axial components of the magnetic field produced by the "rings" of $SmCo_5$ magnets and the cathode magnet, using the 2-axis gaussmeter probe and positioning mechanism shown in Figure 2-7. The resultant magnetic field was calculated from the measured components of B, and contours of the scalar fields are shown in Figures 2-5 and 2-8 to lie approximately normal to the field lines obtained from iron filings and parallel to the chamber boundaries.

The axial magnetic field on the discharge-chamber axis can be varied during thruster operation using the movable cathode-magnet arrangement shown in Figure 2-3. The axial field is produced by the contributions of the $SmCo_5$ magnets located on the chamber sidewall and endwall, and the cathode magnet, which is a cylindrical array of Alnico-V rods with an iron end-cap used to concentrate the field on axis. The variation of the axial magnetic field on the chamber axis is presented in Figure 2-9, with the location (L) of the movable cathode magnet as a parameter.

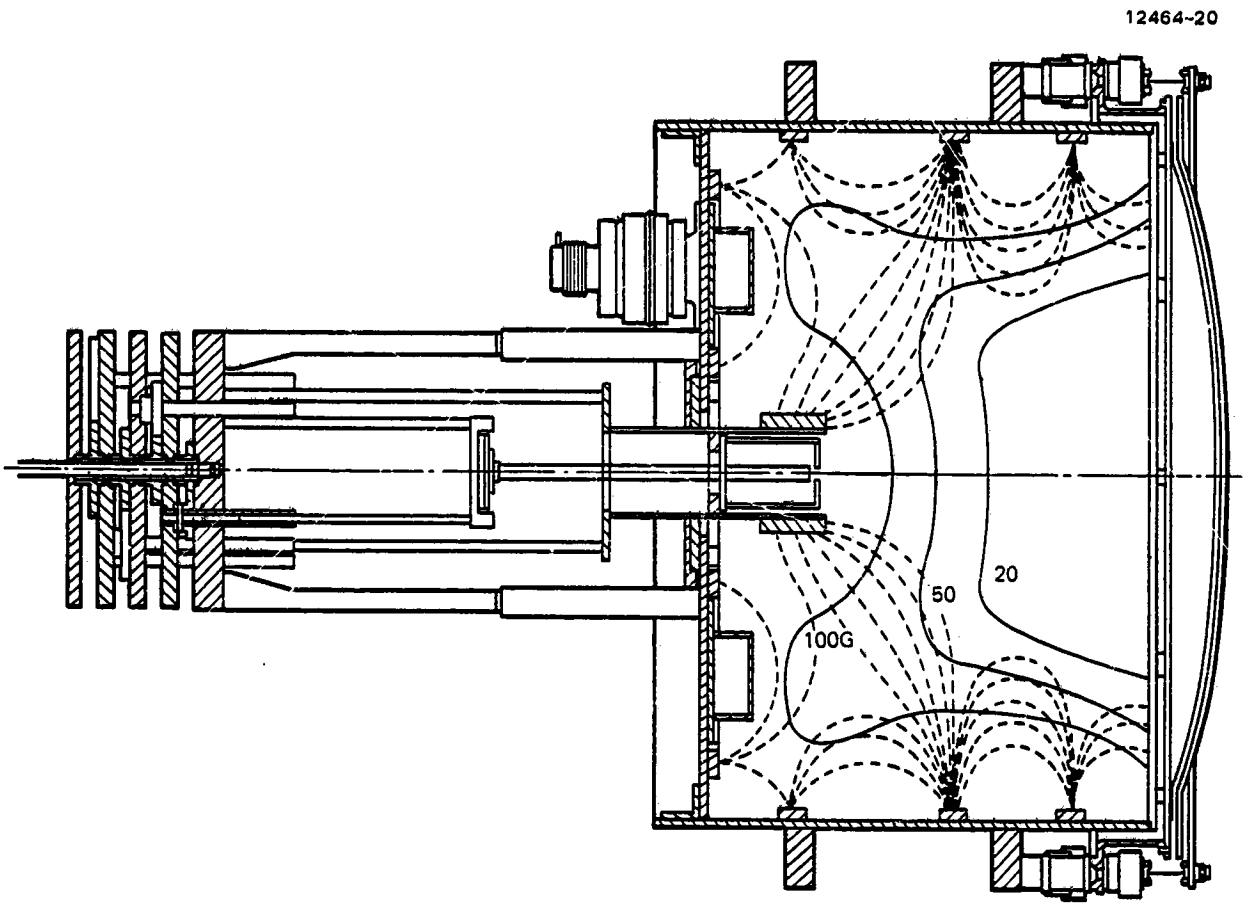

Figure 2-5. Contours of the magnitude of the resultant magnetic field vectors in the ring-cusp discharge chamber. Results of iron-filings measurements are shown superimposed as dashed lines.

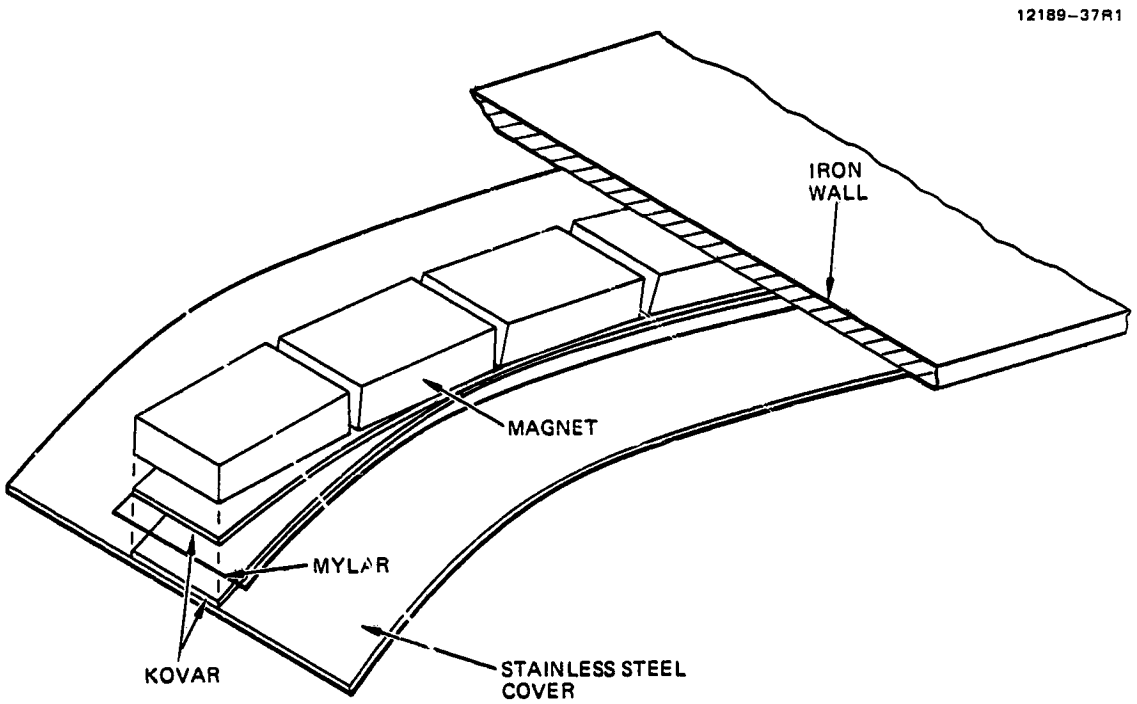

Figure 2-6. Details of the magnet-cover arrangement that enables the electron current to the anode rings to be measured.

M14390 12189-35

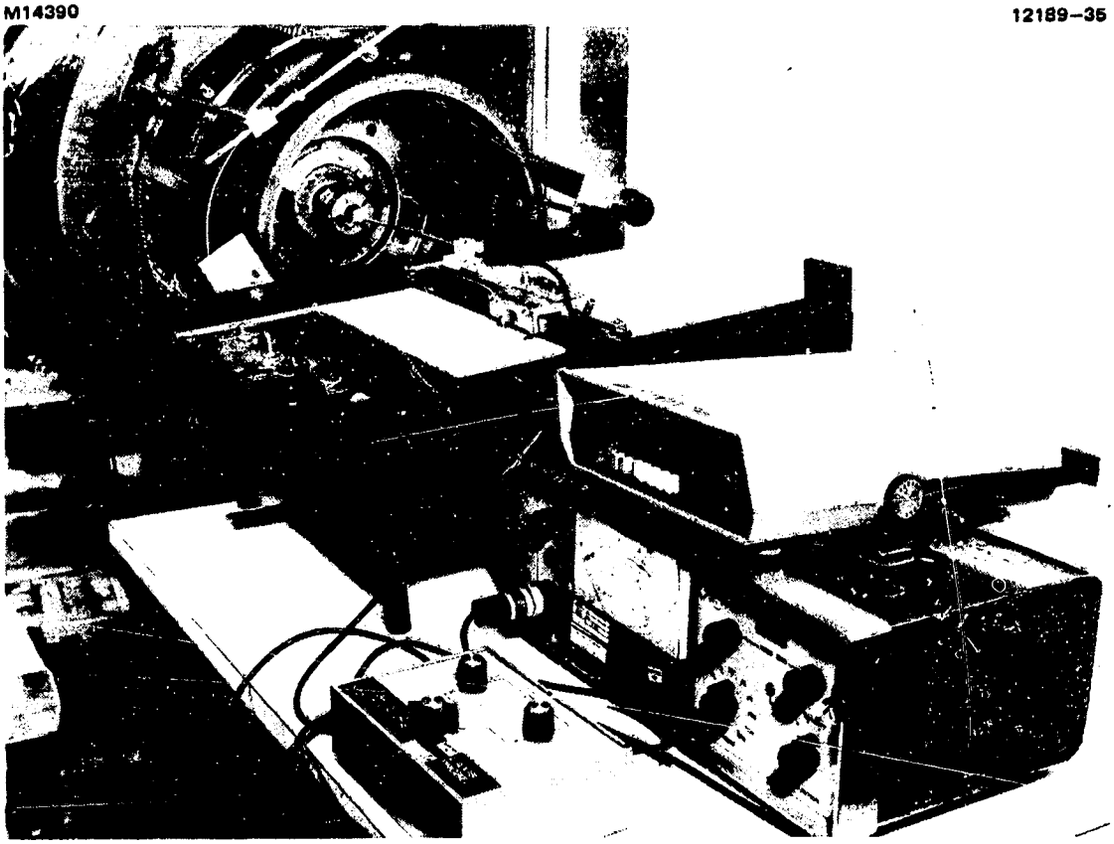

Figure 2-7. Photograph of the magnetic-field-measurement arrangement that was used for documenting the field in the ring-cusp discharge chamber.

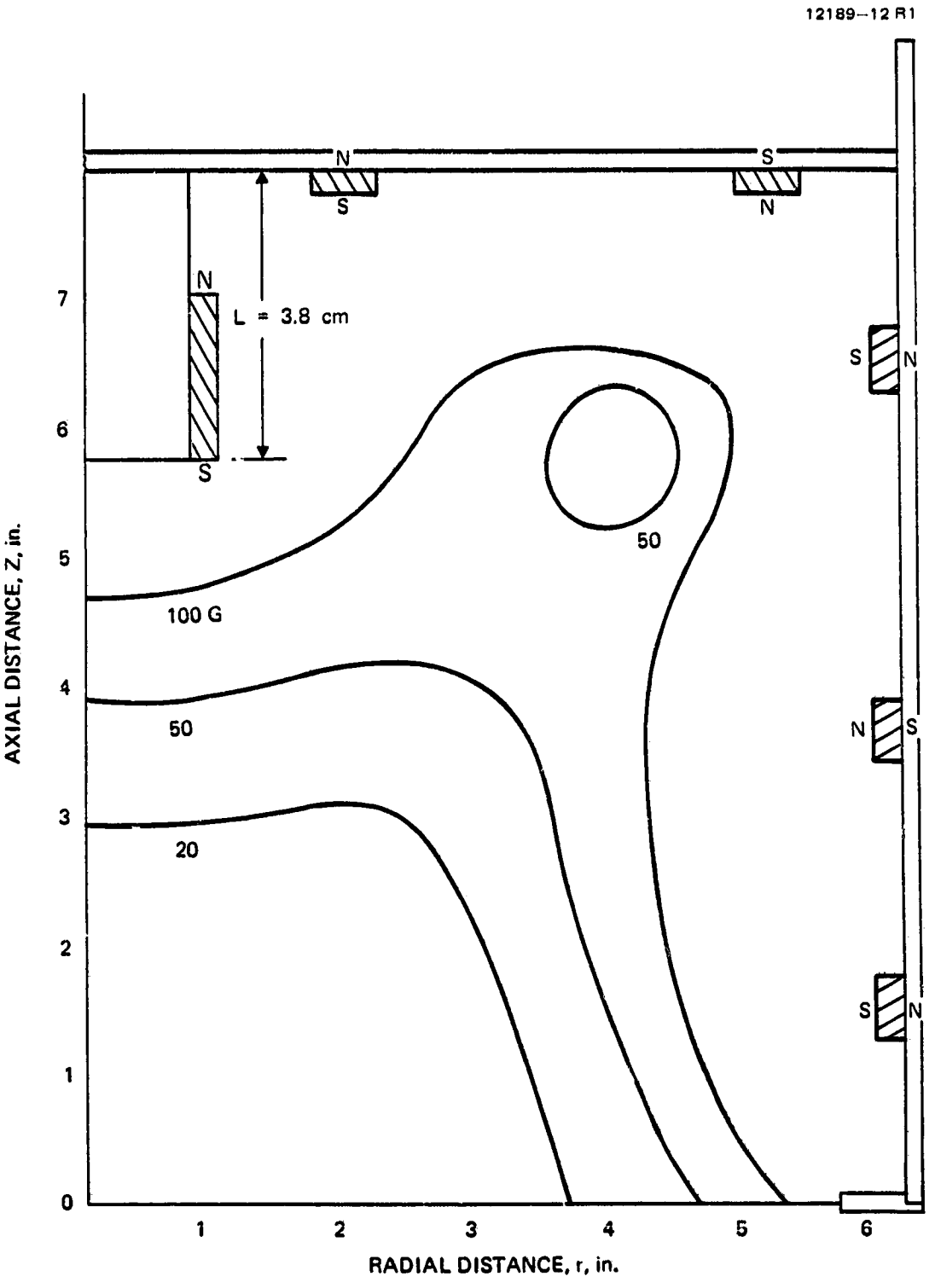

Figure 2-8. Computer-generated magentic-field contours obtained from magnetic-field measurements performed in the ring-cusp discharge chamber.

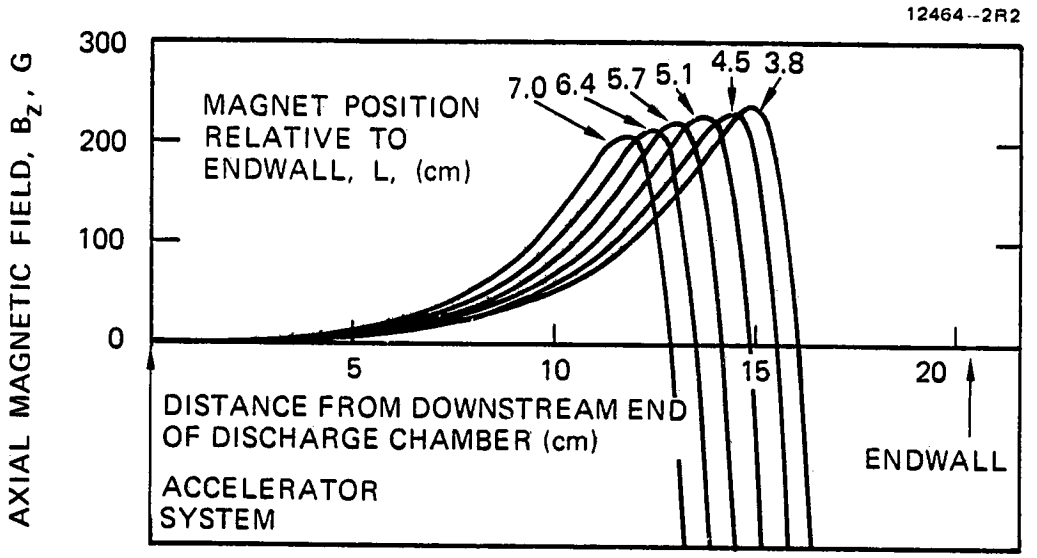

Figure 2-9. Variation of axial magnetic field on the axis of the ring-cusp thruster, with cathode-magnet location as a parameter.

Figure 2-10 presents a schematic that shows the power-supply arrangement used in testing the thruster and defines the electrical quantities that were measured. Equations used in calculating thruster performance are summarized in Table 2-1.

1. Performance Characteristics

Initial testing of the ring-cusp discharge chamber established the minimum-emission-current requirement (minimum eV/ion) for discharge voltages in the range $28\ V < V_D < 44\ V$. Figure 2-11 presents the variation of cathode- and main-vaporizer temperatures* with emission current, J_E, and discharge voltage, V_D, for a beam current of $J_b = 2$ A. These measurements documented the current-voltage characteristics of the discharge chamber, and they established the sensitivity of the cathode and main flow rates to the operating parameters, J_E and V_D. The "knees" of the curves define the minimum emission current (minimum ε_i), and from Figure 2-11 it is evident that they also correspond to a rapid increase in main propellant flow and a rapid decrease in cathode flow. The baseline-performance level is also apparent in the variation of accelerator current, J_A, with emission current, as shown in Figure 2-12. The vertical part of these curves defines the minimum ion-production cost, which lies in the range $120 < \varepsilon_i < 154$ eV/ion for discharge voltages in the range $44\ V > V_D > 28\ V$. The performance improvement at higher discharge voltages is attributed to the larger ionization cross sections at the higher electron energies and more-efficient ion production associated with the reduction in cathode flow rate (that accompanies operation at higher discharge voltage).

---

*After obtaining these results, it was determined that propellant was leaking from the base of the main vaporizer. Therefore, the results of Figures 2-11 and Figures 2-13 to 2-15 give correct trends, but they are not absolute measurements.

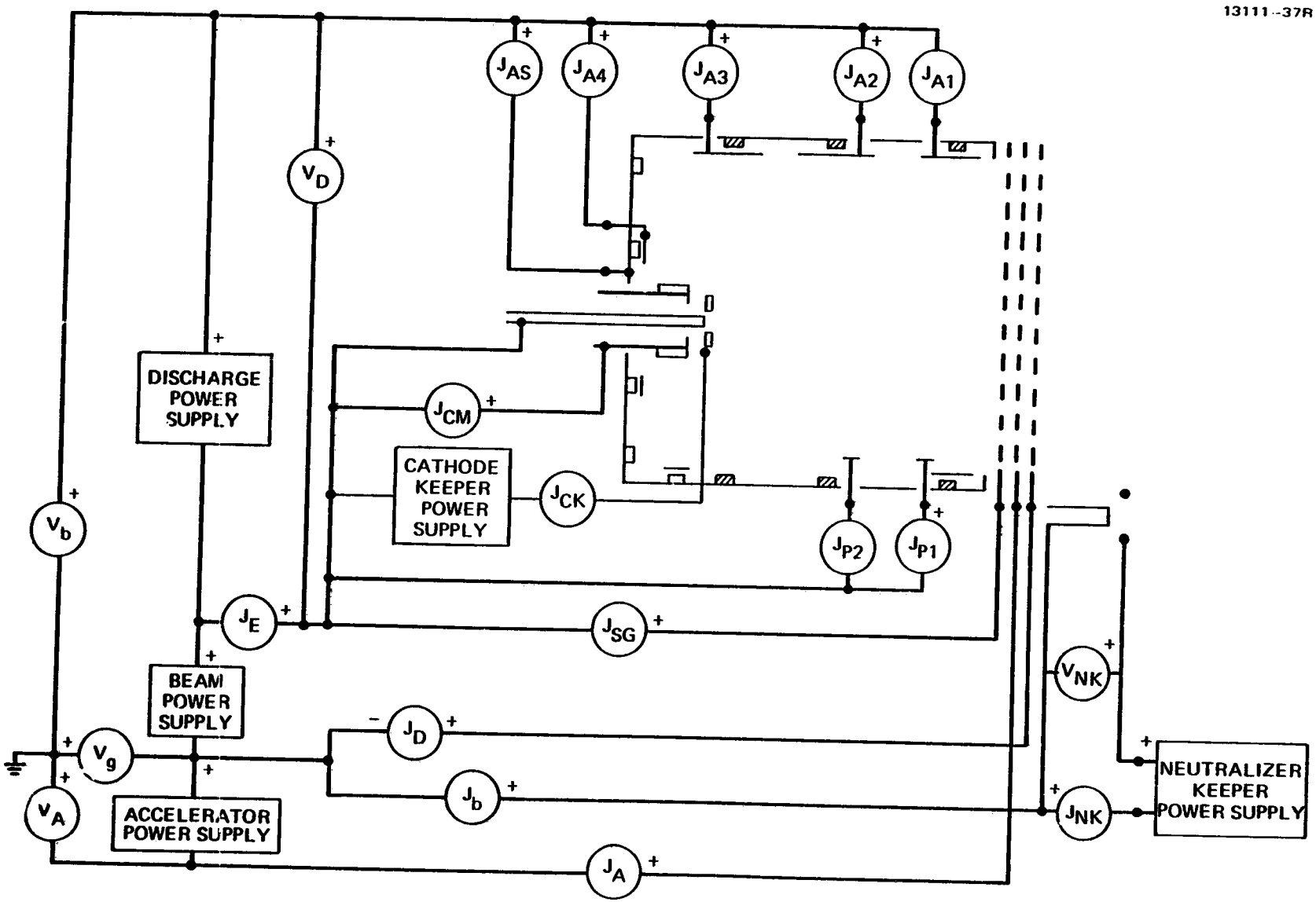

Figure 2-10. Principal power-supply arrangement and electrical quantities measured during ring-cusp thruster testing.

Table 2-1. Summary of Equations used to Calculate Performance of Ring-Cusp Thruster

PERFORMANCE QUANTITY	EQUATION
DISCHARGE POWER	$P_D = V_D J_E$
ION-PRODUCTION COST	$\varepsilon_I = \frac{P_D}{J_b}$
DISCHARGE CURRENT	$J_D = J_b + J_E$
BEAM POWER	$P_b = V_b J_b$
TOTAL POWER*	$P_{TOT} = P_b + P_D + V_g J_b + V_{NK} J_{NK} + V_{CK} J_{CK}$
ELECTRICAL EFFICIENCY	$\eta_e = \frac{P_b}{P_{TOT}}$
TOTAL EFFICIENCY	$\eta_T = \gamma^2 \eta_e \eta_M$
SPECIFIC IMPULSE	$I_{SP} = \frac{\gamma \eta_m}{g_o} \left(\frac{2eV_b}{m_i}\right)^{1/2}$
THRUST	$F = \alpha F_t J_b \left(\frac{2 m_i V_b}{e}\right)^{1/2}$
*NEGLECTS ACCEL, DECEL, AND VAPORIZER POWER	

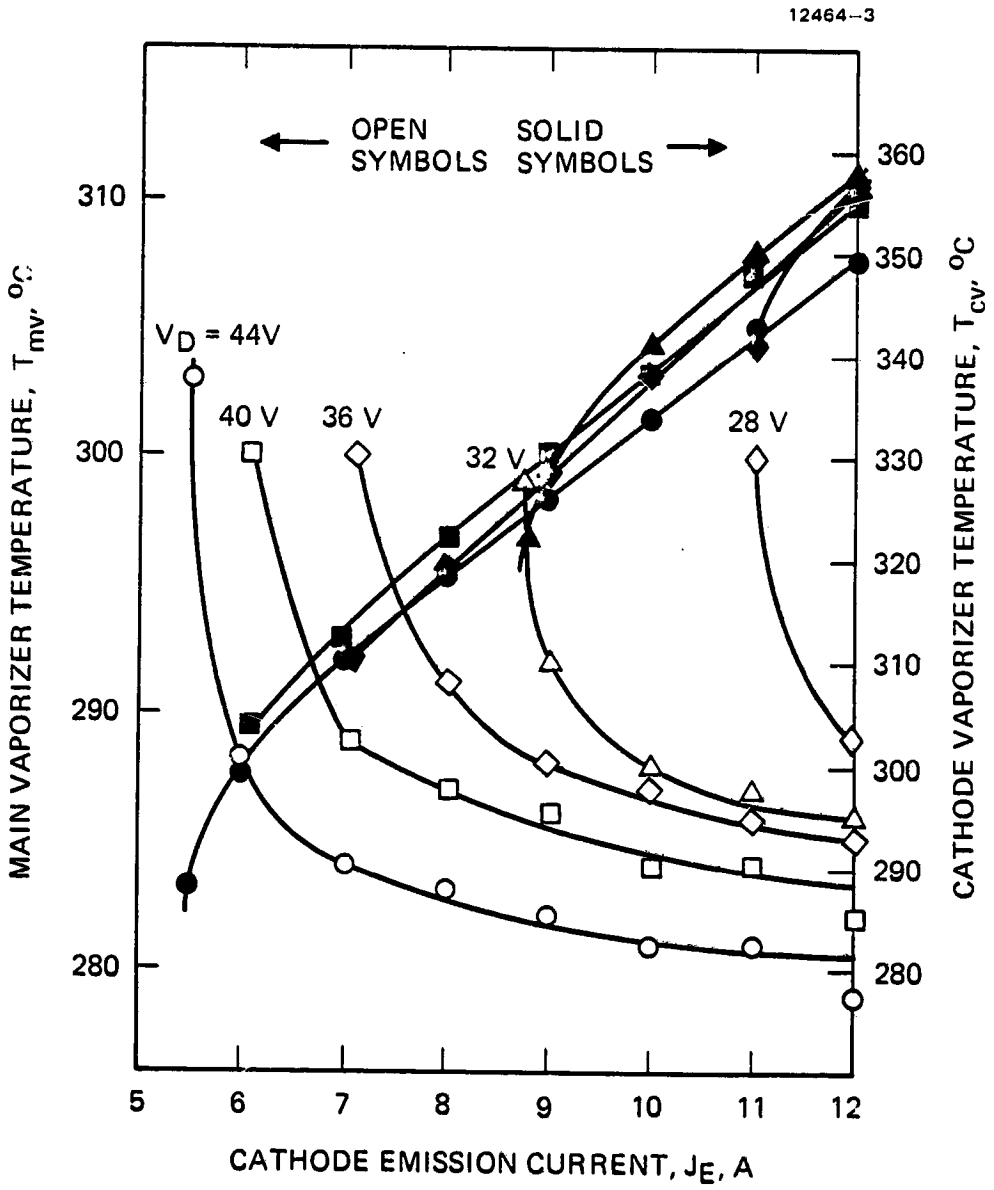

Figure 2-11. Variation of cathode and main-vaporizer temperature with cathode-emission current (J_b = 2 A).

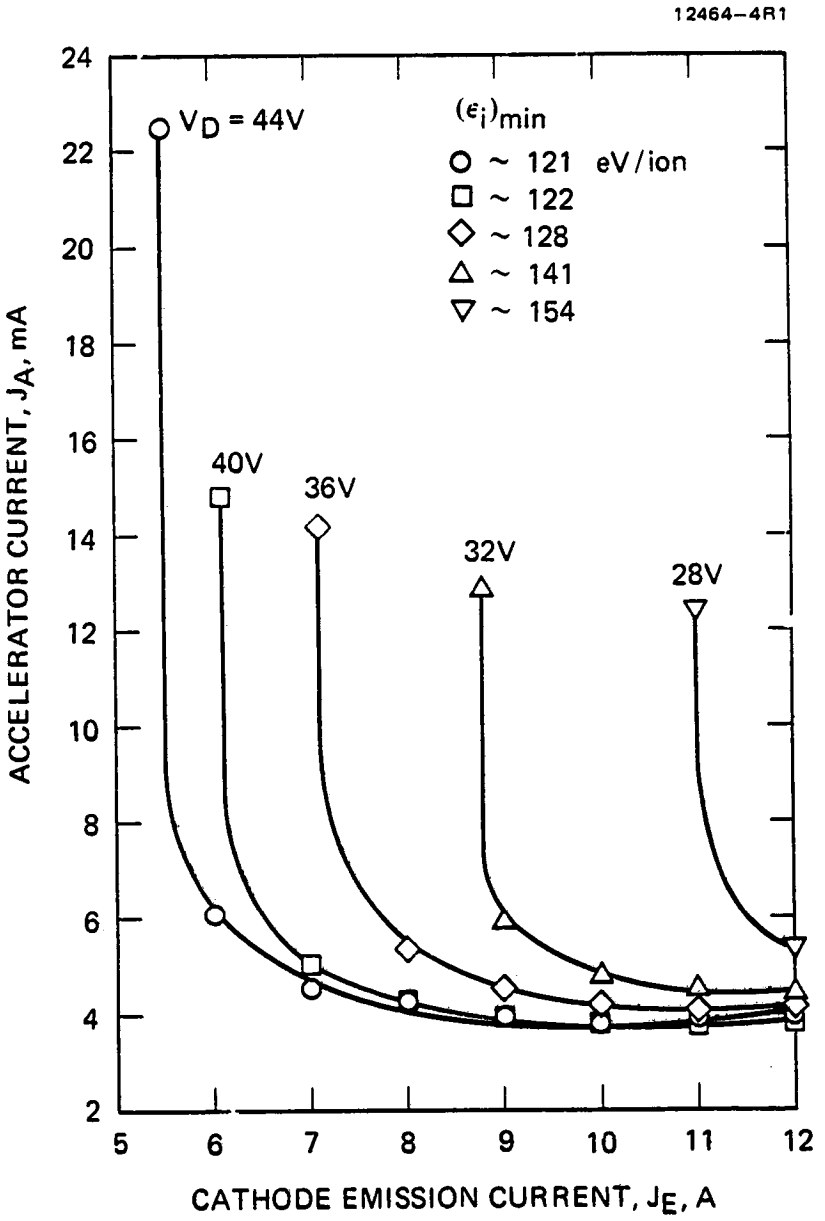

Figure 2-12. Variation of accelerator current with cathode-emission current for the ring-cusp thruster operated with a three-grid ion-extraction assembly.

2. Optimization of the Cathode/Keeper Assembly and Cathode-Magnet Locations

The effects of the locations of the cathode/keeper assembly and cathode magnet are illustrated in Figure 2-13, which shows cathode- and main-vaporizer temperatures as a function of the axial position of these components. The temperature measurements show that for a given location of the cathode-keeper assembly, the magnet position has little, if any, effect on main flow rate, while the cathode flow rate is minimized by increasing the distance between the cathode magnet and cathode orifice. The $\vec{B}$ measurements presented in Figure 2-9 and the temperature/position curves of Figure 2-13 allow one to infer that lower cathode flows are associated with a magnetic-field gradient that points toward the cathode, while the higher flows are associated with a gradient that points away from the cathode. Because of the positive and negative slopes of the vaporizer-temperature curves of Figure 2-13, it is natural to question whether or not an optimum location of the cathode/keeper and magnet exists which would minimize the sum of the cathode- and main-vaporizer flow rates, maximizing the propellant-utilization efficiency. Using the vaporizer-calibration curves of Figure 2-14, we converted the temperature data of Figure 2-13 to flow rates and then used these calibrated flows to calculate propellant-utilization efficiencies. Our results are presented in Figure 2-15, which shows that the relative propellant-utilization efficiency is a maximum for the cathode/keeper located nearest the endwall. With the location of the cathode defining the "virtual" endwall, or chamber length, this finding is equivalent to achieving increased propellent utilization with increased neutral residence time.

3. Extended-Performance Operation

Having demonstrated superior performance (low baseline ε_i) of the ring-cusp thruster design over that of the state-of-the-art J-series thruster for operation at the nominal design

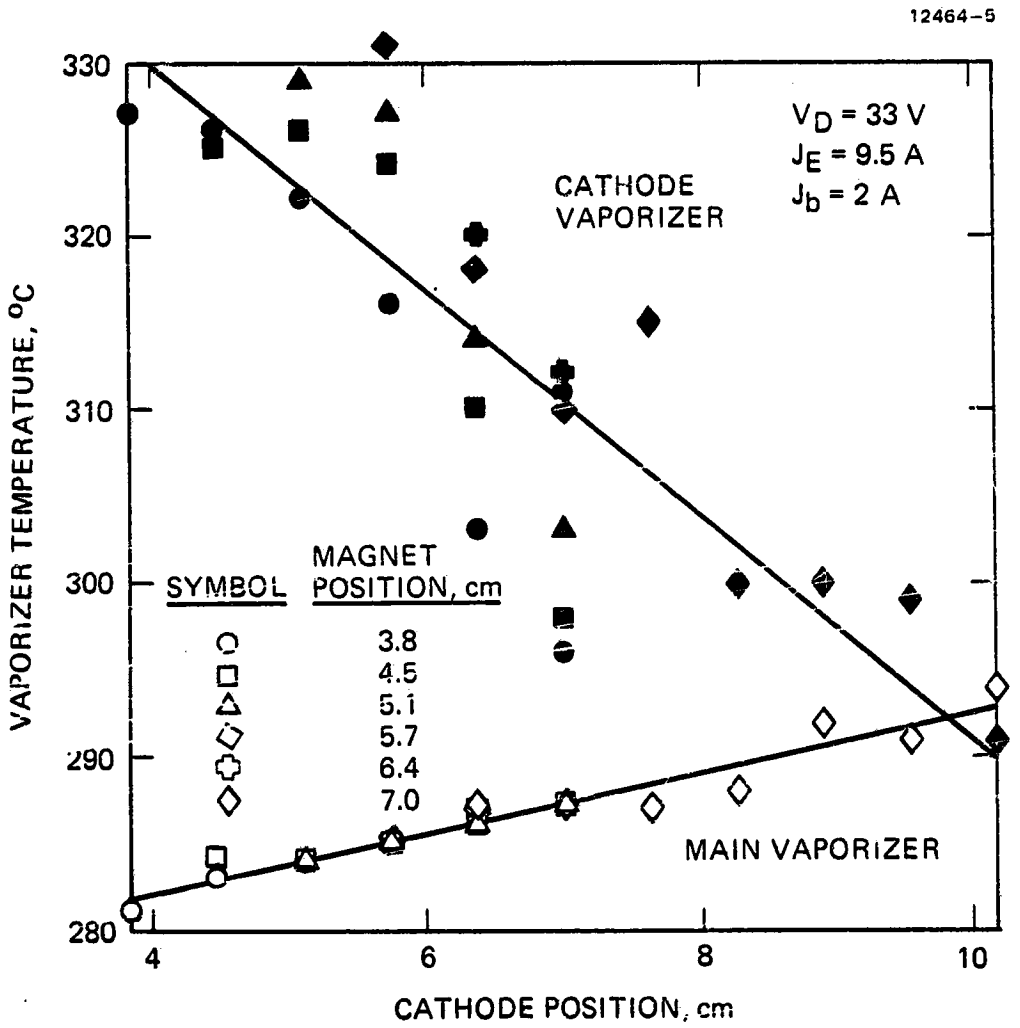

Figure 2-13. Summary of cathode and main-vaporizer-temperature measurements obtained using the movable cathode/cathode-magnet arrangement in the ring-cusp thruster. (Dimensions are relative to the thruster endwall).

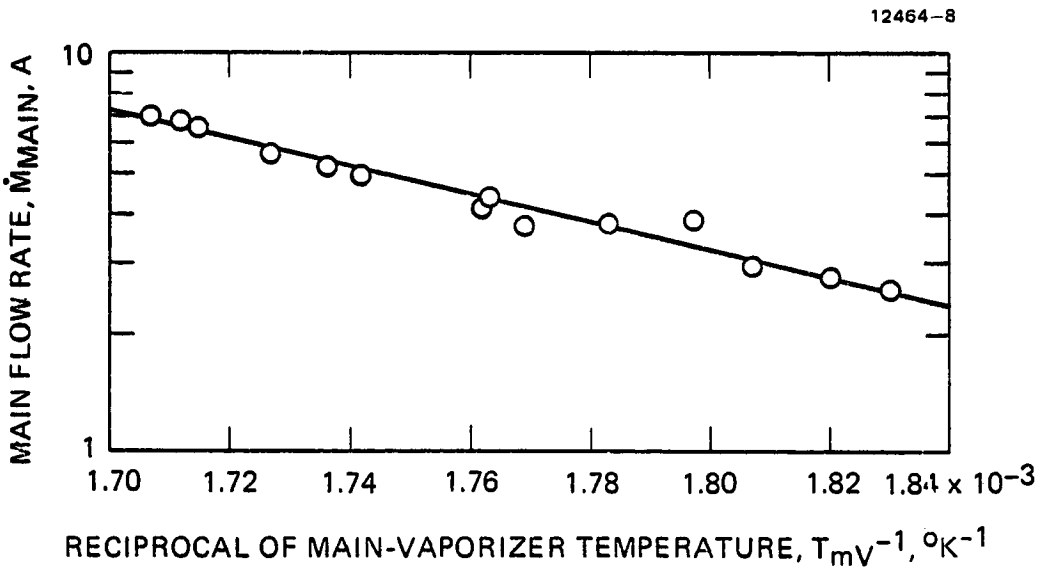

a. MAIN VAPORIZER

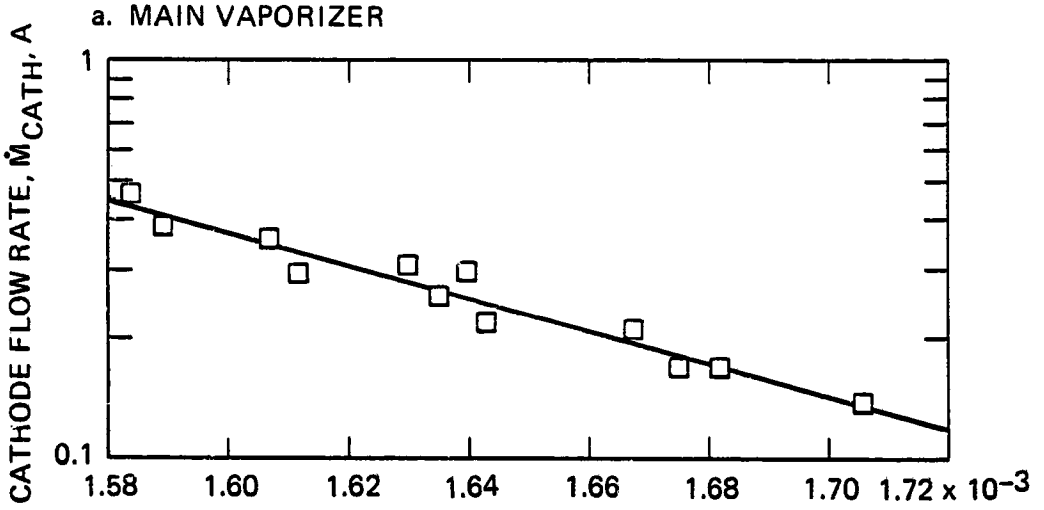

b. CATHODE VAPORIZER

Figure 2-14. Vaporizer calibration curves. (Not absolute measurements)

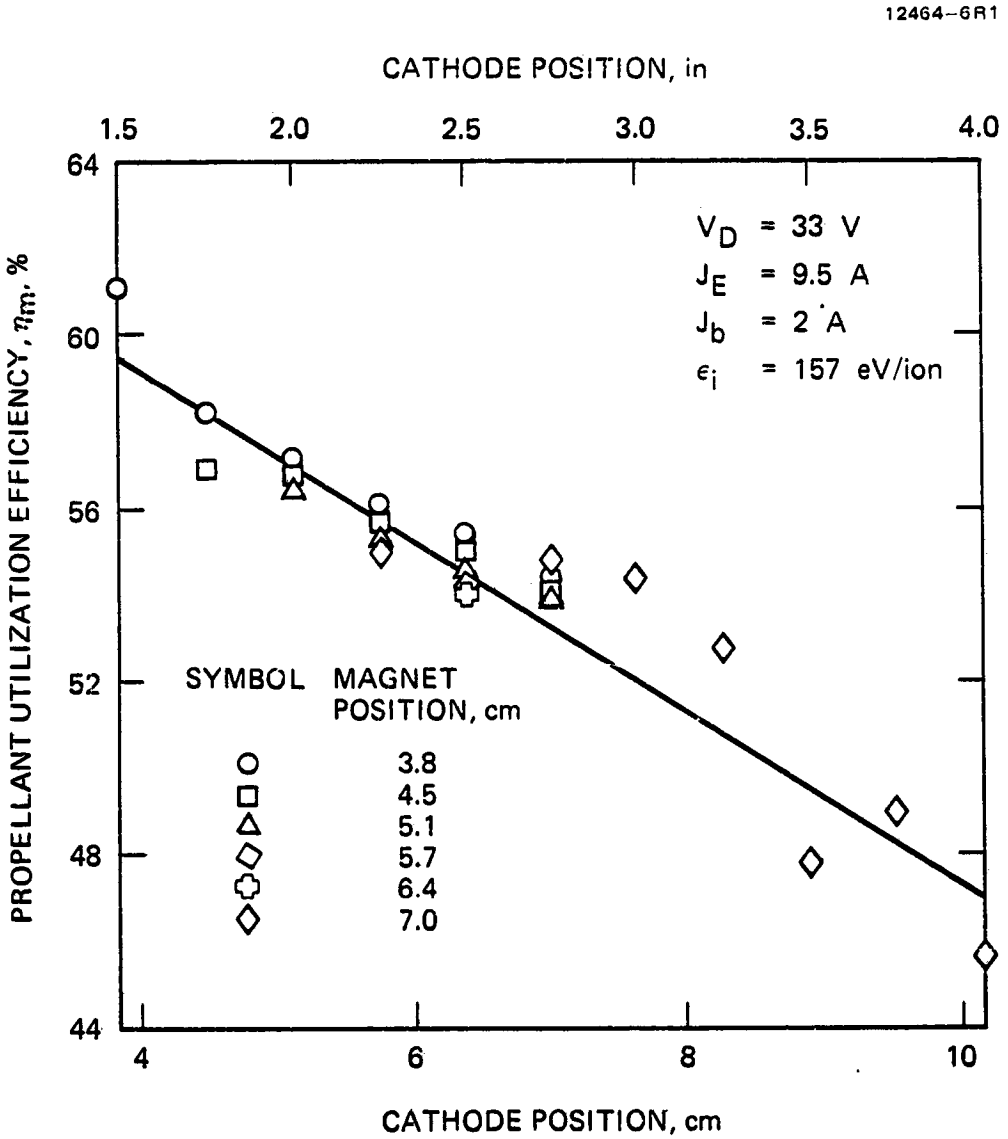

Figure 2-15. Effect of cathode and cathode-magnet positions on relative propellant-utilization efficiency. (Not absolute measurements)

point of J_b = 2 A, we investigated its performance at higher power levels. Figure 2-16 presents performance measurements for the ring-cusp thruster operated over the beam-current range 2 A $\leq J_b \leq$ 5 A. These results suggest a "knee" performance of about 125 eV/ion and show that little gain in propellant utilization occurs above 180-200 eV/ion. The increase in maximum-propellant-utilization efficiency with beam current is consistent with Kaufman's theory of constant neutral loss rate. The 4-A and 5-A curves do not cover the range $\varepsilon_i > 180$ eV/ion because the maximum power that the laboratory-model thruster can dissipate without exceeding 260°C magnet temperature is about 750 W. This arbitrary upper limit on allowable magnet temperature was selected to provide a comfortable margin-of-safety below the maximum safe value of 325°C.

The propellant-utilization efficiencies of Figure 2-16 have not been corrected for the effects of multiply charged ions, so that values of η_m greater than 100% are indicated. Inasmuch as the effects of multiply charged ions are expected to be relatively small at lower discharge voltages and beam currents, the high propellant-utilization efficiencies observed at V_D = 32 V and J_b = 2 A suggest that the ring-cusp discharge chamber is also highly efficient in this aspect of its performance.

Table 2-2 summarizes the electrical measurements and performance calculated from these measurements for operation near the "knee" of the performance curves. The (uncorrected) thrust corresponding to a beam current of J_b = 5 A is about a factor-of-three greater than that produced by the J-series thruster.

4. Beam-Current-Density Profile

We operated the ring-cusp discharge chamber with a three-grid ion-extraction assembly (described in the Section 3) for beam currents up to J_b = 5.3 A. The extracted ion-current-density profiles measured 3-mm downstream of the decelerator

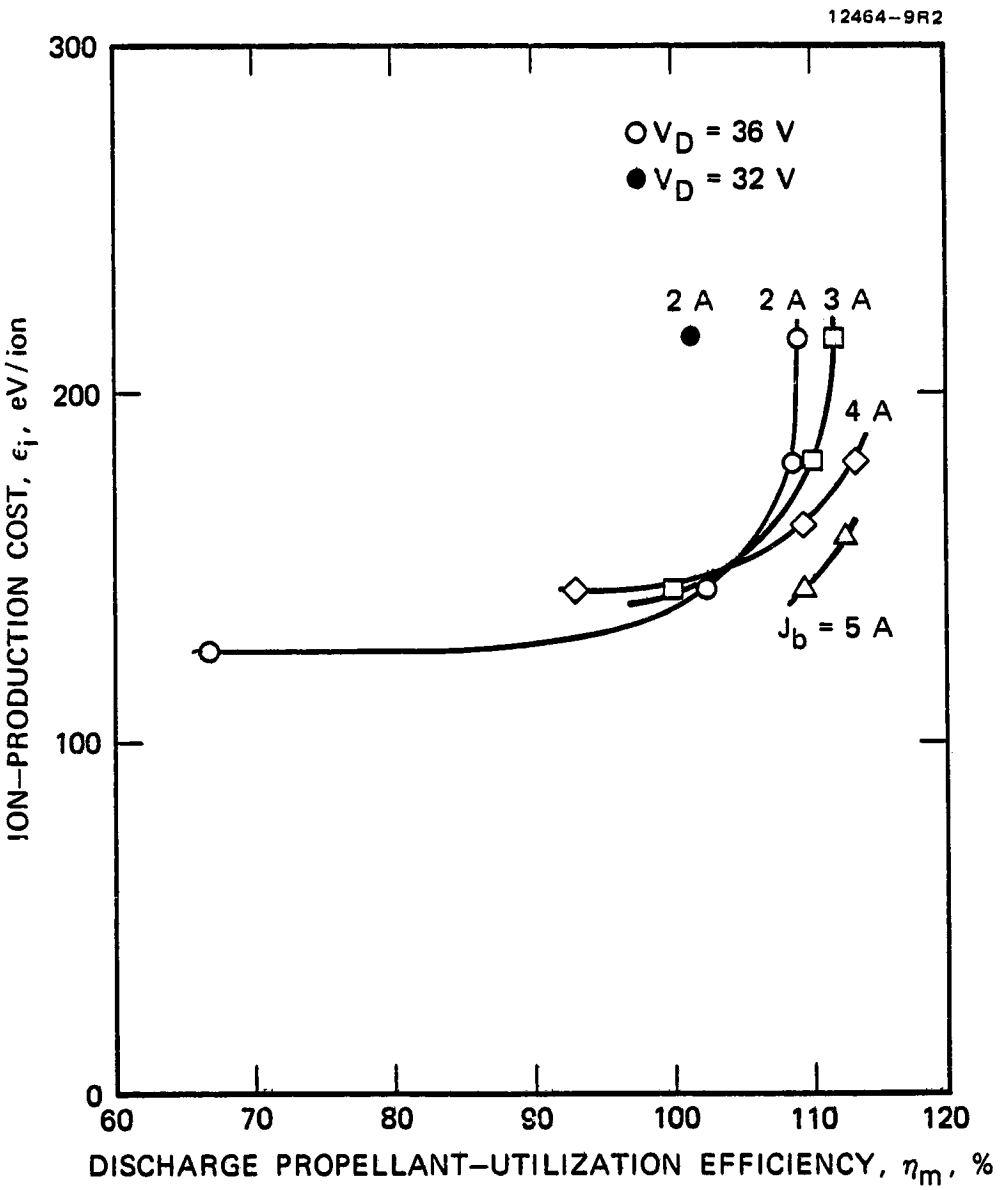

Figure 2-16. Ring-cusp-thruster performance measurements. (Propellant-utilization efficiencies uncorrected for multiply charged ions.)

Table 2-2. Summary of Electrical and Performance Measurements for the Ring-Cusp Thruster

		TEST NUMBER											
		1	2	3	4	5	6	7	8	9	10	11	12
V_b	V	1200	1200	1200	1200	1325	1325	1325	1290	1290	1290	1225	1225
J_b	A	2.0	2.0	2.0	2.0	3.0	3.0	3.0	4.0	4.0	4.0	5.0	5.0
V_D	V	36.0	36.0	36.0	36.0	36.0	36.0	36.0	36.0	36.0	36.0	36.0	36.0
J_D	A	9.0	10.0	12.0	14.0	15.0	18.0	21.0	20.0	22.0	24.0	25.0	27.0
J_E	A	7.0	8.0	10.0	12.0	12.0	15.0	18.0	16.0	18.0	20.0	20.0	22.0
J_{DECEL}	mA	4.95	1.17	1.19	1.50	1.98	2.13	2.33	3.13	3.18	3.50	5.40	4.47
V_{CK}	V	13.0	10.9	10.0	9.44	10.2	9.69	8.90	9.96	9.29	9.20	9.70	9.23
J_{CK}	A	1.0	1.0	1.0	1.0	1.0	1.0	1.0	1.0	1.0	1.0	1.0	1.0
V_{ACCEL}	V	-300	-300	-300	-300	-525	-525	-523	-860	-860	-860	-1225	-1125
J_{ACCEL}	mA	14.0	4.83	4.08	3.88	8.35	6.72	5.74	13.75	10.6	8.98	21.5	13.1
V_{NK}	V	15.5	15.5	15.5	15.5	15.3	15.3	15.5	14.0	13.9	13.9	14.4	14.5
J_{NK}	A	2.0	2.0	2.0	2.0	2.0	2.0	2.0	2.5	2.5	2.5	3.1	3.1
V_G	V	11.0	10.3	10.2	10.2	12.4	12.2	12.4	11.3	12.3	12.3	12.7	13.3
$\dot{m}_{MV}$	eq A	2.894	1.818	1.629	1.524	2.836	2.452	2.286	4.122	3.392	3.192	4.361	4.167
$\dot{m}_{CV}$	eq A	0.090	0.139	0.212	0.308	0.164	0.271	0.403	0.182	0.265	0.341	0.207	0.286
$\dot{m}_{TOTAL}$	eq A	2.984	1.957	1.841	1.832	3.000	2.723	2.689	4.304	3.657	3.533	4.568	4.453
$\eta_{mD\,(UNC)}$	%	67.0	102.2	108.6	109.2	100.0	110.2	111.6	92.9	109.4	113.2	109.5	112.3
P_b	W	2400	2400	2400	2400	3975	3975	3975	5160	5160	5160	6125	6125
P_{TOT} (1)	W	2718	2751	2821	2893	4485	4592	4700	5826	5901	5973	6963	7038
η_e (1)	%	88.3	87.3	85.1	83.0	88.6	86.6	84.6	88.6	87.4	86.4	88.0	87.0
ε_i	W/A	126	144	180	216	144	180	216	144	162	180	144	158
F (2)	mN	141.3	141.3	141.3	141.3	222.7	222.7	222.7	292.9	292.9	292.9	356.8	356.8
I_{SP} (2,3)	sec	2323	3544	3765	3786	3643	4015	4066	3340	3933	4069	3836	3934
η_T (1,2,3)	%	59.2	89.2	92.4	90.6	88.6	95.4	94.4	82.3	95.6	97.8	96.4	97.7

1. Neglects vaporizer power
2. $\alpha F_t = 1.0$
3. Neglects neutralizer flow

electrode are presented in Figure 2-17 for beam currents in the range 1 A $\leq J_b \leq$ 5 A. The calculated beam-flatness parameter for these profiles is approximately F = 0.4, which is about equal to that of divergent-field designs such as the 30-cm J-series thruster. The relatively non-uniform profile (as compared to those of the single-cusp and multipole discharge chambers discussed below) is believed to be a result of the strong magnetic field, which penetrates into the bulk of the discharge-chamber volume, giving rise to plasma-density gradients.

5. Wall-Probe Measurements

We measured the distribution of electron and ion currents to the chamber boundaries using the anode-cover arrangement of Figure 2-6 to measure the electron currents to the magnet rings, and using the ion-flux probe illustrated in Figure 2-18 to measure local ion currents collected by the chamber sidewall. We also documented the electron current collected by the propellant plenum and the ion flux to the cathode magnet and screen electrode under various operating conditions, and with these latter electrodes biased 27-V negative with respect to the cathode to ensure ion saturation.

Figure 2-19 shows the distribution of electron and ion currents to the chamber boundaries and internal electrodes. The electron current is observed to be almost entirely collected by the two magnet rings located near the ion-extraction assembly. The ion current densities derived from the wall-probe data are only about 1/10 as large as the current density at the ion-extraction assembly, suggesting that ions preferentially drift to the downstream end of the chamber.

When the wall probes were electrically connected to the cathode (through the current meters shown in Figure 2-10) their net current was positive (ion collection exceeded electron collection) and essentially independent of ion-production cost

12464-7R1

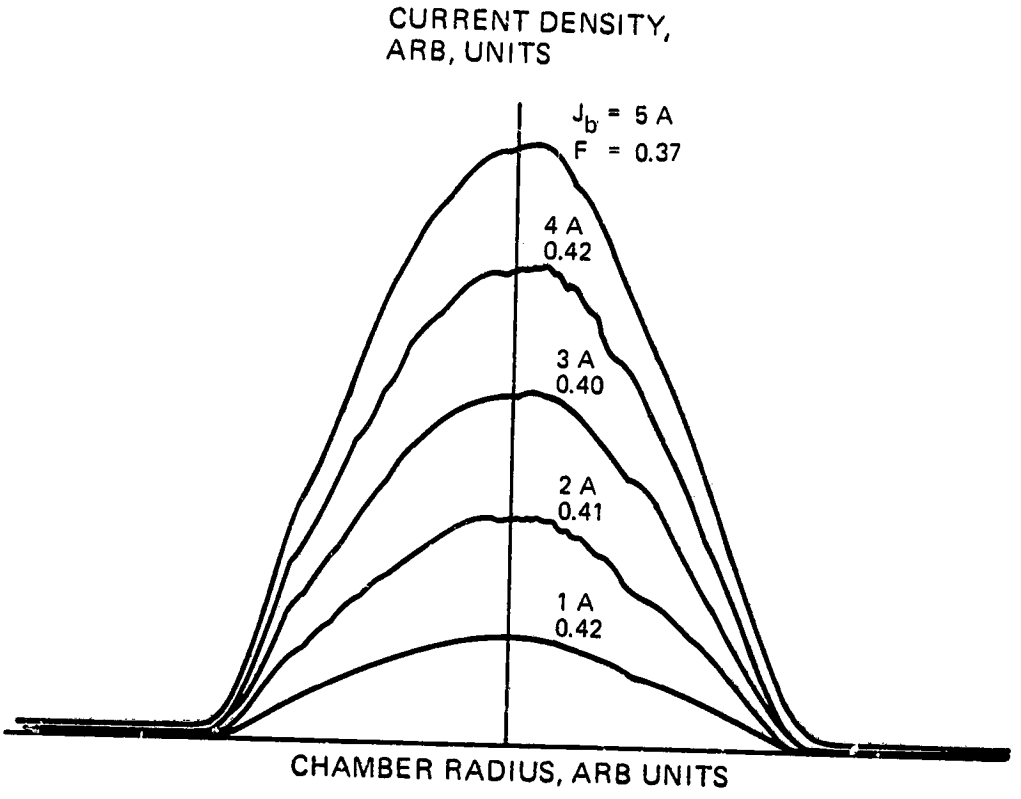

Figure 2-17. Ring-cusp-thruster beam profiles.

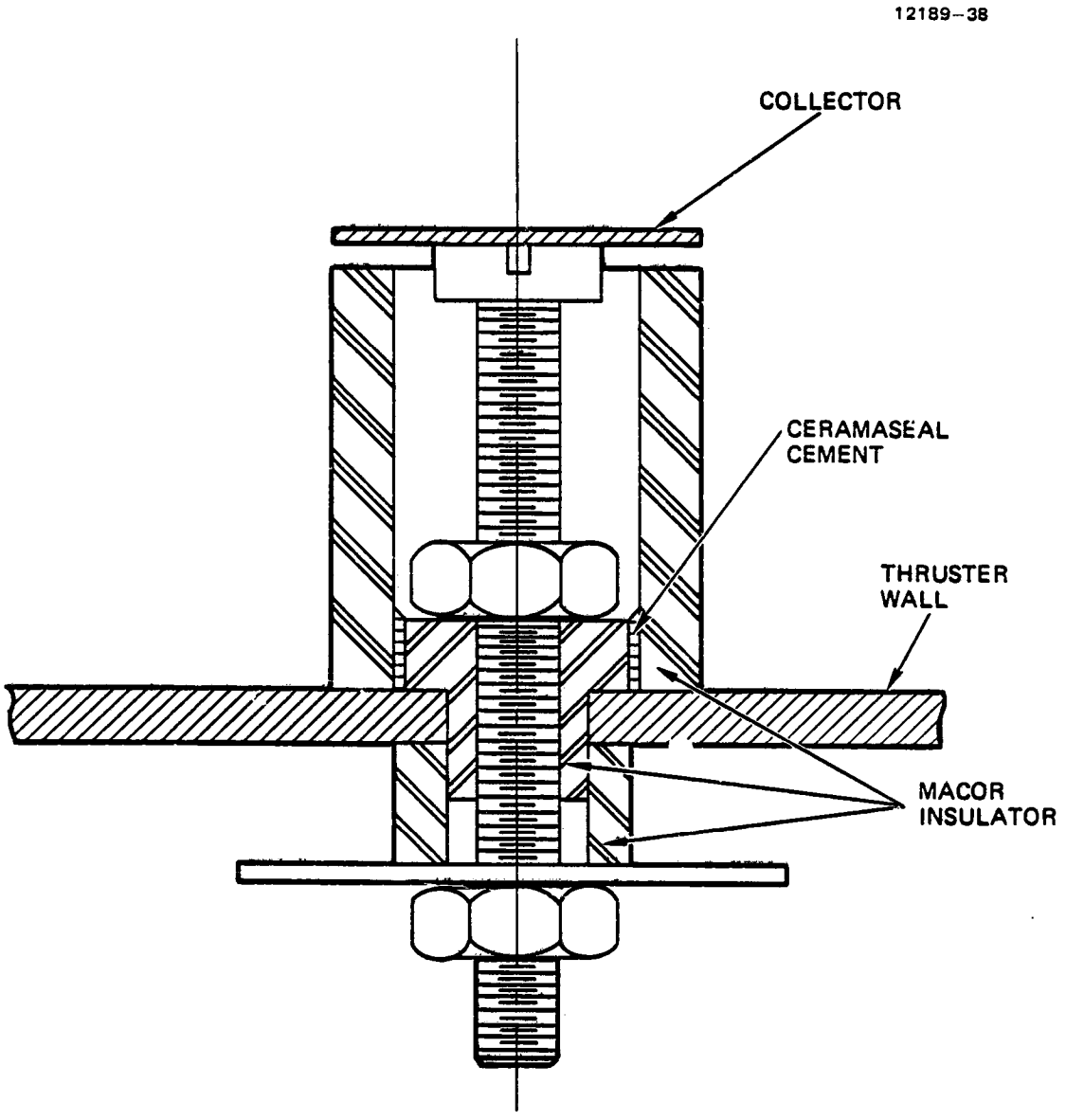

Figure 2-18. Construction details of ion-flux probe. (Collector area is 0.74 cm^2.)

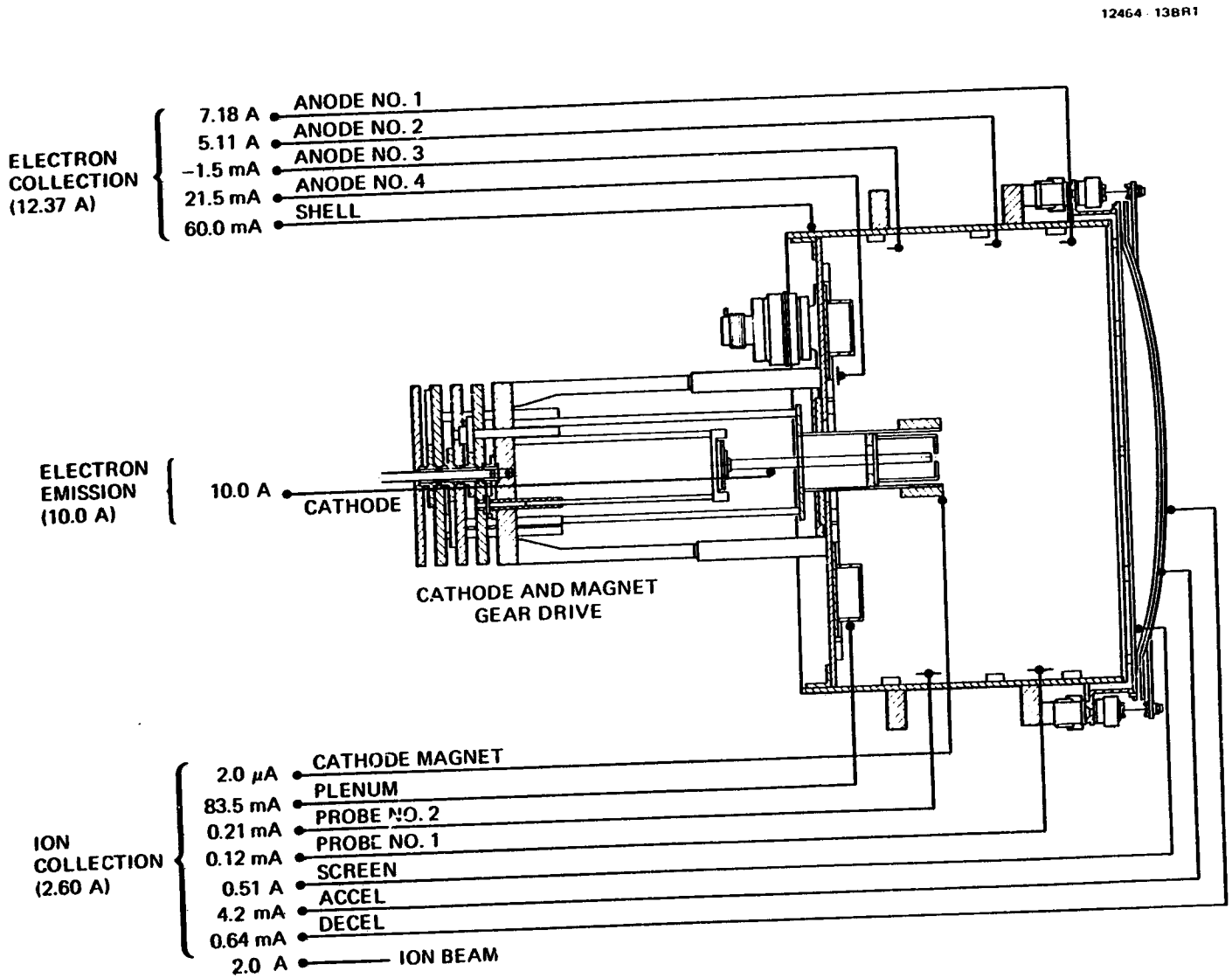

Figure 2-19. Distribution of electron and ion currents in the ring-cusp thruster.

(cathode-emission current), as shown in Figure 2-20. The screen grid, on the other hand, was observed to change from a condition of net-ion current collection to one of net-electron current collection as the ion-production cost was increased. These measurements are also shown in Figure 2-20, which indicates that the net-electron current tends to saturate at about ε_i = 180 eV/ion. The transition from net-ion collection to net-electron collection occurs at about J_E = 8.5 A, which corresponds to the "knee" of the performance curve (≈150 eV/ion for these conditions).

6. Langmuir-Probe Measurements

We documented the transition from net-ion to net-electron current collection by performing Langmuir-probe surveys under operating conditions that placed us on either side of the transition point. The diagnostic measurements were conducted using the probe-sweep and data-acquisition system shown in Figure 2-21. The sweep circuit varies the probe voltage from -20 V to +80 V (with respect to cathode potential) over a period of about 1 sec. Isolation amplifiers are used to isolate the probe circuit from the data-acquisition system, which consists of a multiplexed, 16-channel analog-to-digital converter interfaced with an S-100 Microsystems computer. The digital results are stored on floppy disks, with the information later used by a VAX 11/780 computer that performs the numerical analysis[2-4] leading to the plasma properties.

Interpretation of the probe characteristics showed that the electron-energy-distribution function is predominantly Maxwellian beyond a central "core" which extends downstream of the cathode. Within the core, the distribution function is the sum of a monoenergetic (or primary) plus a Maxwellian contribution (see Appendix A). The spatial variation of the plasma properties shows that the two-group description fits the measurements quite well throughout the cross-hatched region shown in Figure 2-22. In this sense, the spatial variation of

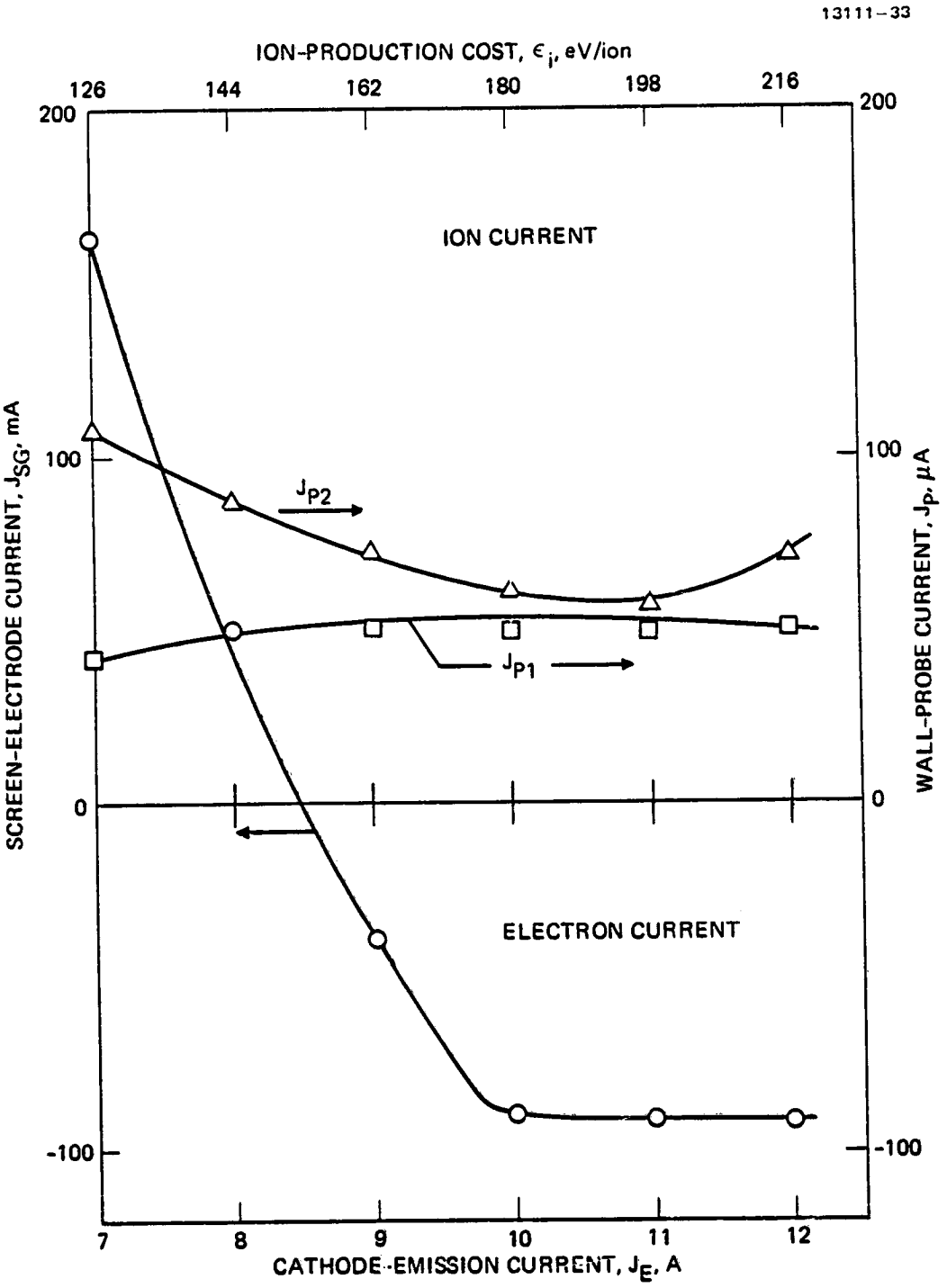

Figure 2-20. Electron and ion currents to the screen electrode and wall probes in the ring-cusp thruster.

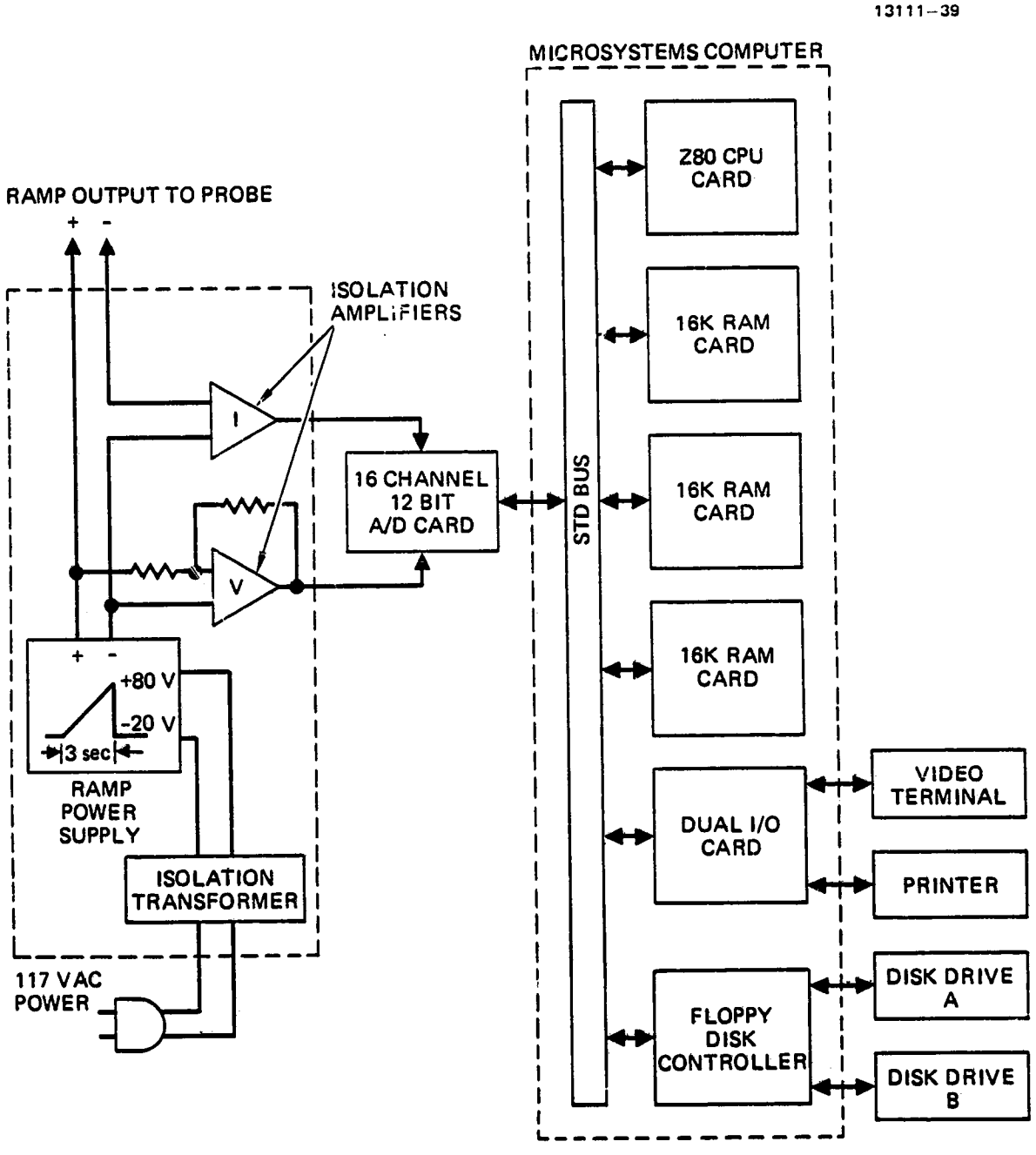

Figure 2-21. Block diagram of probe-sweep and data-aquisition system used for conducting Langmuir-probe measurements.

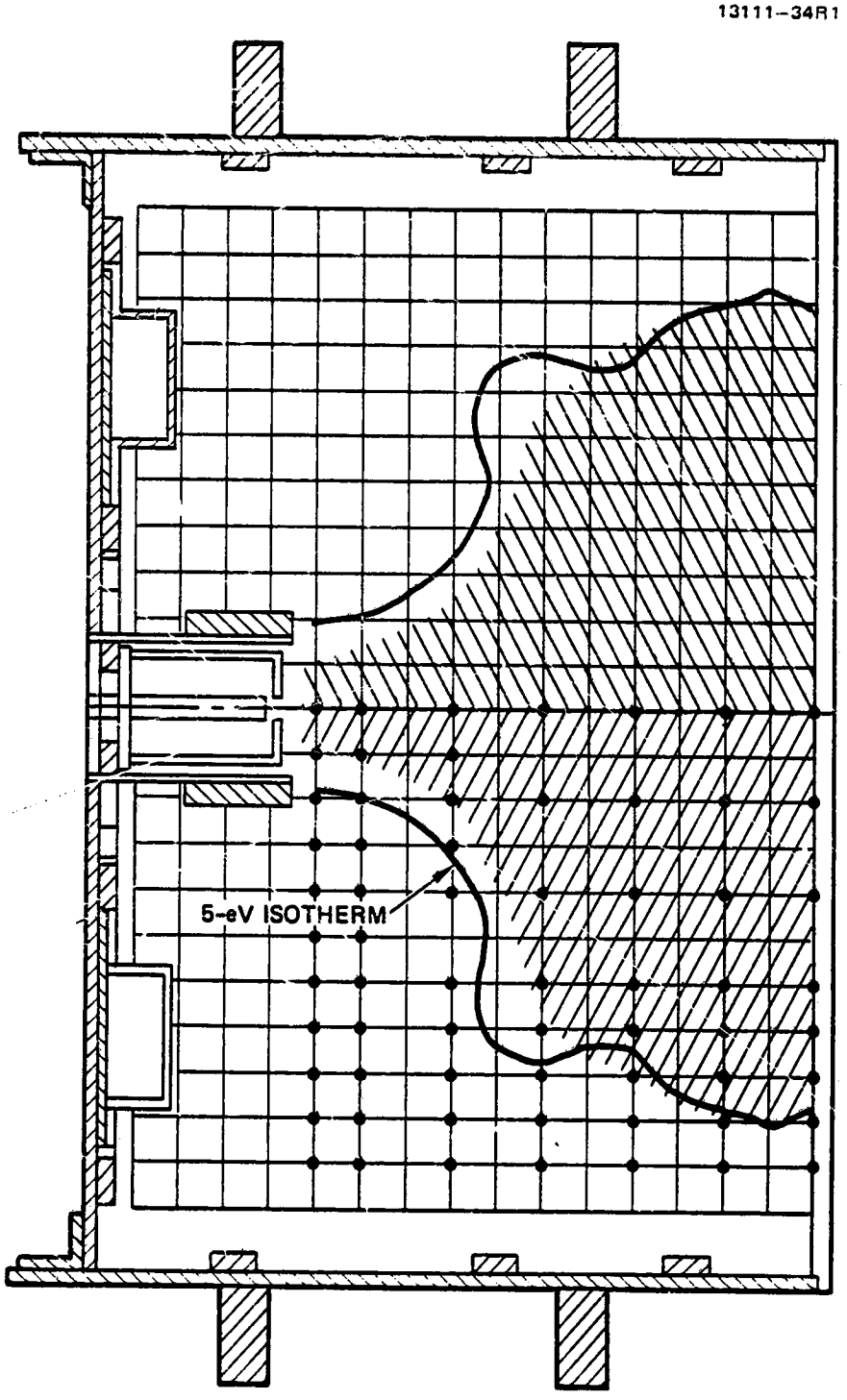

Figure 2-22. Region of the ring-cusp discharge chamber where the two-group-plasma assumption is valid.

of the electron-energy-distribution function within the ring-cusp discharge chamber is similar to those observed in other configurations (such as the divergent-field thruster); the primary electrons exist predominately in the central region defined by the location of the cathode and the "critical magnetic-field line." Beyond this boundary the electron energy and ionization rate drop rapidly.[2-5]

An indication of the location of the gradients in plasma properties is evident in Figure 2-22 in the form of the density of the "dots", which denote the locations at which we performed our final probe measurements. An initial survey was conducted in which we determined the minimum number of probe locations required to characterize the plasma by performing measurements at each of the locations indicated by the mesh points of Figure 2-22. The closeness of the "dots" representing the probe-measurement locations is an indicator of the regions where steep gradients in plasma properties could be detected by comparing the probe characteristics. Figure 2-22 also shows the 5-eV Maxwellian-electron isotherm, which is seen to roughly coincide with the boundary of the "core" region of the plasma, separating the uniform and non-uniform regions.

Viewing the ring-cusp discharge chamber as others (such as the divergent field and single-cusp configurations) have been in the past allows one to deduce that the primary ionization volume is bounded at one end of the chamber by the electron-emitting cathode, and at the other end by the cathode-potential screen grid. The remaining boundary is established by the surface of revolution defined by the magnetic-field lines that pass near the cathode orifice and terminate on the magnet rings. This description leads to a predicted ion-production volume that has the approximate geometry shown in Figure 2-23.

The electron-temperature distribution is shown in Figure 2-24. The isotherms have nearly the same shape as the

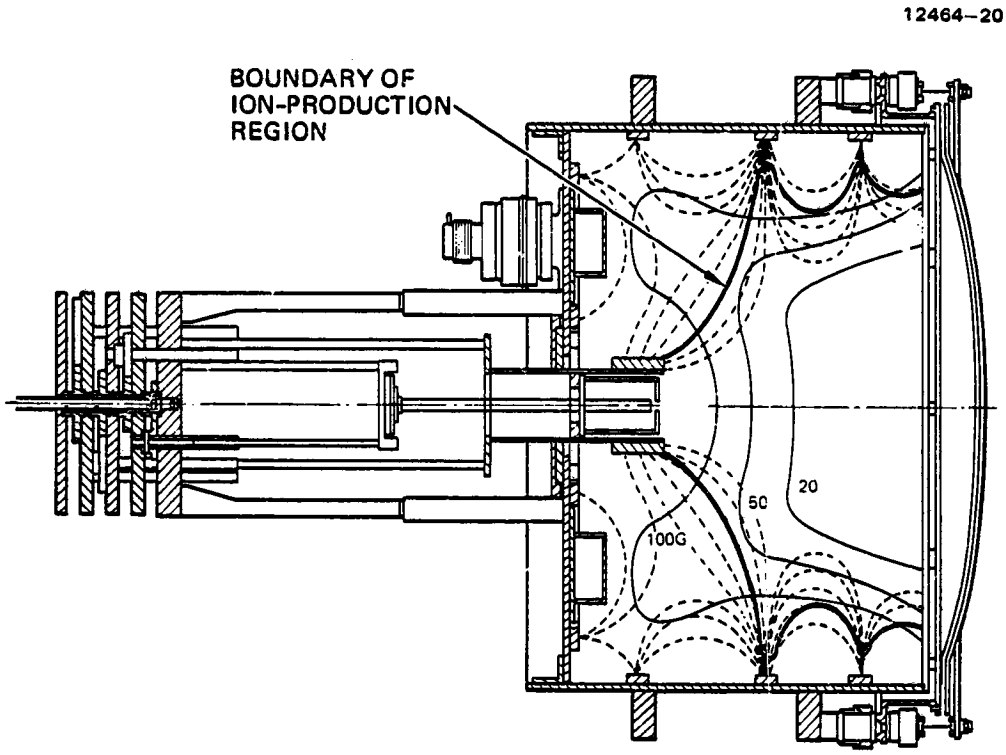

Figure 2-23. Predicted shape of the boundary of the ion-production region in the ring-cusp discharge chamber.

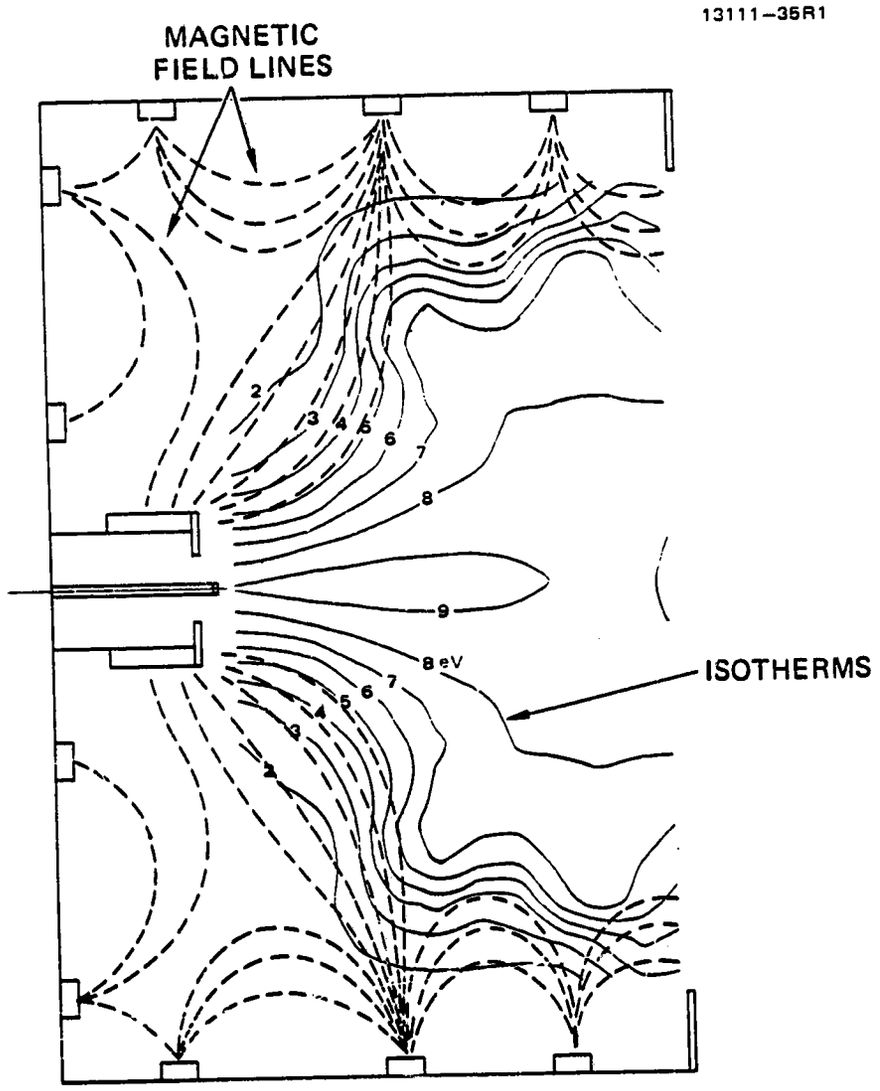

Figure 2-24. Maxwellian-electron isotherms in the mercury ring-cusp thruster, corresponding to operation near the "knee" of the performance curve.

magnetic flux lines [2-6]; their divergence into the volume downstream of the cathode results in relatively high (≈ 8 eV) temperature in the region near the screen electrode. The electron-density contours have the same general shape as the isotherms. The ionization collision frequency (defined* as $\nu = n_e Q_o^+$, where n_e is the electron density and Q_o^+ is the temperature-dependent ionization reaction rate) is presented in contour form in Figure 2-25 (the ionization collision frequencies have been normalized to the maximum value, ν_{max}), again showing the same general shape[2-5] as the magnetic field lines. The strong gradients in plasma properties are especially evident in this form, which shows that most of the ion-production occurs in the downstream region of the chamber, and that the bulk of the volume in the region upstream of the cathode contributes little or nothing to the ionization process. Plasma-potential contours are presented in Figure 2-26, showing the presence of a favorable potential gradient in the region upstream of the screen electrode, where most of the ionization occurs.

For purposes of comparison, Figure 2-27 presents collision-frequency contours for a 30-cm-diameter state-of-the-art J-series-equivalent thruster that were obtained under NASA contract NAS 3-21040. The contours diverge in the downstream direction, consistent with the divergence of the magnetic field. The spatial extent of the ion-production region in the upstream end of the chamber is noticeably greater than it is in the ring-cusp chamber (Figure 2-25) due to "spreading" of the source of electrons by the baffle and polepiece. The Maxwellian-electron isotherms have a shape similar to the collision-frequency contours, but the temperature near the center of the screen grid in the J-series-equivalent thruster is substantially lower than it is in the ring-cusp configuration.

*To simplify the calculations, we neglected the contribution due to the primary-electrons and used the plasma properties obtained under the assumption of a strictly Maxwellian distribution function.

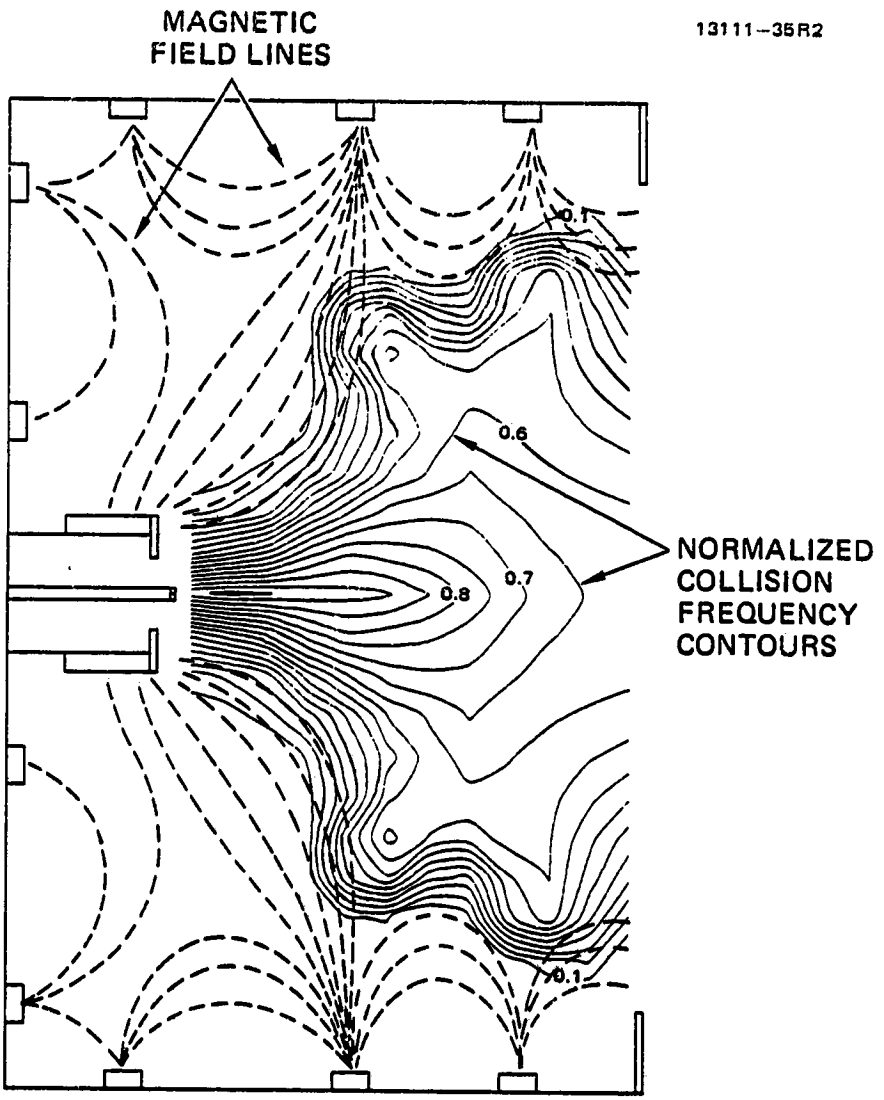

Figure 2-25. Contours of the ionization collision frequency in the mercury ring-cusp thruster, corresponding to operation near the "knee" of the performance curve.

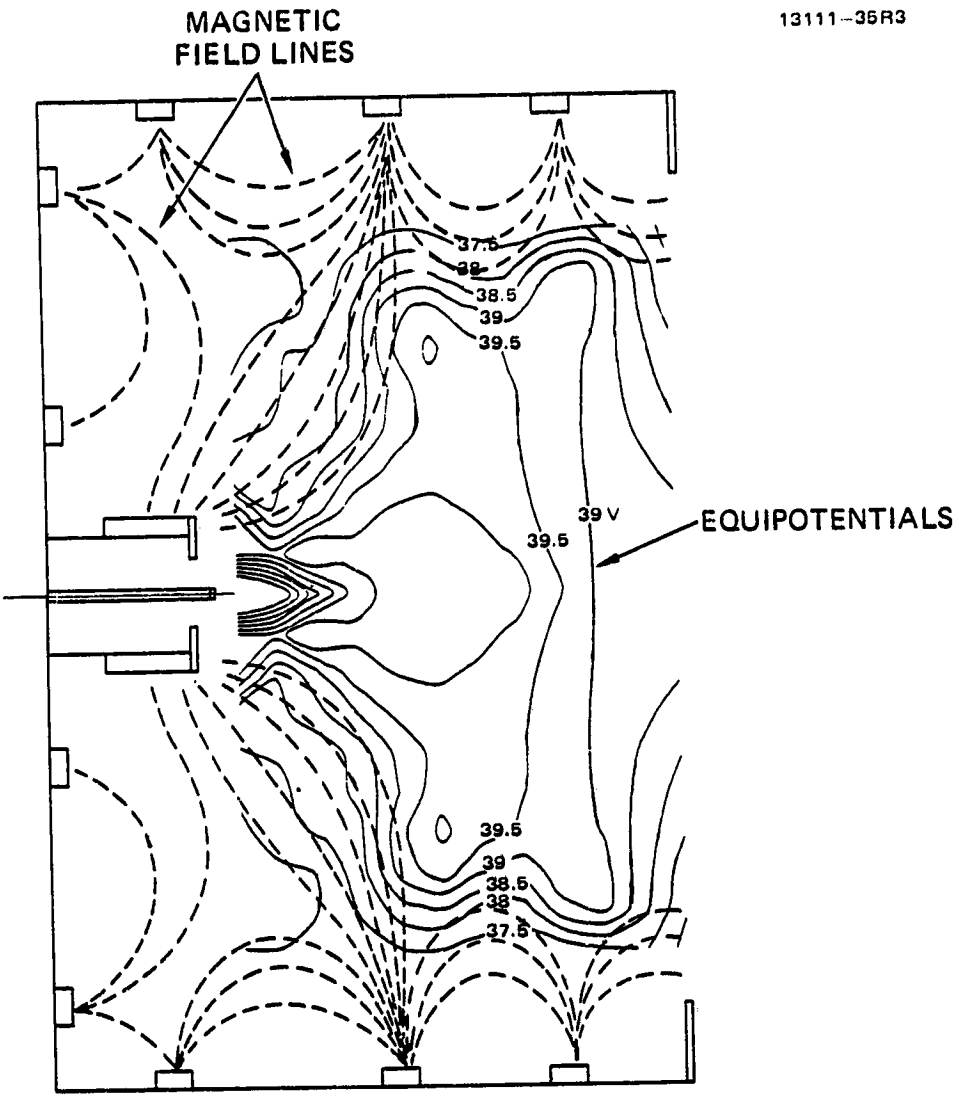

Figure 2-26. Plasma-potential contours in the mercury ring-cusp thruster.

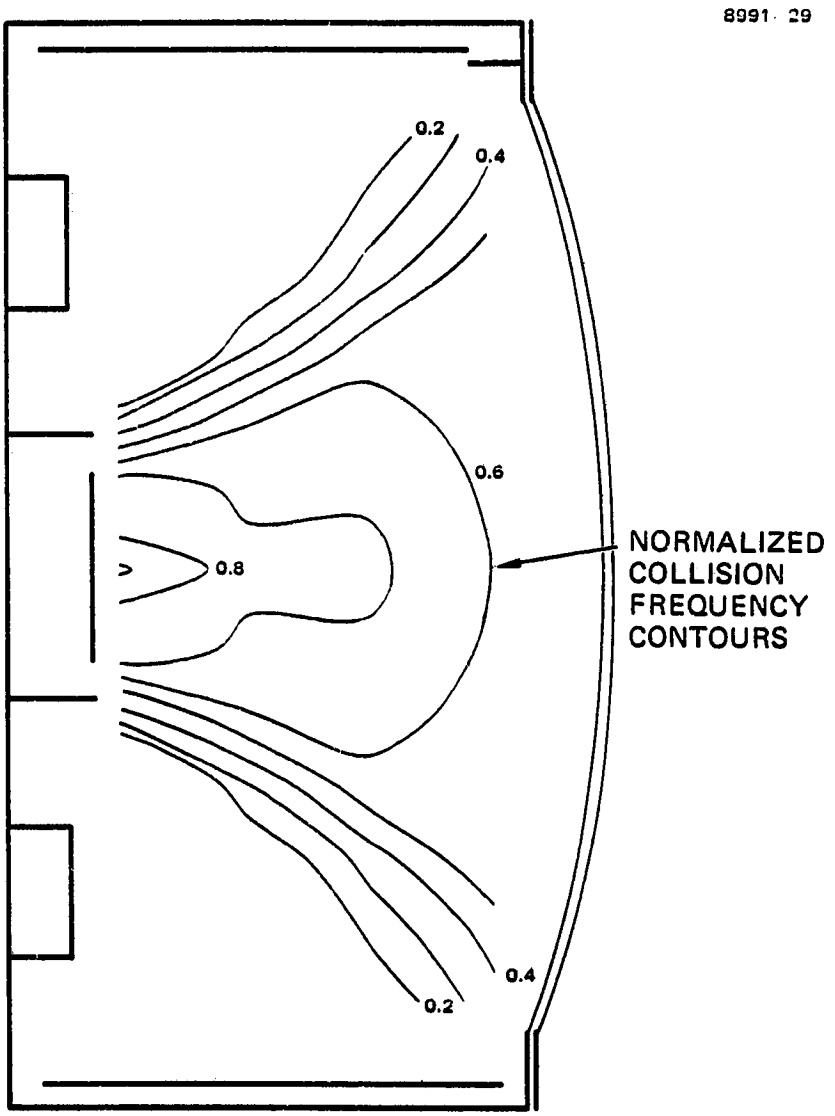

Figure 2-27. Contours of the ionization collision frequency in a 30-cm-diameter J-series-equivalent thruster.

The results presented in Figures 2-24 through 2-26 correspond to operation near the "knee" of the performance curve, which in the discussion of boundary currents was indicated to be characterized by net-electron current collection at the cathode-potential screen electrode. Plasma-property measurements at lower eV/ion (where net-ion current is collected) have the same general characteristics as those obtained at higher eV/ion. However, the electron temperature is substantially lower when the thruster is operated under the less-efficient discharge conditions. This effect is evident by comparing Figure 2-24 with similar results presented in Figure 2-28. The overall temperature is higher and the isotherms are much more divergent under the high-eV/ion operating conditions. The temperature near the center of the screen grid is > 8 eV, allowing electrons in the high-energy tail of the distribution function to reach the cathode-potential surface. Probes located downstream of the accelerator electrode (no ion-beam extraction) in an inert-gas thruster[2-7] show that the collection of net-electron current occurs only in the center of the ion-extraction assembly, supporting the argument presented above.

7. Preliminary Model of the Ring-Cusp Discharge Chamber

Using the results presented above, we can formulate the following (partial) description of the plasma processes occurring within the ring-cusp discharge chamber:

- The bulk of the plasma is concentrated in the downstream end of the discharge chamber by the divergent-cusp magnetic field.
- Electrons emitted by the cathode are "guided" into the ion-production volume by the magnetic-field lines passing through the region near the cathode orifice.

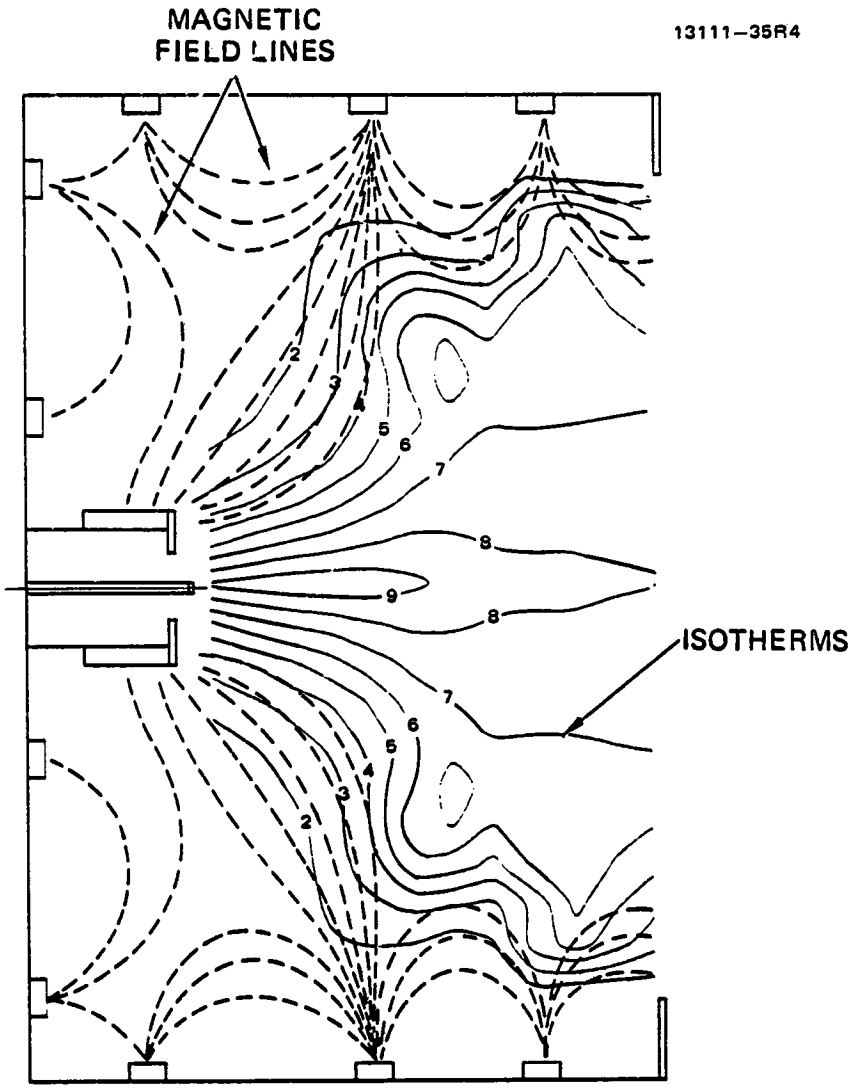

Figure 2-28. Maxwellian-electron isotherms in the mercury ring-cusp thruster, corresponding to operation below the "knee" of the performance curve.

- Electrons are repelled from the chamber (anode) boundaries by the large values of the integral $\int B d\ell$, and are predominantly collected by the cusp regions of the magnets located in the downstream end of the discharge chamber.

- Ions are preferentially lost to the downstream boundaries

In conventional divergent-field, single-cusp, and multipole discharge chambers, the magnetic fields are on the order of 100 G and, therefore, have little effect on ion trajectories. However, with magnetic fields on the order of 1,000 G typical of the ring-cusp thruster, the ion motion can be altered. Kaufman[2-8] has formulated the magnetic-field integral necessary to repel an electron of energy, ζ_p (eV), from a magnetically shielded anode as

$$\int B d\ell > 6.74 \sqrt{\zeta_p} \text{ , G-cm} \quad , \qquad (2\text{-}2)$$

where $\int B d\ell$ is the integral of the magnetic-field component perpendicular to the path ℓ. Using a similar approach, the magnetic-field integral required to repel a mercury ion travelling with the Bohm velocity* in a direction normal to a magnetically shielded surface can be formulated as

$$\int B d\ell > 1442 \sqrt{T_m} \text{ , G-cm} \quad , \qquad (2\text{-}3)$$

where T_m is the electron temperature in eV. The results obtained from Equations (2-2) and (2-3) are plotted in Figure 2-29, showing that for typical plasma conditions of ζ_p = 30 eV and T_m = 5 eV, the corresponding magnetic-field integrals are about 40 and 3,000 G-cm for electrons and mercury ions, respectively. For argon ions, the integral drops to about 1,400 G-cm because of the reduction in atomic mass.

*This approach is conservative, since there is evidence[2-10] that ions approach magnetically shielded anode-potential surfaces at a rate substantially less than that corresponding to Bohm diffusion.

12189-10

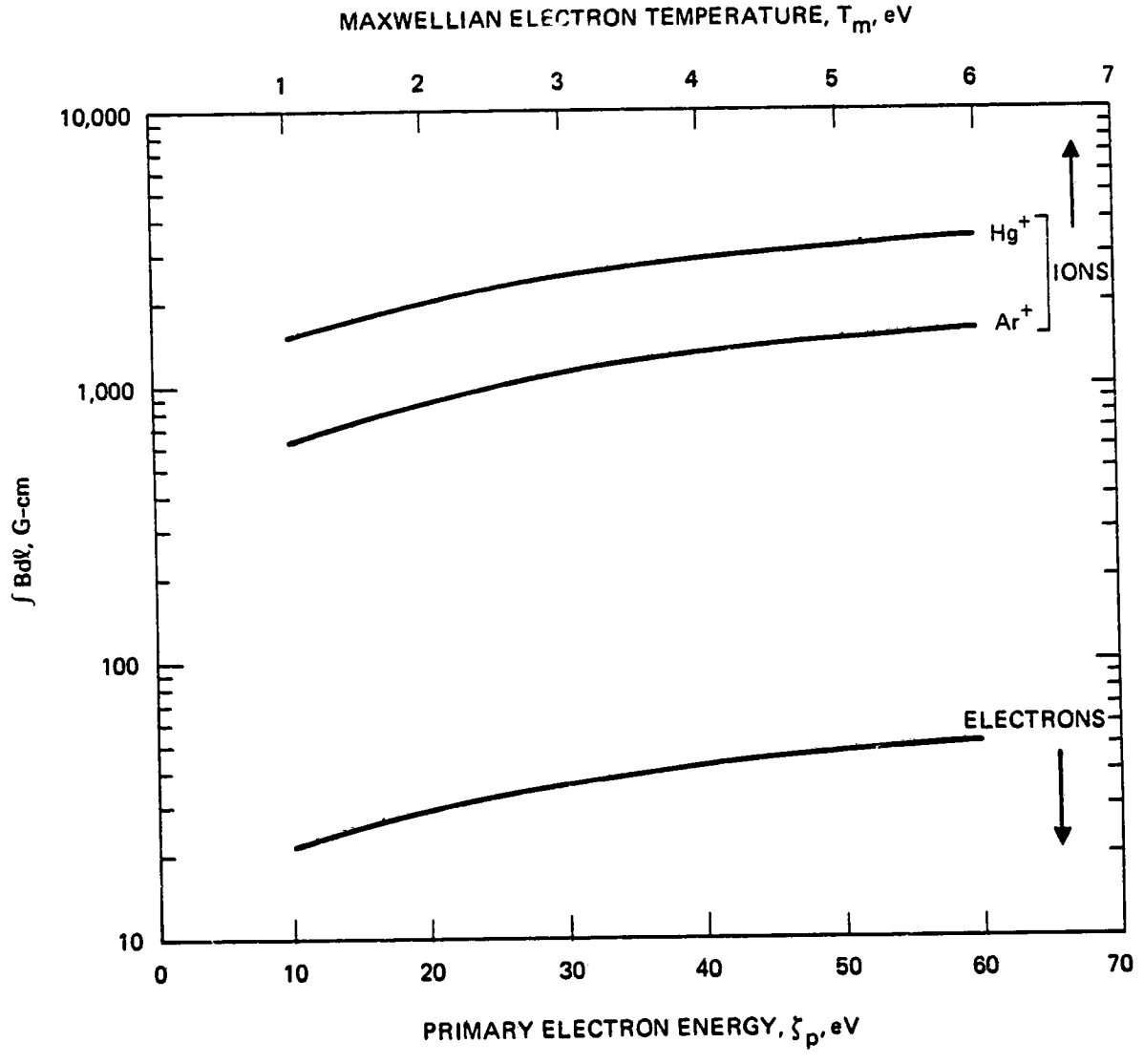

Figure 2-29. Values of the integral $\int Bd\ell$ required to repel electrons and ions from magnetically shielded chamber walls.

Using the magnetic-field measurements described above, we calculated values of the integral $\int B d\ell$ along various paths to the chamber walls. Our results are shown in Figure 2-30, indicating that values of the integral on the order of 1,000 G-cm are typical of this design. We believe, therefore, that ion trajectories can be influenced by the strong magnetic fields established by the ring-cusp confinement scheme. The magnetic deflection scales as the square root of atomic mass, so that lighter ions such as argon would be influenced to a greater degree. This should lead to better performance with lighter gases, a prediction that is borne out by the experimental results[2-7] obtained with a ring-cusp geometry similar to the one investigated here, and which performed somewhat better (25% lower eV/ion, using argon as the propellant).

B. SINGLE-CUSP DISCHARGE CHAMBER

In addition to the high-performance ring-cusp discharge chamber, we also investigated two alternative designs (the single-cusp and multipole) that employ weaker, boundary-type magnetic fields to produce a relatively field-free plasma volume, which should permit full utilization of the lifetime and perveance capabilities of the ion-extraction assembly. The single-cusp-magnetic-field configuration is conceptually similar to that of the ring-cusp arrangement, but with fewer cusps and weaker fields. The multipole-magnetic-field configuration is similar to the single-cusp arrangement, but with an increase in the number of cusps. In both the ring-cusp and single-cusp configurations, the electrons emitted by the cathode have access to the plasma volume bordering the ion-extraction assembly by transport along the diverging magnetic field lines, much like the conventional divergent-field design. By contrast, the electrons in the multipole-magnetic-field arrangement are emitted into a weak-field region, with the strong-field region near the chamber sidewall and endwall used to repel the energetic electrons.

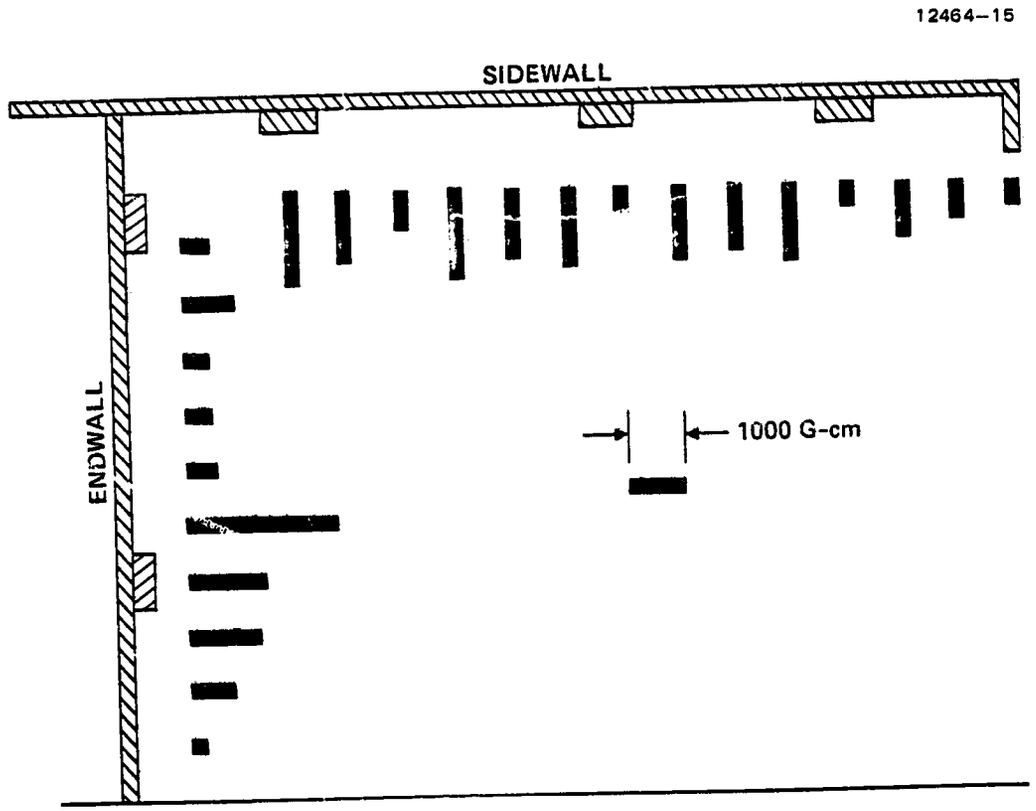

Figure 2-30. Measured values of the integral $\int B d\ell$ in the ring-cusp discharge chamber.

A sketch of the laboratory-model single-cusp thruster is shown in Figure 2-31. The discharge-chamber configuration is arrived at by incorporating a relatively minor structural modification in the state-of-the-art J-series thruster (the addition of an upstream anode and pole piece) to produce the desired magnetic-field geometry. Axial and radial electromagnets are employed in the laboratory-model configuration, permitting rapid variation of the magnetic-field strengths. Separate power supplies (and a switching arrangement) enable the magnetic-field geometry (in the operating thruster) to be changed from the conventional divergent-field geometry to the advanced single-cusp configuration. This feature allowed the effects of a radical change in plasma-confinement technique to be evaluated in real-time, while maintaining essentially constant thruster-operating conditions.

The discharge chamber was equipped with the movable cathode assembly shown in Figure 2-32. We designed and fabricated this highly functional apparatus, and we utilized it to optimize the locations of the cathode and associated components in each of the discharge-chamber configurations that we investigated (the ring-cusp, single-cusp, and multipole). The movable-cathode arrangement of Figure 2-32 enabled the axial position of the cathode pole piece, magnet pole piece, baffle, and cathode-keeper assembly to be independently varied during thruster op ration. This is accomplished using a single drive shaft to engage one of the four drive gears that transfer motion to the corresponding cathode component. The appropriate gear is selected using a "gear-shift" arrangement, and the location of each component is tracked and displayed using a potentiometer and a digital readout. A solenoid positioned around the outside of the cathode pole piece was used to produce the magnetic field within the baffle-aperture region; the open area of this region could be varied by replacing the (movable) baffle plate. The pole piece, baffle, and baffle supports were fabricated using low-sputter-yield niobium.

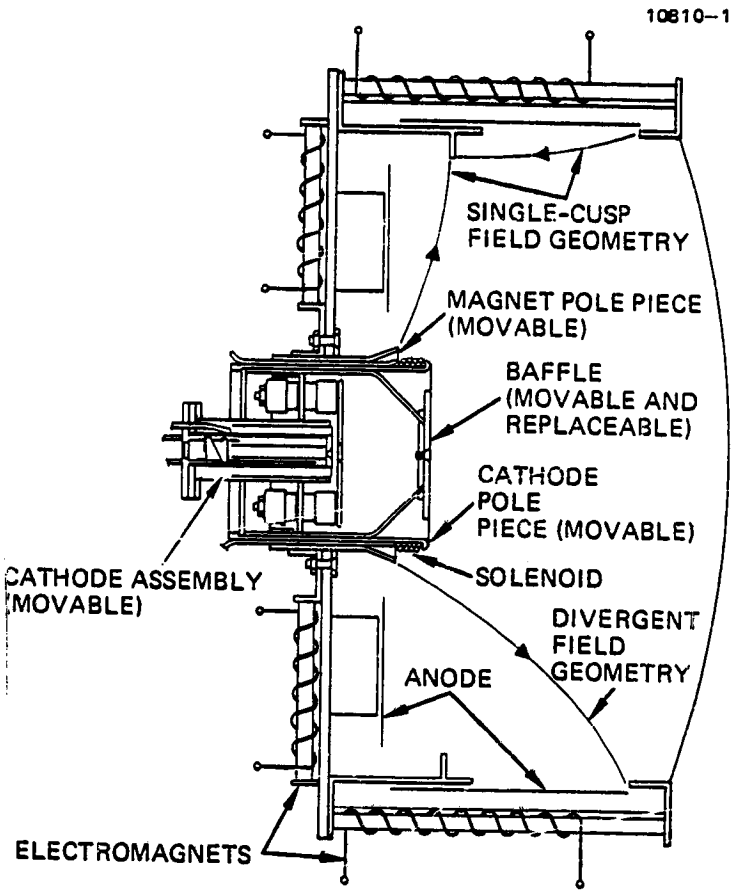

Figure 2-31. Schematic of Hughes 30-cm single-cusp thruster (shown with high-emission-current cathode described in Section 4).

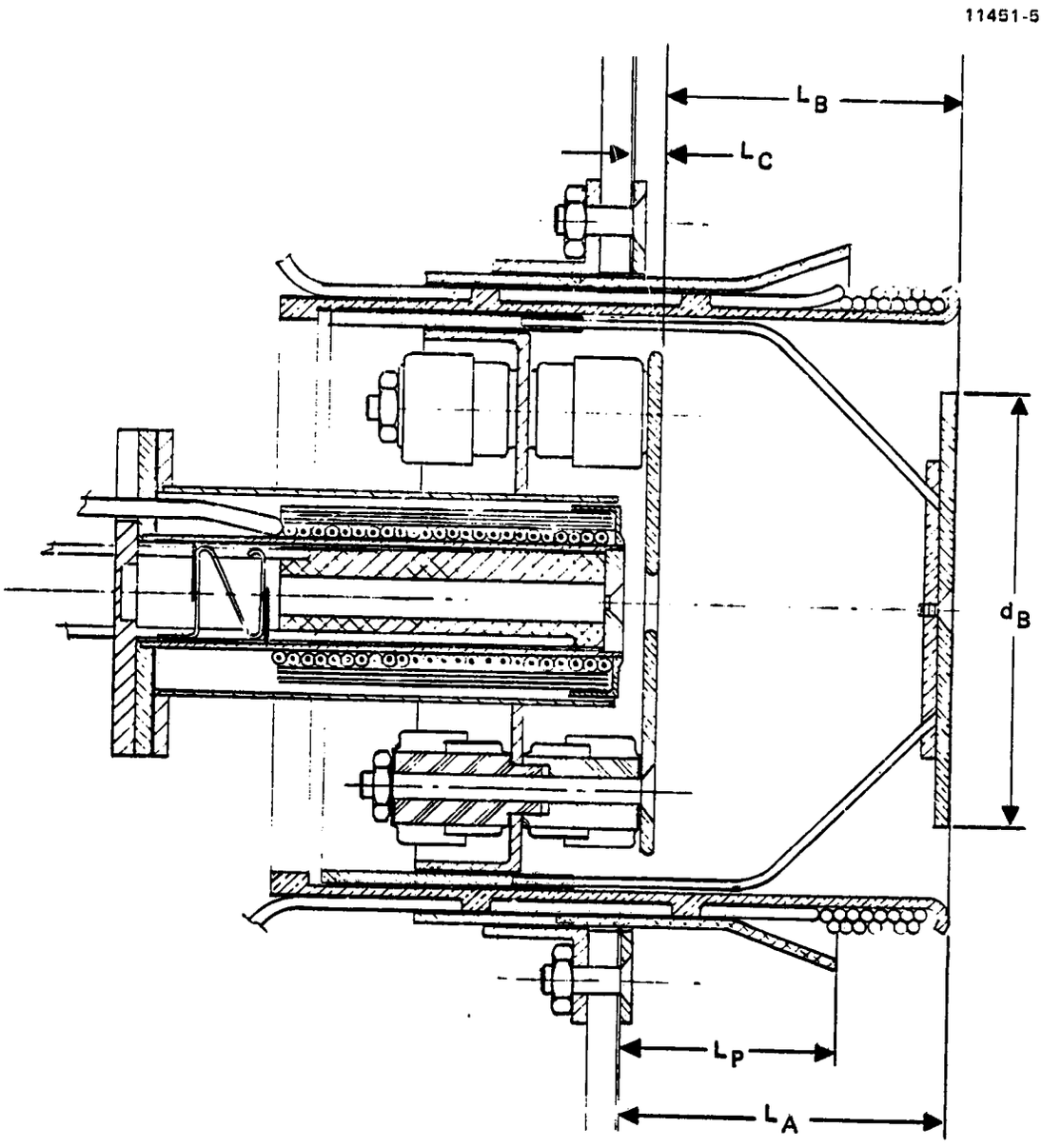

Figure 2-32. Geometric variables and arrangement of the movable cathode/polepiece/baffle assembly (shown with high-emission-current cathode described in Section 4).

Figure 2-33 presents performance measurements obtained with this thruster (operated as both a conventional divergent and advanced single-cusp configuration), showing that good performance (comparable to that of the highly optimized J-series thruster) was obtained with both magnetic-field arrangements. A comparison of the beam-current-density profiles obtained with the single-cusp and divergent magnetic-field arrangements is presented as Figure 2-34. The single-cusp profile is much more uniform, as anticipated. The reduction in maximum current density results in a 45% increase in the beam-flatness parameter, which implies a corresponding increase in the lifetime of the screen electrode.[2-11] The calculated flatness parameter of the single-cusp profile of Figure 2-34 is F = 0.85, based on the active area of the electrodes. This high degree of uniformity is comparable to the results presented below for the multipole thruster.

C. MULTIPOLE DISCHARGE CHAMBER

The design details of the 30-cm-diameter multipole thruster are shown in Figure 2-35. The sidewall of the discharge chamber uses 2.7-cm-wide sections consisting of the magnets, pole pieces, anode, and insulators. These sections are "stacked" together to produce the desired overall chamber length. The criteria we followed in designing the chamber was to provide an integral of magnetic-field strength (along a path perpendicular to the surface of the anode) of sufficient magnitude to deflect energetic electrons away from the anode. Following the work of Kaufman,[2-8] a value of the integral $\int B d\ell$ equal to 60 Gauss-cm is sufficient to "repel" a 60-eV primary electron. The multipole discharge chamber was initially set up to provide about 1.5 times this value of $\int B d\ell$, and through the use of overlapping, variable-length anodes, we could increase or decrease this value to optimize the discharge-chamber performance. During preliminary tests we (iteratively) re-positioned the anodes (relative to the pole pieces) to provide nearly equal anode current

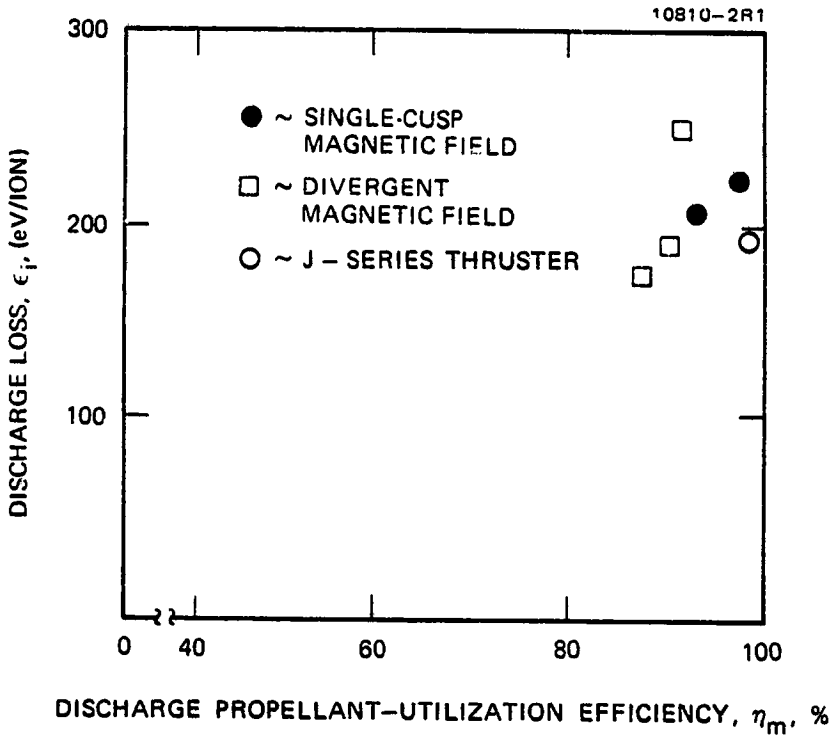

Figure 2-33. Performance measurements obtained with the single-cusp thruster operated with two magnetic-field geometries (J_b = 2 A, V_D = 32 V).

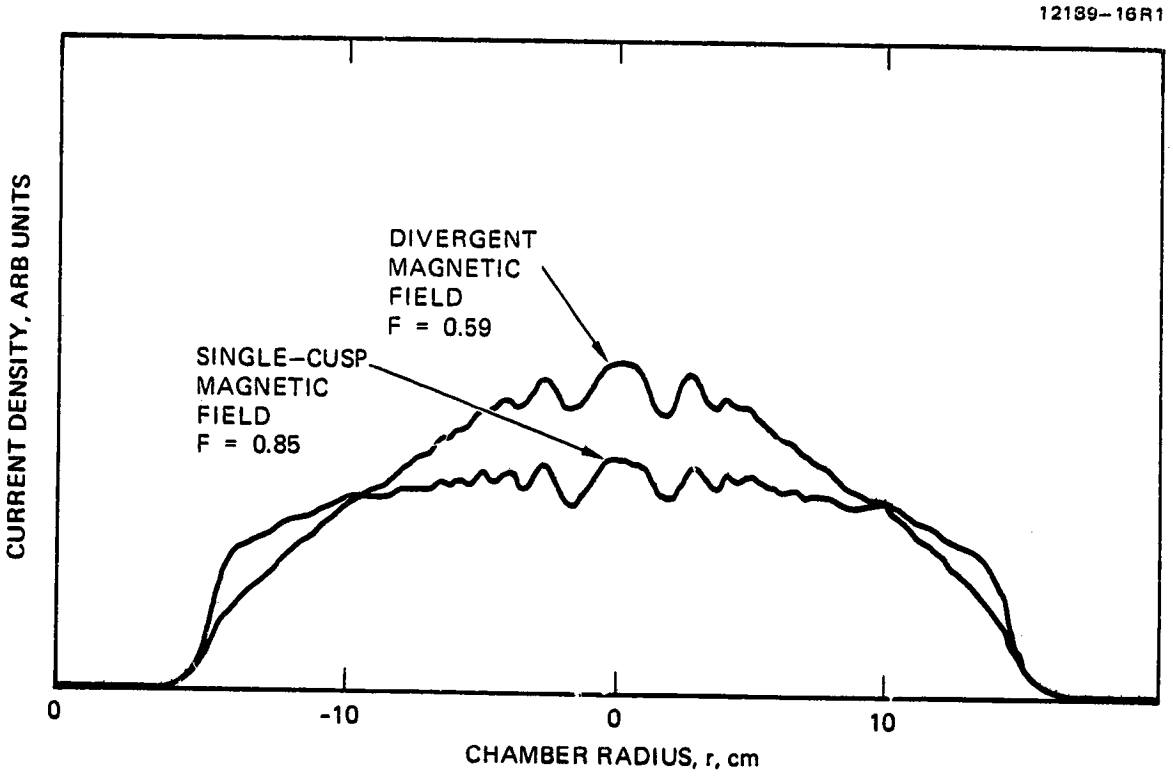

Figure 2-34. Beam profiles obtained with the single-cusp thruster operated with two magnetic-field geometries (J_b = 1.3 A, V_D = 32 V).

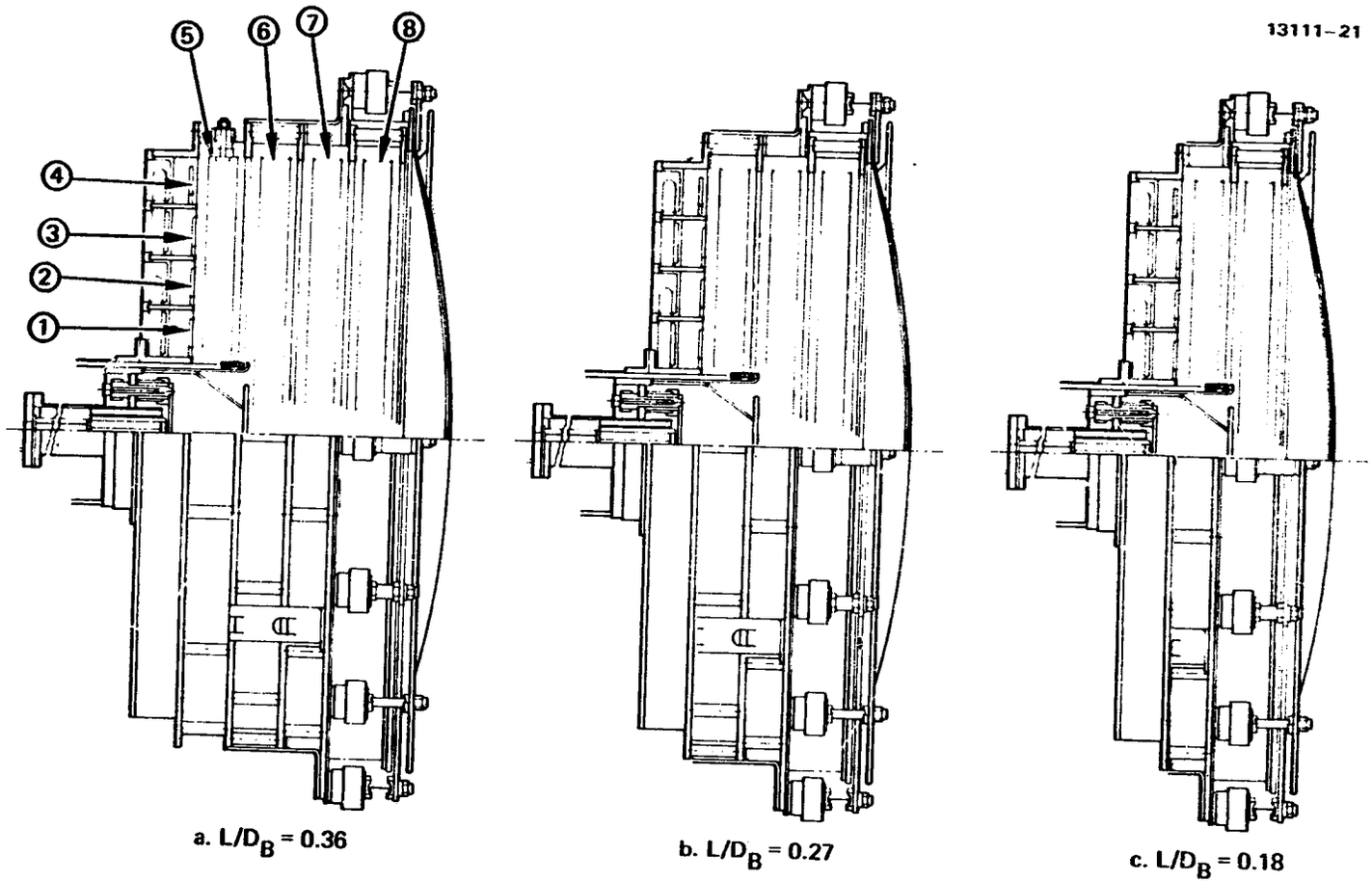

Figure 2-35. Variable-length multipole thruster.

densities, while at the same time satisfying the requirement of the magnetic-field integral. An example of the results of such an iteration is presented in Table 2-3.

We evaluated the performance of the 30-cm-diameter multipole discharge chamber over a range of length-to-diameter ratios by removing sections of the cylindrical sidewall, as shown in Figure 2-35. The performance variation is shown in Figure 2-36, and the corresponding beam-current-density profiles are presented in Figure 2-37. The performance data show the anticipated reduction in maximum propellant utilization as the chamber length (neutral residence time) is reduced. Little reduction in baseline eV/ion was realized as a result of shortening the chamber, suggesting that the sidewall losses were not as significant as the endwall and screen-electrode web losses.

We measured ion losses to the chamber anodes (which comprise most of the interior area) by biasing them (individually) 20-V negative with respect to the cathode. The results are presented in Table 2-4 for the discharge-chamber configuration of Figure 2-35(c), which has a length-to-diameter ratio of $L/D_b = 0.18$. The results are presented as current densities, where we used the width of the anode to define the ion-loss area. Table 2-4 also presents the discharge current densities, where the area between adjacent pole pieces was used to define the electron-collection area. The average ion flux to the screen electrode is given by

$$j_s = \frac{J_b}{A_b \phi_s} \quad , \qquad (2\text{-}3)$$

where A_b is the beam area (641 cm^2), and ϕ_s is the ion transmission of the screen grid. Using $\phi_s = 0.674$ (geometrical transmission) gives $j_s = 3.5$ mA/cm^2 for a beam current of $J_b = 1.5$ A. A comparison of this value with the measured results of Table 2-4 indicates a significantly higher ion flux

Table 2-3. Normalized Anode Current Densities in the Multipole Thruster (Anode Numbering Scheme is Shown in Figure 2-35)

ANODE NO.	NORMALIZED CURRENT DENSITY	
	Before Repositioning Anodes	After Repositioning Anodes
1	.20	.10
2	.24	.08
3	.23	.16
4	.12	.10
5	.08	.19
6	.04	.14
7	.05	.12
8	.04	.11

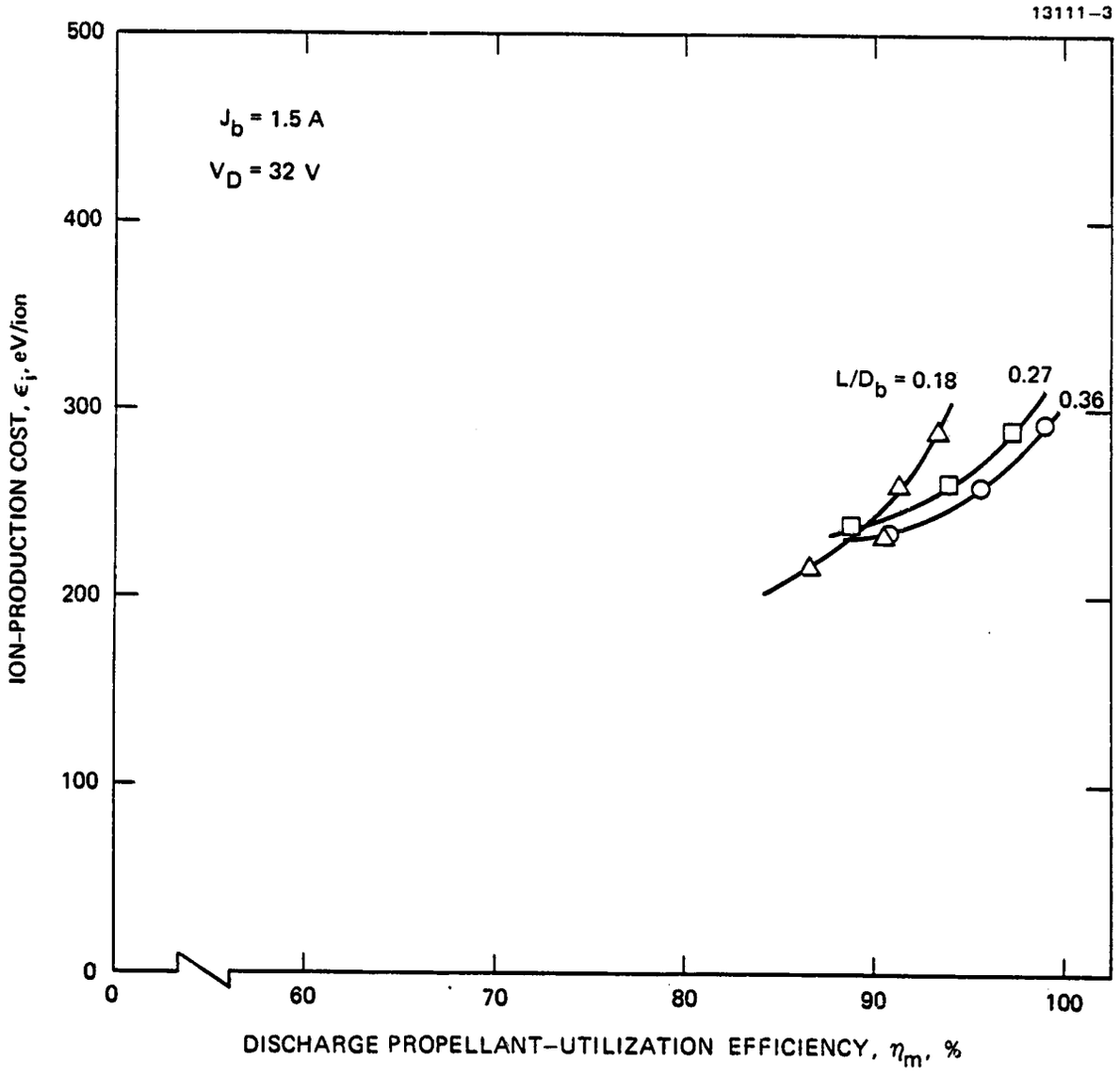

Figure 2-36. Performance obtained with the multipole thruster configurations shown in Figure 2-35.

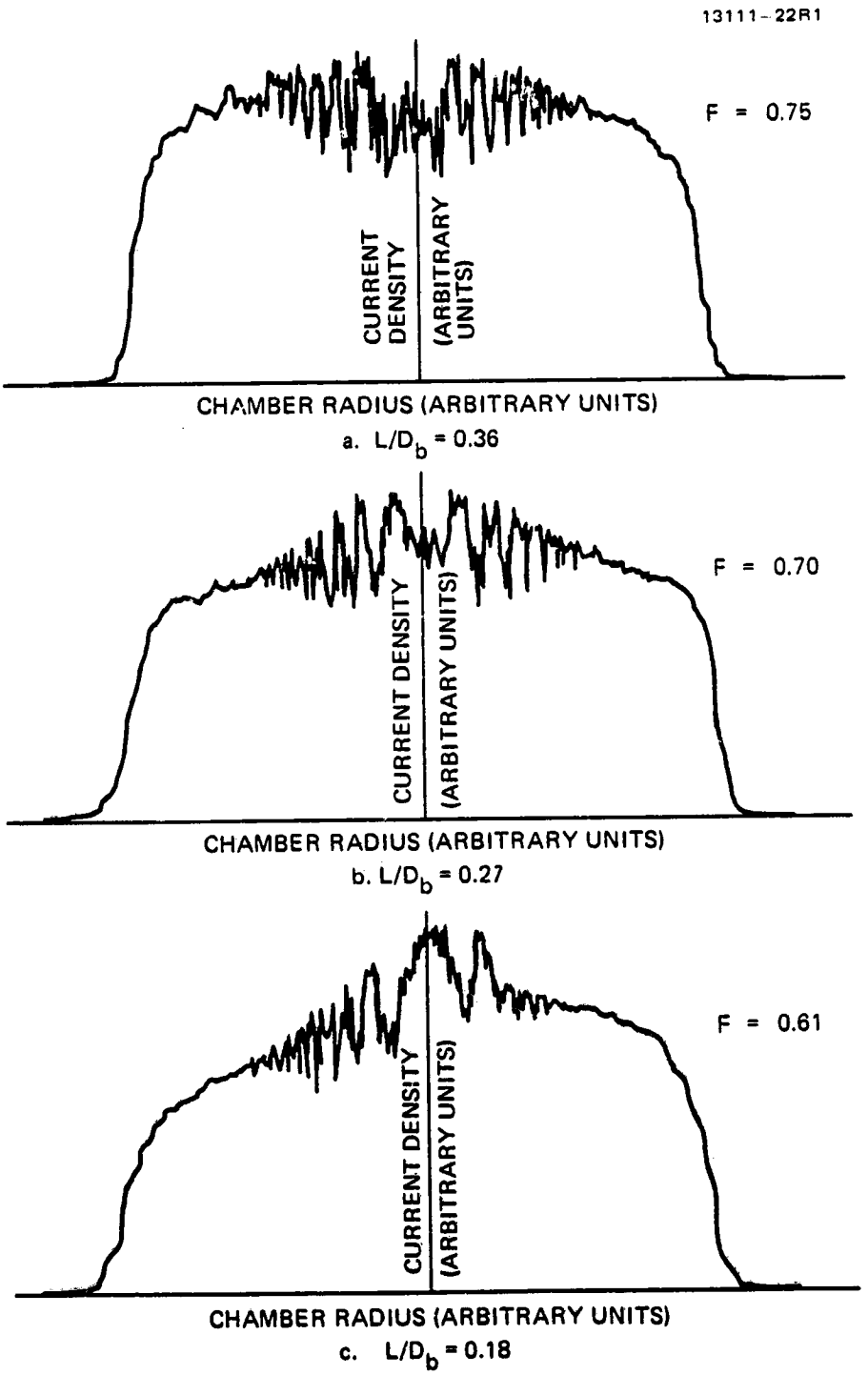

Figure 2-37. Beam-current-density profiles obtained with the multipole thruster configurations shown in Figure 2-35.

Table 2-4. Discharge and Ion Current Densities in the Multipole Thruster Showing the Effect of Anode Position (L/D_b = 0.18)

Anode No.	Current Density, mA/cm^2			
	Before Recessing Anode #3		After Recessing Anode #3	
	Electron	Ion	Electron	Ion
1	6.78	1.65	7.37	1.66
2	5.94	2.21	6.96	2.24
3	15.84	3.04	6.94	2.00
4	8.92	1.98	10.49	2.07
5	21.84	2.79	24.84	---
6	14.4	1.88	15.05	1.99

density at the screen electrode.* Comparing the ion current arriving at the screen electrode (J_b/ϕ_s) with the sum of the measured ion currents indicates that about one-half the ions produced in the discharge arrive at the screen electrode even though it comprises only about one-third of the total bounding area.

Both the electron and ion-current-density measurements suggest that anodes #3 and #5 act as a plasma sink. To verify this, we recessed anode #3 to see if any performance improvement could be realized. Table 2-4 presents the corresponding current-density measurements, showing a substantial reduction in both the electron and ion losses for anode #3. Inasmuch as the baseline discharge losses for this configuration were about ε_i = 225 eV/ion, we concluded that recessing anode #5 to achieve more uniform electron and ion losses would probably not improve the performance in any significant manner. Considering the high performance demonstrated by the ring-cusp discharge chamber, no attempts to optimize the performance of the multipole configuration were made beyond those described above.

Although the performance of the multipole discharge chamber was somewhat below our calculated predictions, some valuable information related to preferential ion drift and sensitivity to chamber length was obtained. In addition, it was shown that the conductivity in the baffle-aperture region can be controlled using a magnetic-baffle arrangement that does not require an iron circuit. In the cathode pole piece/baffle design of Figure 2-32, the magnetic field in the vicinity of the baffle aperture is produced by the fringe field of the external coil. Figure 2-38 presents measurements showing the effects of magnet-coil current, J_{mb}, on cathode-vaporizer temperature, T_{cv}. These results, and

*More recent results obtained by Kaufman[2-9] and Wilbur[2-10] have shown that for a variety of ion-chamber configurations, the ions preferentially drift toward the cathode-potential surfaces (as compared to magnetically shielded anode-potential surfaces).

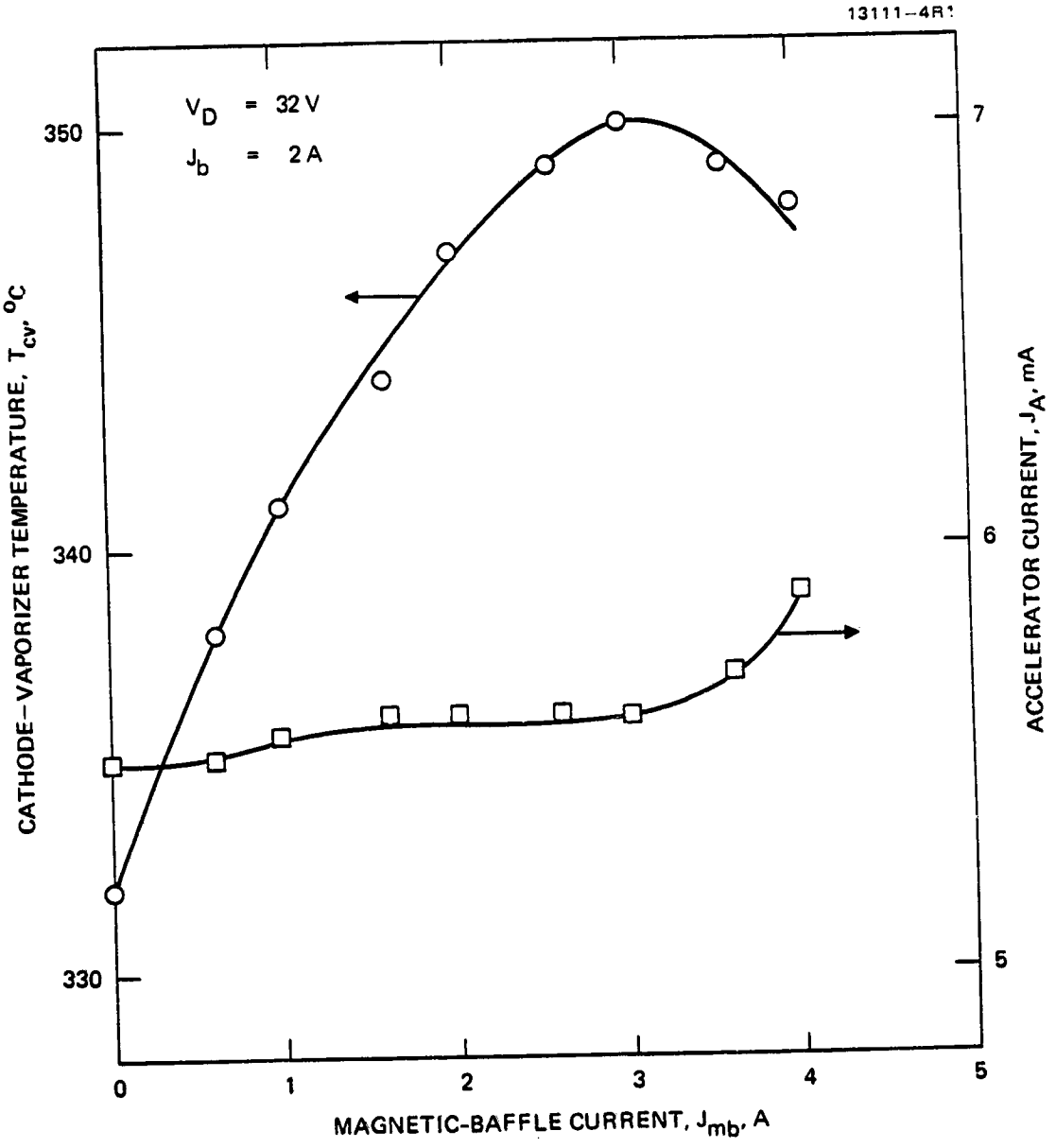

Figure 2-38. Magnetic-baffle characterization in the multipole thruster.

the calibration of Figure 2-14(b), allow one to infer that the fringe-field baffle arrangement can be used to vary the cathode flow rate over a wide range (to permit discharge-voltage control or to accommodate throttling).

Perhaps the most outstanding performance characteristic of the multipole discharge chamber is the attainment of highly uniform plasma conditions within the relatively magnetic-field-free volume of the plasma. This uniformity is manifest in an extremely uniform beam-current-density profile. Figure 2-39 presents the beam-current-density variation for the multipole thruster operated at a beam current of J_b = 4 A. The flatness parameter for this profile based on the active (apertured) area of the electrodes is F = 0.95, which we believe to be the highest value that has been reported to date.

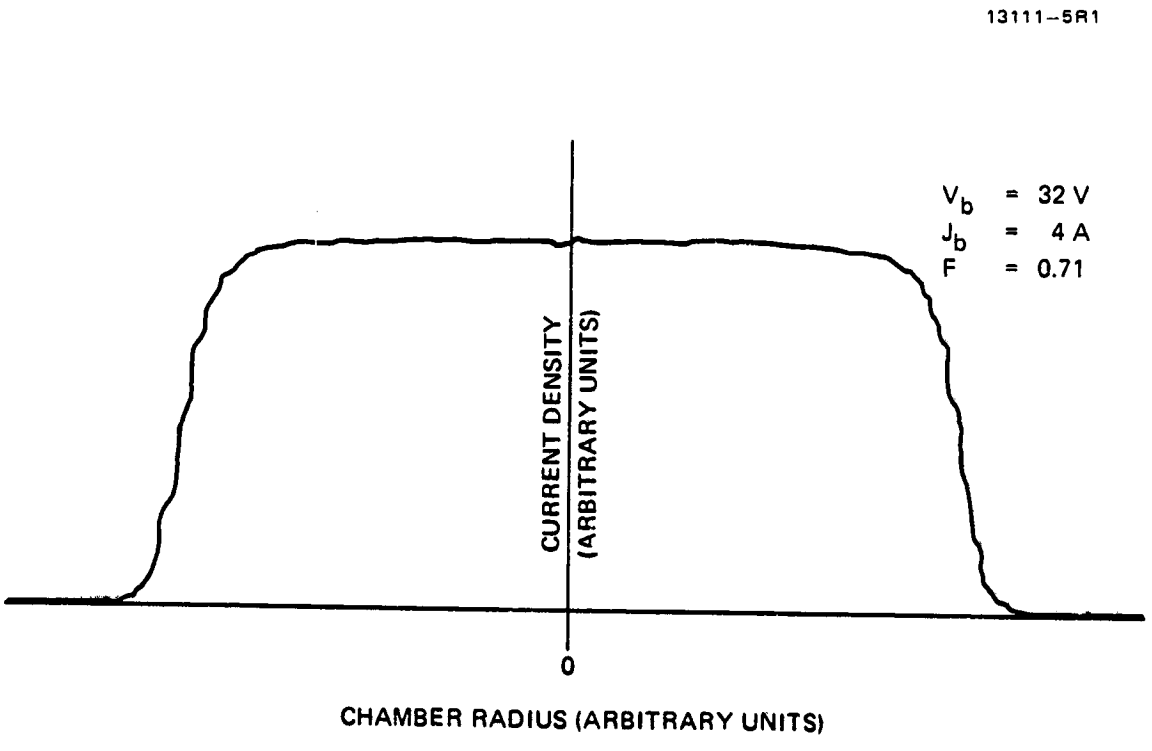

Figure 2-39. Beam-current-density profile of the multipole thruster operated at J_b = 4 A (L/D_B = 0.36).

SECTION 3

ION-EXTRACTION-ASSEMBLY EVALUATION

High perveance ion-extraction assemblies require an electrode-mounting arrangement that is dimensionally stable over a wide range of input (discharge-chamber) power. Thermo-mechanical analysis[3-1] has shown that the "cold" interelectrode spacing of the state-of-the-art J-series ion-extraction assembly shown in Figure 3-1(a) decreases during operation as a result of thermal expansion of the electrodes and mounting rings. The analysis also showed that flexible "leaf spring" supports permit the screen-electrode and mounting-ring assembly to freely expand, resulting in less interaction with the optics mounting ring and an increase in the dish depth of this electrode. The use of rigid posts for supporting the accelerator-electrode mounting ring, on the other hand, results in a bending moment that deforms this mounting ring and inhibits downstream displacement of the electrode. This same study showed that the flexible accel-support-ring mount of Figure 3-1(b) allows the electrode and support ring to freely expand, increasing the dish depth and resulting in reduced sensitivity of the interelectrode spacing to variations in discharge power.

Extracting high beam currents at low specific impulse can be accomplished by the addition of a decelerator electrode to enable the ratio of net-to-total accelerating voltage to be reduced to as low as R = 0.2 without experiencing excessive beamlet divergence. The three-grid ion-extraction assembly of Figure 3-1(c) employs flexible mounting-ring supports for all three electrodes and was developed for the high-discharge-power and low-beam-power operation required of the advanced ion-thruster designs. Both advanced-technology ion-extraction assemblies of Figure 3-1 were investigated under this program. The electrode-aperture geometries are indicated in Figure 3-2.

8996-17R1

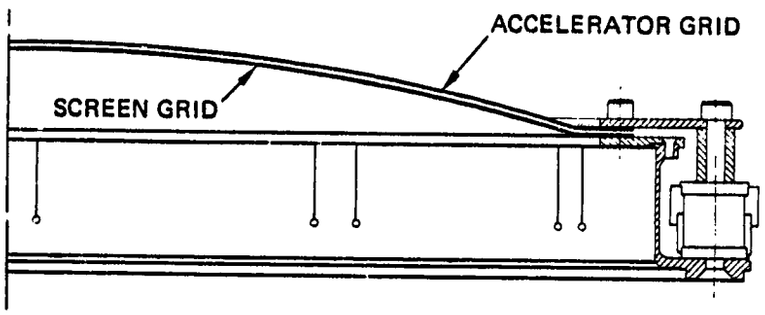

a. J-SERIES DESIGN ("STANDARD")

8998-18R2

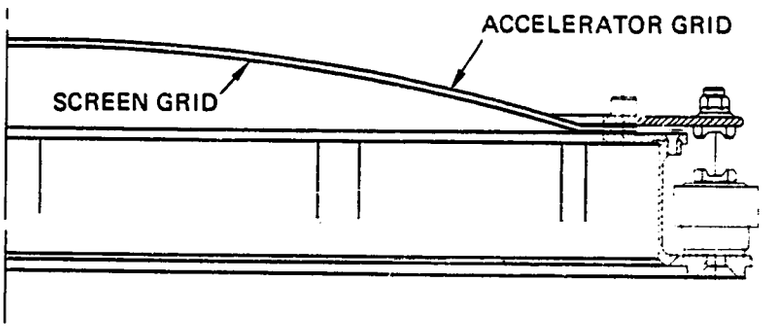

b. ADVANCED TECHNOLOGY 2-GRID DESIGN

8998-18R3

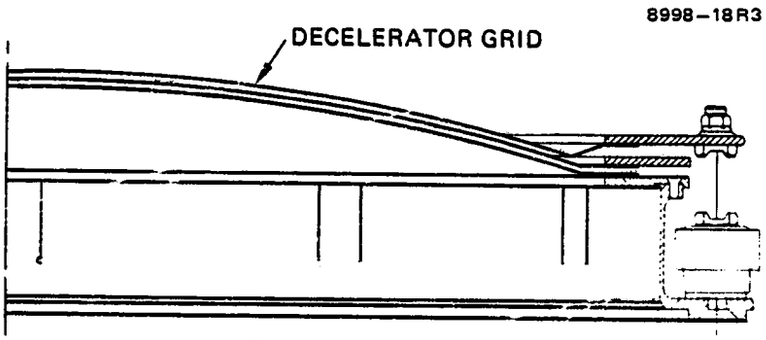

c. ADVANCED TECHNOLOGY 3-GRID DESIGN

Figure 3-1. Cross sections of the state-of-the-art and advanced-technology ion-extraction assemblies.

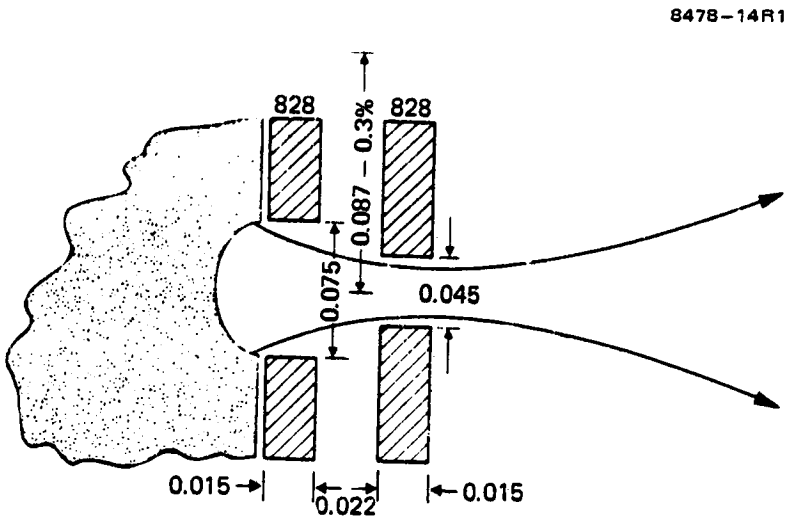

(a) TWO-GRID OPTICS S/N 917

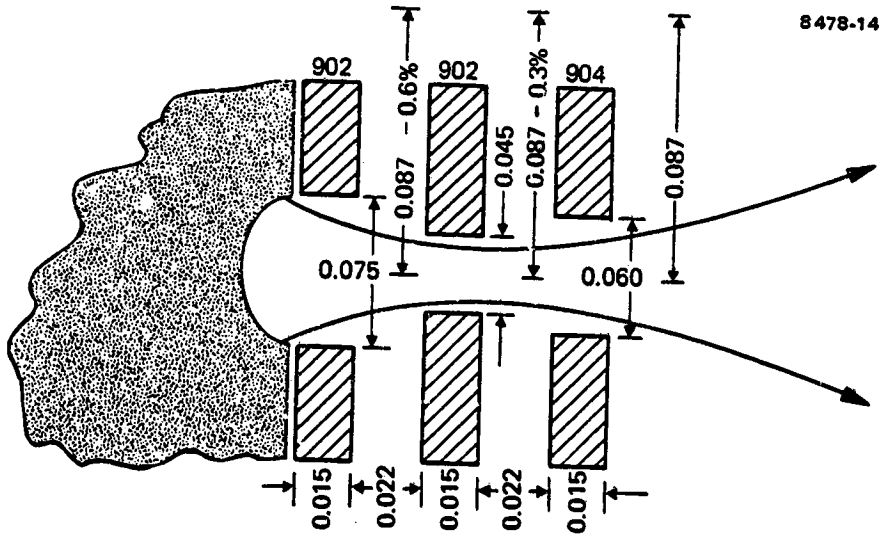

(b) THREE-GRID OPTICS S/N 914

Figure 3-2. Electrode geometries of the ion-extractions assemblies that were evaluated. (Dimensions in inches.)

A. TWO-GRID ASSEMBLY

The perveance of an ion-extraction assembly should be independent of thruster operating conditions as long as the interelectrode spacing remains constant and the current density profile does not change. However, measurements conducted using the ion-extraction assembly of Figure 3-1(b) and a conventional J-series-equivalent thruster (S/N 301J) are presented in Figure 3-3, showing that that the perveance increases with discharge voltage. The measurements were performed under conditions of constant discharge power, and, therefore, the perveance variation cannot be attributed to power-induced changes in interelectrode spacing. Instead, it is attributed to the increase in multiple ionization that accompanies the improvement in propellant-utilization efficiency that is characteristic of operation at higher discharge-voltage and beam-current levels. The analysis presented in Appendix B shows that the measured perveance should be corrected for the presence of multiply charged ions since the theoretical perveance scales as the square root of the charge-to-mass ratio of the ion. The relationship between measured and corrected perveance is shown to be

$$P_{corrected} = \alpha P_{measured} \quad , \qquad (3\text{-}1)$$

where P is the perveance, and α is the thrust factor that corrects measured thrust for the presence of multiply charged ions. Using this relationship to correct the measured perveance we generated the lower curve of Figure 3-3 which shows that the corrected perveance is invariant with discharge voltage.* These results indicate that meaningful perveance comparisons should be made only after correcting the measured results for the effects of multiply charged ions.

*The discharge-voltage-independent results of Figure 3-2 were obtained using the average value of the correction factor α. The centerline or peak value "over corrects" the perveance results, consistent with the results presented below, showing that the location of the perveance limit is off-axis.

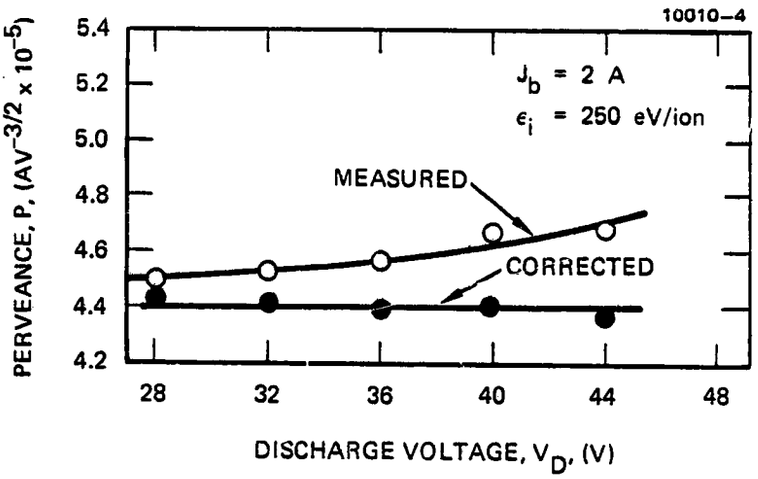

Figure 3-3. Variation of perveance with discharge voltage for thruster S/N 301J equipped with the advanced-technology ion-extraction assembly S/N 917 shown in Figure 3-1(a).

Figure 3-4 presents the variation of accelerator drain current with total accelerating voltage and beam current, and the perveance lines (corrected for doubly charged ions) derived from these data. The change in perveance (30%) over the beam-current range 0.75 A < J_b < 2.0 A is less than half that observed with the state-of-the-art ion-extraction assembly, indicating that the interelectrode spacing of the advanced ion-extraction design could be less sensitive to variations in discharge power. As a result of maintaining nearly constant interelectrode spacing, the perveance of the advanced ion-extraction assemblies should be less sensitive to discharge power, permitting stable operation over a wider range of input power. Starting with identical "cold" interelectrode spacings, the J-series ion-extraction assembly can be expected to have higher perveance (as compared to the advanced ion-extraction assembly) as the power is increased and the interelectrode spacing becomes smaller. This expectation was verified by comparing the minimum-total-voltage requirements of the advanced ion-extraction design with those representative of the J-series thruster. Figure 3-5 presents the comparison, which shows that the advanced-technology ion-extraction assembly exhibits comparable or higher perveance for beam currents up to $J_b \cong 1.3$ A. At higher current levels, the perveance of the J-series ion-extraction assemblies is greater; this could be an indication of a larger reduction in their interelectrode spacings. The lower perveance of the flexible-accel-support design should, however, be offset by an increase in its maximum current-extraction capability which results from the improved dimensional stability.

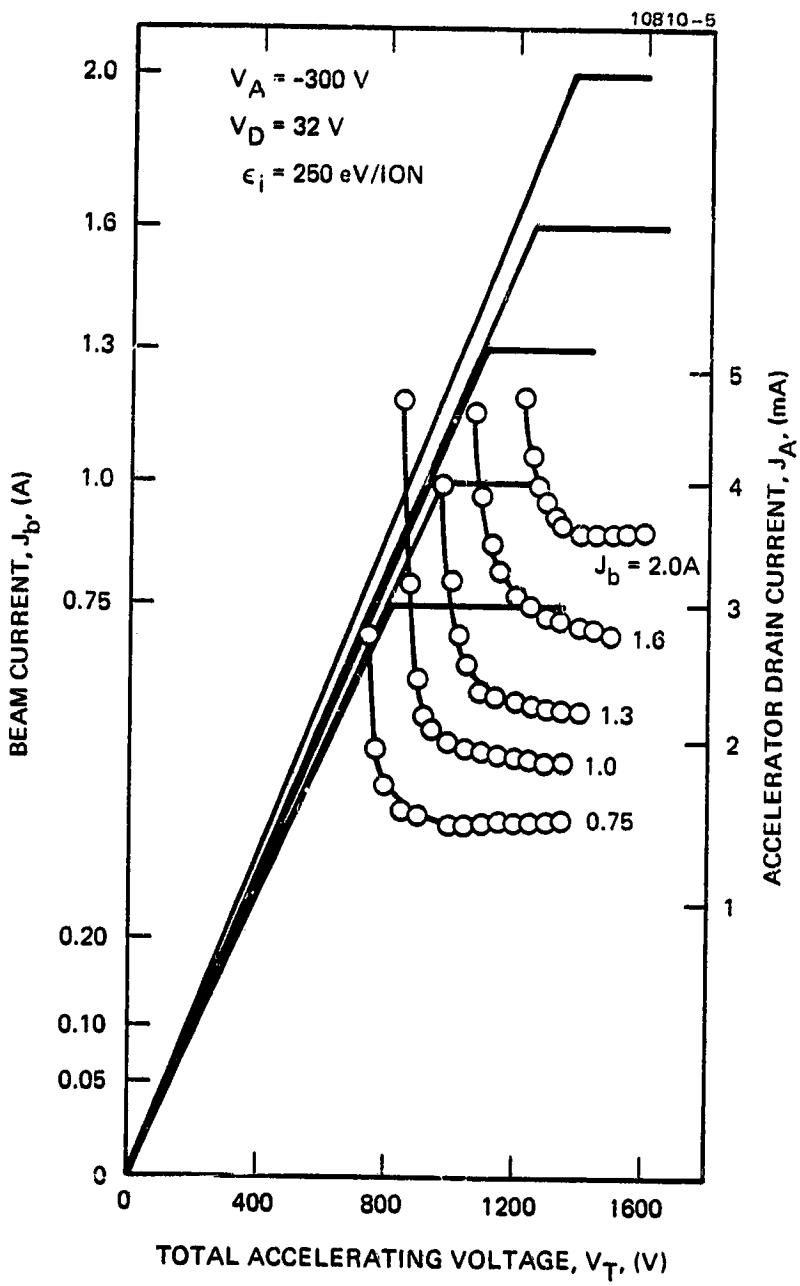

Figure 3-4. Variation of accelerator current with total accelerating voltage for thruster S/N 301J equipped with the advanced-technology ion-extraction assembly S/N 917, shown in Figure 3-1(a).

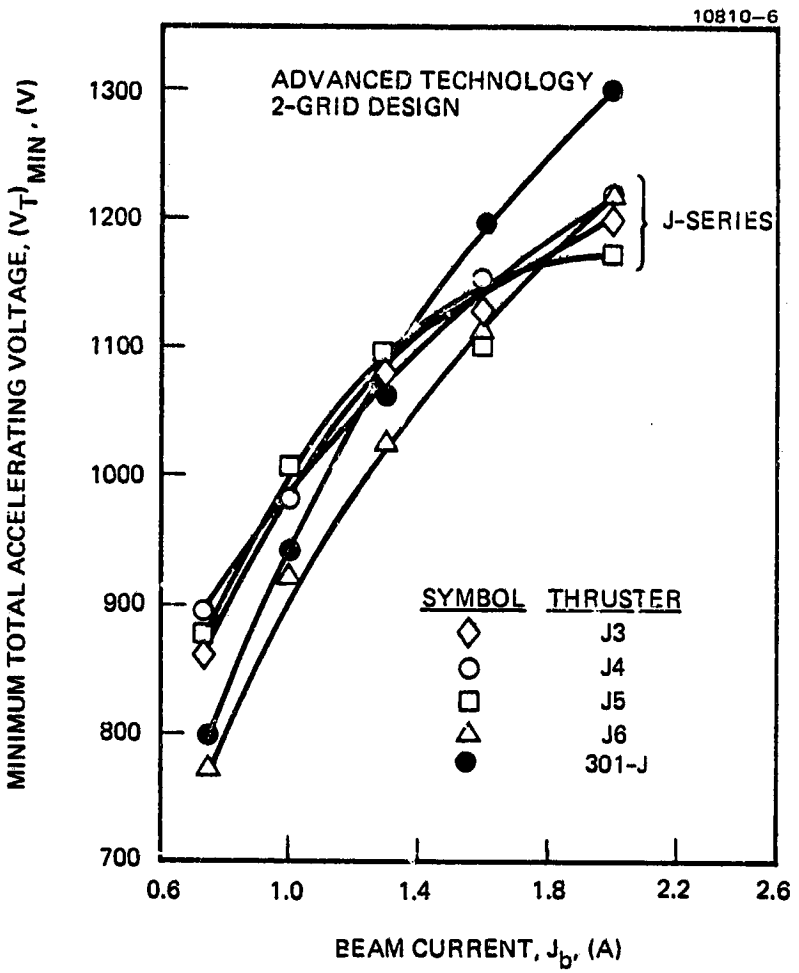

Figure 3-5. Comparison of the minimum total accelerating voltage for J-series and advanced-technology ion-extraction assembly S/N 917 (ε_i = 250 eV/ion, V_D = 32 V, and V_A = -300 V).

Figure 3-6 presents perveance measurements that were performed with the multipole thruster described above, and using the rigid and flexible mounting arrangements of Figures 3-1(a) and 3-1(b) to support the same pair of electrodes (with the same "cold" interelectrode spacing). The results of Figure 3-6 show that the perveance of the flex-mount ion-extraction assembly is greater than that corresponding to the rigid-mount arrangement. This result is contrary to the stress-analysis results which predicted that the interelectrode spacing of the flexible-mount arrangement would remain nearly constant, while that of the rigid-mount arrangement would decrease with increasing power level. The results of Figure 3-5 were obtained with a J-series-equivalent thruster (peaked plasma-density profile), while those of Figure 3-6 were obtained using the multipole thruster (uniform plasma-density profile). Therefore, we speculate that the thermally dependent perveance characteristics are also a function of the local plasma-density (and power) distribution.

The results of our measurements suggest that the location of the perveance limit is not necessarily at the location of highest current density (center of the electrodes). The bases for this argument are the results discussed above, plus two additional measurements in which we showed that (1) the perveance of an ion-extraction assembly that was operated with uniform and nonuniform beam profiles was higher for the more peaked profile, and (2) the perveance of an ion-extraction assembly was independent of the aperture displacement at the boundary of the electrodes. In the first measurement, the single-cusp thruster was operated at constant discharge power and beam current, but with the magnetic field arranged to produce either the uniform or peaked beam-current-density profiles of Figure 2-34. Contrary to our expectations, the flatter profile exhibited lower perveance, suggesting that the perveance limit occurs off-axis; i.e., beyond

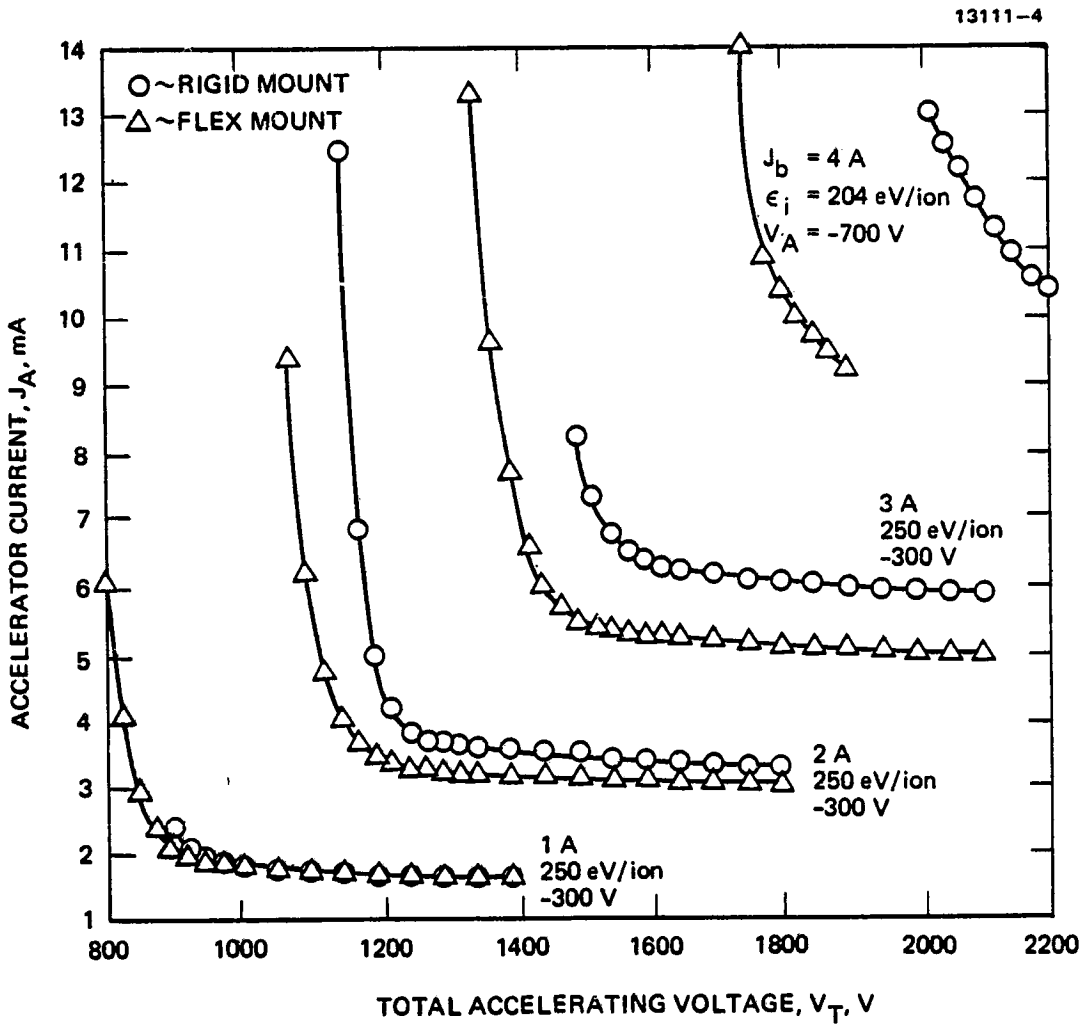

Figure 3-6. Performance of ion-extraction assembly S/N 917 operated on the multipole thruster. The electrode mounts were changed from the rigid ones shown in Figure 3-1(a) to the flexible ones shown in Figure 3-1(b), while retaining the same electrodes.

the radial location defined by r = 10 cm, where the current density of the uniform profile exceeds that of the nonuniform distribution. In the second measurement, we performed perveance measurements using an electrode set that had substantial aperture offset in the region defined by r > 12 cm. The (unintentional) aperture misalignment was large enough to cause elongation of the accelerator apertures due to direct impingement of high-energy ions. Accelerator-current measurements obtained with this electrode set are presented in Figure 3-7. The measurements were performed about two-hours apart and indicate that the baseline accel current was decreasing at the rate of about 1 mA/hr due to elongation of the apertures located at the periphery of the accelerator grid. If, however, the baseline accelerator current is subtracted from both sets of measurements, the resultant data fall on the same curve (Figure 3-7); therefore, the perveance is unchanged (independent of edge-aperture geometry, which did change). Since the perveance limit corresponds to a condition of excessive accelerator current, we concluded that the radial location of the perveance limitation had to be less than that corresponding to the edge apertures which were already operating under conditions of excessive impingement current.

Other measurements[3-3] obtained using a single-aperture electrode arrangement with aperture displacement and current representative of the electrode compensation and plasma-density profile of the J-series thruster showed that the location of the perveance limit is in the region 9 cm < r < 12 cm. These findings suggest that an increase in the perveance of the J-series ion-extraction assembly could be achieved by eliminating the aperture compensation, or by increasing the accelerator-aperture diameter in the region 9 cm < r < 12 cm.

B. THREE-GRID ASSEMBLY

We conducted both an experimental and analytical investigation of three-grid ion-extraction assemblies. The experimental study was carried out using a government-furnished ion-extraction

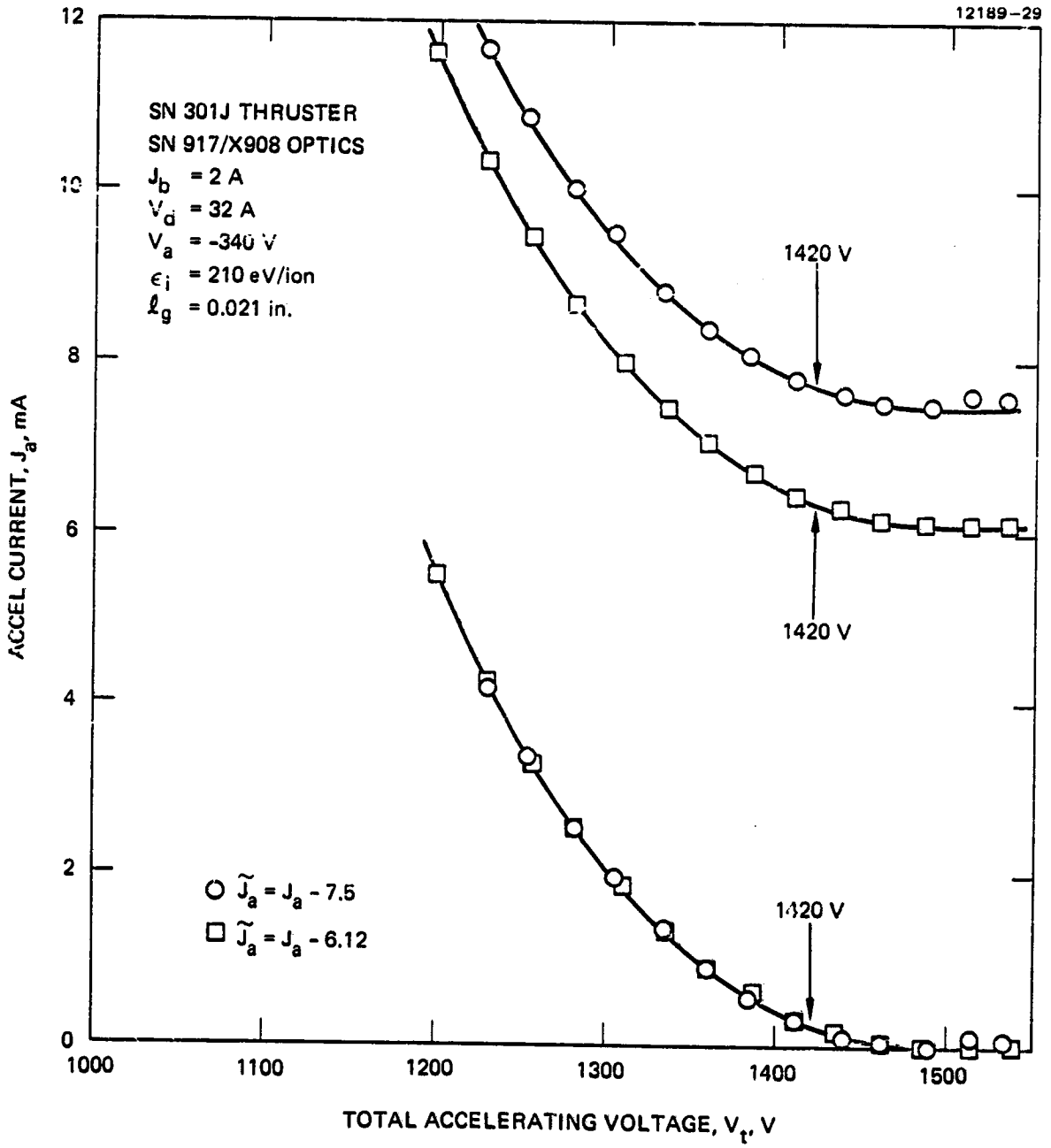

Figure 3-7. Variation of accelerator current with total accelerating voltage for electrodes that had poorly aligned apertures in the region near the periphery.

assembly that employs the design features shown in Figures 3-1(c) and 3-2(b). The analytical study was carried out using an adaptation of a three-electrode beam-steering model that was developed by Conrad.[3-2]

1. Experimental Investigation

Extracting beam currents as high as J_b = 6 A at low specific impulse (low beam voltage V_b) requires a decelerator electrode to position the neutralization plane close to the accel electrode, enabling the net-to-total accelerating-voltage ratio to be reduced to as low as R = 0.2 without experiencing excessive beamlet divergence. The three-grid ion-extraction arrangement of Figure 3-1(c) was designed for the high-beam-current and low-specific-impulse operation required of the extended-performance thruster; flexible mounting-ring supports are used for all three electrodes. Extrapolating the results of the thermomechanical analysis[3-1] described above indicates that this arrangement will allow the electrode-supporting rings to expand radially as they are heated by the discharge, maintaining nearly constant interelectrode spacing.

The three-grid ion-extraction assembly was operated with the ring-cusp discharge chamber for beam currents up to J_b = 5.3 A. Measurements showing the variation of accel and decel currents with total accelerating voltage are presented in Figures 3-8 and 3-9 for beam currents in the range 2 A < J_b < 5 A. Figures 3-10 and 3-11 present the measured variations of accel- and decel-electrode currents with net-to-total accelerating-voltage ratio, R. These results* demonstrated the ability to successfully operate the 3-grid design of Figure 3-1(c) over a net-to-total accelerating-voltage-ratio range of 0.2 < R < 0.8 for beam currents in the range 2 A < J_b < 5 A.

*The aperture pattern in the ion-extraction assembly was undercompensated, resulting in excessive decelerator-electrode currents and noticeable elongation of the decel apertures near the periphery of the electrodes. The design information presented in Section 3.B.2 should allow future designs to be properly compensated.

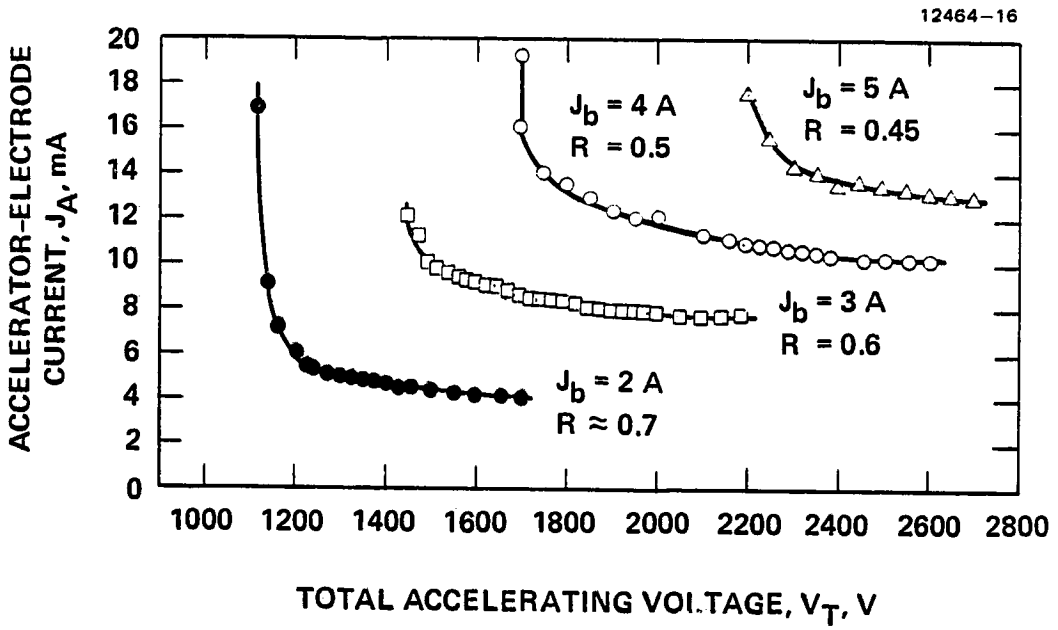

Figure 3-8. Variation of accelerator-electrode current with total accelerating voltage for the ring-cusp thruster equipped with the three-grid ion-extraction assembly S/N 914.

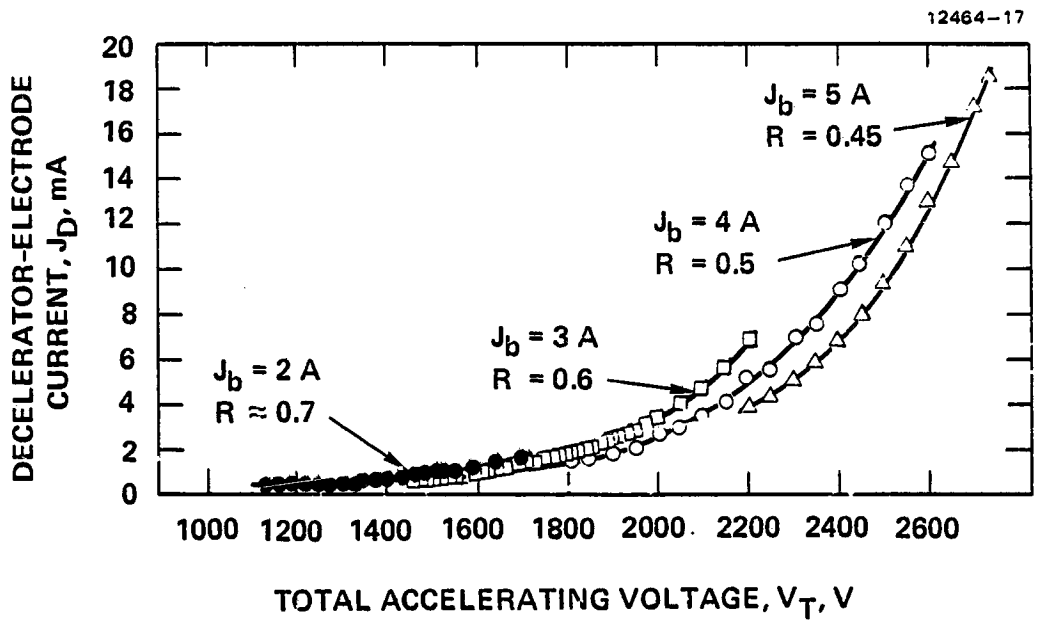

Figure 3-9. Variation of decelerator-electrode current with total accelerating voltage for the ring-cusp thruster equipped with the three-grid ion-extraction assembly S/N 914.

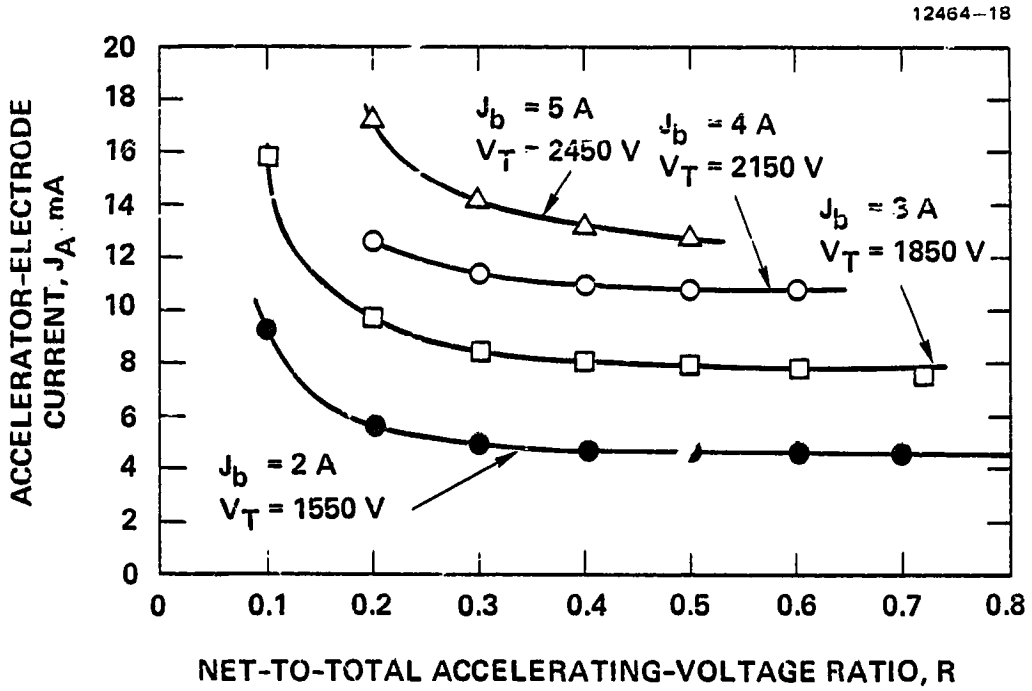

Figure 3-10. Variation of accelerator-electrode current with the ratio of net-to-total accelerating voltage for the ring-cusp thruster equipped with the three-grid ion-extraction assembly S/N 914.

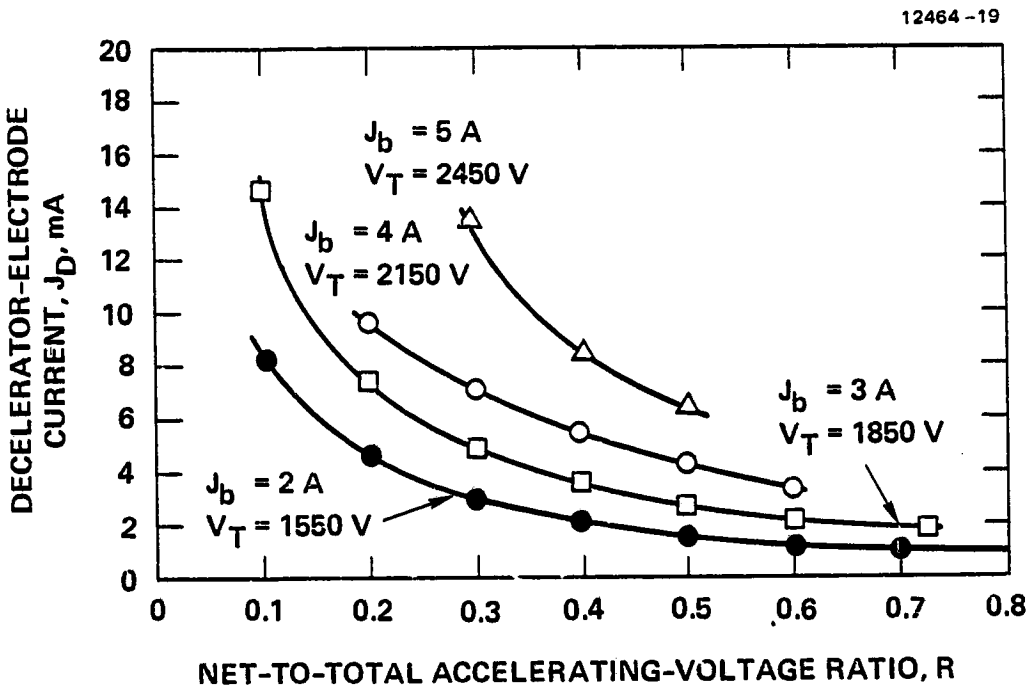

Figure 3-11. Variation of decelerator-electrode current with the ratio of net-to-total accelerating voltage for the ring-cusp thruster equipped with the three-grid ion-extraction assembly S/N 914.

2. Analytical Investigation

Figure 3-12 presents the electrode compensation, $C_\lambda^{s,d}$, necessary to align the apertures along the radius of curvature, R_c, as a function of the aperture separation, $\ell_e^{s,d}$, defined as

$$\ell_e^{s,d} = 2\ell_g + t_{s,d} + t_a \quad . \tag{3-2}$$

The subscripts and superscripts s, a, and d refer to screen, accel, and decel, respectively, and t represents the electrode thickness and ℓ_g is the interelectrode spacing. In performing the calculations, we assumed that the accel-aperture pattern would not be compensated. In this case, the screen-electrode compensation, C_λ^s, is negative (screen apertures moved closer together), while the decel-aperture compensation, C_λ^d, is positive (decel apertures moved farther apart) and the amount of compensation is determined by the following geometric relationship:

$$C_\lambda^{s,d} = \pm \frac{50}{\sqrt{(R_c^2 - R_g^2)}} \ell_e^{s,d} \quad , \tag{3-3}$$

where R_g is the radius of the active region of the electrodes. The results of Figure 3-12 are applicable to both 2-grid and 3-grid ion-extraction assemblies; compensating by these amounts should produce beamlets leaving the accelerator system in a direction normal to its surface. For the J-series ion-extraction assembly the beamlet-normal compensation is calculated by Equations (3-2) and (3-3) to be $C_\lambda^s = -0.183$.

The additional compensation necessary to vector the beamlets parallel to the thrust axis was calculated for 3-grid ion-extraction assemblies using a theoretical beam-steering model.[3-2]

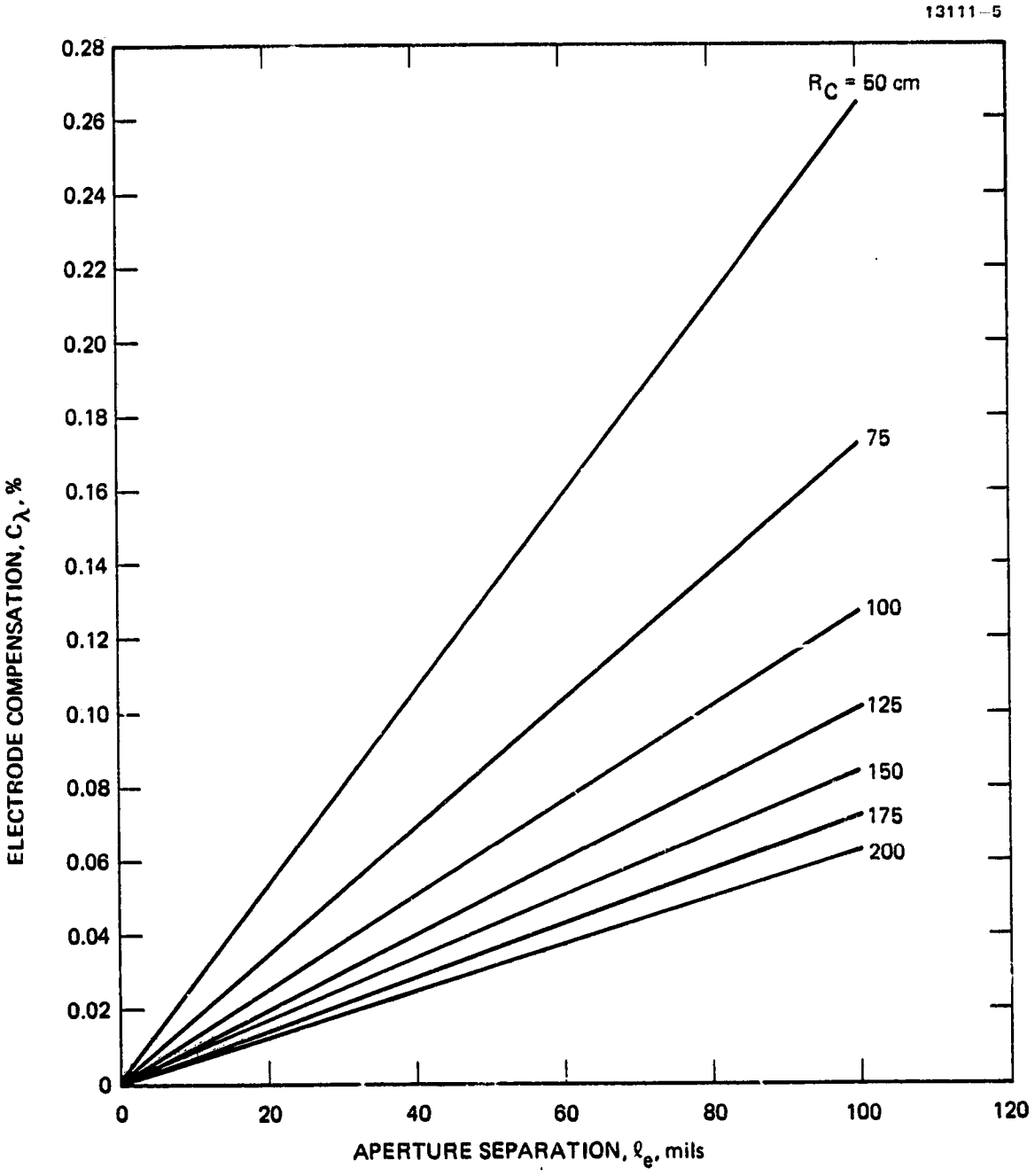

Figure 3-12. Electrode compensation required to align the apertures along the radius of curvature for the 30-cm-diameter thruster (29-cm beam diameter).

This theory relates the vectoring angle γ to the displacements of the accel and decel apertures through the expression

$$\gamma = - \frac{\partial \gamma}{\partial y_a} y_a - \frac{\partial \gamma}{\partial \gamma_b} y_b \quad , \tag{3-4}$$

where y_a and y_b are the displacements of the accel and decel apertures, respectively, and $\partial\gamma/\partial y_a$, $\partial\gamma/\partial y_b$ are the vectoring sensitivities, which are functions of the aperture geometry and the net-to-total accelerating-voltage ratio, R. Figure 3-13 shows the geometry and defines the nomenclature used in the model.

In ion-propulsion applications it is desirable to use the same tooling for fabricating accel electrodes of both 2-grid and 3-grid assemblies. Therefore, Equation 3-4 can be written for the case where the screen and accel apertures are displaced by y_s and y_d (relative to the accel aperture), using the transformations

$$y_a = - y_s \quad , \tag{3-5}$$

and

$$y_b = - y_s + y_d \quad . \tag{3-6}$$

This gives

$$\gamma = \left(\frac{\partial \gamma}{\partial y_a} + \frac{\partial \gamma}{\partial y_b} \right) y_s - \frac{\partial \gamma}{\partial y_b} y_d \quad . \tag{3-7}$$

2 OF 3

B5-15806 UNC

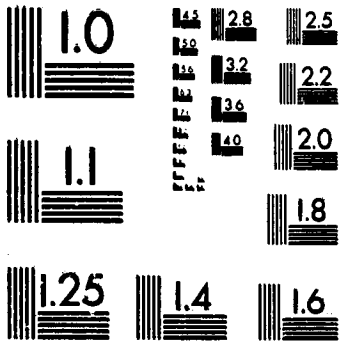

MICROCOPY RESOLUTION TEST CHART
NATIONAL BUREAU OF STANDARDS
STANDARD REFERENCE MATERIAL 1010a
(ANSI and ISO TEST CHART No. 2)

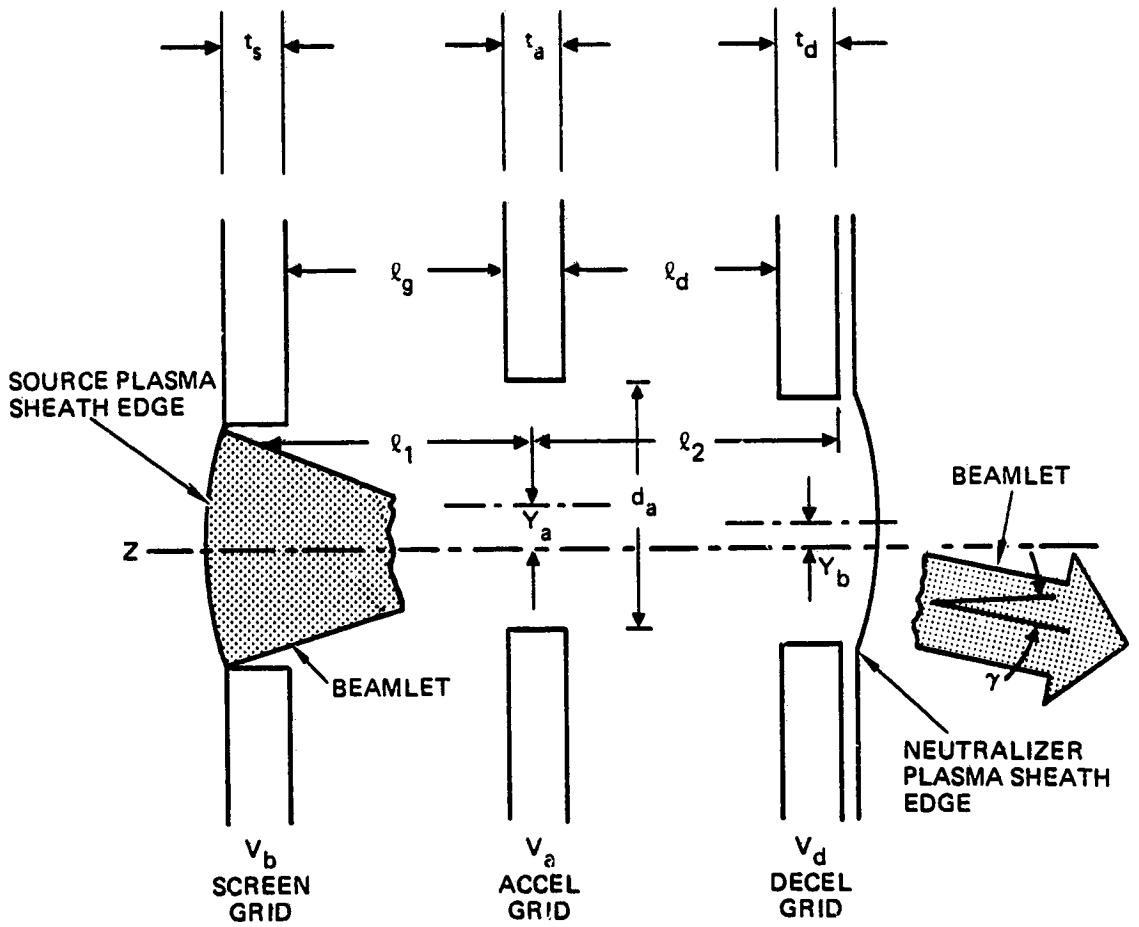

Figure 3-13. Geometry used in beam-steering model.

Figures 3-14 through 3-21 present the variation of vectoring sensitivities with net-to-total accelerating-voltage ratio R for various values of the aperture dimension, d_a, and the parameters, ℓ_1 and ℓ_2, given by

$$\ell_1 = \ell_g + t_s + \frac{t_a}{2} \quad , \tag{3-8}$$

and

$$\ell_2 = \ell_d + t_d + \frac{t_a}{2} \quad , \tag{3-9}$$

where the terms were defined in Figure 3-13. The calculated results indicate a much greater sensitivity of beam steering to accel-aperture displacement and show that the vectoring direction is opposite in sign for displacement of the decel apertures. Also, the effect of the decel electrode is diminished as R approaches unity (electric field between accel and decel electrodes approaches zero). Because of the difference in vectoring direction associated with displacement of the accel and decel apertures, maximum vectoring sensitivity is realized by displacing these apertures in opposite directions. Since the positive displacement of the accel aperture corresponds to negative displacement of the screen aperture, maximum vectoring is achieved by displacing the screen and decel apertures in the same direction. Moving the decel aperture in the direction of beamlet vectoring should also reduce the possibility of direct interception on this electrode.

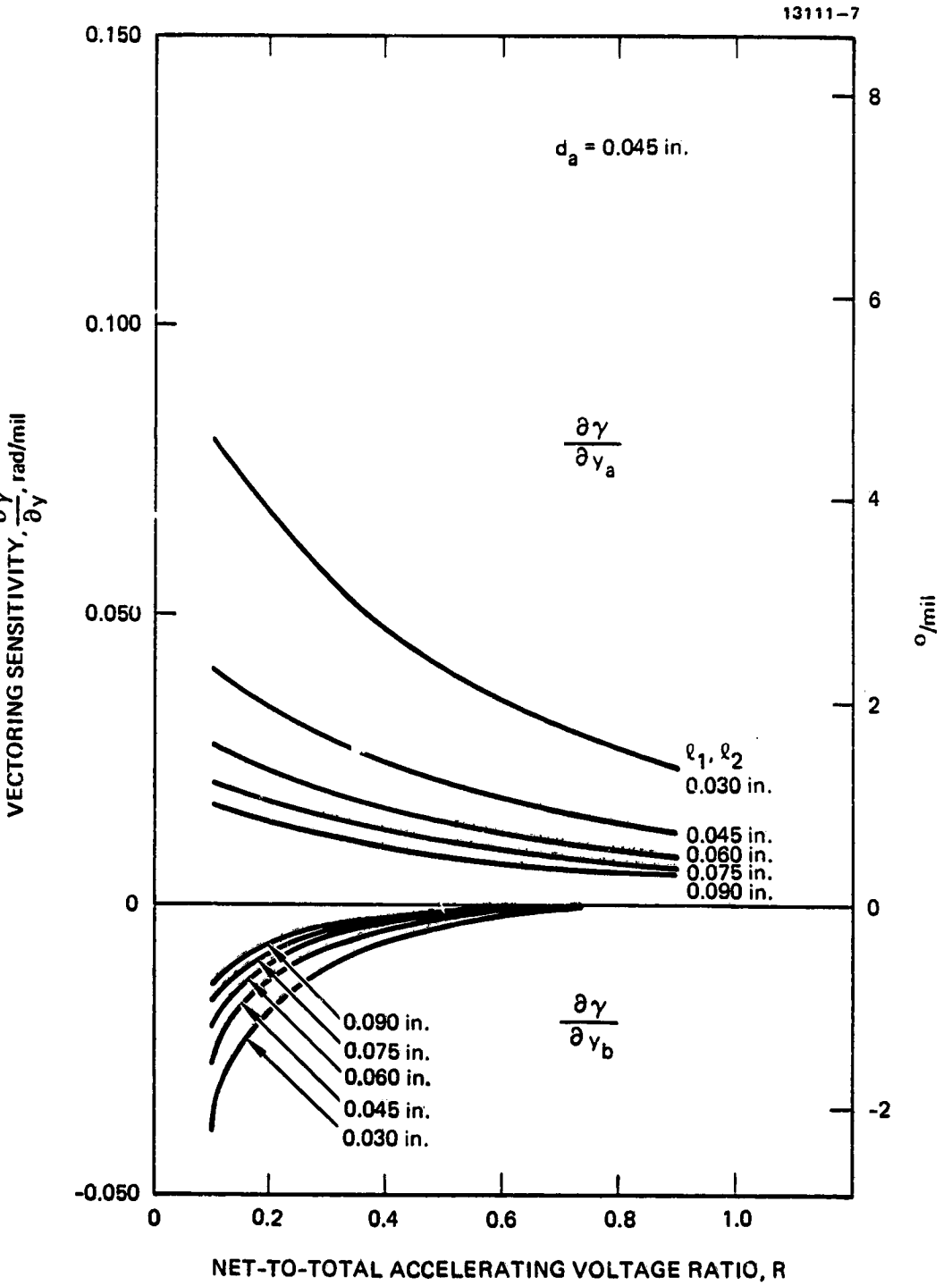

Figure 3-14. Variation of vectoring sensitivities with R (d_a = 45 mils).

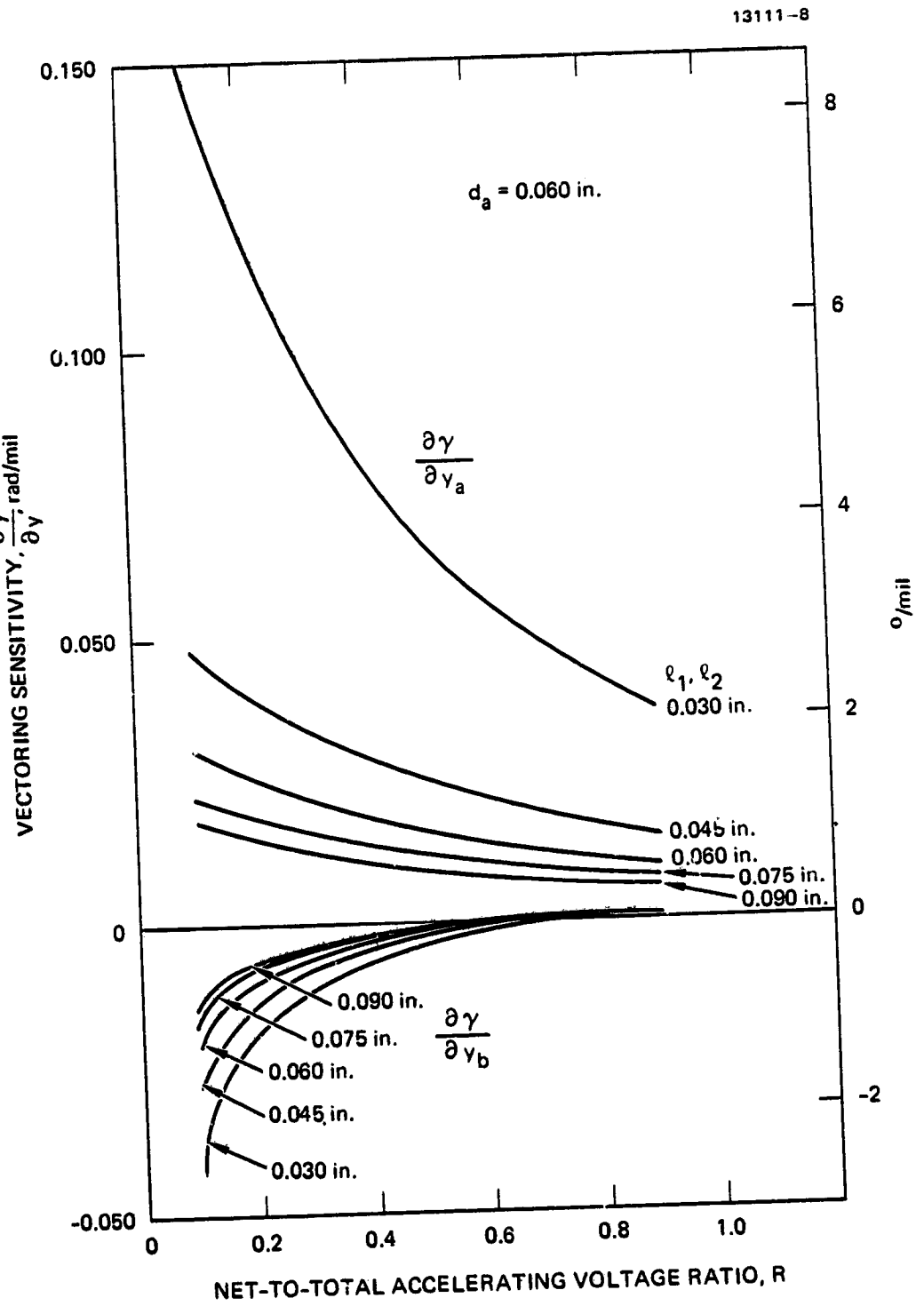

Figure 3.15. Variation of vectoring sensitivities with R (d_a = 60 mils).

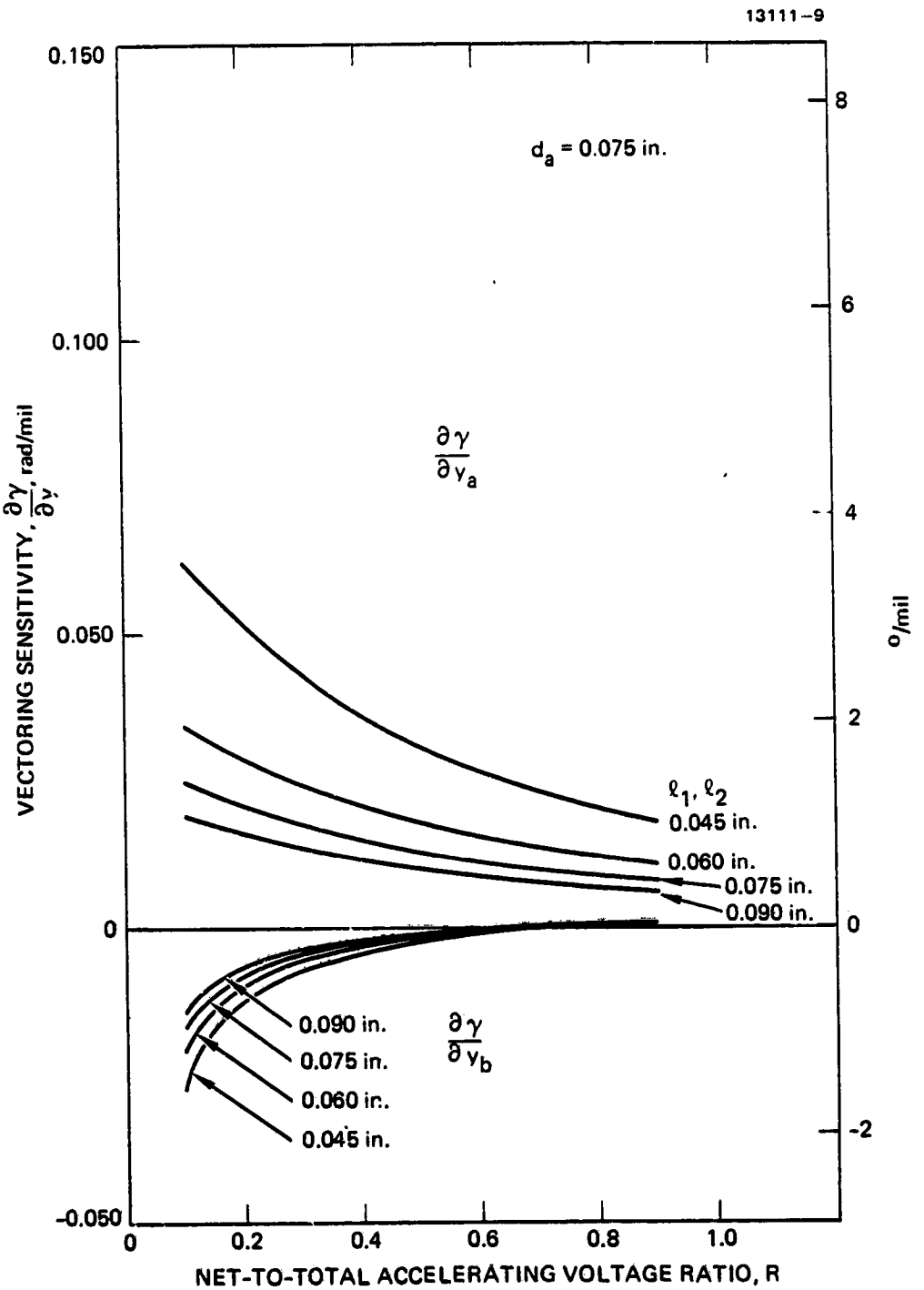

Figure 3-16. Variation of vectoring sensitivities with R (d_a = 75 mils).

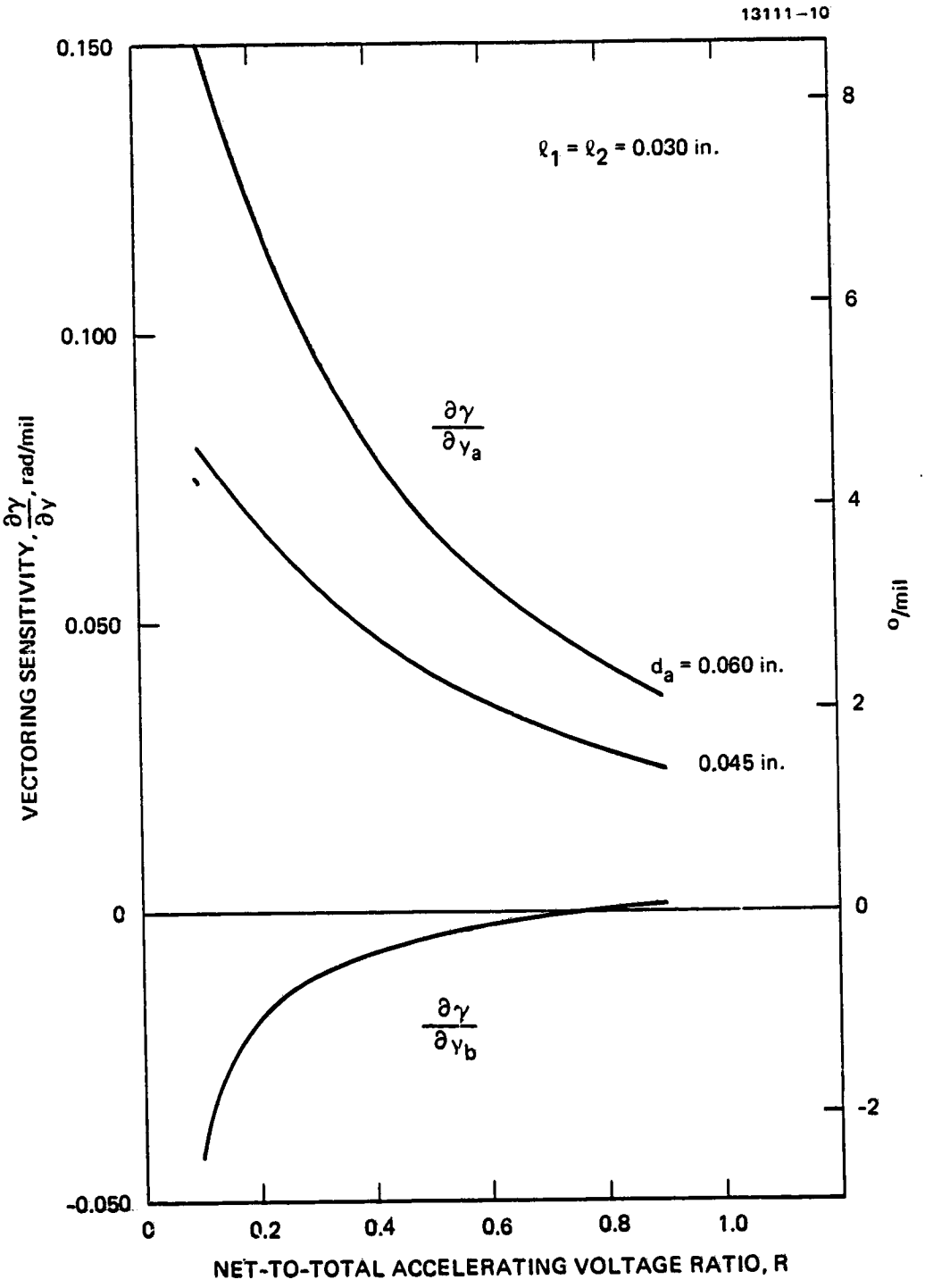

Figure 3-17. Variation of vectoring sensitivities with R ($\ell_1 = \ell_2 = 30$ mils).

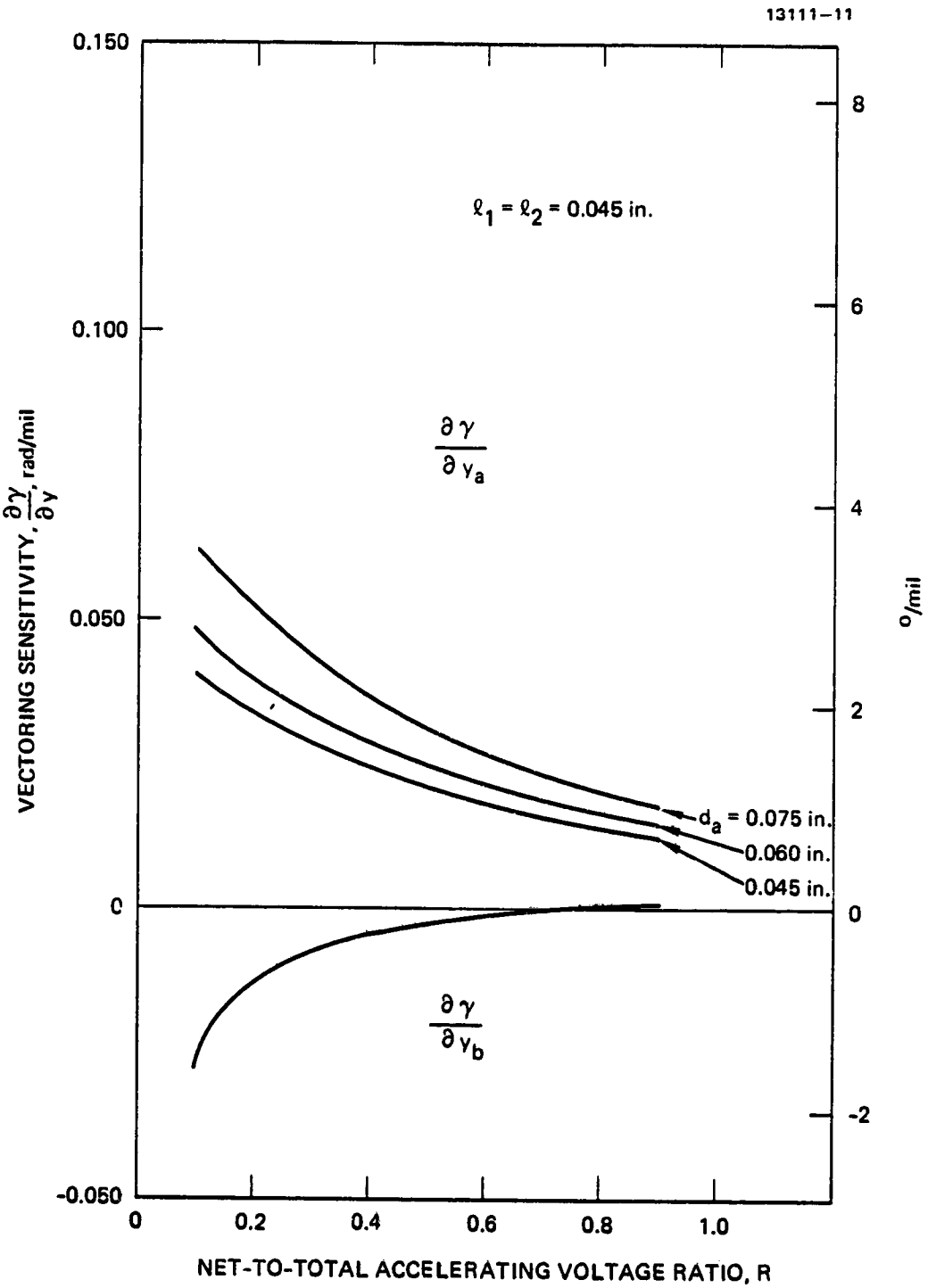

Figure 3-18. Variation of vectoring sensitivities with R ($\ell_1 = \ell_2 = 45$ mils).

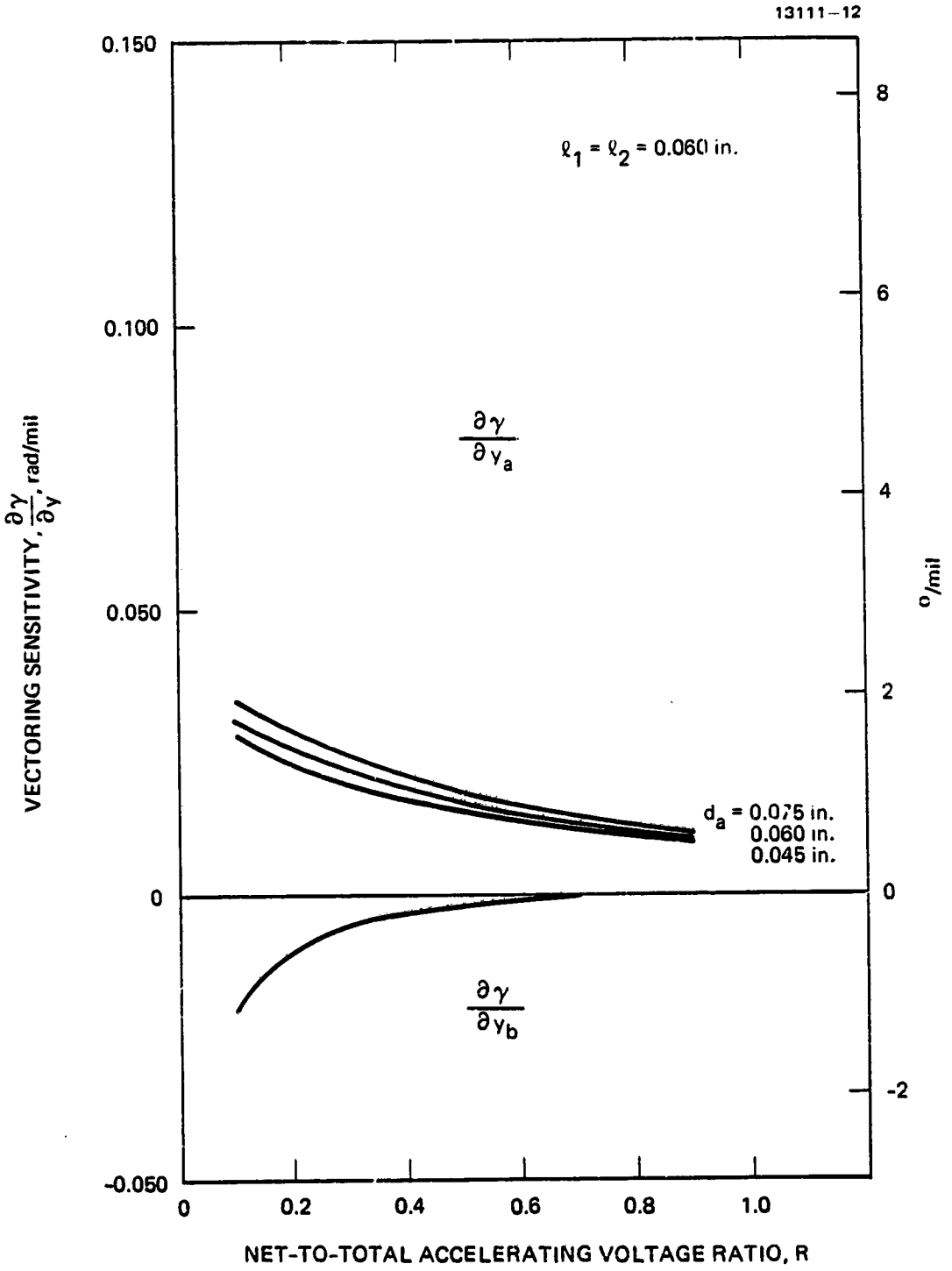

Figure 3-19. Variation of vectoring sensitivities with R ($\ell_1 = \ell_2 = 60$ mils).

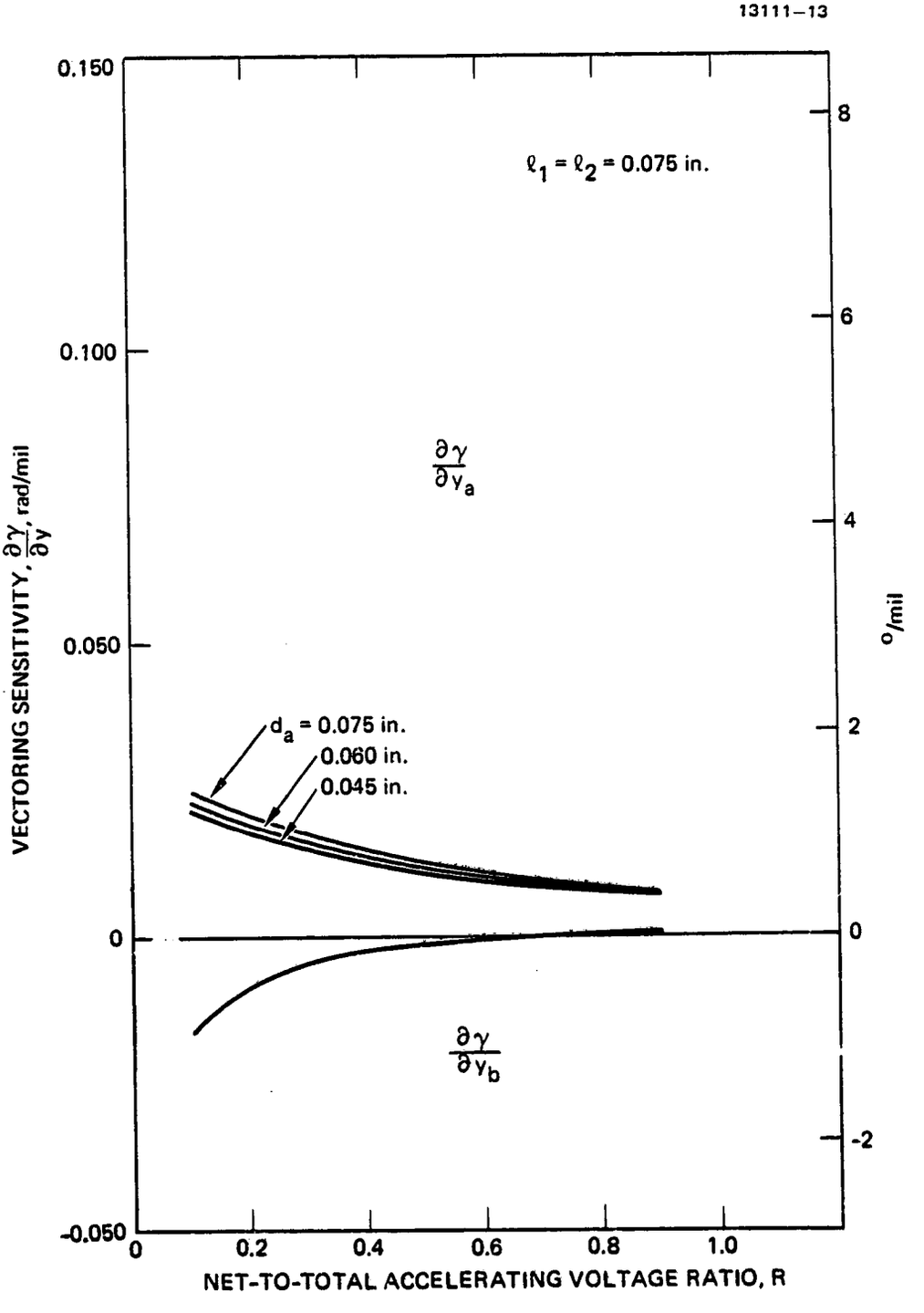

Figure 3-20. Variation of vectoring sensitivities with R ($\ell_1 = \ell_2 = 75$ mils).

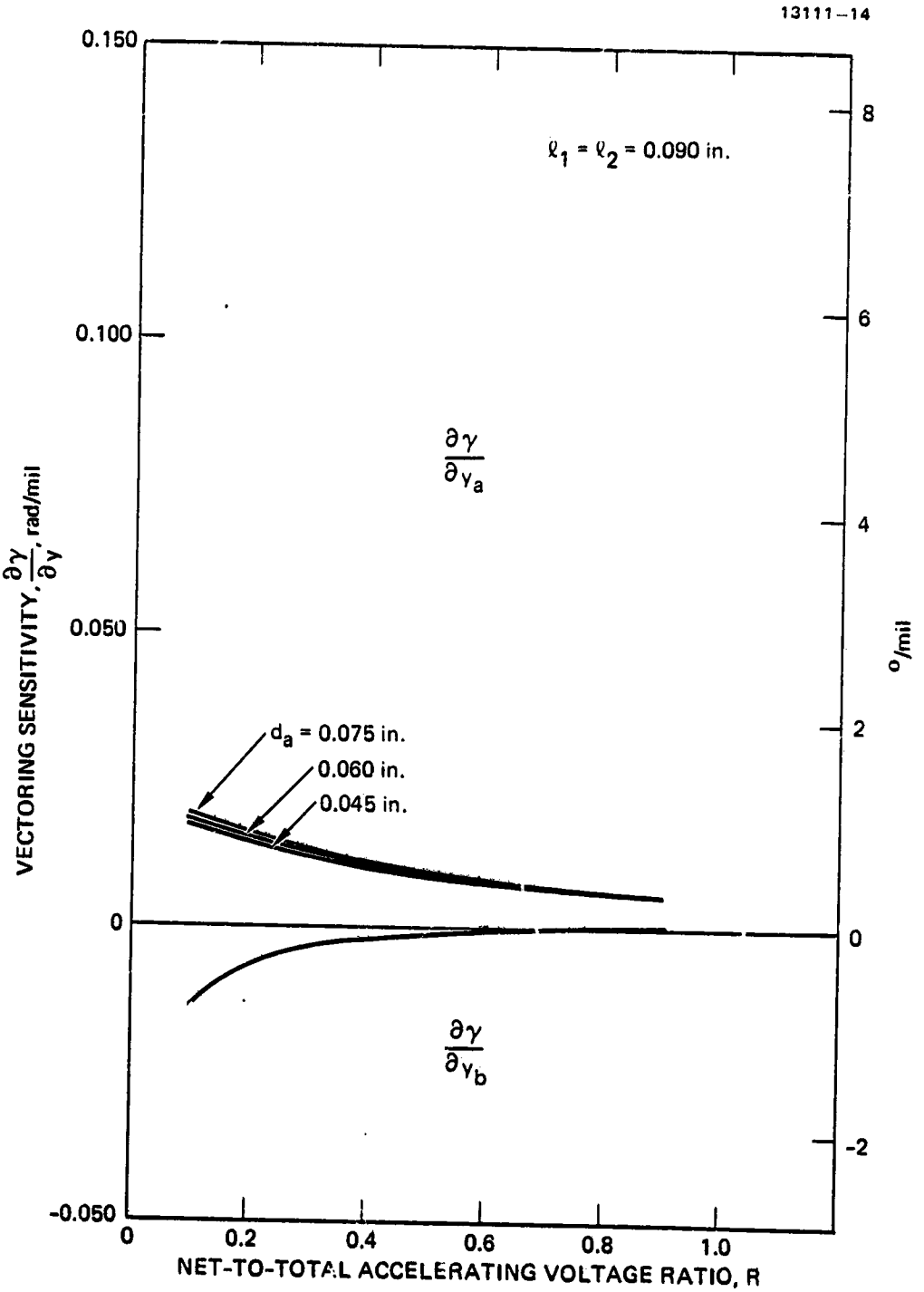

Figure 3-21. Variation of vectoring sensitivities with R ($\ell_1 = \ell_2 = 90$ mils).

The results of Figures 3-14 through 3-21 show that the effect of displacing the screen aperture is maximized by using large accel apertures* (large d_a) and closely spaced electrodes (small ℓ_1 and ℓ_2). The effect of displacing the decel apertures is also dependent on the interelectrode spacing and thickness, but, according to the model, it is independent of accel-aperture size.

*The reduction in beamlet vectoring predicted for small accel apertures is consistent with the experimental observation that the J-series ion-extraction electrodes do not completely vector the beamlets parallel to the thrust axis, whereas the electrodes used in earlier designs (larger accel apertures) did.

SECTION 4

HIGH-EMISSION-CURRENT CATHODE STUDY

In order to satisfy a cathode-emission-current requirement of $J_E > 30$ A and a lifetime goal of $L_c > 15{,}000$ hr requires that the state-of-the-art cathode design shown in Figure 4-1(a) be scaled for higher current operation. The basis that we used for scaling the cathode-insert design to a high-current version was to maintain conditions within the cathode that produce a low-voltage-arc discharge mode, and, as a result, efficient and long-life operation. This discharge mode requires a certain minimum value of the product of pressure and characteristic dimension.[4-1] Therefore, the fundamental design consideration was to keep the pressure-distance product constant when scaling the dimensions of the J-series insert for use in the high-emission-current cathode. The characteristic dimension of the hollow cathode was assumed to be the inside diameter of the insert, d_i.

The cathode-orifice diameter, d_o, should scale with emission current according to the relation

$$d_o \sim J_E^{\,n} \quad , \tag{4-1}$$

where the exponent lies in the range $0.5 \leq n \leq 1$. The lower value of n corresponds to constant-emission-current-density scaling, while the upper value of n is based on a correlation of experimental results.[4-2] Depending on the value of n, Equation (4-1) predicts that the cathode orifice diameter for $J_E = 40$ A should be increased by a factor of 1.7 to 2.8 over the value used in the J-series cathode ($J_E = 12$ A). Because increasing the orifice diameter would require an increase in cathode flow rate

8991-1R2

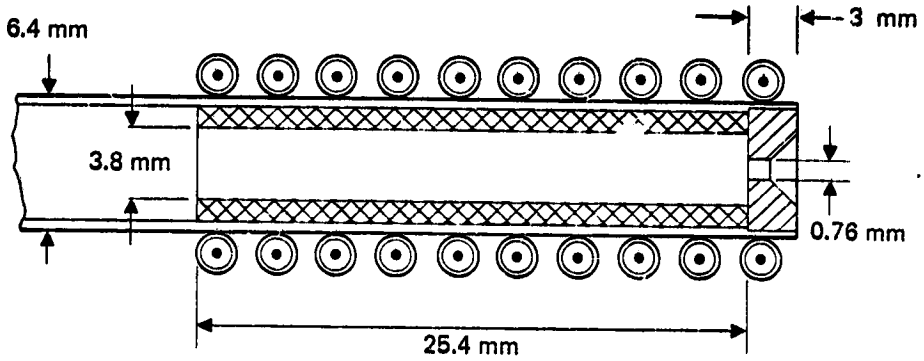

a. J-SERIES DESIGN

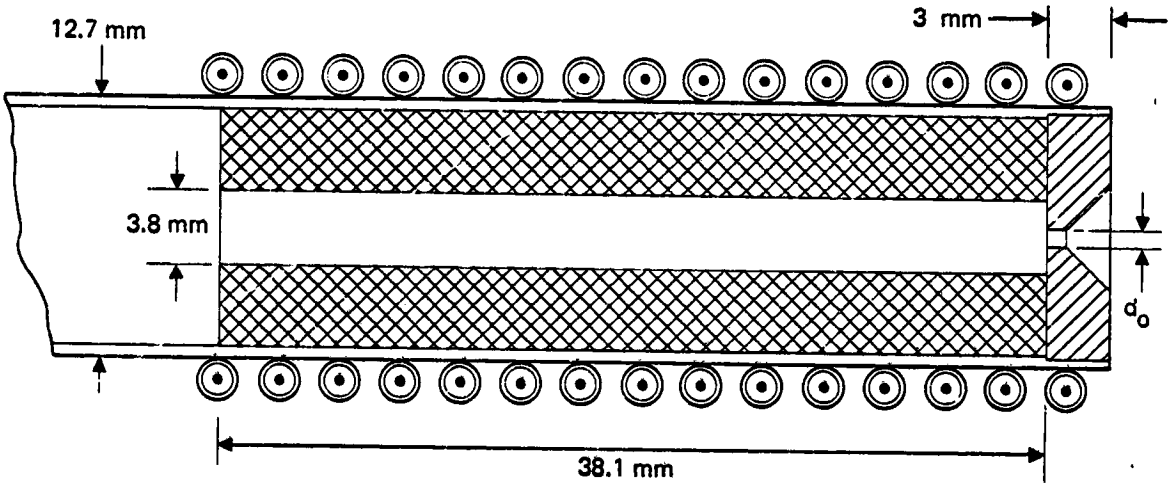

b. HIGH-EMISSION-CURRENT DESIGN

Figure 4-1. Cross sections of the J-series and high-emission-current hollow cathodes.

(to maintain constant-pressure conditions), we kept the inside diameter of the insert constant in the scaled design.

The scaling considerations discussed above led to the high-emission-current cathode design shown in Figure 4-1,b). The orifice plate is removable, which permitted us to evaluate different aperture diameters, d_o, using the same cathode/insert configuration. The insert was instrumented with thermocouples to enable us to assess the effects of various operating conditions on insert temperature.

The high-emission-current cathode of Figure 4-1(b) was evaluated using the three aperture diameters listed in Figure 4-2. We operated each cathode in a bell jar for a period of 500 hr at an emission current of J_E = 40 A. A summary of operating conditions for these tests is presented in Table 4-1.

Figure 4-3 presents the variation of insert temperature with cathode emission current for both the high-emission-current and conventional cathode designs. The cathodes used a conventional (scaled) keeper and were operated in a diode arrangement using a water-cooled electrode to collect the emission current. A liquid-nitrogen trap between the bell jar and the mercury diffusion pump maintained the bell-jar pressure at about 5×10^{-5} Torr during the tests. These results show that the maximum insert temperature of the high-emission-current cathode (operated at J_E = 34 A) is only slightly higher than the corresponding insert temperature of the conventional cathode (operated at an emission current of J_E = 12 A). A model[4-3] developed by Hughes under NASA Contract NAS 3-21040 relates cathode lifetime to insert temperature through the depletion of barium from the porous-tungsten matrix. Based on this model, the results of Figure 4-3 indicate that the lifetime of the insert used in the high-emission-current cathode should be comparable to that used in conventional designs ($\cong$ 30,000 hr).

A scanning electron microscope (SEM) was used to examine the cathode orifice plates prior to and at the conclusion of each

10810-7R1

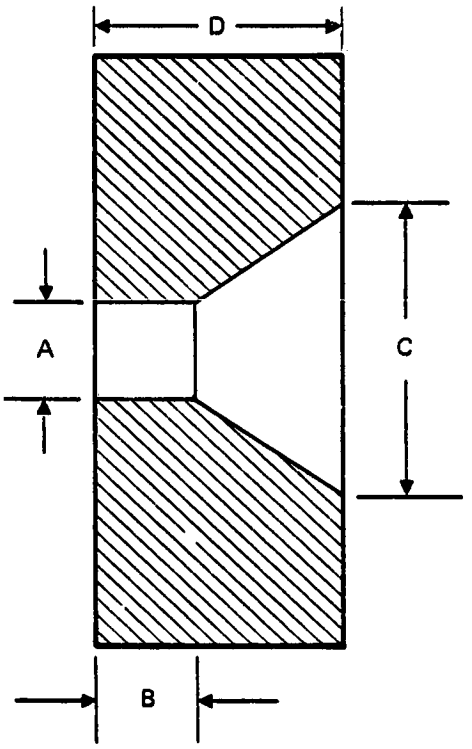

ORIFICE PLATE NO.	DIMENSIONS (mm)			
	A	B	C	D
1	0.76	0.51	5.84	3.0
2	1.02	0.51	6.10	3.0
3	1.27	0.51	6.35	3.0

Figure 4-2. Dimensions of the cathode orifice plates evaluated in the 20,000 A-hr tests.

Table 4-1. Time-Averaged Cathode Operating Conditions for the 20,000 A-hr Tests of the High-Emission-Current Cathodes

Cathode No.	Orifice Diameter, d_o, mm	Flow Rate, mA	Keeper Voltage V	Anode Voltage, V	Insert Temperature	
					Downstream, T_1, °C	Upstream, T_2, °C
1	0.76	191	6.3	14.1	----	----
2	1.02	238	4.8	14.0	1178	1096
3	1.27	221	5.0	14.0	1164	1084

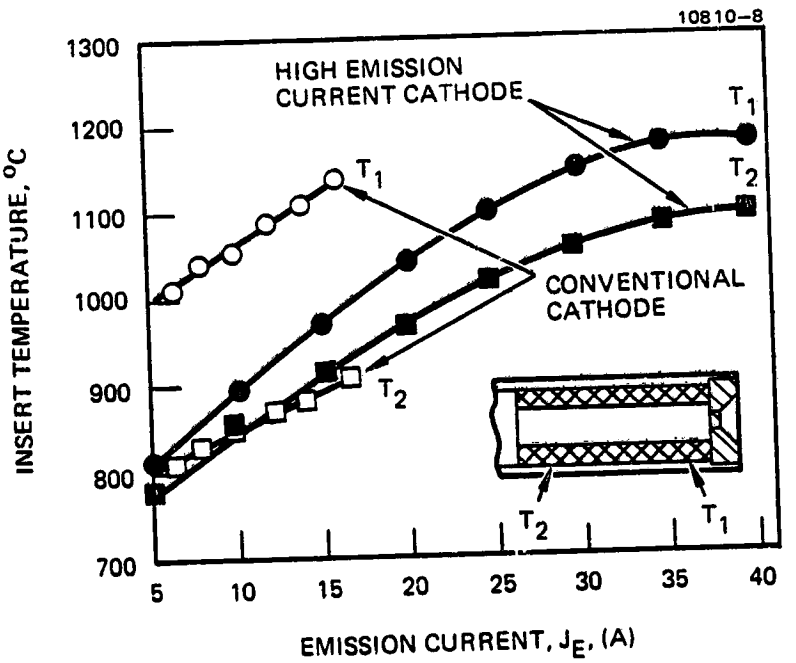

Figure 4-3. Variation of cathode-insert temperature with emission current (d_o = 1.02 mm).

500-hr test. Figure 4-4 presents photographs of the orifice plates, showing the appearance of the apertures after the 20,000 A-hr tests. Substantial erosion of the 0.76-mm-diameter aperture is apparent in Figure 4-4(a). The dimensions of the 1.0- and 1.27-mm-diameter apertures appear to have changed very little, although the surface conditions do show the characteristic faceted appearance of a surface that has undergone ion sputtering. Figure 4-5 presents a comparison of shadowgraphs taken of impressions of the downstream side of the orifice plates, indicating that the cylindrical throat region of the 0.76-mm-diameter aperture was completely eroded away. The 1.0-mm-diameter aperture plate shown in Figure 4-5(b) shows evidence of similar damage. The 1.27-mm-diameter orifice plate is shown in Figure 4-5(c), with only slight evidence of aperture erosion apparent. The dimensions of this aperture were measured after the test, and they were within the specified fabrication tolerances.

14415-3

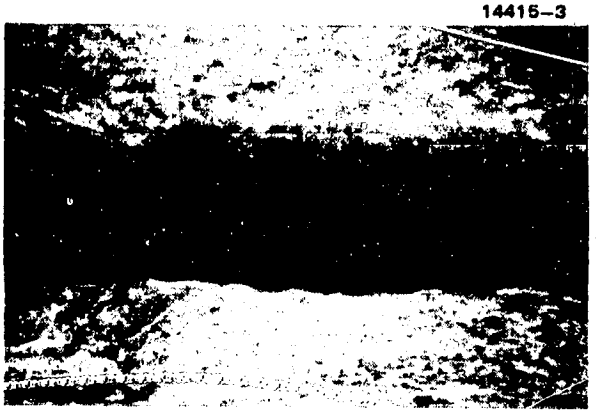

(a) d_o = 0.76 mm (78° VIEW, 137 x MAGNIFICATION)

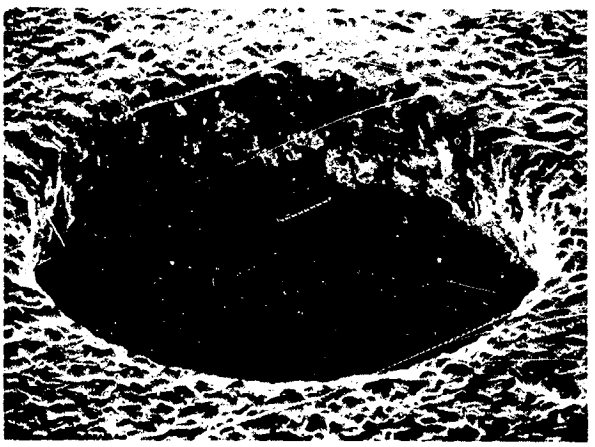

(b) d_o = 1.02 mm (60° VIEW, 71 x MAGNIFICATION)

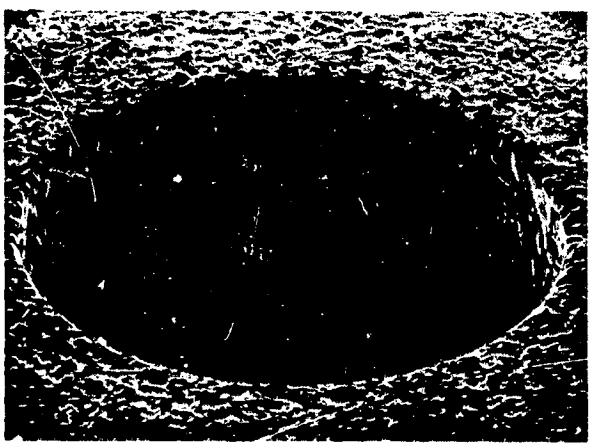

(c) d_o = 1.27 mm (60° VIEW, 65 x MAGNIFICATION)

Figure 4-4.
Photographs showing the upstream sides of the cathode orifice plates and the appearance of the apertures after operating at an emission current of J_E = 40 A for 500 hr.

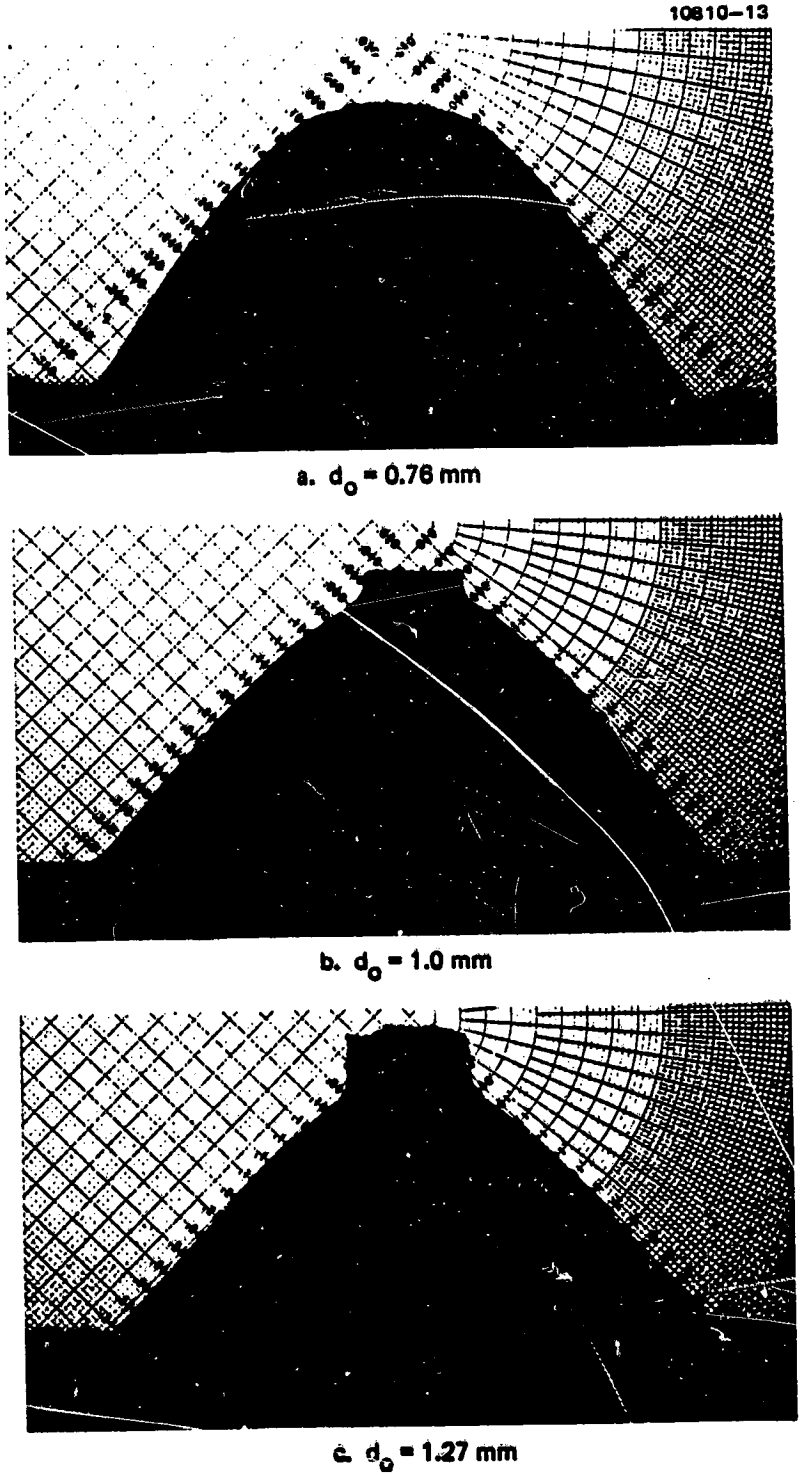

a. d_o = 0.76 mm

b. d_o = 1.0 mm

c. d_o = 1.27 mm

Figure 4-5. Shadowgraphs of impressions made of the cathode orifice plates after operating at an emission current of J_E = 40 A for 500 hr.

SECTION 5

ISOLATOR BREAKDOWN-VOLTAGE MEASUREMENTS

To operate an extended-performance thruster at high beam current and high specific impulse requires beam voltages greater than the voltage-standoff capability of the J-series-thruster propellant-flow electrical isolator shown in Figure 5-1. However, scaling the isolator to a higher voltage rating is readily accomplished by adding a sufficient number of isolating sections,* provided that the minimum breakdown voltage of individual sections is known.

The breakdown voltage of adjacent pairs of isolator sections was measured using the instrumented seven-section propellant-flow electrical isolator shown in Figure 5-2. The instrumented isolator was fabricated under NASA Contract NAS 3-21040, where it was used to measure the voltage variation along the length of the isolator using electrical leads that attach directly to the wire-mesh screens and exit through the isolator body. Figure 5-3 is a schematic showing the setup used in conducting the breakdown-voltage measurements of individual sections of the isolator. The results are presented in Figure 5-4 where breakdown voltages are plotted as a function of propellant flow rate, $\dot{m}$. These results show that the breakdown voltage decreases with increasing flow rate, and, in general, increases with distance along the isolator. These trends are consistent with Paschen's Law and are a result of the pressure rise accompanying higher flow rates and the pressure drop along the length of the isolator. The results of Figure 5-4 indicate a conservative voltage rating of ≈340 V per section, suggesting a total voltage standoff of about 2,400 V.

---

*The present design incorporates seven sections and has a conservative voltage-standoff rating of 1,500 V.

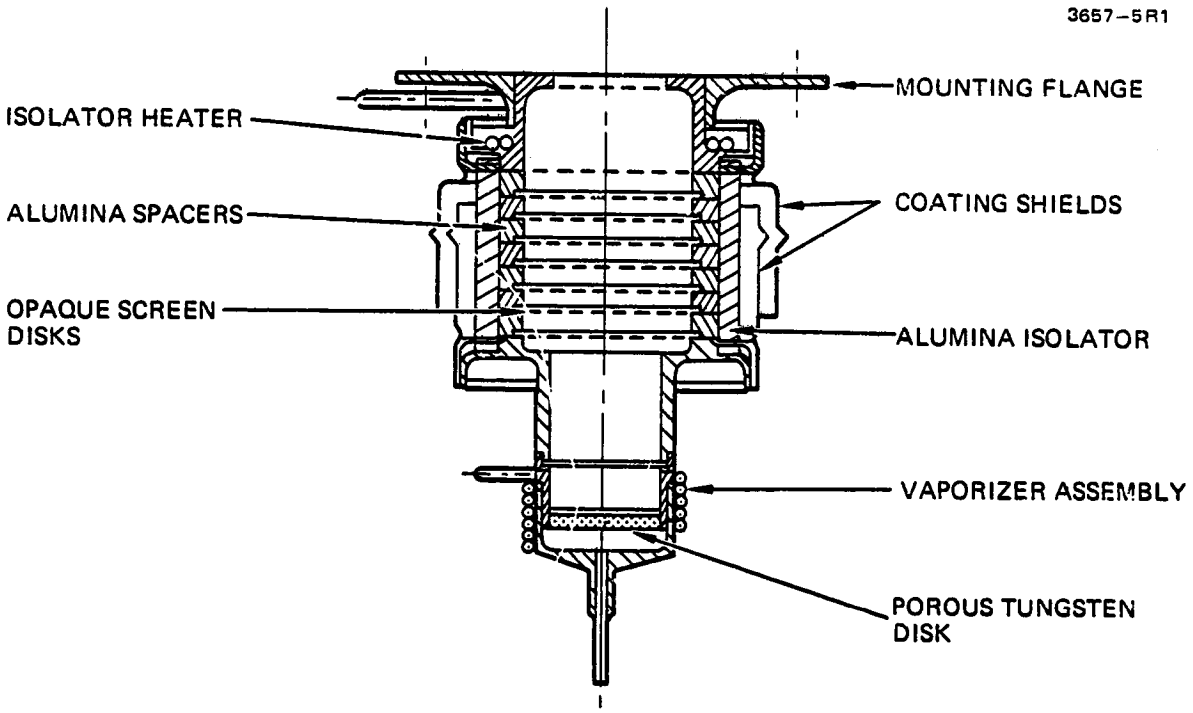

Figure 5-1. Propellant-flow electrical isolator used in the J-series thruster.

M12823

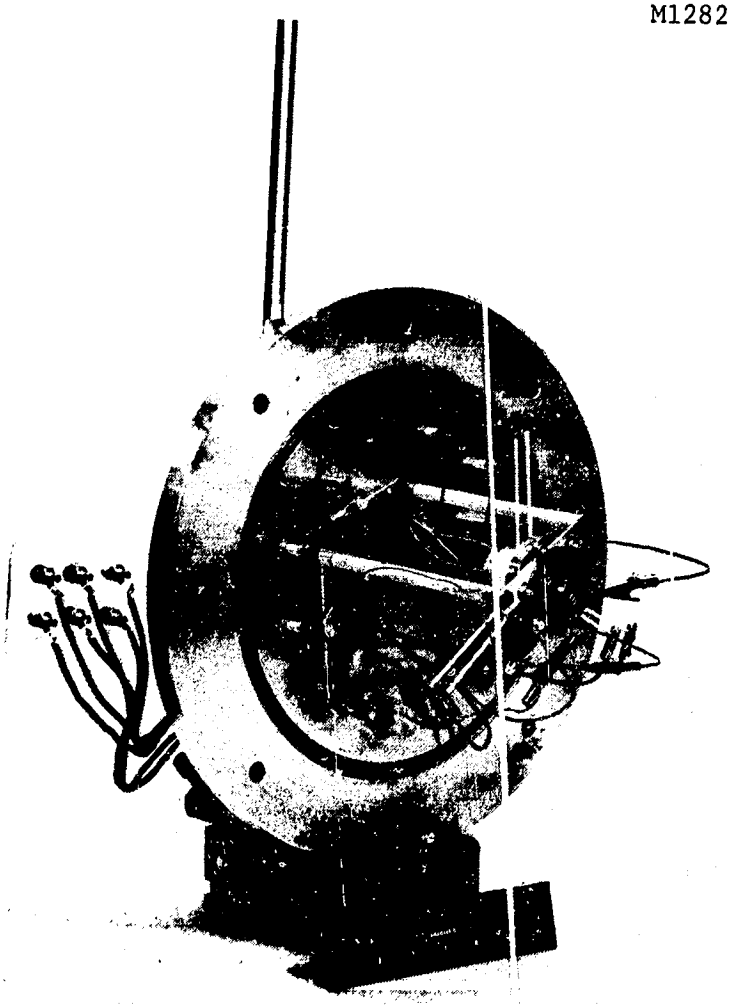

Figure 5-2. Photograph of the instrumented propellant-flow electrical isolator showing electrical connections for each isolating mesh.

13111-15

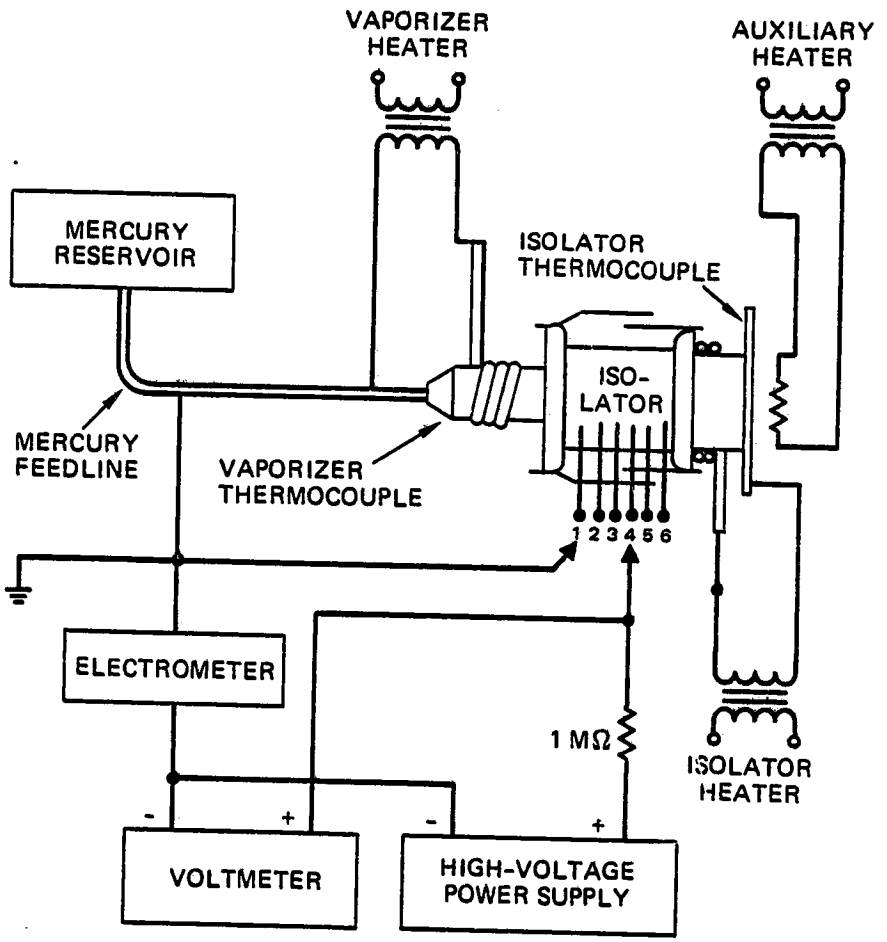

Figure 5-3. Schematic of the test setup used for performing isolator breakdown-voltage measurements.

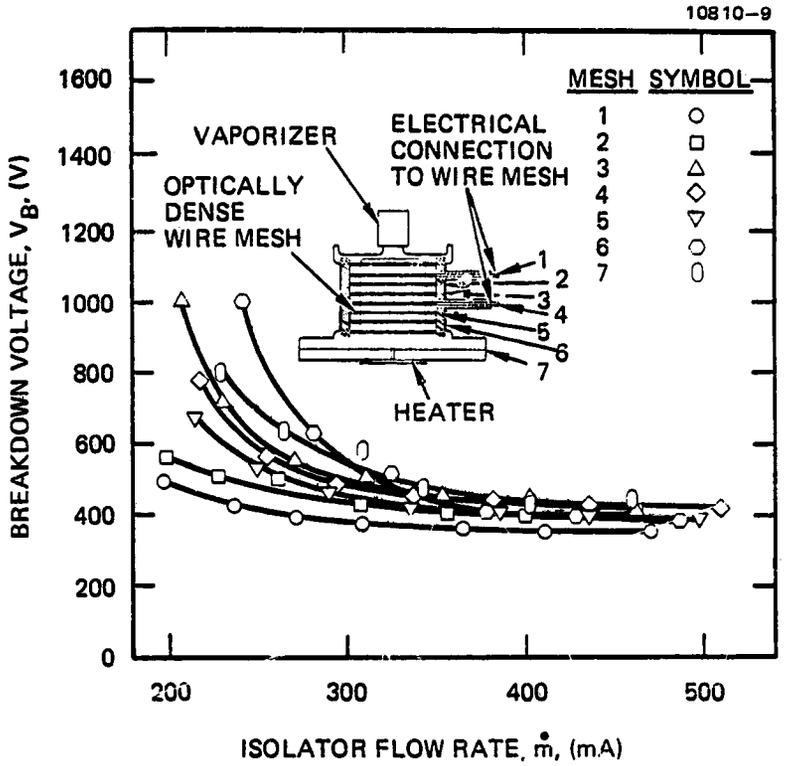

Figure 5-4. Variation of breakdown voltage with flow rate for each chamber of the instrumented propellant-flow electrical isolator.

We also performed breakdown-voltage measurements for multiple isolator sections in order to verify that the total voltage-standoff is the product of the number of isolator sections and the breakdown-voltage per section. These tests were conducted at an isolator-base temperature of T_{base} = 320°C, and at a vaporizer temperature corresponding to a flow rate in the range 450 mA < $\dot{m}$ < 500 mA. Figure 5-5 presents the measured breakdown voltages plotted as a function of the number of isolator sections, indicating a linear relationship between the two variables. All of our data tend to follow the same curve, indicating the absence of any "end effects." The slope of the line drawn through the data points is 330 V/section, which agrees with the section breakdown-voltage measurements of Figure 5-4 to within the precision of the measurements.

The effect of varying the isolator-base temperature is illustrated in Figure 5-6, which presents the breakdown-voltage measurements for the sixth section of the seven-section isolator for base temperatures of 260°C and 320°C. Under low-flow conditions, a reduction in isolator-base temperature results in a substantial reduction in breakdown voltage. This effect is a consequence of Paschen's Law, which (in general form) relates the breakdown voltage, V_B, to the product of gas density, n, and interelectrode distance, d. The temperature dependence arises from the equation of state, resulting in $n \sim p/T$ for an ideal gas. This allows Paschen's Law to be formulated as

$$V_B = f\left(\frac{pd}{T}\right) \quad , \tag{5-1}$$

which reduces to the more familiar form, $V_B = g(pd)$, for constant temperature, T. The discussion leading to Equation (5-1) suggests that the curves of Figure 5-6 should coincide if the

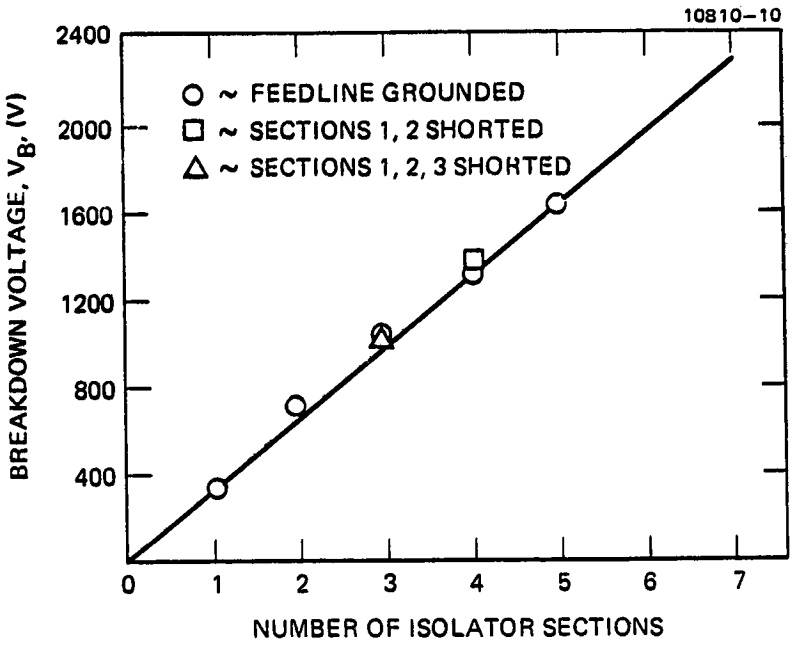

Figure 5-5. Variation of breakdown voltage with the number of isolating sections.

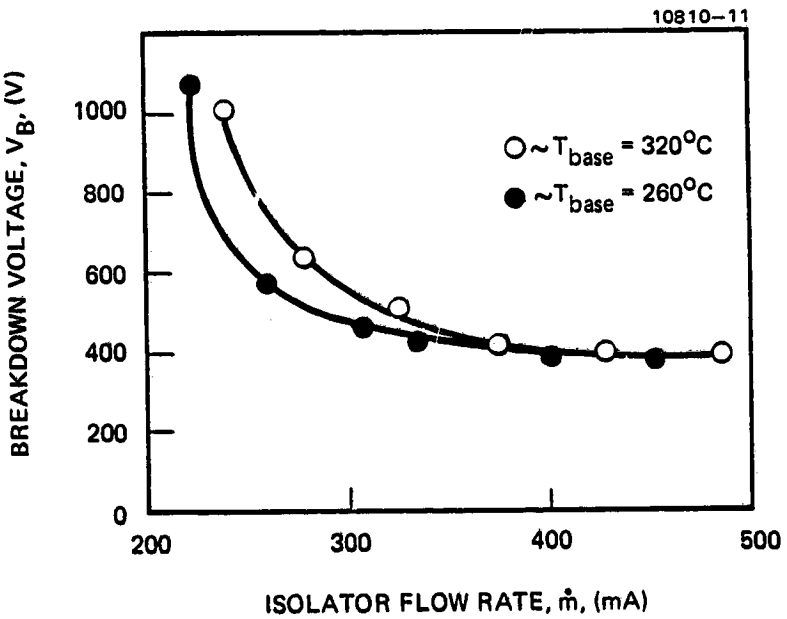

Figure 5-6. Effect of isolator base temperature on the breakdown voltage of the instrumented propellent-flow electrical isolator.

flow-rate data are divided by the absolute temperature of the gas, which can be assumed to be roughly the same as the isolator-base temperature. Figure 5-7 presents the results we obtained by replotting the data of Figure 5-6 versus the parameter $\dot{m}/T_{base}$ and shows that the data points fit a single curve quite well.

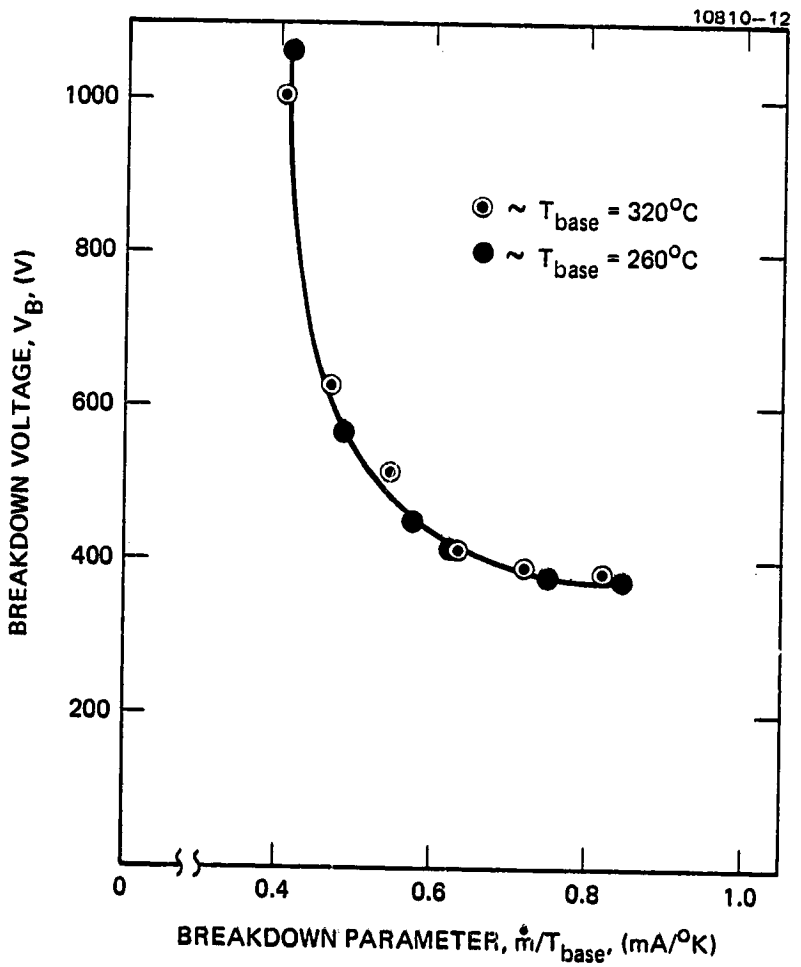

Figure 5-7. Variation of the isolator-section breakdown voltage with the parameter $\dot{m}/T_{base}$.

SECTION 6

POWER-PROCESSOR SIMPLIFICATIONS

Various approaches to reducing the number of power supplies required to operate the J-series thruster have been investigated,[6-1,6-2] and it has been demonstrated[6-1] that the number of individual power supplies can be reduced from twelve to five, using switching, combining, and power-absorbing techniques. Under this program, we investigated two approaches for simplifying the vaporizer power supplies of the J-series thruster, using efficient techniques that do not involve power absorption.

The first concept uses a multiple-output power supply that provides for closed-loop control of the main, cathode, and neutralizer vaporizers, using the three switching regulators shown in Figure 6-1. This design requires three separate output filters (L_1 and C_1) which are the largest contributors to the volume and mass of the power supply. The remainder of the circuit consists of three high-speed switching transistors, Q_2, three fast-recovery diodes, CR_1, and three analog switching-regulator control circuits, U_1.

The second concept uses a time-shared or multiplexed power supply employing a switching regulator to sequentially provide power to each of the three vaporizers. A schematic of this design is shown in Figure 6-2. The multiplexed power supply eliminates many of the large and costly components of the multiple-output power supply by substituting low-level digital circuitry that is relatively small, lightweight, and inexpensive. This tradeoff is apparent in Table 6-1, which shows the parts required for each power-supply design. The multiplexed power-supply concept was selected as the most attractive candidate for further investigation because it offers a 70% reduction in parts count (and a corresponding increase in reliability).

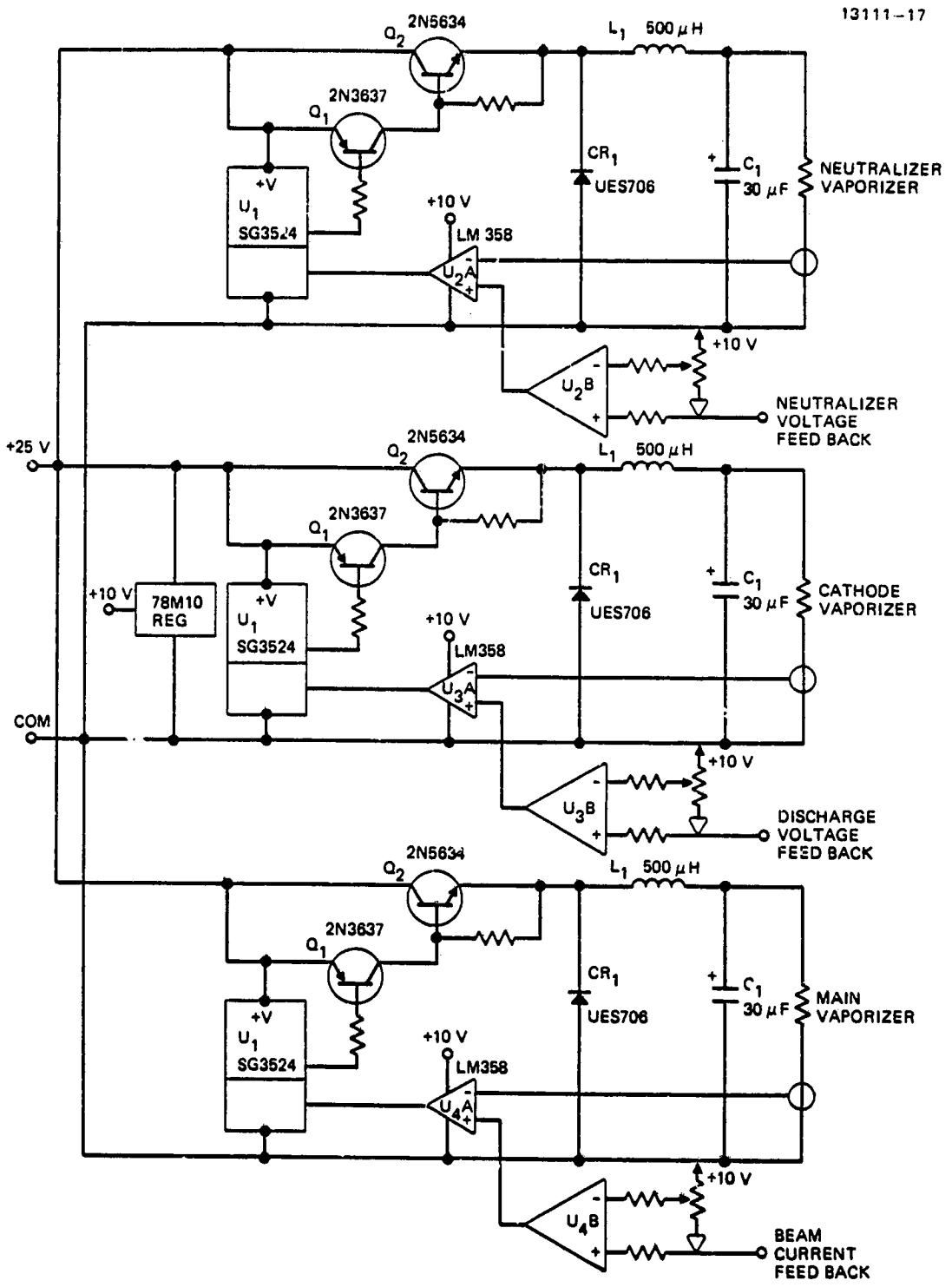

Figure 6-1. Schematic of the multiple-output vaporizer power supply.

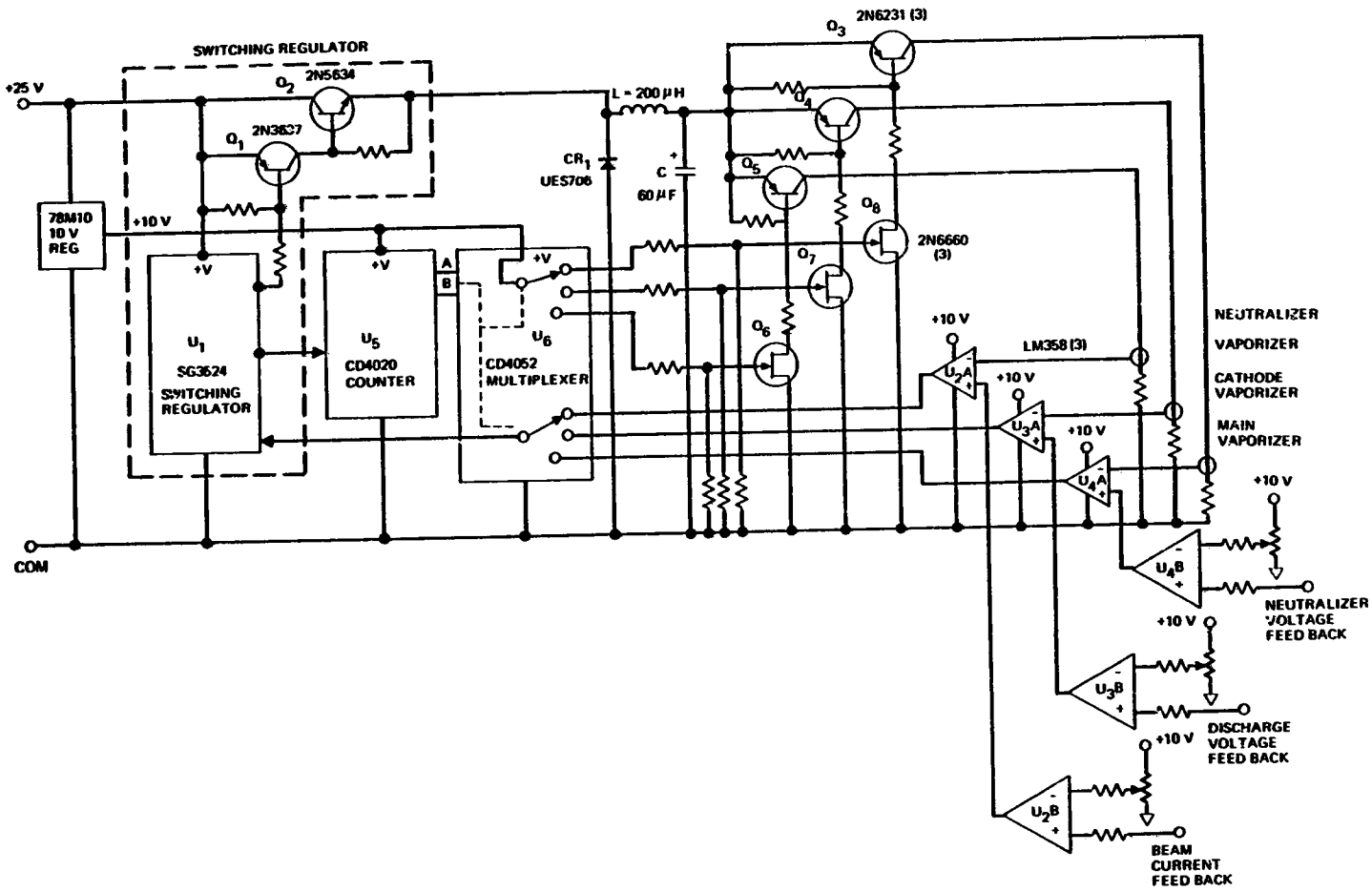

Figure 6-2. Schematic of the multiplexed vaporizer power supply.

Table 6-1. Comparison of Parts Required for 30-cm-Thruster, Multiple Output, and Multiplexed Vaporizer Power Supplies

Component	30-cm Thruster Supplies Qty	Size	Multiple Output Supply Qty	Size	Multiplexed Supply Qty	Size
Pulse Width Modulated Control Circuit I.C. (U1) SG3524	-	-	3	16-Pin DIP	1	16 Pin DIP
Voltage Regulator 10 V 78M10	-	-	1	TO-220	1	TO-220
Driver Transistor (Q1) 2N3637	-	-	3	TO-5	1	TO-5
Power Transistor, High Speed Switch (Q2) 2N5634	6	TO-3	3	TO-3	1	TO-3
Commutating Diode, Fast Recovery, (CR1) UES706	18	3-5A DO-7 Type (Axial Lead)	3	1/4" Stud	1	1/4" Stud
Power Choke (L1)	3 6	10 kHz Power Transformer Control Transformer	3	L = 500 μH 26-mm Pot Core	1	L = 200 μH 36-mm Pot Core
Output Capacitor (C1)	3	C = 22 μF	3	C = 30 μF	1	C = 100 μF
Control Circuit OP Amp (U2)	- 21	- 14 Pin DIP	3	8 Pin DIP	3	8 Pin DIP
Multiplexer Circuit						
(U5) Counter CD4020	-	-	-	-	1	16 Pin DIP
(U6) Multiplexer CD4053	-	-	-	-	1	16 Pin DIP
Power Transistor (Q3, Q4, Q5) Low Speed Switch	-	-	-	-	3	TO-3
Driver Tansistor (Q6, Q7, Q8)	-	-	-	-	3	TO-5
TOTAL PARTS	57		22		18	

We designed the multiplexed power supply of Figure 6-2 to provide 5-msec current pulses to the cathode, main, and neutralizer vaporizers at an operating frequency of 67 Hz. The power supply was fabricated, and then evaluated using the J-series-equivalent thruster S/N 301J. The tests were performed using a two-inverter power processor that was supplied by NASA, with the multiplexed power supply used to replace its (three) individual vaporizer power supplies.

Figure 6-3 presents a strip-chart recording showing the vaporizer-current waveforms of the multiplexed power supply. The vaporizer control loops are uncompensated, and we made no attempt to optimize their gain. Despite this, the power supply performed extremely well in these tests, and we were able to demonstrate the validity of the time-sharing concept. Figures 6-4 through 6-6 show the response of the controlled variables (V_D, J_b, and V_{NK}) to step changes in the vaporizer currents that were obtained by momentarily reducing the output current to zero. The results demonstrate the stability of the unoptimized control system, and show recovery times on the order of $\leq$ 40 sec (based on 1% deviation from steady-state values). Although we did not pursue the development further, we believe the system response and recovery time could be significantly improved through a modest optimization effort.

The multiplexed vaporizer-power-supply concept represents a significant reduction in the mass and parts count of the three individual power supplies presently used in the power processor of the J-series thruster. This reduction is illustrated in Table 6-1 which compares the parts required for the J-series vaporizer supplies, along with the requirements for the Hughes multiple-output and multiplexed designs. The benefits are readily apparent by comparing the requirements for transformers, power transistors, and commutating diodes. The simplification is achieved at the expense of the low-level multiplexer logic circuitry.

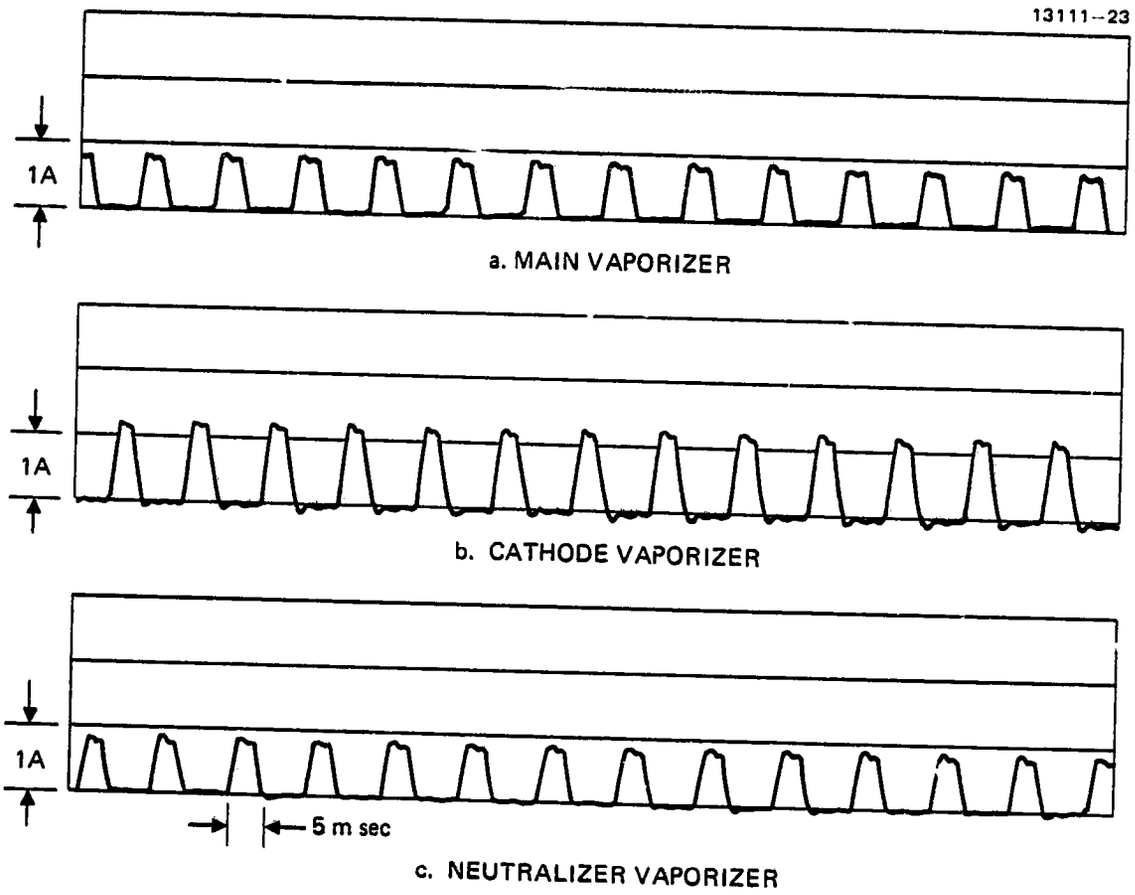

Figure 6-3. Current waveforms of the multiplexed vaporizer power supply operated at 67-Hz.

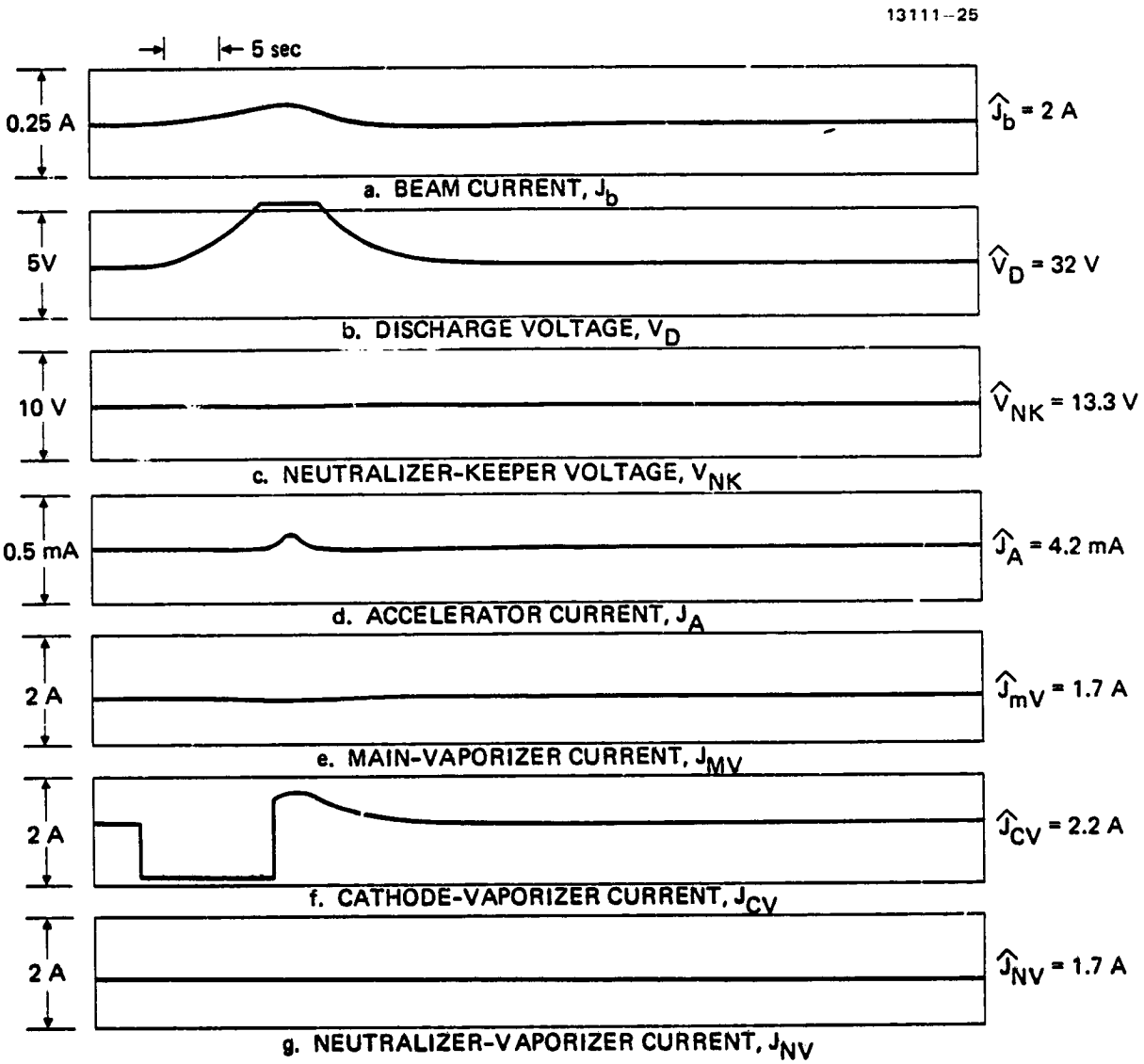

Figure 6-4. Response of the discharge voltage to a step change in the cathode-vaporizer output of the multiplexed power supply.

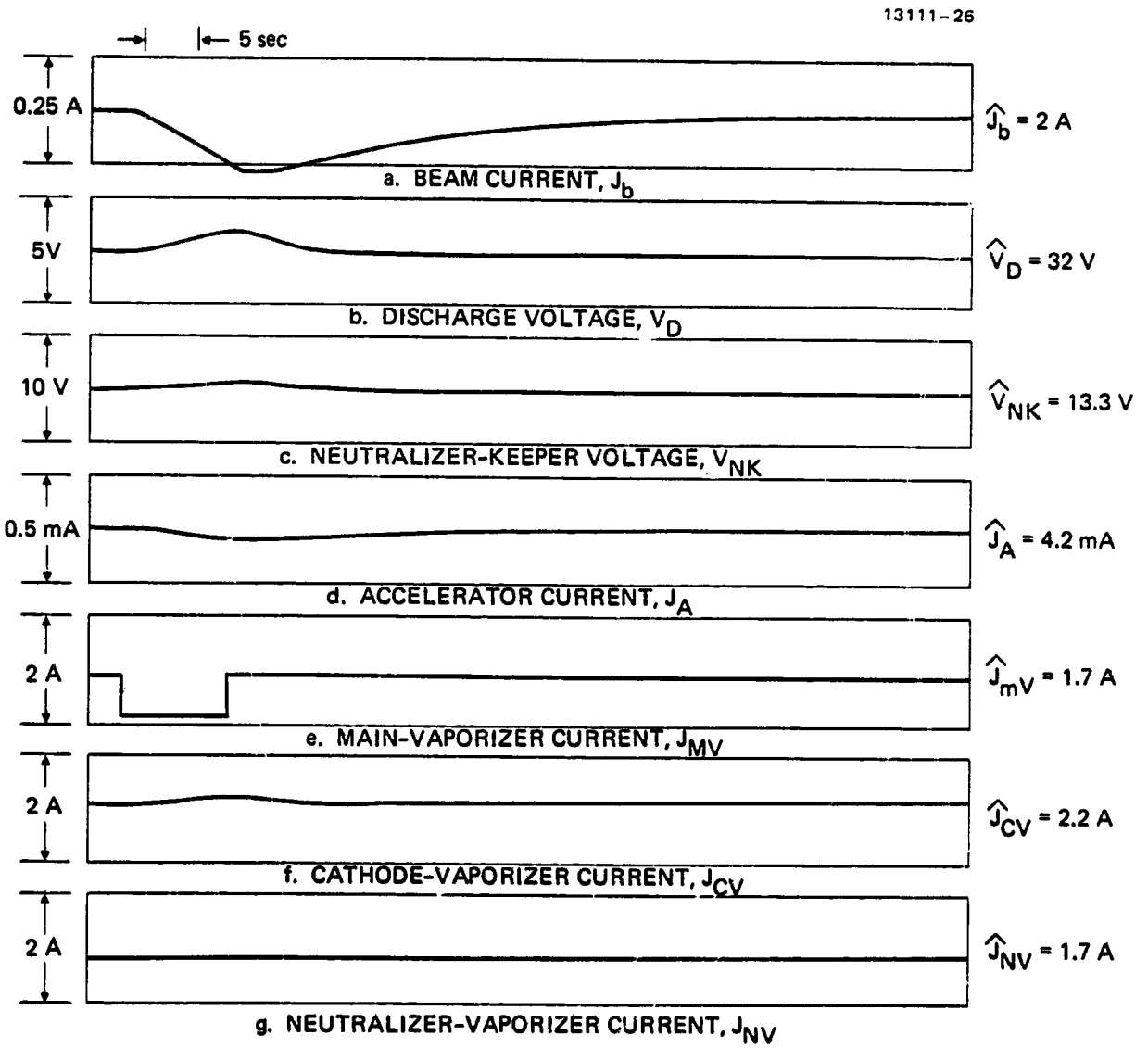

Figure 6-5. Response of the beam current to a step change in the main-vaporizer output of the multiplexed power supply.

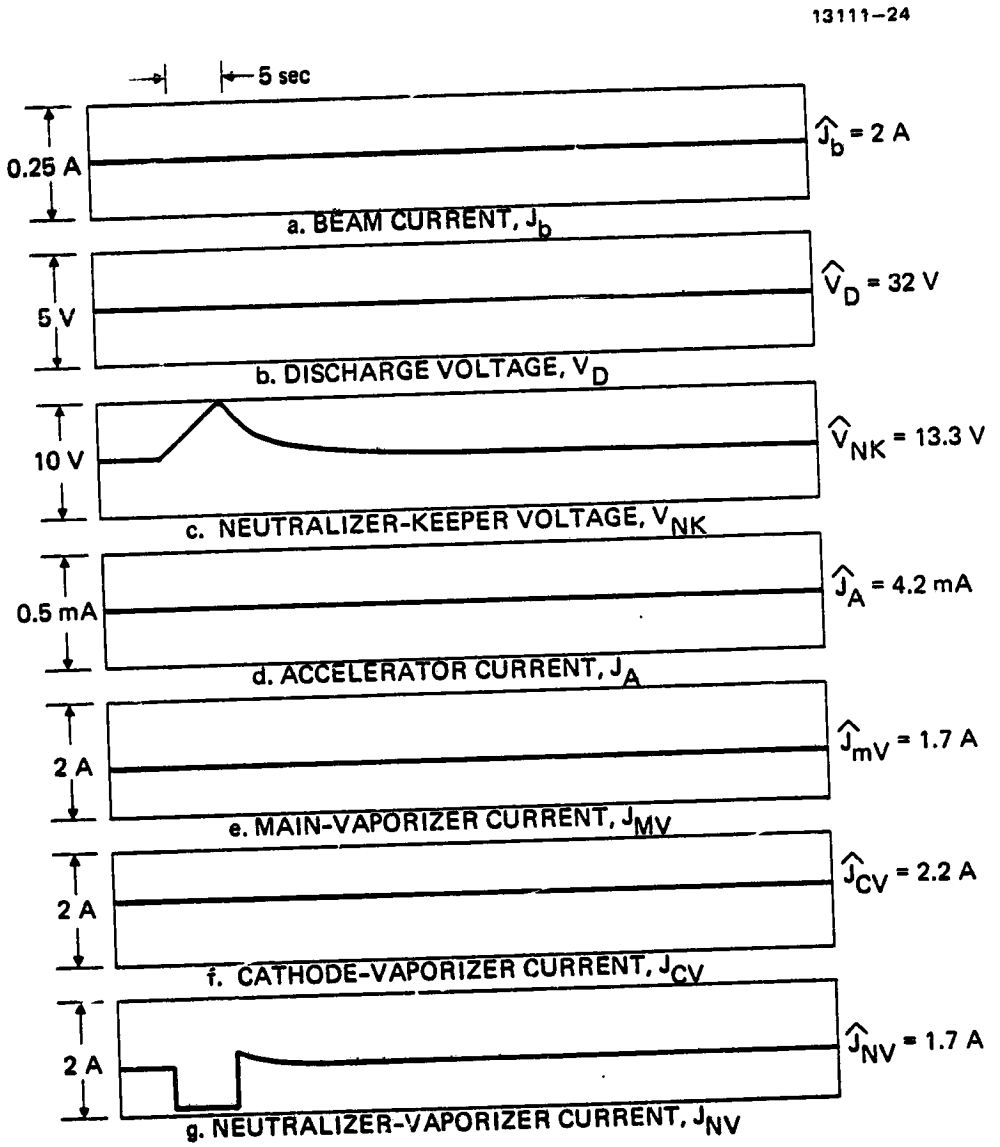

Figure 6-6. Response of the neutralizer-keeper voltage to a step change in the neutralizer-vaporizer output of the multiplexed power supply.

SECTION 7

THRUST-LOSS-MEASUREMENT ERROR ANALYSIS

Accurate predictions of net thrust are required for planetary applications of ion-propulsion technology, since even small deviations could cause a significant loss in total impulse and pointing accuracy (when integrated along the flight path). The net thrust is obtained by correcting the thrust calculated from measured values of beam current, J_b, and beam voltage, V_b, for losses resulting from beamlet divergence and multiply charged ions. These losses arise from (1) the reduced thrust-to-power ratio of multiply charged ions, (2) diverging ion trajectories caused by transverse electric fields within the acceleration region, and (3) vectoring caused by the non-planar shape of the electrodes and aperture displacement. The effects of multiply charged ions are accounted for in the factor α, while the effects of divergence and vectoring are accounted for in the factor F_t. Both correction factors are less than unity (by definition), reducing the calculated thrust according to the relationship,

$$F = \alpha F_t F_c \quad , \tag{7-1}$$

where F is the true thrust, and F_c is the thrust calculated by

$$F_c = J_b \left(2mV_b/e\right)^{1/2} \quad , \tag{7-2}$$

where m is the mass of the ion, and e is the electronic charge. The accuracy of determining α, F_t, and F_c depends on both experimental and computational errors that are inherent in the measurement technique. This section describes an analytical and

experimental investigation of the procedures that we use to determine the factors α and F_t. A comprehensive examination of the measurement technique, assumptions, and equations used in the calculations leads to the identification of possible sources of error or uncertainty. An estimate of the overall accuracy of the thrust-correction factors is calculated using standard error-analysis techniques and estimates of the uncertainties in each of the variables.

A. PROCEDURE FOR DETERMINING THE THRUST-LOSS FACTORS

Obtaining the thrust-loss factors α and F_t requires a measurement that can determine the singly and doubly charged ion-current-density vectors as a function of the polar coordinates r and ϕ defined in Figure 7-1. Assuming symmetry about the thrust axis simplifies the measurement by eliminating the variable ϕ, reducing the problem to that of determining the current density of each ion species as a function of the radial coordinate r. The measurement is performed using an articulating probe that can view a small region of the ion-accelerator electrode from different angles, ϕ_p, and separate the total current leaving this region according to velocity (charge state). This gives the currents $i_n(r,\phi_p)$, where the index n is used to denote the charge state. Integrating these currents over the angle ϕ_p gives the magnitude of the current-density vector, $\vec{j}(r)$, and the angle ϕ that this vector makes with respect to the thrust axis; Figure 7-2 illustrates the geometry.

1. Velocity Analyzer Probe

The total current emanating from the active region of the accelerator electrode is separated into the current components, $i_n(r, \phi_p)$, using a series arrangement of a particle collimator and velocity filter. The collimator restricts the viewing area and transmits a highly collimated beam to the velocity filter.

11268-1

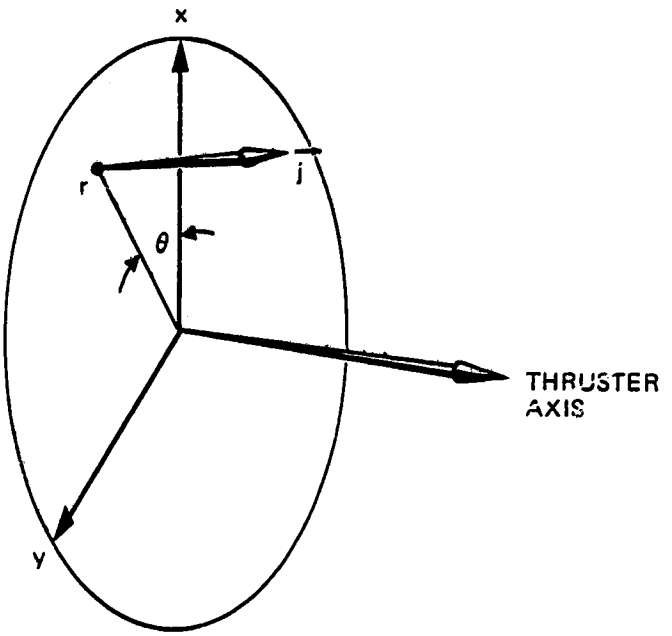

Figure 7-1. Definition of the polar coordinate system used to describe the current-density vector $\vec{j}$.

11268-2R1

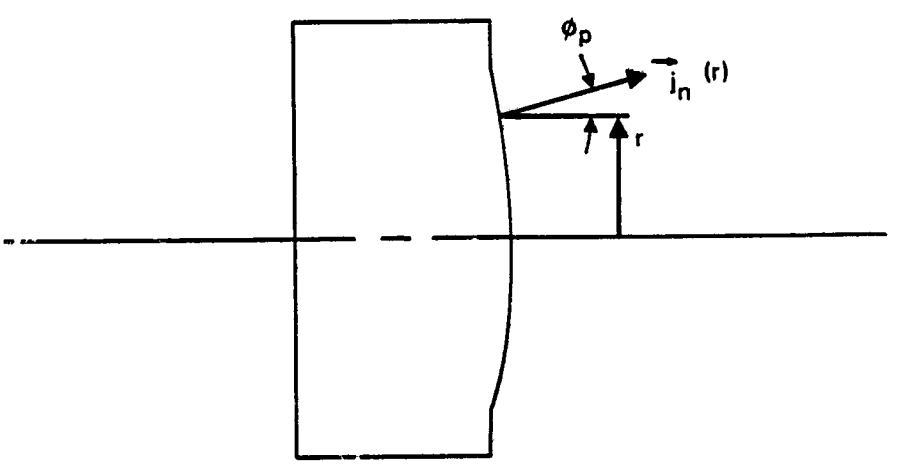

Figure 7-2. Illustration of the geometric variables describing the current density at the accelerator grid.

The transmission of the collimator is illustrated in Figure 7-3, which shows its response to a parallel beam inclined at an angle ϕ_o. The transmission is unity* when the collimator is aligned with the beam ($\phi_p = \phi_o$) and rapidly drops to zero for angles $\pm\psi$ about ϕ_o. The angle ψ is the acceptance half-angle and is small enough ($\psi = 0.29°$) to enable the probe response at any angle ϕ_o to be interpreted as the response due to particles that leave the viewing area and which follow straight-line trajectories inclined at an angle (ϕ_p) with respect to the thruster axis.

The velocity filter is composed of orthogonal electric and magnetic fields ($\vec{E}$ and $\vec{B}$, as shown in Figure 7-4) and transmits only those particles having velocity equal in magnitude to the ratio E/B. All other particles are "filtered out" by an imbalance in the electric and magnetic forces which deflects the particles up or down, depending upon whether the particle speed is greater than or less than the ratio E/B. The series arrangement of the collimator and velocity filter results in a probe output corresponding to collection of those particles having velocity vectors with magnitude E/B, and with direction in the range $\phi_p - \psi \leq \phi \leq \phi_p + \psi$.

A schematic of the velocity-analyzer or $\vec{E}x\vec{B}$ probe that was developed[7-1] by Hughes for measuring $i_n(r,\phi_p)$ is presented in Figure 7-5. The probe assembly consists of a collimator, velocity filter, drift tube, electron suppressor, and current collector. The collimator apertures have a diameter of 0.25 mm, resulting in an acceptance half-angle of $\psi = 0.29°$. With this geometry, and with the probe positioned 38 cm downstream of the accelerator grid, the viewing area is 0.13 cm^2, or the equivalent of about three accelerator apertures in the J-series ion-extraction assembly. The separator provides orthogonal electric

*The mathematical formulation and physical significance of the collimator transmission is described in Appendix D.

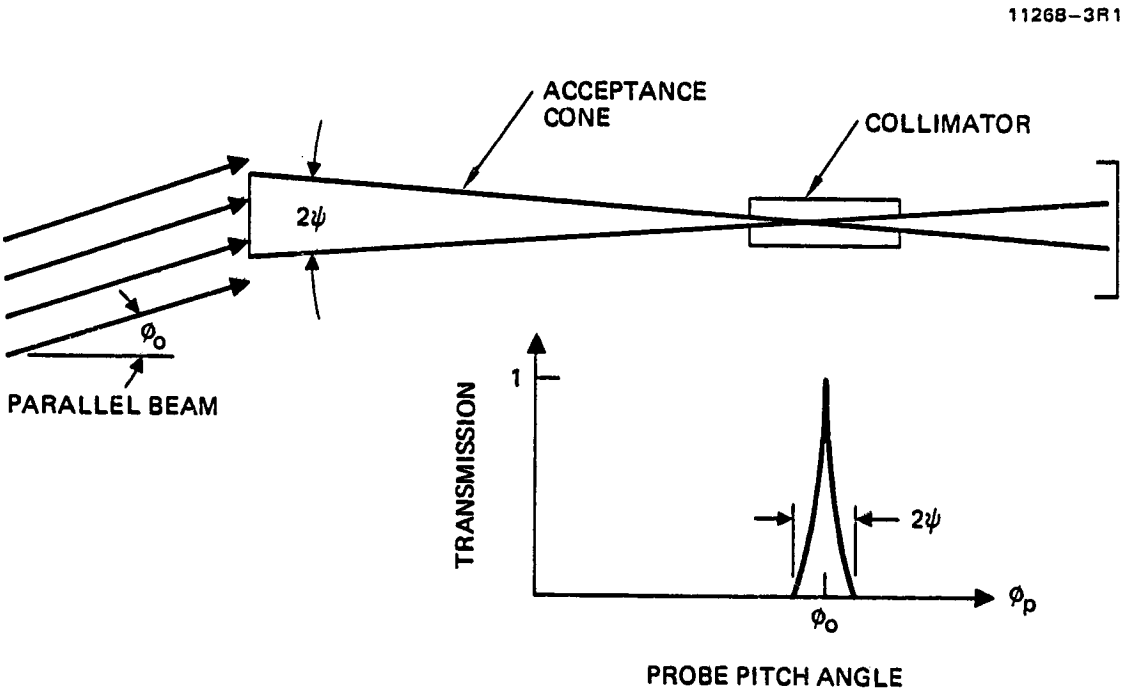

Figure 7-3. Angular response of the collimator.

11268-4

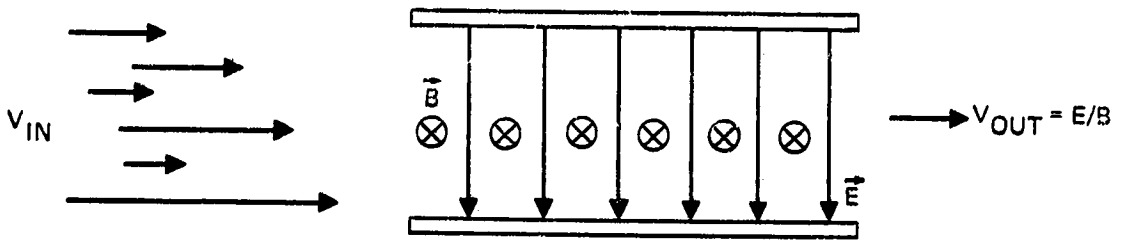

Figure 7-4. $\vec{E}x\vec{B}$ velocity filter used for separating ions according to their velocity.

11268-5

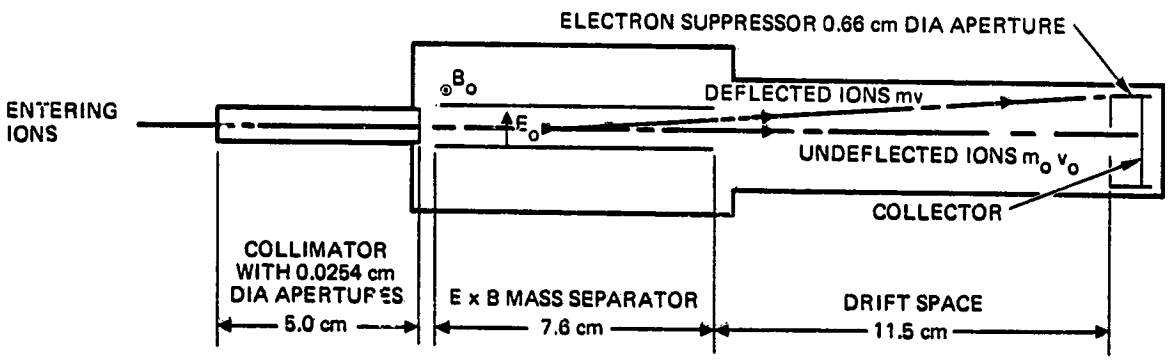

Figure 7-5. Schematic of Hughes $\vec{E}x\vec{B}$ probe.

and magnetic fields $\vec{E}$ and $\vec{B}$. The electric field is established by the potential applied to parallel plates, and the magnetic field is provided by a permanent magnet. Varying the plate potential changes the ratio, E/B, allowing ions of different velocities to traverse the separator undeflected, and to reach the collector. The collector aperture is biased 45 V negative with respect to the probe assembly in order to return secondary electrons to the collector.

The dimensions of the collimator result in a small viewing area, but one which is large enough to provide a readily measurable current ($\approx 10^{-9}$ A). The drift-tube length and collector-aperture diameter ensure collection of the entire collimated and undeflected beam of interest. Figure 7-6 presents collector current as a function of plate voltage and demonstrates the ability of the probe to resolve the peaks associated with singly and doubly charged ions; these measurements were obtained at an unusually high discharge voltage to exaggerate the Hg++ peak and to enable the Hg+++ peak to be resolved. The nearly rectangular shape of the peaks enables their height to be used as an indication of the total current of each species, simplifying the data acquisition and analysis.

2. Test Facility

A sketch of the probe setup used in the Hughes 9-ft-diameter vacuum chamber is presented in Figure 7-7. A precision stepping motor located on top of the vacuum chamber is used to move the probe vertically in or out of the thrust beam to vary the coordinate r. The pitch angle, ϕ_p, is controlled using a precision stepping motor located inside the vacuum chamber. A potentiometer and digital readout provide a visual display of the probe pitch angle. The probe yaw angle can be adjusted to position the probe axis parallel to the thruster axis. The vacuum feedthrough is located off-center in the flange shown in Figure 7-7, enabling the lateral position of the probe to be adjusted (over a narrow range) so that its translational axis intersects the thruster axis.

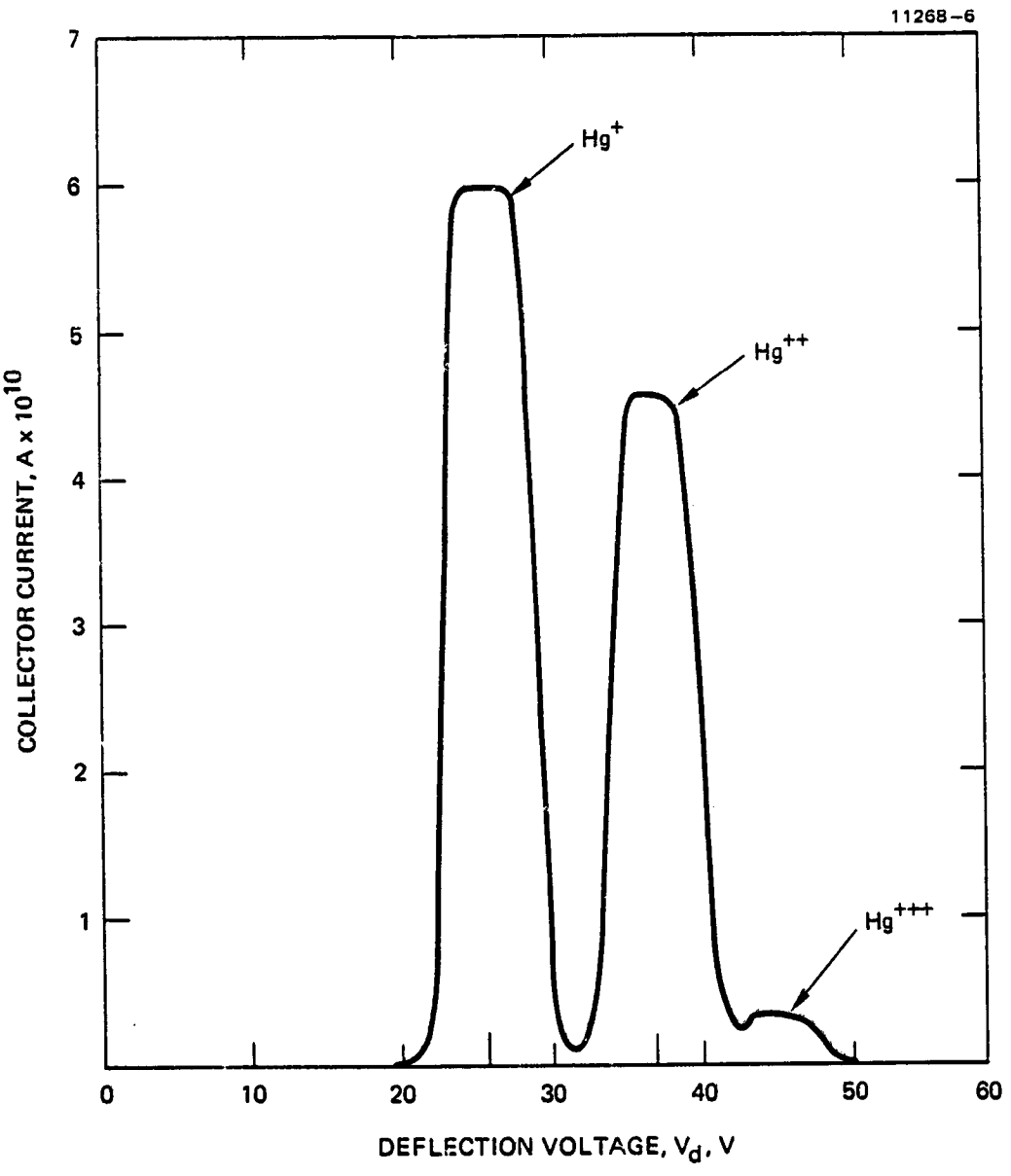

Figure 7-6. Example of current output of the $\vec{E}x\vec{B}$ probe as a function of deflection-plate voltage (with the probe inserted in the thruster beam).

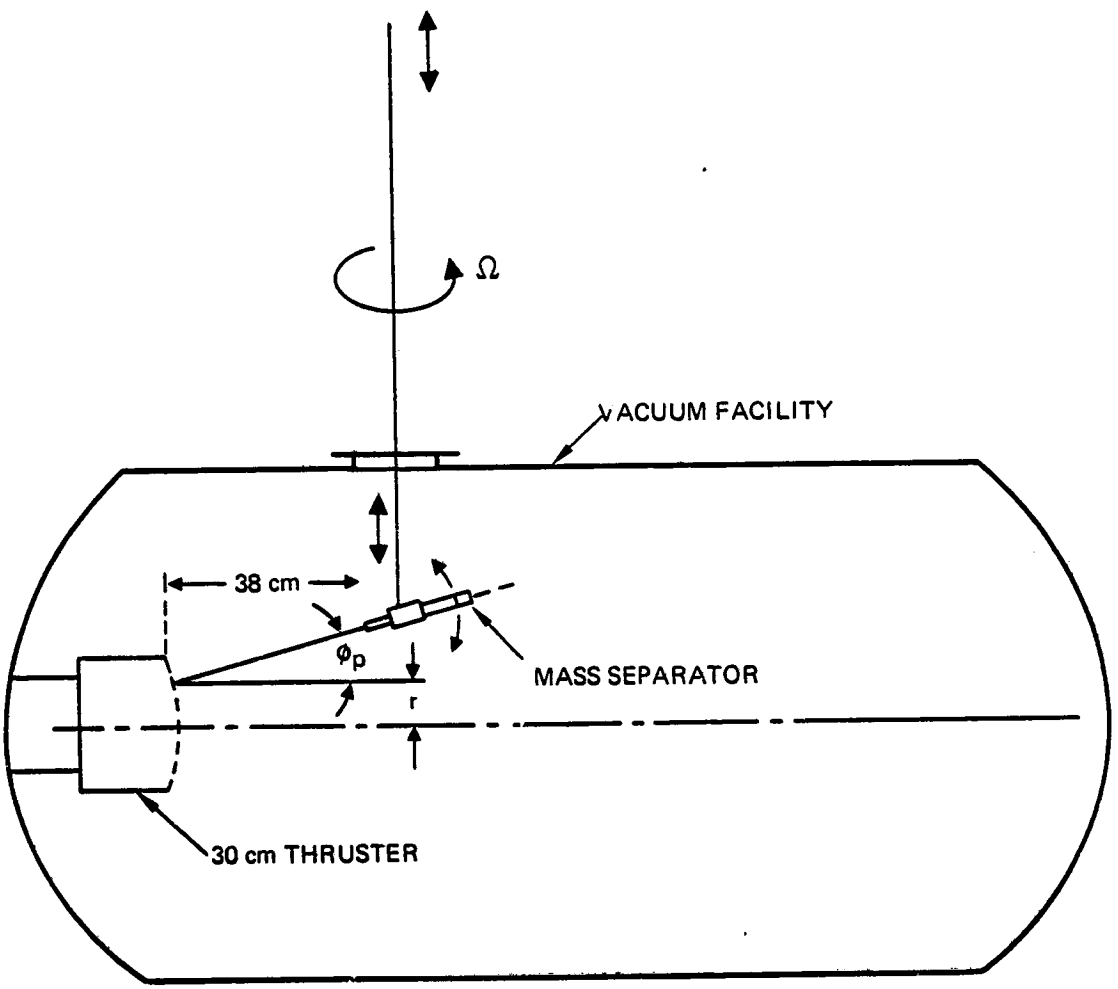

Figure 7-7. $\vec{E}\times\vec{B}$ probe installation in Hughes 9-ft-diameter vacuum chamber.

The only maintenance required of the probe assembly is an occasional need to replace the collimator aperture, which eventually disintegrates as a result of sputtering by the ion beam. The absence of the collimating aperture is easily detected by the operator in the form of an increase in collector current and the inability to resolve the peaks corresponding to the individual ion species.

3. Thruster Alignment

The probe-to-thruster alignment is accomplished by aligning both the thruster and the probe with respect to the chamber axis. This approach minimizes setup time because the probe-to-tank alignment is required only after removal and reinstallation of the probe. The thruster-to-tank alignment is accomplished by aligning the thruster with respect to the axis of the vacuum-enclosure flange, as shown in Figure 7-8. The thruster support and vacuum-enclosure flange position the thruster with respect to the tank axis, and the angular alignment of the thruster axis is accomplished using the dial indicator to locate the edge of the accelerator grid at 90° intervals. In order to ensure that the angle between the thruster and flange axis is less than 1°, the difference between the readings obtained 180° apart must not exceed 0.5 cm. If the difference is greater, the mounting fasteners are loosened and the thruster is repositioned to obtain the necessary tolerance.

4. Data Acquisition

The probe-positioning and data-acquisition system is semi-automated, requiring that the operator select the probe pitch angle, locate the beam edge, and determine the plate potentials corresponding to the various ion species.* The first step that

*The normal operating conditions of the 8- and 30-cm thrusters result in a negligible population of triply charged ions. Therefore, the standard practice has been to measure only the singly and doubly charged ion currents. The probe system does, however, have the capability of measuring triply charged ions, which may not be negligible in thrusters that operate at high beam currents.

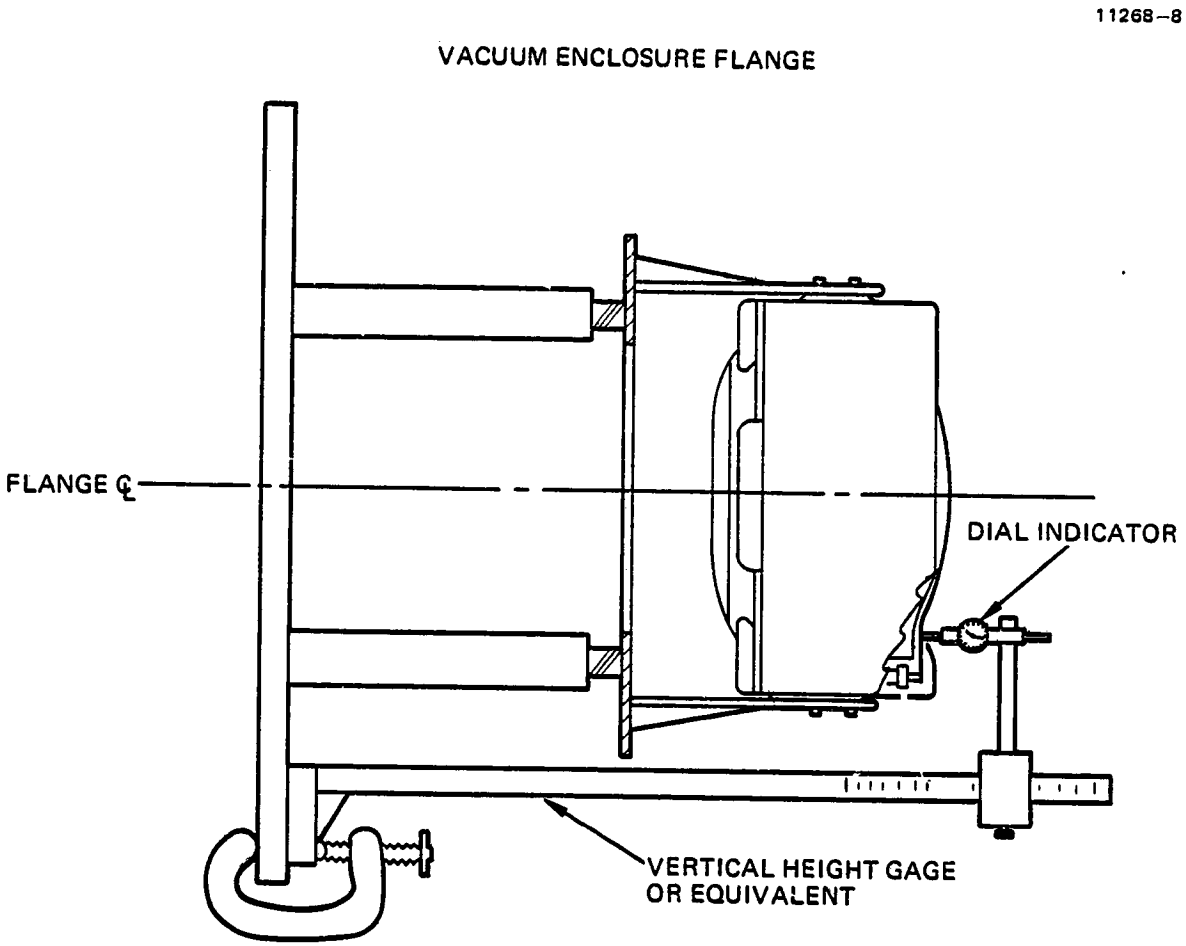

Figure 7-8. Illustration of the procedure used for aligning thrusters with the vacuum-enclosure flange.

the operator performs in conducting a beam scan is to set the probe pitch angle to $\phi_p = 0$, and then drive the probe down and into the beam until a collector current is detected. This locates the edge of the beam at the plane of the accelerator grid and provides a reference for subsequent movement of the probe into the beam, a total distance equal to one-half the diameter of the active region of the electrodes. If either the thruster or probe are removed from the test facility, then upon reinstallation the probe-to-thruster alignment is checked by varying the probe yaw angle, Ω, until the probe current is at a maximum. With the probe-travel and thruster axes aligned, this step ensures that the viewing axis of the probe is coincident with the thruster axis.

Next, the operator varies the output of the electric-field power supply to determine the voltages, V_+ and V_{++}, corresponding to the peaks of the i_+ and i_{++} current profiles (see Figure 7-4). These voltages are then input to the data-acquisition system via potentiometers located on a control panel. Next, the probe is driven up and out of the beam, and the pitch angle, ϕ_p, is set to the maximum negative value to be sampled (usually -15°). The probe is then driven down to locate the beam edge, which is always determined by moving the probe in the downward direction. This eliminates the possibility of a position error that could be caused by hysteresis in the positioning mechanism. At this point the operator places the system in the auto mode, causing the following steps to be executed

- The probe is driven downward a distance equal to one-fourth the radius of the active region of the electrodes.
- Any vibration of the probe caused by the directed motion is allowed to damp out.

- The currents i_+ and i_{++} are sampled, printed, and punched on paper tape.

The sequence described above is automatically repeated a total of four times, with the last measurement performed on the thruster axis. In the final step, the operator drives the probe up and out of the beam, increases the pitch angle by 5°, locates the beam edge, and resets the auto mode (which causes the steps outlined above to be repeated).

In developing the computer program[7-1] used for analyzing the probe data, one of the primary objectives was to minimize the number of input data points, subject to the constraint that the accuracy of the reduced data should be at least comparable to that of the raw probe data (± 2% of full scale, based on the manufacturers specifications on the accuracy of the electrometer). Minimizing the data-collection time ensures that the thruster operating conditions remain constant during the data scan, and relieves the operator of the time-consuming task of taking more data than is necessary. After the initial installation of the probe, scans having a different number of data points were taken. It was determined[7-1] that four equally spaced radial values and seven equally spaced angular values were near optimum. A larger number of radial data points produced essentially the same results, while a smaller number produced discontinuous-appearing curves. While six angular values for each radial value were usually satisfactory, seven were better for more divergent beams. The final technique chosen was to use four radial values and seven angular values, resulting in 56 data points per scan (28 each for i_+ and i_{++}). In practice, the operator may conduct the scan using as many as nine pitch angles, ϕ_p, so that the symmetry of the angular dispersion profiles can be checked, enabling the most symmetrical data to be used as input to the data-analysis routine.

B. DATA-ANALYSIS PROCEDURE

The equations used to calculate the thrust-loss factors, α and F_t are derived in Appendix C. The calculations are performed using the magnitude, $j(r)$, and direction, $\phi(r)$, of the current-density vector at the ion-extraction accelerator grid. These variables are calculated from the $\vec{E}x\vec{B}$ probe measurements, using the procedure derived and discussed in Appendix D. During the present investigation, we found discrepancies in the analysis procedure that had been employed to interpret the probe data, and we modified the procedure accordingly. Therefore, the description presented here differs from that presented in the original reference[7-1] describing the Hughes $\vec{E}x\vec{B}$ probe.

The angle ϕ is calculated at each radial coordinate using the expression,

$$\phi = \cos^{-1}\left[\frac{\int_{\phi_{min}}^{\phi_{max}} \left[i_+ + \frac{\sqrt{2}}{2} i_{++}\right] \cos^2\phi_p \sec^2(\phi_p-\phi_o)\left|\tan(\phi_p-\phi_o)\right| d\phi_p}{\int_{\phi_{min}}^{\phi_{max}} \left[i_+ + \frac{\sqrt{2}}{2} i_{++}\right] \cos\phi_p \sec^2(\phi_p-\phi_o)\left|\tan(\phi_p-\phi_o)\right| d\phi_p}\right], \quad (7\text{-}3)$$

where $i_n(r, \phi_p)$ is the probe current corresponding to species n, ϕ_p is the probe angle, and ϕ_o is the probe angle corresponding to the peak in the current profile. The magnitude of the current-density vector, $j(r)$, is calculated using the expression,

$$j_n(r) = \frac{4\pi L^2 \sec^3\phi_o}{A_o A_p \cos(\gamma-\phi)} \int_{\phi_{min}}^{\phi_{max}} i_n(r,\phi_p)\cos\phi_p \sec^2(\phi_p-\phi_o)\left|\tan(\phi_p-\phi_o)\right| d\phi_p \quad (7\text{-}4)$$

where A_p and A_o are the probe-aperture area and probe-viewing area, respectively. The variable, L, is the distance from the probe to the accelerator electrode and is given by

$$L = L_o + R_c(1 - \cos\gamma) \quad , \quad (7\text{-}5)$$

where L_o is the distance from the probe to the electrode on the thruster axis, and R_c is the radius of curvature of the electrodes (R_c is positive for electrodes that are dished outward). The angle γ is given by

$$\gamma = \sin^{-1} (r/R_c) \quad . \tag{7-6}$$

The total current density is obtained by adding the species current densities calculated from Equation 7-4; the total current of species n is calculated using the expression*

$$J_n = \int_0^{R_g} j_n \cos(\gamma - \phi) \frac{2\pi r dr}{\cos \gamma} \quad , \tag{7-7}$$

where R_g is the radius of the active region of the accelerator electrode. The thrust-loss factors α and F_t are calculated using the expressions

$$\alpha = \frac{J_+ + \frac{\sqrt{2}}{2} J_{++}}{J_+ + J_{++}} \quad , \tag{7-8}$$

and

$$F_t = \frac{\int_{A_g} (j_+ + \frac{\sqrt{2}}{2} j_{++}) \cos(\gamma-\phi) \cos \phi dA}{\int_{A_g} (j_+ + \frac{\sqrt{2}}{2} j_{++}) \cos(\gamma-\phi) dA} \tag{7-9}$$

$$= \frac{2\pi \int_0^{R_g} (j_+ + \frac{\sqrt{2}}{2} j_{++}) \cos(\gamma-\phi) \frac{\cos\phi r dr}{\cos \gamma}}{J_+ + \frac{\sqrt{2}}{2} J_{++}} \tag{7-10}$$

*Equation (7-7) is obtained by combining Equations (C-1), (C-2), and (C-4) of Appendix C.

Integration of Equations (7-8) through (7-10) is performed using a second-order interpolation scheme, with the probe current extrapolated to zero to determine the integration limits ϕ_{min} and ϕ_{max}.

The output of the data-analysis routine contains both graphical and numerical results. The plotted output consists of the angular dispersion profiles (a total of eight, corresponding to the two species and the four radial locations), and the radial current-density profiles (a total of three, corresponding to the two species and their sum). The tabulated output consists of the values j_+, j_{++}, and ϕ (calculated at each radial location) and the thrust-loss factors, α and F_t. The tabulated results also contain the ratio of doubly to singly charged ion currents, and the propellant-utilization correction factor β, defined as

$$\beta = \frac{J_+ + J_{++}/2}{J_+ + J_{++}} \quad . \tag{7-11}$$

C. ERROR ANALYSIS

The standard approach[7-2] used in evaluating the uncertainty U_f, in a derived quantity $f(x_i)$ is to calculate the sensitivity of f to each independent variable, x_i, and then to estimate the uncertainty U_{x_i}, in each of these variables. For equal odds on the uncertainties present, the overall uncertainty is given by

$$U_f = \left[\left(\frac{\partial f}{\partial x_1} U_{x_1}\right)^2 + \left(\frac{\partial f}{\partial x_2} U_{x_2}\right)^2 + \ldots\right]^{1/2} \quad , \tag{7-12}$$

where $\partial f/\partial x_i$ is the sensitivity of the derived quantity, f, to the independent variable, x_i.

The thrust equation is

$$F = \alpha F_t F_c \quad , \tag{7-13}$$

and the uncertainty in the thrust can be written as

$$U_F = \sqrt{\left(\frac{\partial F}{\partial \alpha} U_\alpha\right)^2 + \left(\frac{\partial F}{\partial F_t} U_{F_t}\right)^2 + \left(\frac{\partial F}{\partial F_c} U_{F_c}\right)^2} \quad . \qquad (7\text{-}14)$$

To simplify the discussion, we will assume that the uncertainty in the calculated thrust is negligible. In this case, the equation above simplifies to

$$U_F = \sqrt{F_t^2 U_\alpha^2 + \alpha^2 U_{F_t}^2} \; F_c \quad . \qquad (7\text{-}15)$$

Therefore, the overall uncertainty in the thrust can be estimated if the uncertainties in the factors α and F_t can be determined. Because of the complicated form of the equations used in calculating the factors α and F_t, our approach was to determine the variables that affect the calculated values of these factors, and then to assess the sensitivity of the calculated results to uncertainties in these variables. By estimating the uncertainties in the independent variables, the overall uncertainty could then be calculated using a relationship similar to that given by Equation 7-15.

Our discussion of the $\vec{E}x\vec{B}$ probe technique and the equations used to analyze the probe output showed that the primary variables appearing in the expressions for α and F_t are the coordinates r and ϕ_p.* Therefore, the error analysis must identify all the factors that could lead to significant errors or uncertainties in these coordinates. After reviewing the $\vec{E}x\vec{B}$ measurement procedure, we identified the primary quantities listed in Table 7-1 as position variables that could introduce uncertainties into the variables, r and ϕ_p. Definitions of the coordinate uncertainties are provided in Figures 7-9 through 7-11.

*The expressions for both α and F_t involve ratios of currents, and, therefore, many of the geometric characteristics of the probe system have no effect on the calculated results.

Table 7-1. Position Variables That Could Introduce Errors in the Thrust-Loss Measurement

Symbol	Definition
r -	Radial coordinate.
ϕ_p -	Angular coordinate.
R_g -	Electrode radius (active region).
γ_p -	Inclination of plane of probe travel with respect to vertical diameter of thruster.
R_p -	Position of plane of probe travel with respect to vertical plane passing through the axis of the vacuum chamber.
ψ_p -	Probe yaw angle.
ϕ_T -	Thruster pitch angle.
ψ_T -	Thruster yaw angle.
R_T -	Position of vertical diameter of thruster with respect to vertical plane passing through the axis of the vacuum chamber.

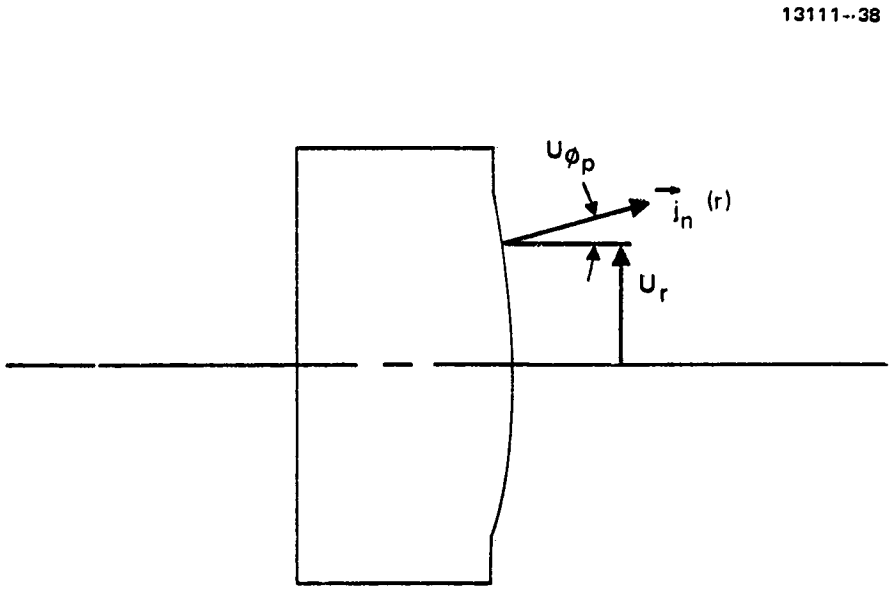

Figure 7-9. Definition of the coordinate uncertainties for the variables r and ϕ.

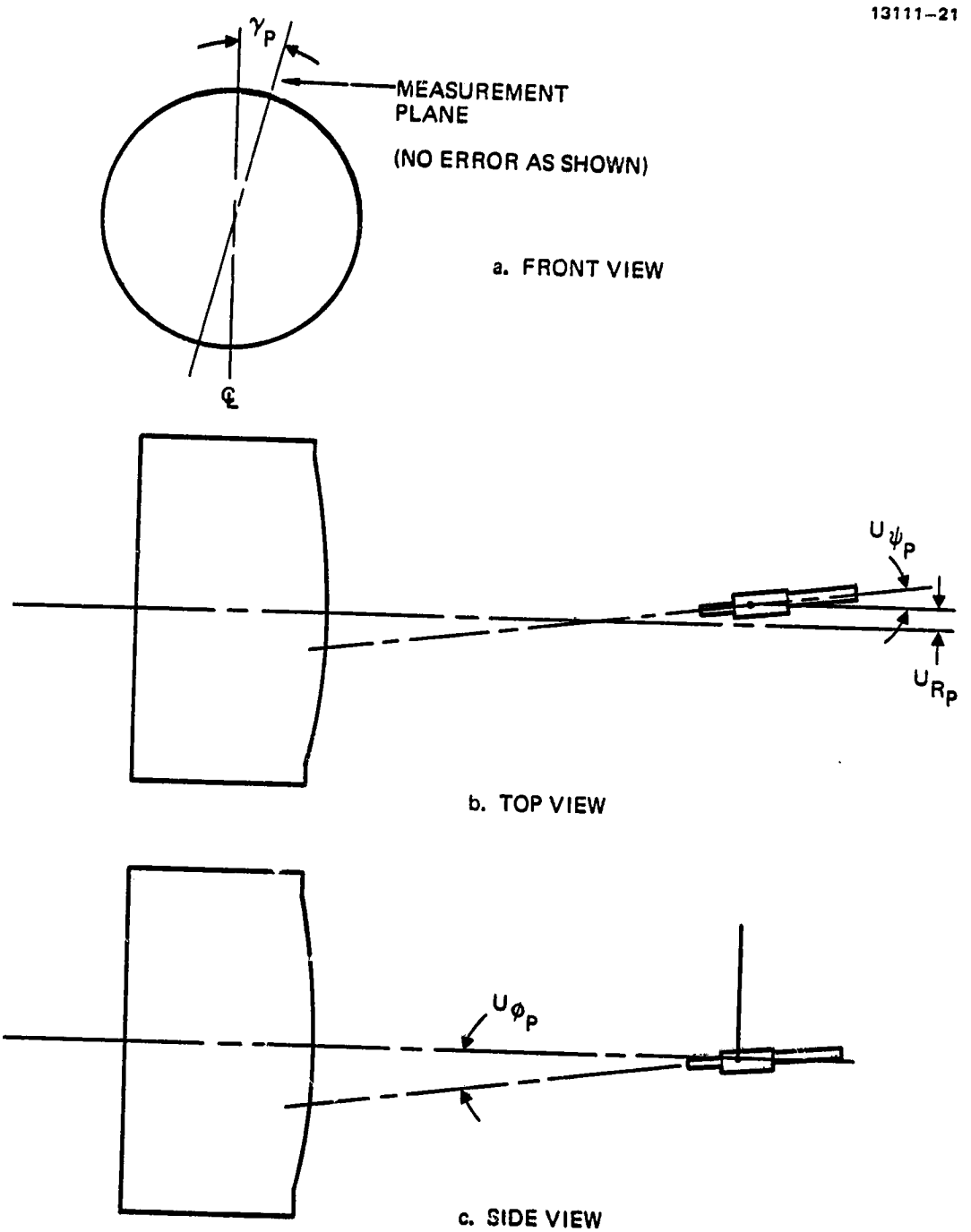

Figure 7-10. Definition of the coordinate uncertainties for the variables R_p, γ_p, and ψ_p.

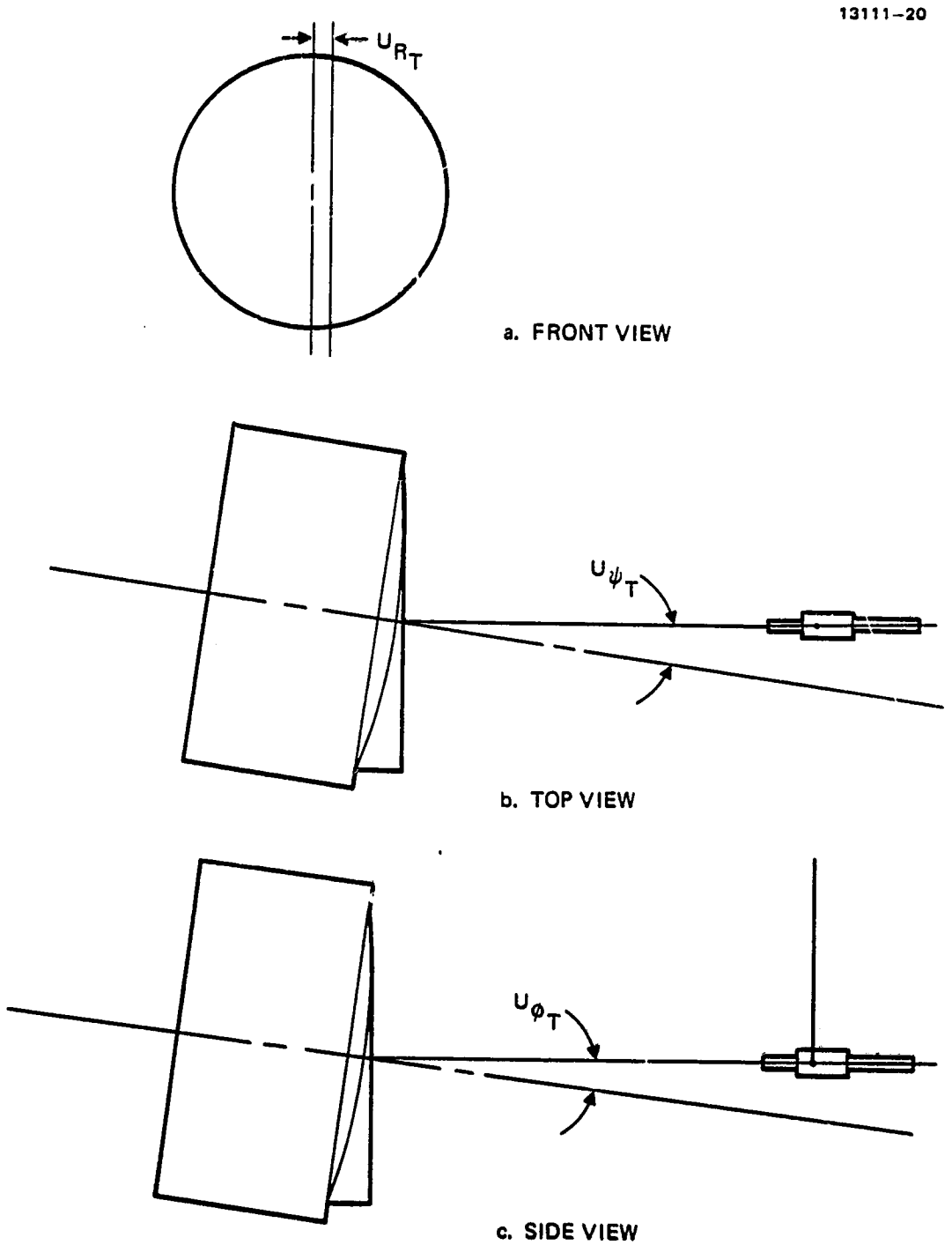

Figure 7-11. Definition of the coordinate uncertainties for the variables R_T, ϕ_T, and ψ_T.

1. Sensitivity Estimates

We performed analyses to determine the sensitivity of the thrust-loss factors to the coordinates r and ϕ_p using the computer program described above to perform the numerical calculations. The baseline input data were taken from actual probe measurements obtained with a 30-cm J-series thruster operated at J_b = 2 A and V_D = 32 V. This same set of probe-current measurements was also used as input to the program, but with the probe angle, ϕ_p, displaced ±5°. The computer output for these three sets of input data is presented in Figure 7-12, showing (reasonably so) that the principal error introduced by an uncertainty or error in the probe pitch-angle is in the thrust-loss factor, F_t. Figure 7-13 shows the results of Figure 7-12 plotted versus the error in probe angle, ϕ_p, and a linear approximation of these results gives the numerical value of the sensitivity as $\partial F_t/\partial \phi_p = 0.0017\ \text{deg}^{-1}$.

In a similar manner, we evaluated the sensitivity of the thrust-loss factors to the radial coordinate, r, by changing the input values of the measurement coordinates. Figure 7-14 shows the output of the computer program (using the same input data described above), indicating that the principal effect of an error in the radial coordinate is manifest in the calculated value of the ratio J^{++}/J^{+}. (Fortunately, the thrust-correction factor α is relatively insensitive to this ratio.) The results of Figure 7-14 are plotted in Figure 7-15, and linearization gives the sensitivity as $\partial(J^{++}/J+)/\partial r = 0.0096\ \text{cm}^{-1}$.

2. Uncertainty Estimates

We estimated the uncertainties in the coordinates of Table 7-1 using the experimental setups indicated in Figures 7-16 to 7-18. In the optical measurements depicted in Figure 7-16 we used a laser to calibrate the indicated probe pitch angle with

THIS IS THE INPUT DATA

PHIP(DEG)	r=0.75R		r=0.50R		r=0.25R		r=0.00R	
	J+(nA)	J++(nA)	J+(nA)	J++(nA)	J+(nA)	J++(nA)	J+(rA)	J++(nA)
-15.0000	0.2280	0.0130	0.0830	0.0080	0.0160	0.0000	0.0020	0.0000
-10.0000	0.3860	0.0190	0.3610	0.0500	0.1370	0.0270	0.0480	0.0050
-5.0000	0.1520	0.0050	0.4380	0.0640	0.4540	0.1190	0.1700	0.0450
0.0000	0.0350	0.0000	0.1720	0.0230	0.3870	0.1030	0.4960	0.1560
5.0000	0.0000	0.0000	0.0290	0.0000	0.0980	0.0180	0.3090	0.0900
10.0000	0.0000	0.0000	0.0000	0.0000	0.0110	0.0000	0.0910	0.0220
15.0000	0.0000	0.0000	0.0000	0.0000	0.0000	0.0000	0.0100	0.0000

SUMMARY OF THRUST PARAMETERS

	r=0.75R	r=0.50R	r=0.25R	r=0.00R
j+(ma/cm2)	1.3754	1.7484	1.6593	1.9453
j++(ma/cm2)	0.0557	0.2036	0.3507	0.4846
(j++/j+)	0.0405	0.1164	0.2113	0.2491
PHI(DEG)	9.7832	8.3044	6.1942	7.5282

ALPHA	Ft	(J+)+(J++) (AMPS)	BETA	J++/J+
0.97455	0.98845	0.92185	0.95656	0.09516

(a) $\delta\phi_p = 0$

Figure 7-12. Computer printout showing the sensitivity of thrust-loss factors to an uncertainty in the angular coordinate, ϕ_p.

THIS IS THE INPUT DATA

	r=0.75R		r=0.50R		r=0.25R		r=0.00R	
PHIP(DEG)	J+(nA)	J++(nA)	J+(nA)	J++(nA)	J+(nA)	J++(nA)	J+(nA)	J++(nA)
-10.0000	0.2280	0.0130	0.0830	0.0080	0.0160	0.0000	0.0020	0.0000
-5.0000	0.3860	0.0190	0.3610	0.0500	0.1370	0.0270	0.0480	0.0050
0.0000	0.1520	0.0060	0.4380	0.0640	0.4540	0.1190	0.1700	0.0450
5.0000	0.0350	0.0000	0.1720	0.0230	0.3870	0.1030	0.4960	0.1560
10.0000	0.0000	0.0000	0.0290	0.0000	0.0980	0.0180	0.3090	0.0900
15.0000	0.0000	0.0000	0.0000	0.0000	0.0110	0.0000	0.0910	0.0220
20.0000	0.0000	0.0000	0.0000	0.0000	0.0000	0.0000	0.0100	0.0000

SUMMARY OF THRUST PARAMETERS

	r=0.75R	r=0.50R	r=0.25R	r=0.00R
j+(ma/cm2)	1.3363	1.7255	1.6492	1.9722
j++(ma/cm2)	0.0543	0.2013	0.3491	0.4908
(j++/j+)	0.0407	0.1166	0.2117	0.2489
PHI(DEG)	6.4621	6.2393	7.1826	9.4812

ALPHA	Ft	(J+)+(J++) (AMPS)	BETA	J++/J+
0.97431	0.99340	0.90180	0.95614	0.09616

(b) $\delta\phi_p = +5°$

Figure 7-12. Continued.

THIS IS THE INPUT DATA

	r=0.75R		r=0.50R		r=0.25R		r=0.00R	
PHIP(DEG)	J+(nA)	J++(nA)	J+(nA)	J++(nA)	J+(nA)	J++(nA)	J+(nA)	J++(nA)
-20.0000	0.2280	0.0130	0.0830	0.0080	0.0160	0.0000	0.0020	0.0000
-15.0000	0.3860	0.0190	0.3610	0.0500	0.1370	0.0270	0.0480	0.0050
-10.0000	0.1520	0.0060	0.4380	0.0640	0.4540	0.1190	0.1700	0.0450
-5.0000	0.0350	0.0000	0.1720	0.0230	0.3870	0.1030	0.4960	0.1560
0.0000	0.0000	0.0000	0.0290	0.0000	0.0980	0.0180	0.3090	0.0900
5.0000	0.0000	0.0000	0.0000	0.0000	0.0110	0.0000	0.0910	0.0220
10.0000	0.0000	0.0000	0.0000	0.0000	0.0000	0.0000	0.0100	0.0000

SUMMARY OF THRUST PARAMETERS

	r=0.75R	r=0.50R	r=0.25R	r=0.00R
j+(ma/cm2)	1.4440	1.8045	1.7007	1.9626
j++(ma/cm2)	0.0581	0.2097	0.3588	0.4894
(j++/j+)	0.0403	0.1162	0.2110	0.2494
PHI(DEG)	14.0870	12.1488	8.5916	8.4528

ALPHA	Ft	(J+)+(J++) (AMPS)	BETA	J++/J+
0.97480	0.97606	0.95743	0.95698	0.09414

(c) $\delta\phi_p = -5°$

Figure 7-12. Concluded.

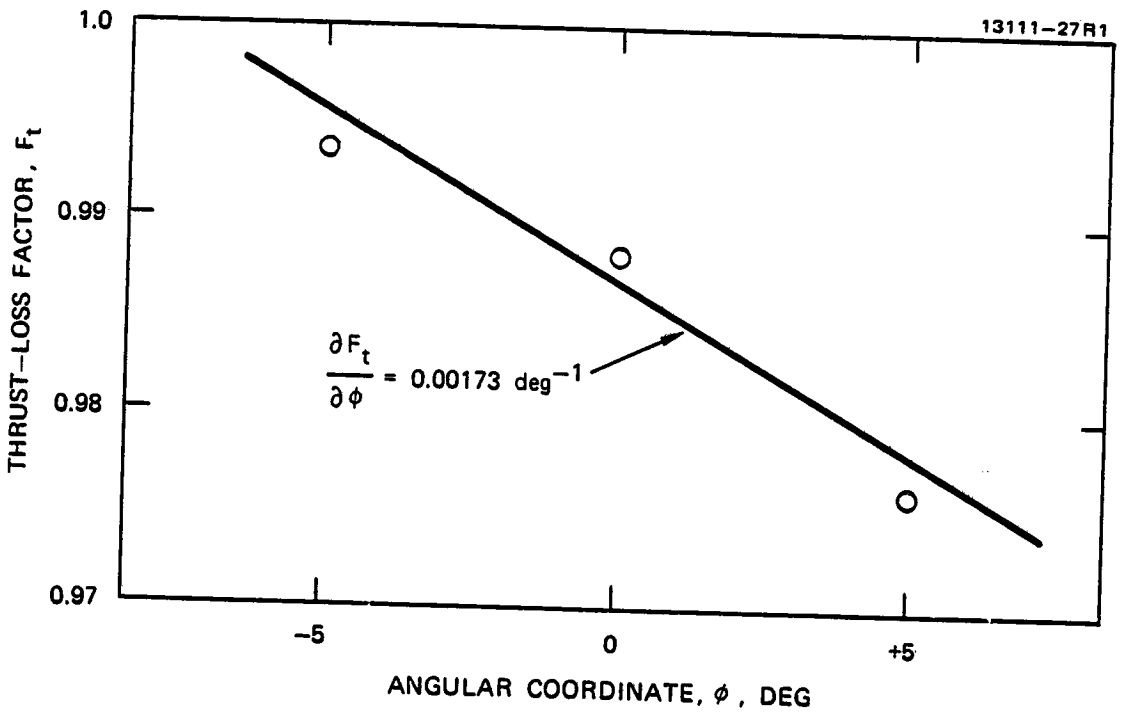

Figure 7-13. Sensitivity of the thrust factor F_t to an uncertainty in the angular coordinate ϕ.

THIS IS THE INPUT DATA

	r=0.75R		r=0.50R		r=0.25R		r=0.00R	
PHIP(DEG)	J+(nA)	J++(nA)	J+(nA)	J++(nA)	J+(nA)	J++(nA)	J+(nA)	J++(nA)
-15.0000	0.2280	0.0130	0.0830	0.0080	0.0160	0.0000	0.0020	0.0000
-10.0000	0.3860	0.0190	0.3610	0.0500	0.1370	0.0270	0.0480	0.0050
-5.0000	0.1520	0.0060	0.4380	0.0640	0.4540	0.1190	0.1700	0.0450
0.0000	0.0350	0.0000	0.1720	0.0230	0.3870	0.1030	0.4960	0.1560
5.0000	0.0000	0.0000	0.0290	0.0000	0.0980	0.0180	0.3090	0.0900
10.0000	0.0000	0.0000	0.0000	0.0000	0.0110	0.0000	0.0910	0.0220
15.0000	0.0000	0.0000	0.0000	0.0000	0.0000	0.0000	0.0100	0.0000

SUMMARY OF THRUST PARAMETERS

	r=0.75R	r=0.50R	r=0.25R	r=0.00R
j+(ma/cm2)	1.3754	1.7484	1.6593	1.9453
j++(ma/cm2)	0.0557	0.2036	0.3507	0.4846
(j++/j+)	0.0405	0.1164	0.2113	0.2491
PHI(DEG)	9.7832	8.3044	6.1942	7.5282

ALPHA	Ft	(J+)+(J++) (AMPS)	BETA	J++/J+
0.97455	0.98845	0.92185	0.95656	0.09516

(a) $\delta r = 0$

Figure 7-14. Computer printout showing the sensitivity of the thrust-loss factors to an uncertainty in the radial coordinate r.

THIS IS THE INPUT DATA

	r=0.75R		r=0.50R		r=0.25R		r=0.00R	
PHIP(DEG)	J+(nA)	J++(nA)	J+(nA)	J++(nA)	J+(nA)	J++(nA)	J+(nA)	J++(nA)
-15.0000	0.2280	0.0130	0.0830	0.0080	0.0160	0.0000	0.0020	0.0000
-10.0000	0.3860	0.0190	0.3610	0.0500	0.1370	0.0270	0.0480	0.0050
-5.0000	0.1520	0.0060	0.4380	0.0640	0.4540	0.1190	0.1700	0.0450
0.0000	0.0350	0.0000	0.1720	0.0230	0.3870	0.1030	0.4960	0.1560
5.0000	0.0000	0.0000	0.0290	0.0000	0.0980	0.0180	0.3090	0.0900
10.0000	0.0000	0.0000	0.0000	0.0000	0.0110	0.0000	0.0910	0.0220
15.0000	0.0000	0.0000	0.0000	0.0000	0.0000	0.0000	0.0100	0.0000

SUMMARY OF THRUST PARAMETERS

	r=0.75R	r=0.50R	r=0.25R	r=0.00R
j+(ma/cm2)	1.3754	1.7484	1.6593	1.9453
j++(ma/cm2)	0.0557	0.2036	0.3507	0.4846
(j++/j+)	0.0405	0.1164	0.2113	0.2491
PHI(DEG)	9.7832	8.3044	6.1942	7.5282

ALPHA	Ft	(J+)+(J++) (AMPS)	BETA	J++/J+
0.97525	0.98830	0.94600	0.95775	0.09030

(b) δr = 1 cm

Figure 7-14. Continued.

THIS IS THE INPUT DATA

	r=0.75R		r=0.50R		r=0.25R		r=0.00R	
PHIP (DEG)	J+ (nA)	J++ (nA)	J+ (nA)	J++ (nA)	J+ (nA)	J++ (nA)	J+ (nA)	J++ (nA)
-15.0000	0.2280	0.0130	0.0830	0.0030	0.0160	0.0000	0.0020	0.0000
-10.0000	0.3860	0.0190	0.3610	0.0500	0.1370	0.0270	0.0480	0.0050
-5.0000	0.1520	0.0060	0.4380	0.0640	0.4540	0.1190	0.1700	0.0450
0.0000	0.0350	0.0000	0.1720	0.0230	0.3370	0.1030	0.4960	0.1560
5.0000	0.0000	0.0000	0.0290	0.0000	0.0980	0.0180	0.3090	0.0900
10.0000	0.0000	0.0000	0.0000	0.0000	0.0110	0.0000	0.0910	0.0220
15.0000	0.0000	0.0000	0.0000	0.0000	0.0000	0.0000	0.0100	0.0000

SUMMARY OF THRUST PARAMETERS

	r=0.75R	r=0.50R	r=0.25R	r=0.00R
j+ (ma/cm2)	1.3754	1.7484	1.6593	1.9453
j++ (ma/cm2)	0.0557	0.2036	0.3507	0.4846
(j++/j+)	0.0405	0.1164	0.2113	0.2491
PHI (DEG)	9.7832	8.3044	6.1942	7.5282

ALPHA	Ft	(J+)+(J++) (AMPS)	BETA	J++/J+
0.97356	0.98866	0.88644	0.95486	0.09993

(c) $\delta r = -1$ cm

Figure 7-14. Concluded.

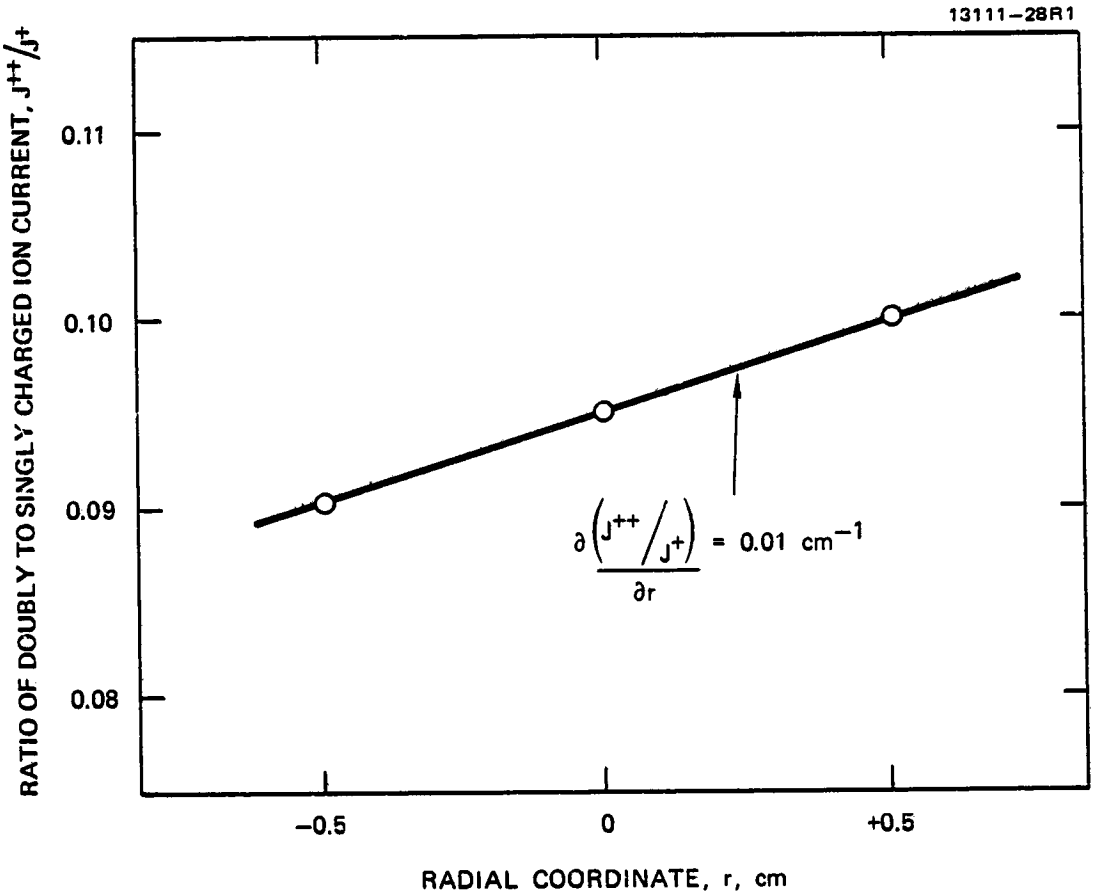

Figure 7-15. Sensitivity of the current ratio J_{++}/J_{+} to an uncertainty in the radial coordinate r.

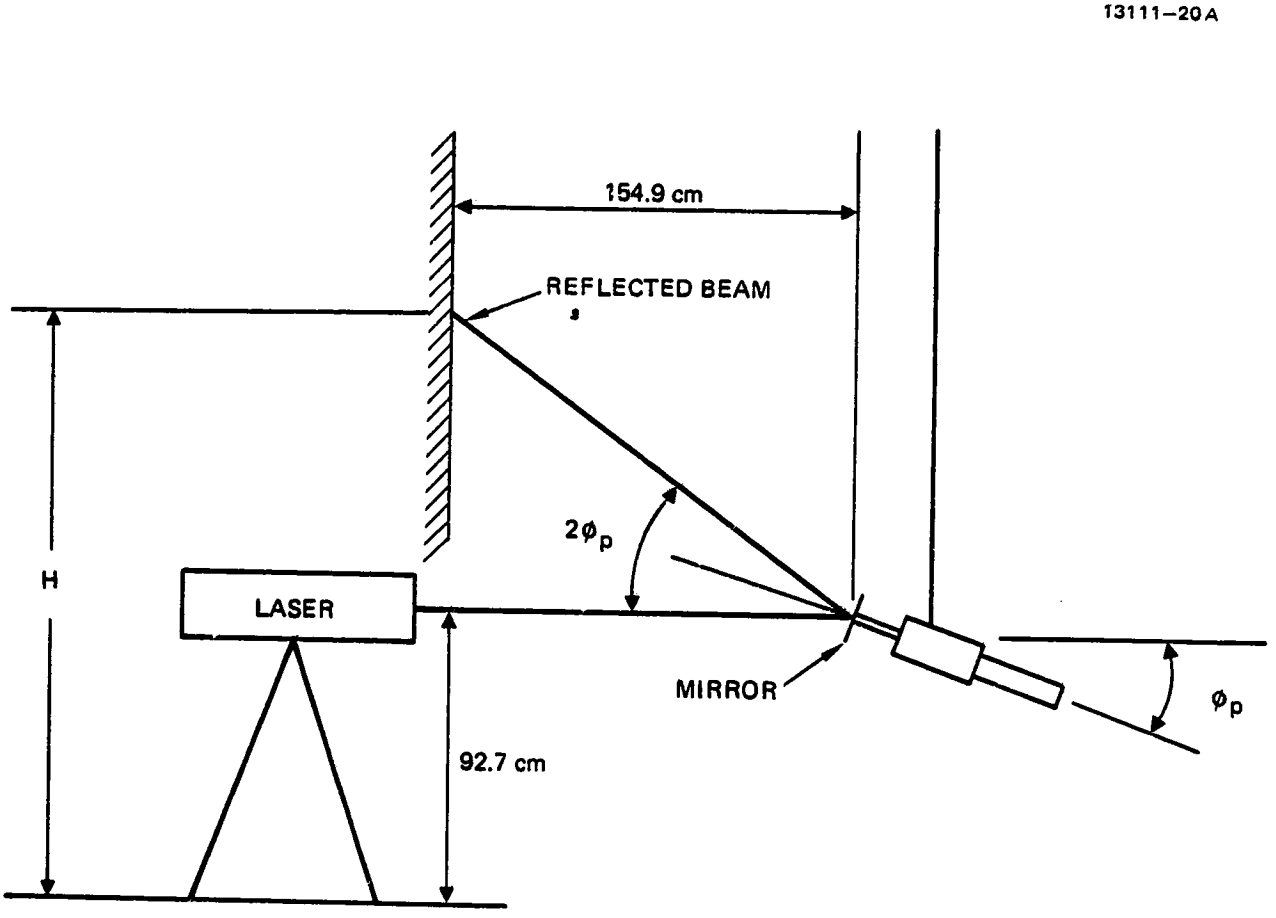

Figure 7-16. Optical arrangement used to measure the uncertainty in the probe pitch angle, ϕ_p.

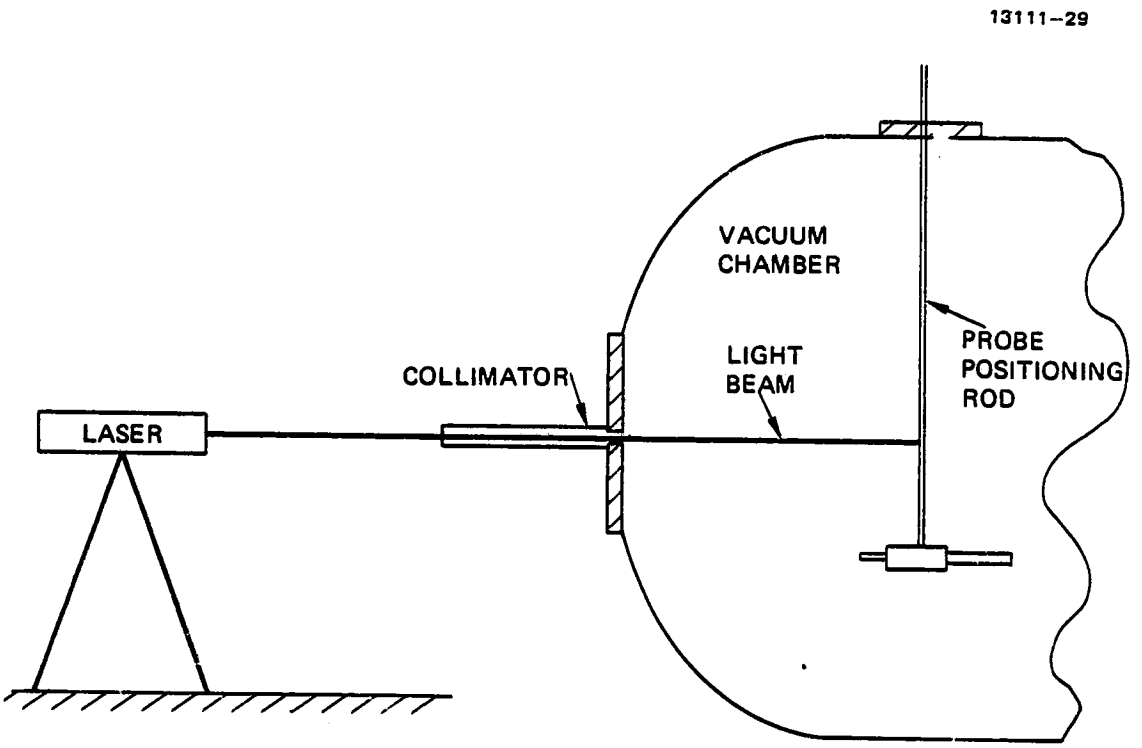

Figure 7-17. Optical arrangement used to measure the uncertainty in the probe position, R_p.

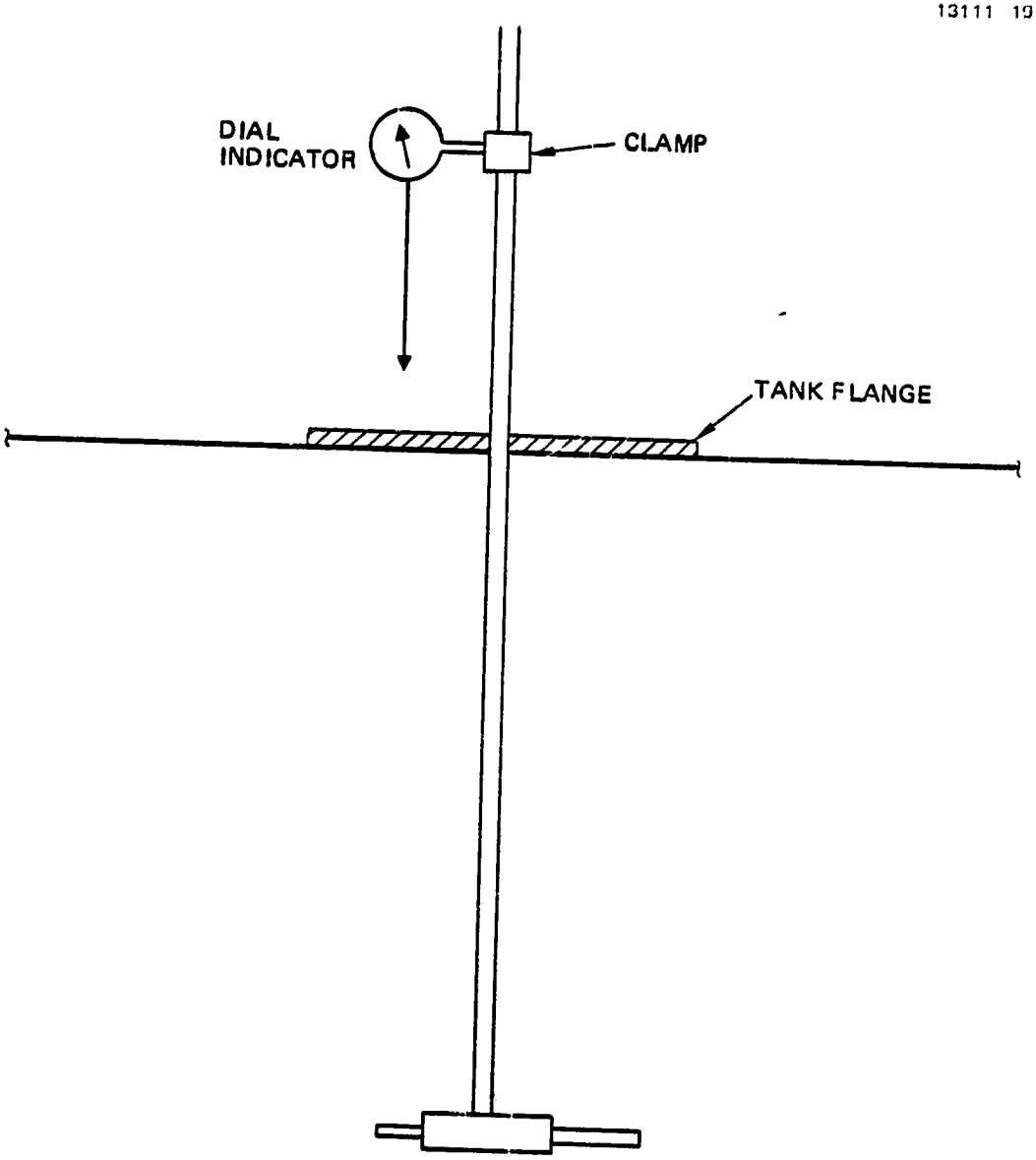

Figure 7-18. Dial-indicator arrangement used to measure the uncertainty in the radial coordinate, r.

the coordinate H. Then we calculated the angle ϕ_p using the geometrical relationship given by

$$\phi_p = \frac{1}{2} \tan^{-1} \left[(H - 92.7)/154.9 \right] . \qquad (7\text{-}16)$$

The results of this calibration established the uncertainty in the angular coordinate as $U_{\phi p} = 0.45°$.

The uncertainty in the location of the probe with respect to the vacuum-chamber axis was determined using the laser and bore-sight arrangement illustrated in Figure 7-17. The collimating tube established the location of the tank axis, using the same positioning pins that are used to align the thruster-mounting flange during installation of a thruster. With the chamber axis determined in this manner, the laser beam was adjusted to allow it to pass through the small-diameter (0.3 cm) apertures in the collimator. We observed that the probe-positioning rod (probe translational axis) was illuminated by the laser light, establishing the uncertainty (conservatively) as $U_{R_p} = 0.6$ cm — the radius of the positioning rod.

The uncertainty in the radial coordinate r was determined using the precision dial indicator shown in the setup of Figure 7-18. Using this arrangement and a stepping-motor calibration factor (that was established at the time of the initial installation[7-1] of the probe in the vacuum chamber) of 514 steps = 3.625 cm, we indexed the probe up and down a fixed number of steps and recorded the change in dial-indicator reading. These measurements showed that there is negligible hysteresis in the positioning mechanism. A least-squares fit of our data established a calibration factor of 141.8 steps/cm, in excellent agreement with the original calibration (141.8 steps/cm x 3.625 cm = 513.99 steps). The largest deviation of the dial-indicator reading from the calibrated movement established the uncertainty in the radial coordinate as $U_r = 0.1054$ cm.

3. Overall Uncertainty

A summary of the uncertainties in the variables of Table 7-1 and the sensitivities of the thrust-loss factors α and F_t is presented in Table 7-2. These results establish the overall uncertainties as $U_\alpha = 0.1\%$ and $UF_t = 1.4\%$. Substituting these values of the uncertainties into Equation 7-15 gives the overall uncertainty in the thrust as 1.4% (assuming zero error in the calculated thrust).

Table 7-2. Summary of Sensitivity/Uncertainty Measurements

14617-1

x_i	$\frac{\partial \alpha}{\partial x_i}$	$\frac{\partial F_t}{\partial x_i}$	U_{x_i}	$\left(\frac{\partial \alpha}{\partial x_i} U_{x_i}\right)^2$	$\left(\frac{\partial F_t}{\partial x_i} U_{x_i}\right)^2$
i	~0	~0	3×10^{-11} A	0	0
r	1.69^{-3} cm^{-1}	3.6^{-4} cm^{-1}	5.4^{-3} cm	8.33^{-11}	3.78^{-12}
R_g	1.69^{-3} cm^{-1}	3.6^{-4} cm^{-1}	0.21 cm	1.26^{-7}	5.72^{-9}
γ_p	0	0	N/A	0	0
R_p	~0	~0	0.6 cm	0	0
ψ_p	4.0^{-4} deg^{-1}	9.89^{-3} deg^{-1}	0.95 deg	1.44^{-7}	8.83^{-5}
ϕ_p	-4.9^{-5} deg^{-1}	1.73^{-3} deg^{-1}	0.45 deg	4.86^{-10}	6.06^{-7}
ϕ_T	-4.9^{-5} deg^{-1}	1.73^{-3} deg^{-1}	1 deg	2.4^{-9}	2.99^{-6}
ψ_T	4.0^{-4} deg^{-1}	9.89^{-3} deg^{-1}	1 deg	1.6^{-7}	9.78^{-5}
R_T	~0	~0	0.079 cm	0	0
			SUM	4.33×10^{-7}	1.90×10^{-4}
			$\sqrt{\text{SUM}}$	6.58×10^{-4}	1.38×10^{-2}

SECTION 8

CONCLUSIONS

The ring-cusp discharge chamber equipped with a three-grid ion-extraction assembly has demonstrated highly efficient and stable operating characteristics over a wide range of beam current and net-to-total accelerating-voltage ratio. Specific operating characteristics that were demonstrated include:

- Beam-current throttling over the range $1\ A < J_b < 5\ A$.
- Baseline specific discharge power of $\varepsilon_i = 125$ eV/ion.
- Cathode-flow-dependent plasma conductivity, which enables stable control of discharge voltage over the range $28\ V < V_D < 44\ V$ by regulating cathode flow rate.
- The ability to operate the three-grid ion-extraction assembly over a beam-current range of $1\ A < J_b < 5\ A$ and net-to-total accelerating-voltage ratios in the range $0.2 < R < 0.8$.

Plasma-property measurements obtained with the ring-cusp magnetic-confinement configuration indicate that the boundary of the ion-production region in this discharge chamber is defined by the shape of the confining magnetic-field lines, as it is in other more-conventional geometries. Steep gradients in plasma properties are observed in the vicinity of the magnetic-field lines that pass near the cathode. Essentially no ionization occurs in the volume exterior to these "critical" field lines, and their shape is thought to be an important feature in achieving the high level of performance demonstrated with this magnetic-confinement arrangement.

Two additional discharge-chamber designs that employed single-cusp and multipole boundary-magnetic-field arrangements demonstrated the advantages of this confinement scheme in producing a uniform plasma-density distribution, and their

performance was comparable to that of the highly optimized J-series design.

Perveance measurements obtained with an advanced ion-extraction assembly demonstrated an improvement in dimensional stability (over that of the state-of-the-art design) can be achieved by using flexible mounts for supporting both the screen and accelerator electrodes.

A high-emission-current cathode design was derived from scaling the J-series cathode for long-life operation at emission currents up to J_E = 40 A, and three 20,000 A-hr endurance tests of the scaled cathode were successfully completed. The results of insert-temperature and orifice-plate-erosion measurements have demonstrated that long-life cathode operation should be achievable using a flow-restricting aperture diameter of $d_o > 1.27$ mm.

Measurements of the minimum breakdown voltage for individual sections of the state-of-the-art J-series propellant-flow electrical isolator show that the conservative design value of the section breakdown rating is V_B = 340 V. The breakdown voltage of multiple sections was found to vary linearly, so that the total voltage-standoff rating can be expressed as the product of the number of isolating sections and the section breakdown rating of 340 V.

Estimates of the uncertainties involved in evaluating the thrust-loss factors α and F_t indicate that the overall error in the results should be less than 1.4%.

REFERENCES

2-1. J.R. Beattie, R.L. Poeschel, and R.T. Bechtel, "Extended Performance Thruster Technology Evaluation," AIAA Paper No. 78-666, San Diego, California, April 1978.

2-2. R.L. Poeschel, et al., "2.5 kW Advanced Technology Ion Thruster," NASA CR-135076, Hughes Research Laboratories, Malibu, California, April 1976.

2-3. J.S. Sovey, "Improved Ion Containment Using a Ring-Cusp Ion Thruster," AIAA Paper No. 82-1928, New Orleans, Louisiana, November 1982.

2-4. J.R. Beattie, "Numerical Procedure for Analyzing Langmuir Probe Data," AIAA Journal, Vol. 13, July 1975, pp. 950.

2-5. J.R. Beattie and P.J. Wilbur, "Cusped Magnetic Field Mercury Ion Thruster," Journal of Spacecraft and Rockets, Vol. 14, December 1977, pp. 747.

2-6. G. Longhurst, "Prediction of Plasma Properties in Mercury Ion Thrusters," NASA CR-159488, Colorado State University, Fort Collins, Colorado, December 1978.

2-7. R.L. Poeschel, "Development of Advanced Inert-Gas Ion Thrusters," NASA CR-168206, Hughes Research Laboratories, Malibu, California, June 1983.

2-8. H.R. Kaufman, "Experimental Investigations of Argon and Xenon Ion Sources," NASA CR-134845, Colorado State University, Fort Collins, Colorado, June 1975.

2-9. H.R. Kaufman, R.S. Robinson, and L.E. Frisa, "Ion Flow Experiments in a Multipole Discharge Chamber," AIAA Paper No. 82-1930, New Orleans, Louisiana, November 1982.

2-10. J.R. Brophy and P.J. Wilbur, "The Flexible Magnetic Field Thruster," AIAA Paper No. 82-1936, New Orleans, Louisiana, November 1982.

2-11 J.R. Beattie, "A Model for Predicting the Wearout Lifetime of the LeRC/Hughes 30-cm Mercury Ion Thruster," AIAA Paper No. 79-2079, Princeton, New Jersey, October 1979.

3-1. R.L. Poeschel and J.R. Beattie, "Primary Electric Propulsion Technology Study," NASA CR-159688, Hughes Research Laboratories, Malibu, California, November 1979.

3-2. J.R. Conrad, "Beamlet Steering by Aperture Displacement in Ion Sources with Large Acceleration-Deceleration Ratio," Review of Scientific Instruments, Vol. 51, April 1980, pp. 418.

3-3. G. Aston, "Ion Accelerator Systems for High Power 30-cm Thruster Operation," AIAA Paper No. 82-1983, New Orleans, Louisiana, November 1982.

4-1. R.J. Martin and J.E. Rowe, "Experimental Investigation of the Low-Voltage Arc in Noble Gases," Journal of Applied Physics, Vol. 39, August 1968, pp. 4289.

4-2. H.R. Kaufman, "Technology of Electron-Bombardment Ion Thrusters," Advances in Electronics and Electron Physics, Vol. 36, 1974, pp. 352.

4-3. R.L. Poeschel and J.R. Beattie, "Primary Electric Propulsion Technology Study," NASA CR-159688, Hughes Research Laboratories, Malibu, California, November 1979.

6-1. V.K. Rawlin, "Reduced Power Processor Requirements for the 30-cm Diameter Mercury Ion Thruster," AIAA Paper No. 79-2081, Princeton, New Jersey, October 1979.

6-2. R.P. Gruber, "Simplified Power Supplies for Ion Thrusters," AIAA Paper No. 81-0693, Las Vegas, Nevada, April 1981.

7-1. R.L. Poeschel, et al., "2.5 kW Advanced Technology Ion Thruster," NASA CR-134687, Hughes Research Laboratories, Malibu, California, August 1974.

7-2. J.P. Holman, "Experimental Methods for Engineers," McGraw-Hill Book Company, 1971.

H. Moestue, "The Electric Field and Geometrical Factor of an Annular Curved Plate Electrostatic Analyzer," Review of Scientific Instruments, Vol. 44, December 1973, pp. 1709.

D-2. M.L. Vestal, et al., "New Crossed-Beam Apparatus for the Study of Ion-Molecule Collision Processes," Review of Scientific Instruments," Vol. 47, January 1976, pp. 15.

APPENDIX A

PLASMA PROPERTIES

We conducted Langmuir-probe measurements in the ring-cusp discharge chamber, while operating at cathode-emission currents that placed us on either side of the transition from net-ion to net-electron current collection by the screen electrode. An initial survey of the discharge chamber allowed us to determine the locations of gradients in the plasma, and we used these results to define the locations where probe data would be necessary for defining the extent of the ion-production region.

Figure A-1 shows a grid indicating the locations that were surveyed, with the "dots" indicating the locations where the probe data were recorded and analyzed. The close spacing of the "dots" indicates the regions where gradients in the plasma properties were observed, and (as the results presented in Section 2 showed) it also indicates where the probe characteristics were best represented by a Maxwellian distribution function.

In the central region where the plasma was relatively uniform (and, in particular, near the cathode) we generally found that the probe characteristics were best approximated by a current-voltage relationship that represents the collection of both monoenergetic and Maxwellian electrons (two-group assumption). Figure A-2 shows probe data plotted in semi-logarithmic form for three locations on the chamber axis, ranging from near the cathode (location I-1) to near the screen electrode (location A-1). When probe measurements are presented in this form, the presence of a monoenergetic electron group is manifest as curvature of the the low-voltage part of the characteristic. As the figure indicates, the characteristics change from a curved one (two-group) to a straight-line (Maxwellian), with increasing distance from the cathode. Numerical analysis of a characteristic similar to the one labelled I-1 in Figure A-1 (corresponding to location L-3), shows that a good fit is obtained under the

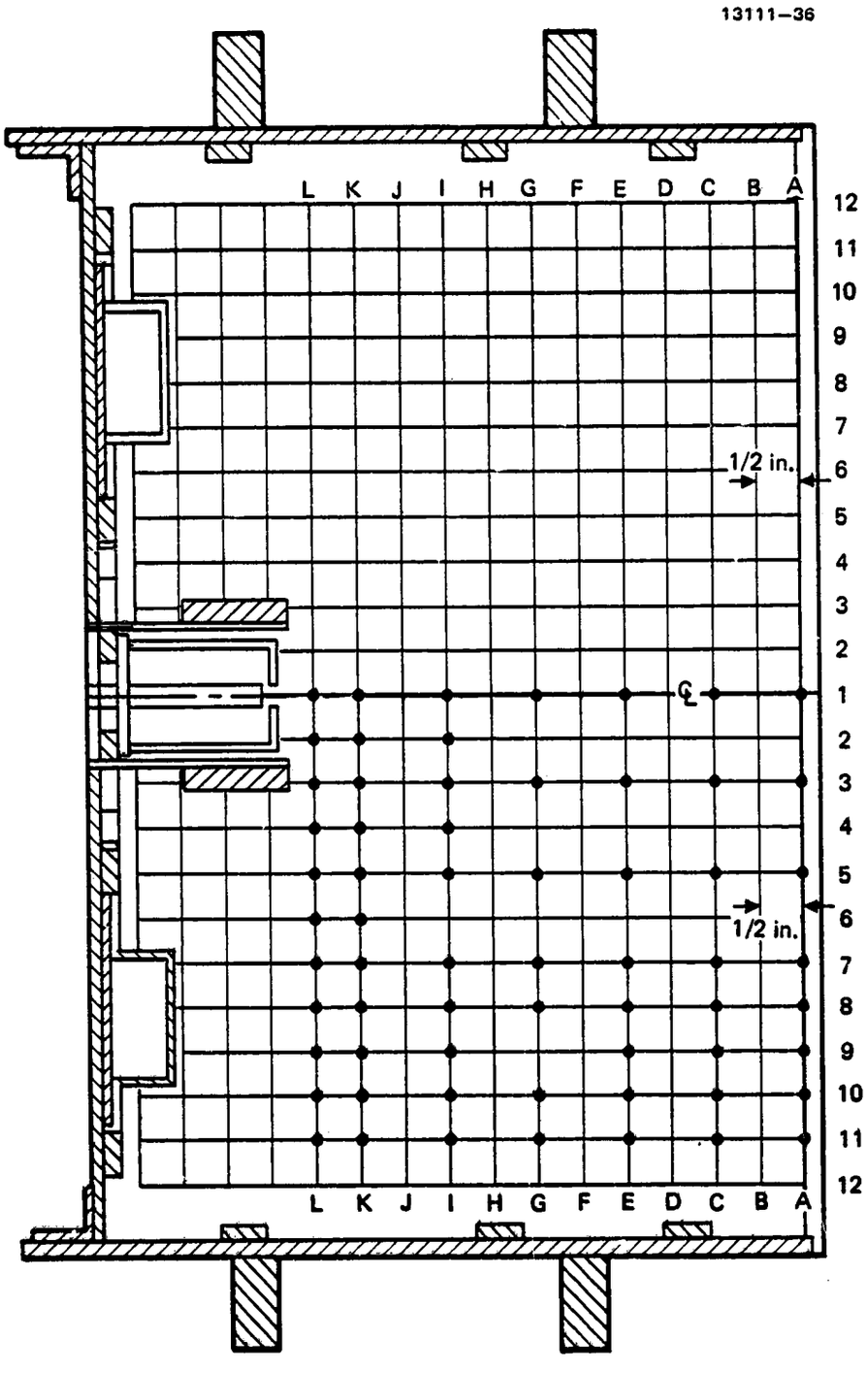

Figure A-1. Locations that can be accessed by the Langmuir probe in the ring-cusp thruster. The mesh points marked by the symbols are the locations where probe data were recorded and analyzed.

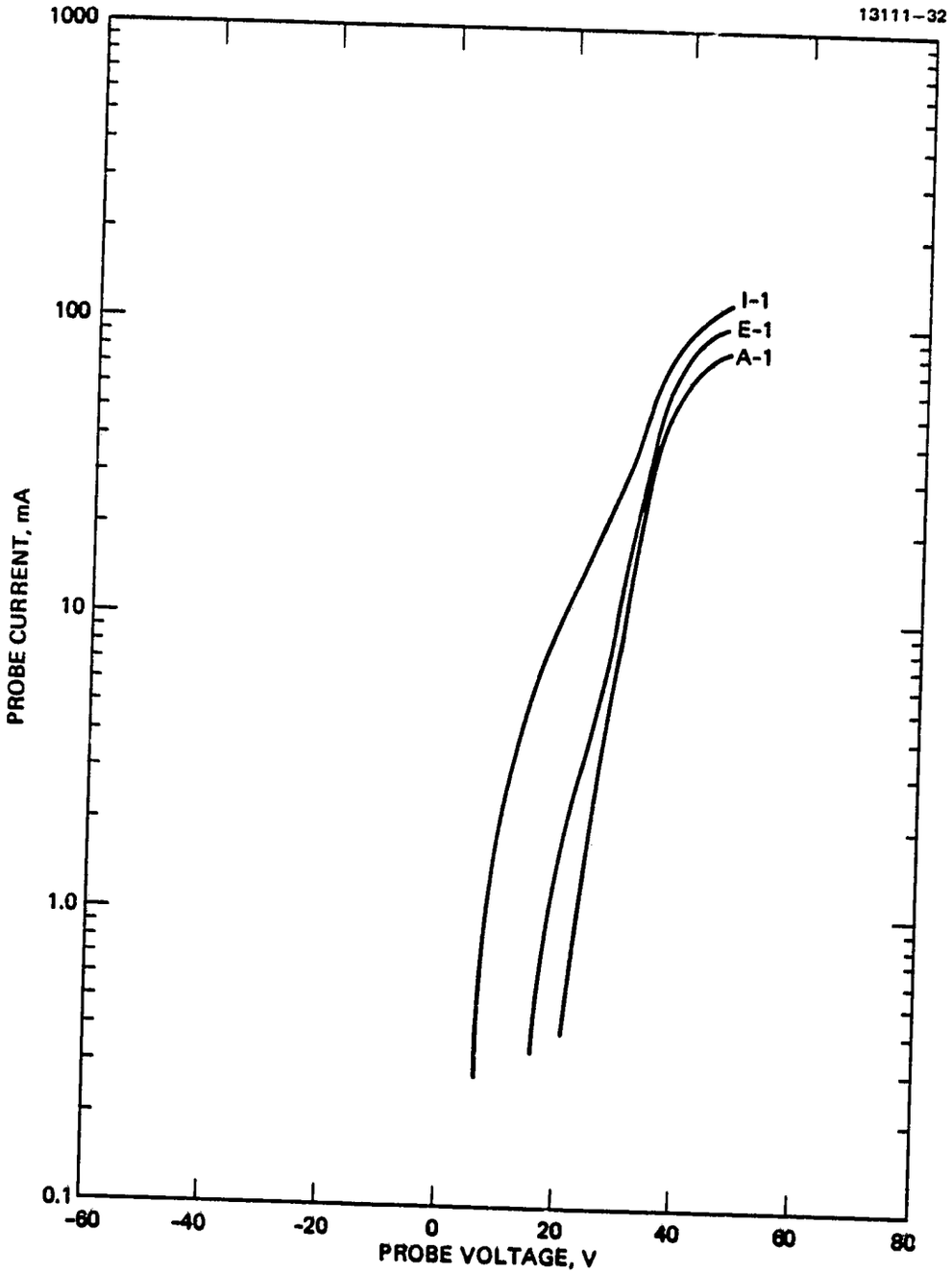

Figure A-2. Langmuir-probe characteristics plotted in semi-logarithmic form. The curves are labeled using the notation of Figure A-1.

two-group assumption, but a single-group (Maxwellian) analysis produced a poor fit. Figures A-3 and A-4 present a comparison of the input current-voltage characteristic with the results obtained by the curve fit, confirming the validity of the two-group model (for this location, which is near the source of emitted electrons).

In most of the region characterized by gradients in the plasma, the numerical-analysis algorithm was unable to obtain a good fit under the assumption of a two-group plasma. To ensure completeness, we analyzed the probe data using both the two-group and single-group assumptions. The results of the two-group analysis are presented in Table A-1, and the results of the single-group analysis are presented in Table A-2. The plasma-property measurements were performed while operating the thruster at J_b = 2 A, J_E = 8 A, and V_D = 36 V, (ε_i = 144 eV/ion), corresponding to net-ion current collection by the screen grid. Results corresponding to net-electron current collection by the screen grid (J_E = 9 A, ε_i = 162 eV/ion) are presented in Table A-3 (two-group analysis) and Table A-4 (single-group analysis).

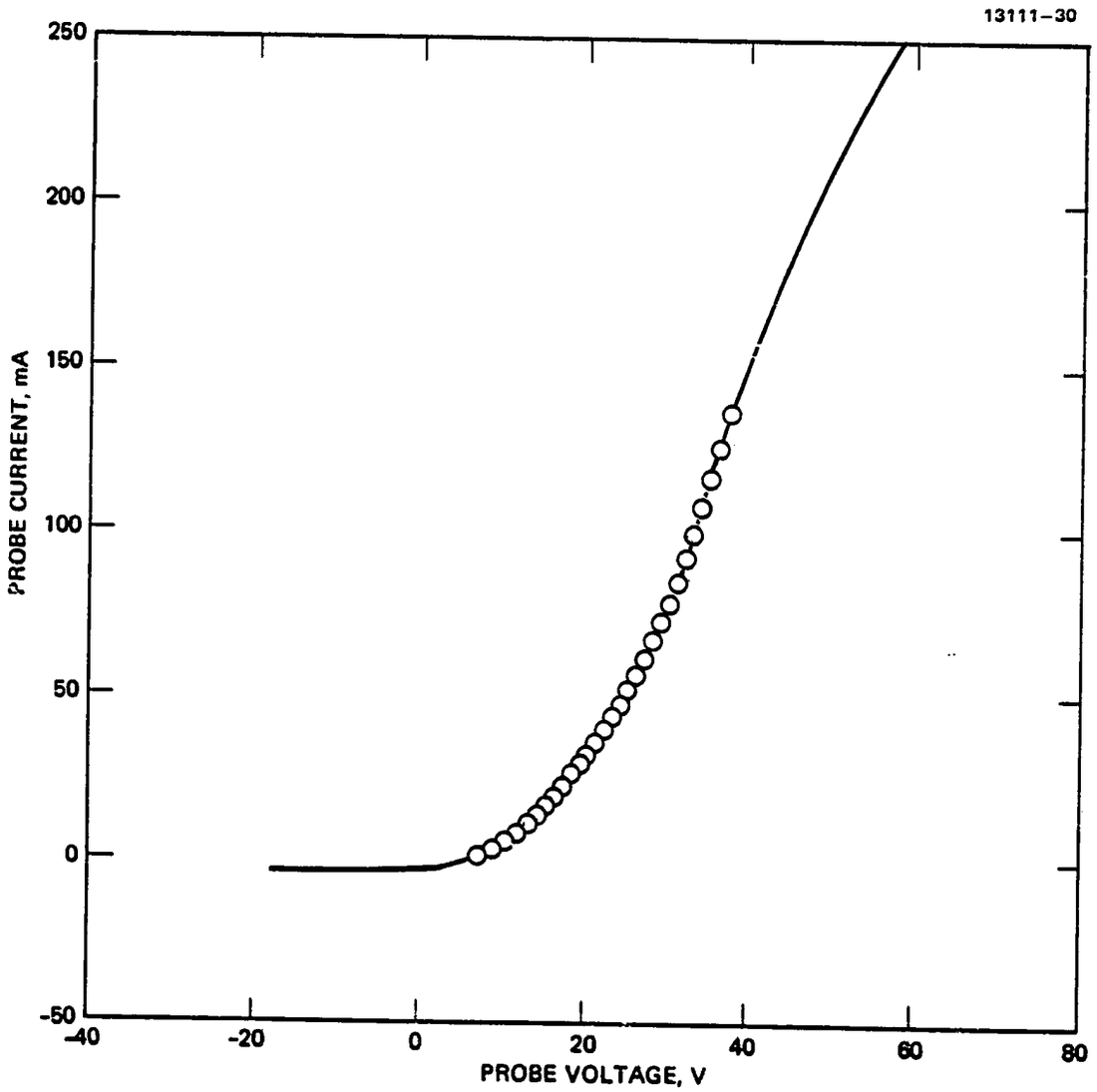

Figure A-3. A comparison of probe data (curve) with calculated results (symbols) that were obtained using a two-group model to analyze the probe characteristic.

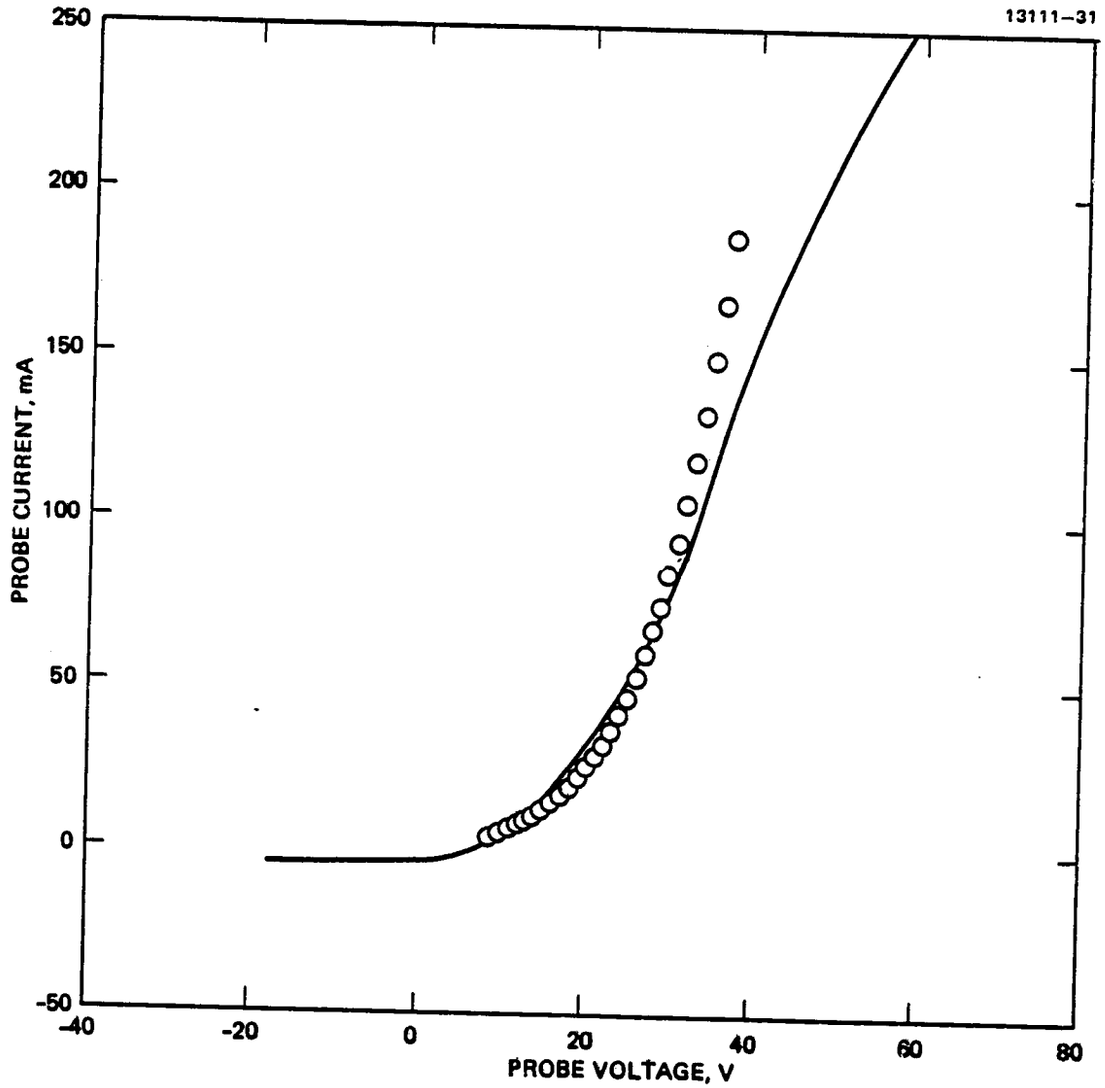

Figure A-4. A comparison of probe data (curve) with calculated results (symbols) that were obtained using a single-group model to analyze the probe characteristic.

Table A-1. Plasma Properties of the Ring-Cusp Thruster Operated with Net-Ion Current Collection by the Screen Grid (Two-Group Analysis)

TEMPERATURE CURVE FIT (EV)	TEMPERATURE MAXWELLIAN SLOPE (EV)	PLASMA POTENTIAL (V)	PRIMARY ELECTRON ENERGY (EV)	MAXWELLIAN SATURATION CURRENT (MA)	PRIMARY ELECTRON DENSITY (PER CC)	MAXWELLIAN ELECTRON DENSITY (PER CC)	NP/NM	ION DENSITY (PER CC)	ION FLUX (MA PER CC)	TRACE NO.
5.89	5.90	37.17	30.98	76.26	0.1422E+11	0.2145E+12	0.066	0.2287E+12	6.369	A1/250B
6.16	6.16	37.54	33.13	79.11	0.1053E+11	0.2177E+12	0.048	0.2282E+12	6.444	A3/250B
5.80	5.80	37.28	29.56	74.47	0.9161E+10	0.2112E+12	0.043	0.2204E+12	6.024	A5/250B
5.08	5.08	36.78	34.07	62.84	0.3037E+10	0.1904E+12	0.016	0.1934E+12	4.882	A7/100B
4.34	4.34	36.18	29.72	51.34	0.2616E+10	0.1684E+12	0.016	0.1710E+12	3.988	A8/100B
3.24	3.24	35.86	16.97	29.56	0.5557E+10	0.1122E+12	0.050	0.1177E+12	2.411	A9/100B
3.40	3.40	36.16	25.33	35.38	0.2015E+10	0.1311E+12	0.015	0.1331E+12	2.748	A9/50B
6.42	6.42	38.52	37.38	93.62	0.7237E+10	0.2523E+12	0.029	0.2596E+12	7.414	C3/250B
5.84	5.83	38.13	31.80	88.90	0.7656E+10	0.2514E+12	0.030	0.2591E+12	7.058	C5/250B
5.65	5.65	38.31	32.53	86.94	0.5211E+10	0.2497E+12	0.021	0.2550E+12	6.804	C9/250B
3.36	3.37	35.93	22.31	56.29	0.9280E+10	0.2093E+12	0.044	0.2186E+12	4.552	C10/100
5.70	5.71	38.65	29.51	96.61	0.1088E+11	0.2762E+12	0.039	0.2871E+12	7.768	E5/250B
3.51	3.51	37.18	20.41	63.53	0.9654E+10	0.2316E+12	0.042	0.2413E+12	5.123	E8/250B
6.74	6.75	39.81	35.89	113.66	0.2036E+11	0.2988E+12	0.068	0.3191E+12	9.518	G1/250B
5.99	5.99	39.42	33.81	104.86	0.7886E+10	0.2927E+12	0.027	0.3006E+12	8.281	G3/250B
4.25	4.25	37.90	25.41	83.31	0.1045E+11	0.2761E+12	0.038	0.2865E+12	6.684	G8/250B
8.38	8.39	41.13	36.19	126.09	0.2704E+11	0.2973E+12	0.091	0.3243E+12	10.895	I1/250B
3.55	3.54	37.31	22.22	80.82	0.1765E+11	0.2934E+12	0.060	0.3110E+12	6.699	I3/250B
9.48	9.51	42.05	35.12	132.80	0.5074E+11	0.2941E+12	0.173	0.3448E+12	12.774	K1/250B
5.14	5.14	38.47	28.83	85.83	0.9858E+10	0.2586E+12	0.037	0.2682E+12	6.881	K2/250B
9.53	9.55	41.28	32.63	108.39	0.7106E+11	0.2395E+12	0.297	0.3106E+12	12.134	L1/250B
4.51	4.51	38.38	23.67	68.39	0.1086E+11	0.2198E+12	0.049	0.2305E+12	5.571	L2/250B

Table A-2. Plasma Properties of the Ring-Cusp Thruster Operated with Net-Ion Current Collection by the Screen Grid (Single-Group Analysis)

TEMPERATURE CURVE FIT (EV)	TEMPERATURE MAXWELLIAN SLOPE (EV)	PLASMA POTENTIAL (V)	PRIMARY ELECTRON ENERGY (EV)	MAXWELLIAN SATURATION CURRENT (MA)	PRIMARY ELECTRON DENSITY (PER CC)	MAXWELLIAN ELECTRON DENSITY (PER CC)	NP/NM	ION DENSITY (PER CC)	ION FLUX (MA PER CC)	TRACE NO.
3.22	3.22	36.90	0.00	17.07	0.0000E+00	0.6497E+11	0.000	0.6497E+11	1.298	A10/50B
1.63	1.63	36.93	0.00	2.03	0.0000E+00	0.1084E+11	0.000	0.1084E+11	0.154	A11/10B
8.01	8.01	38.70	0.00	89.62	0.0000E+00	0.2163E+12	0.000	0.2163E+12	6.801	A1/250B
7.84	7.84	38.67	0.00	89.20	0.0000E+00	0.2176E+12	0.000	0.2176E+12	6.769	A3/250B
7.09	7.09	38.15	0.00	82.76	0.0000E+00	0.2122E+12	0.000	0.2122E+12	6.280	A5/250B
6.06	6.06	37.88	0.00	66.34	0.0000E+00	0.1840E+12	0.000	0.1840E+12	5.035	A7/100B
5.26	5.26	37.36	0.00	54.34	0.0000E+00	0.1618E+12	0.000	0.1618E+12	4.124	A8/100B
4.24	4.24	36.82	0.00	33.99	0.0000E+00	0.1127E+12	0.000	0.1127E+12	2.579	A9/100B
4.46	4.46	37.72	0.00	37.43	0.0000E+00	0.1210E+12	0.000	0.1210E+12	2.841	A9/50B
1.86	1.86	37.10	0.00	9.91	0.0000E+00	0.4968E+11	0.000	0.4968E+11	0.752	C11/50B
8.11	8.11	39.75	0.00	103.02	0.0000E+00	0.2471E+12	0.000	0.2471E+12	7.819	C1/250B
7.74	7.74	39.54	0.00	101.22	0.0000E+00	0.2484E+12	0.000	0.2484E+12	7.682	C3/250B
6.92	6.92	38.89	0.00	96.10	0.0000E+00	0.2495E+12	0.000	0.2495E+12	7.293	C5/250B
6.73	6.73	39.15	0.00	97.52	0.0000E+00	0.2568E+12	0.000	0.2568E+12	7.401	C7/250B
6.60	6.60	39.16	0.00	97.16	0.0000E+00	0.2583E+12	0.000	0.2583E+12	7.373	C8/250B
6.49	6.49	38.97	0.00	91.99	0.0000E+00	0.2466E+12	0.000	0.2466E+12	6.982	C9/250B
5.37	5.37	38.57	0.00	65.34	0.0000E+00	0.1926E+12	0.000	0.1926E+12	4.959	C10/100
1.98	1.98	37.17	0.00	14.18	0.0000E+00	0.6925E+11	0.000	0.6925E+11	1.076	E10/50B
8.36	8.36	40.58	0.00	116.49	0.0000E+00	0.2752E+12	0.000	0.2752E+12	8.840	E1/250B
7.57	7.57	39.94	0.00	110.67	0.0000E+00	0.2748E+12	0.000	0.2748E+12	8.399	E3/250B
6.94	6.94	39.54	0.00	106.40	0.0000E+00	0.2758E+12	0.000	0.2758E+12	8.075	E5/250B
6.01	6.01	39.08	0.00	94.99	0.0000E+00	0.2646E+12	0.000	0.2646E+12	7.209	E7/250B
4.72	4.72	38.41	0.00	71.63	0.0000E+00	0.2252E+12	0.000	0.2252E+12	5.436	E8/250B
2.94	2.84	37.35	0.00	35.19	0.0000E+00	0.1427E+12	0.000	0.1427E+12	2.670	E9/100B
1.89	1.89	37.24	0.00	15.93	0.0000E+00	0.7923E+11	0.000	0.7923E+11	1.209	G10/50B
9.21	9.21	41.47	0.00	133.81	0.0000E+00	0.3012E+12	0.000	0.3012E+12	10.155	G1/250B
7.22	7.22	40.52	0.00	113.09	0.0000E+00	0.2876E+12	0.000	0.2876E+12	8.583	G3/250B
5.70	5.70	39.62	0.00	98.41	0.0000E+00	0.2815E+12	0.000	0.2815E+12	7.468	G5/250B
6.83	6.83	40.20	0.00	109.59	0.0000E+00	0.2863E+12	0.000	0.2863E+12	8.317	G7/250B
5.71	5.71	39.42	0.00	93.03	0.0000E+00	0.2659E+12	0.000	0.2659E+12	7.060	G8/250B

Table A-2. Continued

TEMPERATURE CURVE FIT (EV)	TEMPERATURE MAXWELLIAN SLOPE (EV)	PLASMA POTENTIAL (V)	PRIMARY ELECTRON ENERGY (EV)	MAXWELLIAN SATURATION CURRENT (MA)	PRIMARY ELECTRON DENSITY (PER CC)	MAXWELLIAN ELECTRON DENSITY (PER CC)	NP/NM	ION DENSITY (PER CC)	ION FLUX (MA PER CC)	TRACE NO.
3.21	3.21	37.92	0.00	43.49	0.0000E+00	0.1658E+12	0.000	0.1658E+12	3.300	G9/100B
9.70	9.70	40.54	0.00	146.93	0.0000E+00	0.3222E+12	0.000	0.3222E+12	11.151	I1/250B
7.48	7.48	40.49	0.00	116.67	0.0000E+00	0.2913E+12	0.000	0.2913E+12	8.854	I2/250B
5.61	5.61	39.47	0.00	96.27	0.0000E+00	0.2776E+12	0.000	0.2776E+12	7.306	I3/250B
4.02	4.02	38.63	0.00	74.43	0.0000E+00	0.2535E+12	0.000	0.2535E+12	5.649	I4/250B
3.19	3.19	38.28	0.00	55.78	0.0000E+00	0.2132E+12	0.000	0.2132E+12	4.233	I5/100B
2.70	2.70	37.94	0.00	48.31	0.0000E+00	0.2007E+12	0.000	0.2007E+12	3.667	I6/100B
2.42	2.42	37.72	0.00	41.93	0.0000E+00	0.1841E+12	0.000	0.1841E+12	3.182	I7/100B
2.37	2.37	37.78	0.00	39.42	0.0000E+00	0.1748E+12	0.000	0.1748E+12	2.992	I8/100B
2.16	2.16	37.80	0.00	32.42	0.0000E+00	0.1507E+12	0.000	0.1507E+12	2.461	I9/50B
9.43	9.43	38.51	0.00	166.40	0.0000E+00	0.3700E+12	0.000	0.3700E+12	12.628	K1/250B
9.43	9.43	38.51	0.00	166.40	0.0000E+00	0.3700E+12	0.000	0.3700E+12	12.628	K1/250B
9.43	9.43	38.51	0.00	166.40	0.0000E+00	0.3700E+12	0.000	0.3700E+12	12.628	K1/250B
6.53	6.53	39.75	0.00	94.97	0.0000E+00	0.2537E+12	0.000	0.2537E+12	7.207	K2/250B
6.53	6.53	39.75	0.00	94.97	0.0000E+00	0.2537E+12	0.000	0.2537E+12	7.207	K2/250B
6.53	6.53	39.75	0.00	94.97	0.0000E+00	0.2537E+12	0.000	0.2537E+12	7.207	K2/250B
3.99	3.99	38.65	0.00	57.73	0.0000E+00	0.1974E+12	0.000	0.1974E+12	4.381	K3/100B
3.99	3.99	38.65	0.00	57.73	0.0000E+00	0.1974E+12	0.000	0.1974E+12	4.381	K3/100B
3.99	3.99	38.65	0.00	57.73	0.0000E+00	0.1974E+12	0.000	0.1974E+12	4.381	K3/100B
2.70	2.70	37.86	0.00	41.04	0.0000E+00	0.1705E+12	0.000	0.1705E+12	3.114	K4/100B
2.70	2.70	37.86	0.00	41.04	0.0000E+00	0.1705E+12	0.000	0.1705E+12	3.114	K4/100B
2.70	2.70	37.86	0.00	41.04	0.0000E+00	0.1705E+12	0.000	0.1705E+12	3.114	K4/100B
1.95	1.95	37.33	0.00	29.25	0.0000E+00	0.1432E+12	0.000	0.1432E+12	2.220	K5/50B
1.95	1.95	37.33	0.00	29.25	0.0000E+00	0.1432E+12	0.000	0.1432E+12	2.220	K5/50B
1.95	1.95	37.33	0.00	29.25	0.0000E+00	0.1432E+12	0.000	0.1432E+12	2.220	K5/50B
1.57	1.57	37.51	0.00	21.06	0.0000E+00	0.1147E+12	0.000	0.1147E+12	1.598	K6/50B
1.29	1.29	37.31	0.00	15.78	0.0000E+00	0.9483E+11	0.000	0.9483E+11	1.198	K7/50B
1.12	1.12	37.16	0.00	12.06	0.0000E+00	0.7802E+11	0.000	0.7802E+11	0.916	K8/50B
1.03	1.03	37.13	0.00	10.34	0.0000E+00	0.6967E+11	0.000	0.6967E+11	0.784	K9/50B
9.14	9.14	36.90	0.00	154.23	0.0000E+00	0.3484E+12	0.000	0.3484E+12	11.705	L1/250B

Table A-2. Concluded

TEMPERATURE CURVE FIT (EV)	MAXWELLIAN SLOPE (EV)	PLASMA POTENTIAL (V)	PRIMARY ELECTRON ENERGY (EV)	MAXWELLIAN SATURATION CURRENT (MA)	PRIMARY ELECTRON DENSITY (PER CC)	MAXWELLIAN ELECTRON DENSITY (PER CC)	NP/NM	ION DENSITY (PER CC)	ION FLUX (MA PER CC)	TRACE NO.
5.72	5.72	39.28	0.00	77.22	0.0000E+00	0.2205E+12	0.000	0.2205E+12	5.860	L2/250B
3.32	3.32	38.39	0.00	43.01	0.0000E+00	0.1613E+12	0.000	0.1613E+12	3.264	L3/100B
2.15	2.15	37.65	0.00	28.60	0.0000E+00	0.1333E+12	0.000	0.1333E+12	2.170	L4/100B
1.65	1.65	37.68	0.00	19.75	0.0000E+00	0.1050E+12	0.000	0.1050E+12	1.499	L5/50B
1.16	1.16	37.02	0.00	13.38	0.0000E+00	0.8480E+11	0.000	0.8480E+11	1.016	L6/50B
1.10	1.10	37.13	0.00	10.88	0.0000E+00	0.7076E+11	0.000	0.7076E+11	0.826	L7/50B

Table A-3. Plasma Properties of the Ring-Cusp Thruster Operated with Net-Electron Current Collection by the Screen Grid (Two-Group Analysis)

TEMPERATURE CURVE FIT (EV)	TEMPERATURE MAXWELLIAN SLOPE (EV)	PLASMA POTENTIAL (V)	PRIMARY ELECTRON ENERGY (EV)	MAXWELLIAN SATURATION CURRENT (MA)	PRIMARY ELECTRON DENSITY (PER CC)	MAXWELLIAN ELECTRON DENSITY (PER CC)	NP/NM	ION DENSITY (PER CC)	ION FLUX (MA PER CC)	TRACE NO.
8.66	8.66	38.55	28.05	82.43	0.7278E+10	0.1914E+12	0.038	0.1986E+12	6.616	A1/250C
8.57	8.57	38.41	33.49	83.79	0.2851E+10	0.1955E+12	0.015	0.1983E+12	6.499	A3/250C
6.18	6.18	36.96	28.44	58.77	0.5011E+10	0.1615E+12	0.031	0.1665E+12	4.669	A7/250C
8.81	8.81	39.18	28.55	95.59	0.3409E+10	0.2200E+12	0.015	0.2234E+12	7.428	C1/250C
7.94	7.94	38.90	32.41	90.12	0.7075E+10	0.2184E+12	0.032	0.2254E+12	7.170	C3/250C
7.04	7.04	38.35	30.46	83.45	0.9829E+10	0.2148E+12	0.046	0.2246E+12	6.772	C5/250C
6.86	6.86	38.37	32.17	85.63	0.6973E+10	0.2233E+12	0.031	0.2303E+12	6.807	C7/250C
7.10	7.10	38.82	31.95	88.77	0.4807E+10	0.2275E+12	0.021	0.2323E+12	6.950	C8/250C
6.78	6.78	38.41	34.33	84.23	0.4471E+10	0.2209E+12	0.020	0.2254E+12	6.586	C9/250C
7.97	7.97	39.65	35.54	101.26	0.1105E+11	0.2450E+12	0.045	0.2561E+12	8.215	E1/250C
7.76	7.76	39.41	33.26	98.92	0.7760E+10	0.2425E+12	0.032	0.2503E+12	7.871	E3/250C
7.61	7.61	39.29	36.15	97.72	0.2996E+10	0.2420E+12	0.012	0.2450E+12	7.558	E5/250C
6.38	6.38	38.74	31.23	84.97	0.7426E+10	0.2298E+12	0.032	0.2372E+12	6.766	E7/250C
5.33	5.32	38.34	30.18	68.21	0.3761E+10	0.2019E+12	0.019	0.2057E+12	5.325	E8/100C
8.19	8.21	40.29	35.37	110.83	0.1921E+11	0.2642E+12	0.073	0.2834E+12	9.337	G1/250C
7.59	7 59	39.71	35.47	105.84	0.3944E+10	0.2625E+12	0.015	0.2664E+12	8.213	G3/250C
5.31	5.31	38.47	28.03	83.98	0.1162E+11	0.2489E+12	0.047	0.2605E+12	6.824	G5/250C
6.79	6.79	39.46	32.24	96.95	0.8364E+10	0.2542E+12	0.033	0.2625E+12	7.723	G7/250C
5.46	5.46	38.18	30.44	83.01	0.9247E+10	0.2426E+12	0.038	0.2519E+12	6.662	G8/250C
2.94	2.95	36.96	18.29	38.30	0.6117E+10	0.1524E+12	0.040	0.1585E+12	3.082	G9/100C
9.72	9.74	41.67	35.16	124.65	0.2949E+11	0.2728E+12	0.108	0.3023E+12	11.024	I1/250C
8.03	8.02	40.12	30.29	110.58	0.6809E+10	0.2666E+12	0.026	0.2734E+12	8.716	I2/250C
5.44	5.43	38.60	30.56	86.10	0.8777E+10	0.2523E+12	0.035	0.2611E+12	6.879	I3/250C
3.80	3.80	38.26	17.87	55.07	0.2176E+10	0.1929E+12	0.011	0.1950E+12	4.247	I5/100C
9.12	9.13	40.83	33.49	107.43	0.7686E+11	0.2428E+12	0.317	0.3197E+12	12.306	K1/500C
7.27	7.27	39.58	36.48	93.08	0.1170E+10	0.2358E+12	0.005	0.2370E+12	7.118	K2/250C
3.86	3.86	37.54	25.81	58.56	0.4634E+10	0.1967E+12	0.024	0.2013E+12	4.448	K3/250C
9.72	9.73	40.10	31.73	91.67	0.9820E+11	0.2007E+12	0.489	0.2989E+12	12.637	L1/500C
6.30	6.31	38.95	31.93	78.14	0.5598E+10	0.2125E+12	0.026	0.2181E+12	6.163	L2/250C
3.73	3.73	38.05	16.35	41.63	0.4831E+10	0.1472E+12	0.033	0.1520E+12	3.313	L3/100C

Table A-4. Plasma Properties of the Ring-Cusp Thruster Operated with Net-Electron Current Collection by the Screen Grid (Single-Group Analysis)

TEMPERATURE CURVE FIT (EV)	TEMPERATURE MAXWELLIAN SLOPE (EV)	PLASMA POTENTIAL (V)	PRIMARY ELECTRON ENERGY (EV)	MAXWELLIAN SATURATION CURRENT (MA)	PRIMARY ELECTRON DENSITY (PER CC)	MAXWELLIAN ELECTRON DENSITY (PER CC)	NP/NM	ION DENSITY (PER CC)	ION FLUX (MA PER CC)	TRACE NO.
4.25	4.25	37.05	0.00	15.80	0.0000E+00	0.5232E+11	0.000	0.5232E+11	1.199	A10/50C
2.07	2.07	37.40	0.00	1.55	0.0000E+00	0.7342E+10	0.000	0.7342E+10	0.117	A11/10C
9.06	9.06	38.61	0.00	88.18	0.0000E+00	0.2001E+12	0.000	0.2001E+12	6.692	A1/250C
8.92	8.92	38.58	0.00	86.35	0.0000E+00	0.1975E+12	0.000	0.1975E+12	6.554	A3/250C
8.20	8.20	38.04	0.00	80.19	0.0000E+00	0.1913E+12	0.000	0.1913E+12	6.086	A5/250C
7.02	7.02	37.58	0.00	63.29	0.0000E+00	0.1632E+12	0.000	0.1632E+12	4.803	A7/250C
6.44	6.44	37.24	0.00	53.31	0.0000E+00	0.1435E+12	0.000	0.1435E+12	4.046	A8/250C
5.57	5.57	37.05	0.00	34.70	0.0000E+00	0.1005E+12	0.000	0.1005E+12	2.633	A9/100C
6.46	6.46	38.75	0.00	63.47	0.0000E+00	0.1705E+12	0.000	0.1705E+12	4.817	C10/100
2.37	2.37	37.15	0.00	10.21	0.0000E+00	0.4530E+11	0.000	0.4530E+11	0.775	C11/50C
8.84	8.84	38.97	0.00	97.95	0.0000E+00	0.2251E+12	0.000	0.2251E+12	7.434	C1/250C
8.50	8.50	38.96	0.00	95.96	0.0000E+00	0.2249E+12	0.000	0.2249E+12	7.282	C3/250C
8.11	8.11	38.91	0.00	91.99	0.0000E+00	0.2206E+12	0.000	0.2206E+12	6.981	C5/250C
7.79	7.79	38.96	0.00	92.03	0.0000E+00	0.2253E+12	0.000	0.2253E+12	6.984	C7/250C
7.68	7.68	39.16	0.00	93.08	0.0000E+00	0.2294E+12	0.000	0.2294E+12	7.064	C8/250C
7.60	7.60	39.12	0.00	88.78	0.0000E+00	0.2200E+12	0.000	0.2200E+12	6.737	C9/250C
2.72	2.72	37.48	0.00	14.57	0.0000E+00	0.6034E+11	0.000	0.6034E+11	1.105	E10/50C
9.20	9.20	40.22	0.00	111.35	0.0000E+00	0.2508E+12	0.000	0.2508E+12	8.451	E1/250C
8.51	8.51	39.70	0.00	105.67	0.0000E+00	0.2475E+12	0.000	0.2475E+12	8.020	E3/250C
8.04	8.04	39.55	0.00	100.60	0.0000E+00	0.2424E+12	0.000	0.2424E+12	7.634	E5/250C
7.38	7.38	39.43	0.00	91.81	0.0000E+00	0.2308E+12	0.000	0.2308E+12	6.968	E7/250C
6.17	6.17	39.20	0.00	71.91	0.0000E+00	0.1978E+12	0.000	0.1978E+12	5.458	E8/100C
3.72	3.72	37.76	0.00	34.48	0.0000E+00	0.1221E+12	0.000	0.1221E+12	2.617	E9/100C
2.56	2.56	37.44	0.00	16.20	0.0000E+00	0.6918E+11	0.000	0.6918E+11	1.230	G10/50C
9.51	9.51	40.28	0.00	126.68	0.0000E+00	0.2806E+12	0.000	0.2806E+12	9.612	G1/250C
8.11	8.11	40.09	0.00	109.71	0.0000E+00	0.2630E+12	0.000	0.2630E+12	8.328	G3/250C
6.80	6.80	39.68	0.00	94.50	0.0000E+00	0.2475E+12	0.000	0.2475E+12	7.172	G5/250C
7.78	7.78	40.09	0.00	104.58	0.0000E+00	0.2561E+12	0.000	0.2561E+12	7.937	G7/250C
7.04	7.04	39.78	0.00	92.35	0.0000E+00	0.2378E+12	0.000	0.2378E+12	7.008	G8/250C
4.20	4.20	38.43	0.00	43.48	0.0000E+00	0.1449E+12	0.000	0.1449E+12	3.300	G9/100C

Table A-4. Continued

TEMPERATURE CURVE FIT (EV)	MAXWELLIAN SLOPE (EV)	PLASMA POTENTIAL (V)	PRIMARY ELECTRON ENERGY (EV)	MAXWELLIAN SATURATION CURRENT (MA)	PRIMARY ELECTRON DENSITY (PER CC)	MAXWELLIAN ELECTRON DENSITY (PER CC)	NP/NM	ION DENSITY (PER CC)	ION FLUX (MA PER CC)	TRACE NO.
2.34	2.34	37.67	0.00	25.17	0.0000E+00	0.1123E+12	0.000	0.1123E+12	1.910	I10/50C
1.29	1.29	37.06	0.00	10.01	0.0000E+00	0.6015E+11	0.000	0.6015E+11	0.760	I11/50C
1.29	1.29	37.06	0.00	10.01	0.0000E+00	0.6015E+11	0.000	0.6015E+11	0.760	I11/50C
9.69	9.69	39.08	0.00	142.61	0.0000E+00	0.3129E+12	0.000	0.3129E+12	10.823	I1/250C
8.38	8.38	40.11	0.00	115.86	0.0000E+00	0.2734E+12	0.000	0.2734E+12	8.793	I2/250C
6.79	6.79	39.82	0.00	94.64	0.0000E+00	0.2480E+12	0.000	0.2480E+12	7.182	I3/250C
5.11	5.11	39.01	0.00	73.92	0.0000E+00	0.2233E+12	0.000	0.2233E+12	5.610	I4/250C
4.01	4.01	38.44	0.00	56.70	0.0000E+00	0.1934E+12	0.000	0.1934E+12	4.303	I5/100C
3.24	3.24	38.10	0.00	46.36	0.0000E+00	0.1760E+12	0.000	0.1760E+12	3.518	I6/100C
2.96	2.96	37.90	0.00	40.78	0.0000E+00	0.1618E+12	0.000	0.1618E+12	3.095	I7/100C
2.79	2.79	37.81	0.00	37.61	0.0000E+00	0.1538E+12	0.000	0.1538E+12	2.854	I8/100C
2.62	2.62	37.83	0.00	33.28	0.0000E+00	0.1405E+12	0.000	0.1405E+12	2.526	I9/50C
0.85	0.85	37.12	0.00	5.63	0.0000E+00	0.4185E+11	0.000	0.4185E+11	0.428	K10/10C
9.26	9.26	37.40	0.00	167.91	0.0000E+00	0.3770E+12	0.000	0.3770E+12	12.743	K1/250C
9.26	9.26	37.40	0.00	167.91	0.0000E+00	0.3770E+12	0.000	0.3770E+12	12.743	K1/250C
11.18	11.18	38.94	0.00	162.90	0.0000E+00	0.3328E+12	0.000	0.3328E+12	12.363	K1/500C
11.18	11.18	38.94	0.00	162.90	0.0000E+00	0.3328E+12	0.000	0.3328E+12	12.363	K1/500C
7.45	7.45	39.69	0.00	94.21	0.0000E+00	0.2358E+12	0.000	0.2358E+12	7.150	K2/250C
4.81	4.81	38.52	0.00	60.92	0.0000E+00	0.1897E+12	0.000	0.1897E+12	4.623	K3/250C
3.20	3.20	37.84	0.00	40.02	0.0000E+00	0.1528E+12	0.000	0.1528E+12	3.037	K4/100C
2.39	2.39	37.53	0.00	28.23	0.0000E+00	0.1248E+12	0.000	0.1248E+12	2.142	K5/50C
1.91	1.91	37.40	0.00	20.35	0.0000E+00	0.1006E+12	0.000	0.1006E+12	1.544	K6/50C
1.61	1.61	37.49	0.00	14.42	0.0000E+00	0.7764E+11	0.000	0.7764E+11	1.094	K7/50C
1.17	1.17	36.87	0.00	10.38	0.0000E+00	0.6549E+11	0.000	0.6549E+11	0.788	K8/50C
0.84	0.84	37.15	0.00	4.71	0.0000E+00	0.3504E+11	0.000	0.3504E+11	0.358	L10/10C
0.84	0.84	37.15	0.00	4.71	0.0000E+00	0.3504E+11	0.000	0.3504E+11	0.358	L10/10C
9.08	9.08	36.62	0.00	173.74	0.0000E+00	0.3939E+12	0.000	0.3939E+12	13.186	L1/250C
10.38	10.38	36.35	0.00	156.98	0.0000E+00	0.3329E+12	0.000	0.3329E+12	11.914	L1/500C
7.24	7.24	39.69	0.00	83.53	0.0000E+00	0.2121E+12	0.000	0.2121E+12	6.339	L2/250C
4.15	4.15	38.31	0.00	45.10	0.0000E+00	0.1513E+12	0.000	0.1513E+12	3.423	L3/100C

Table A-4. Concluded

TEMPERATURE CURVE FIT (EV)	TEMPERATURE MAXWELLIAN SLOPE (EV)	PLASMA POTENTIAL (V)	PRIMARY ELECTRON ENERGY (EV)	MAXWELLIAN SATURATION CURRENT (MA)	PRIMARY ELECTRON DENSITY (PER CC)	MAXWELLIAN ELECTRON DENSITY (PER CC)	NP/NM	ION DENSITY (PER CC)	ION FLUX (MA PER CC)	TRACE NO.
2.60	2.60	37.61	0.00	29.06	0.0000E+00	0.1189E+12	0.000	0.1189E+12	2.130	L4/100C
2.60	2.60	37.61	0.00	28.06	0.0000E+00	0.1189E+12	0.000	0.1189E+12	2.130	L4/100C
1.87	1.87	37.47	0.00	18.71	0.0000E+00	0.9347E+11	0.000	0.9347E+11	1.420	L5/50C
1.87	1.87	37.47	0.00	18.71	0.0000E+00	0.9347E+11	0.000	0.9347E+11	1.420	L5/50C
1.41	1.41	37.19	0.00	12.52	0.0000E+00	0.7205E+11	0.000	0.7205E+11	0.950	L6/50C
1.41	1.41	37.19	0.00	12.52	0.0000E+00	0.7205E+11	0.000	0.7205E+11	0.950	L6/50C
1.21	1.21	37.06	0.00	9.41	0.0000E+00	0.5831E+11	0.000	0.5831E+11	0.714	L7/50C
1.21	1.21	37.06	0.00	9.41	0.0000E+00	0.5831E+11	0.000	0.5831E+11	0.714	L7/50C
1.06	1.06	36.83	0.00	8.67	0.0000E+00	0.5752E+11	0.000	0.5752E+11	0.658	L8/50C
1.06	1.06	36.83	0.00	8.67	0.0000E+00	0.5752E+11	0.000	0.5752E+11	0.658	L8/50C
0.91	0.91	36.76	0.00	7.90	0.0000E+00	0.5664E+11	0.000	0.5664E+11	0.600	L9/50C
0.91	0.91	36.76	0.00	7.90	0.0000E+00	0.5664E+11	0.000	0.5664E+11	0.600	L9/50C

APPENDIX B

DERIVATION OF PERVEANCE CORRECTION FACTOR

The space-charge-limited current J_+ that can be extracted by one-dimensional planar electrodes is governed by Child's Law:

$$J^+ = \frac{4\varepsilon_o}{9}\sqrt{\frac{2e}{m}}\,\frac{V_T^{3/2}}{l_e^2}\,A_s \quad , \qquad (B\text{-}1)$$

where V_T is the total voltage, l_e is the effective inter-electrode spacing, e/m is the charge-to-mass ratio, A_s is the effective area, and ε_o is the permittivity. Equation (B-1) applies to a beam composed of singly charged ions; if all the beam ions were doubly charged, the current would be greater by a factor of $\sqrt{2}$. Therefore, in making perveance comparisons, the increase in measured perveance caused by the presence of doubly charged ions should be accounted for by correcting the measured value to obtain an equivalent singly charged ion perveance.

For the case where both singly and doubly charged ions are present, Poisson's equation is

$$\frac{d^2V}{dx^2} = -\frac{1}{\varepsilon_o}\,(J_+ + J_{++}/\sqrt{2})\sqrt{\frac{m}{2e}}\,\frac{V^{-1/2}}{A_s} \quad , \qquad (B\text{-}2)$$

which can be integrated to give the appropriate form of Child's Law describing space-charge-limited flow of a beam composed of singly and doubly charged ions:

$$J_+ + J_{++}/\sqrt{2} = \frac{4\varepsilon_o}{9}\sqrt{\frac{2e}{m}}\ \frac{V_T^{3/2}}{l_e^2}\ A_s \quad . \qquad \text{(B-3)}$$

Rearranging Equation (B-3) gives the familiar expression for the perveance of a planar diode

$$P = \frac{J_+ + J^{++}/\sqrt{2}}{V_T^{3/2}} \qquad \text{(B-4)}$$

$$= \frac{4\varepsilon_o}{9}\sqrt{\frac{2e}{m}}\ \frac{A_s}{l_e^2} \quad . \qquad \text{(B-5)}$$

The measured perveance is given by

$$P_{measured} = \frac{J_+ + J_{++}}{V_T^{3/2}} \quad , \qquad \text{(B-6)}$$

where the sum of the singly and doubly charged ion currents is the measured beam current J_b. Combining Equations (B-4) and (B-6) gives the following relationship between the effective (or corrected) perveance and the measured value:

$$\frac{P_{corrected}}{P_{measured}} = \frac{J_+ + J_{++}/\sqrt{2}}{J_+ + J_{++}} \quad . \qquad \text{(B-7)}$$

The right side of this expression is the definition of the thrust correction factor, α, so that Equation (B-7) can be rewritten as

$$P_{corrected} = \alpha\, P_{measured} \quad . \qquad \text{(B-8)}$$

APPENDIX C

DERIVATION OF EXPRESSIONS FOR THE THRUST-LOSS FACTORS α AND F_t

Expressions for the thrust-loss factors α and F_t can be derived by applying the integral form of the steady-state continuity and momentum equations to the control volume of Figure C-1. The continuity equation for the flow of ions* across the control surface can be written as

$$J_b = J_+ + J_{++}$$

$$= \int_{A_g} (\vec{j}_+ + \vec{j}_{++}) \cdot \hat{n} dA \ , \qquad \text{(C-1)}$$

where J_b is the beam current, $\vec{j}$ is the current-density vector, $\hat{n}$ is the unit vector normal to the small surface element dA, and the integration is over the electrode boundary A_g of the control volume. The scalar product appearing in Eq. C-1 can be written as

$$\vec{j} \cdot \hat{n} = j \cos (\gamma - \phi) \ , \qquad \text{(C-2)}$$

where ϕ and γ are the inclination of the current-density vector and surface normal with respect to the thruster axis. The angle ϕ is determined experimentally; the angle γ is determined by the electrode geometry and is given by the expression

$$\gamma = \sin^{-1} \left(\frac{r}{R_c} \right) , \qquad \text{(C-3)}$$

where r is the radial coordinate, and R_c is the radius of curvature of the electrodes. The area element dA is related to the radial coordinate r (radial symmetry is assumed) by the expression

---

* We assume that the ion beam contains singly and doubly charged ions only.

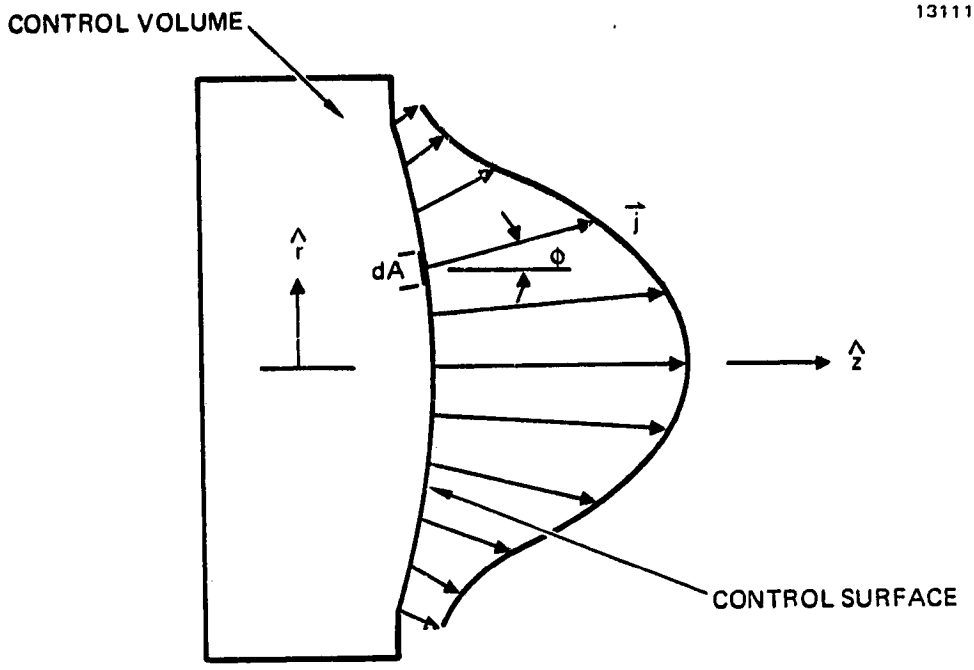

a) CONTROL VOLUME

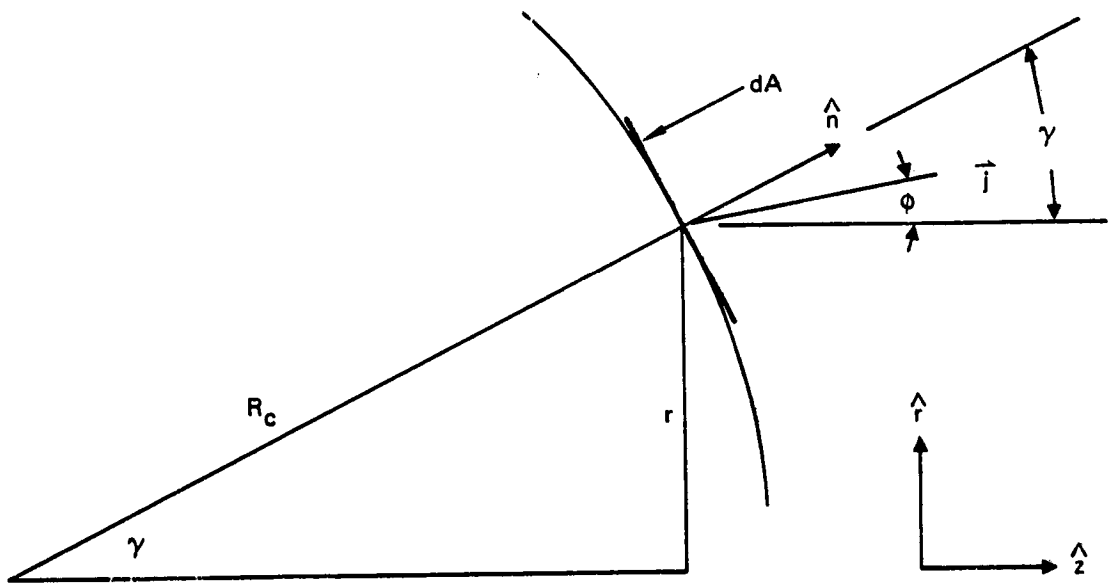

b) GEOMETRY OF SURFACE-AREA ELEMENT dA

Figure C.1. Control volume and coordinates used in deriving expressions for beam current and net thrust.

$$dA = \frac{2\pi r dr}{\cos \gamma} , \qquad (C-4)$$

which is obtained by projecting the area dA onto a circular plane perpendicular to the thruster axis. The thrust is obtained from the momentum equation as

$$\vec{F} = - \frac{m}{e} \int_{A_g} (\vec{j}_+ + \frac{\sqrt{2}}{2} \vec{j}_{++}) \vec{v}_+ \cdot \hat{n} \, dA , \qquad (C-5)$$

where m is the mass of the propellant ion, e is the electronic charge, and $\vec{v}_+$ is the velocity of singly charged ions. In formulating Eq. C-5, we have neglected pressure forces as well as thrust produced by the loss of neutral particles and the impingement of charge-exchange ions. The factor $\frac{\sqrt{2}}{2}$ in Eq. C-5 accounts for the higher velocity and lower mass-to-charge ratio of doubly charged ions. The scalar product in Eq. C-5 can be written as

$$\vec{v}_+ \cdot \hat{n} = v_+ \cos (\gamma - \phi) . \qquad (C-6)$$

The component of thrust parallel to the thruster axis F_{Net} is obtained by using the component $\vec{j} \cdot \vec{z}$ in Eq. C-5

$$F_{Net} = \frac{m v_+}{e} \int_{A_g} (\vec{j}_+ + \frac{\sqrt{2}}{2} \vec{j}_{++}) \cdot \vec{z} \cos (\gamma - \phi) dA, \qquad (C-7)$$

or

$$F_{Net} = \frac{m v_+}{e} \int_{A_g} (j_+ + \frac{\sqrt{2}}{2} j_{++}) \cos \phi \cos (\gamma - \phi) dA . \qquad (C-8)$$

Alternatively, the net thrust is obtained by forming the scalar product of the thrust vector given by Eq. C-5 with the unit vector $\hat{z}$

$$F_{Net} = \vec{F} \cdot \hat{z}$$

$$= \frac{mv_+}{e} F_t \int_{A_g} (j_+ + \frac{\sqrt{2}}{2} j_{++}) \cos (\gamma - \phi) dA \ , \qquad (C\text{-}9)$$

where F_t is the cosine of the average off-axis angle $\bar{\delta}$.
Equating the two expressions for F_{Net} results in an expression for the thrust-loss factor F_t

$$F_t = \frac{\int_{A_g} (j_+ + \frac{\sqrt{2}}{2} j_{++}) \cos (\gamma - \phi) \cos \phi dA}{\int_{A_g} (j_+ + \frac{\sqrt{2}}{2} j_{++}) \cos (\gamma - \phi) \, dA} \ . \qquad (C\text{-}10)$$

Combining Eqs. C-1 and C-9 gives the net thrust in terms of the singly and doubly charged components of beam current J_+ and J_{++}

$$F_{Net} = \frac{mv_+}{e} F_t (J_+ + \frac{\sqrt{2}}{2} J_{++}) \ . \qquad (C\text{-}11)$$

The calculated thrust is given by the expression below which neglects the losses resulting from off-axis trajectories and doubly charged ions

$$F_{Calculated} = \frac{mv_+}{e} J_b$$

$$= \frac{mv_+}{e} (J_+ + J_{++}) \ . \qquad (C\text{-}12)$$

Net thrust is obtained by correcting the calculated thrust using the expression

$$F_{Net} = \alpha F_t \, F_{Calculated} \cdot \qquad (C\text{-}13)$$

Combining Eqs. C-11, C-12, and C-13 gives the following expression for the thrust-loss factor α

$$\alpha = \frac{J_+ + \frac{\sqrt{2}}{2} J_{++}}{J_+ + J_{++}} \cdot \qquad (C\text{-}14) \cdot$$

Eqs. C-1, C-12, and C-13 can be combined to give

$$F_{Net} = \alpha J_b \frac{m}{e} v_+ F_t \cdot \qquad (C\text{-}15)$$

Substituting $v_+ = \sqrt{\frac{2eV_b}{m}}$ gives the following expression for net thrust in terms of beam current J_b and beam voltage V_b

$$F_{Net} = \alpha J_b \sqrt{\frac{2m}{e} F_t^2 V_b} \cdot \qquad (C\text{-}16)$$

In this form, αJ_b represents the equivalent singly charged ion current and $F_t^2 V_b$ is the effective beam voltage.

APPENDIX D

DERIVATION OF EQUATIONS USED TO ANALYZE ExB PROBE DATA

The probe collector current i corresponding to species n is given by the expression*

$$i_n(r,\phi_p) = \iint I_n(r,\phi)\cos(\phi-\phi_p)\{u[\phi-(\phi_p-\psi)]-u[\phi-(\phi_p+\psi)]\}T(\phi_p-\phi)d\omega dA_p \quad , \quad (D-1)$$

where I_n is the intensity of the ion flux, r and ϕ are the coordinates, ϕ_p is the probe angle, ψ is the acceptance half-angle of the collimator, u is the unit step function, T is the transmission of a cylindrical collimator, ω is the solid angle, and A_p is the aperture area. The combination of the transmission and unit step functions in Eq. D-1 effectively "collimates" the incoming flux (as illustrated in Figure D-1), allowing only a fraction of those ions having angles in the range $\phi_p \pm \psi$ to reach the velocity filter. In practice the operator selects the ion species of interest by varying the ratio E/B to match the particle speed. The narrow acceptance angle (2ψ) of the collimator permits the intensity in Eq. D-1 to be replaced by the value corresponding to the probe angle ϕ_p. Since the collimator restricts the angle difference to $\phi - \phi_p \leq \psi$ the cosine can be replaced by unity, and Eq. D-1 can be written as

$$i_n(r,\phi_p) = \iint I_n(r,\phi_p)Td\omega dA_p \quad . \quad (D-2)$$

The narrow field-of-view of the collimator and the small size of the entrance aperture permits us to assume that the ion flux is homogeneous over the aperture area and isotropic within the field-of-view. This enables the intensity to be expressed as

$$I_n = \frac{J_n}{\Omega} \quad , \quad (D-3)$$

*A similar expression is frequently used to describe the response of charged-particle analyzers employed on exploratory spacecraft (Ref. D-1).

3 OF 3

5-15806 UNC

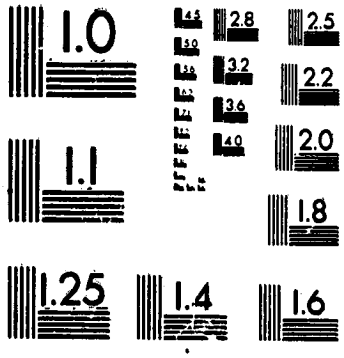

MICROCOPY RESOLUTION TEST CHART
NATIONAL BUREAU OF STANDARDS
STANDARD REFERENCE MATERIAL 1010a
(ANSI and ISO TEST CHART No. 2)

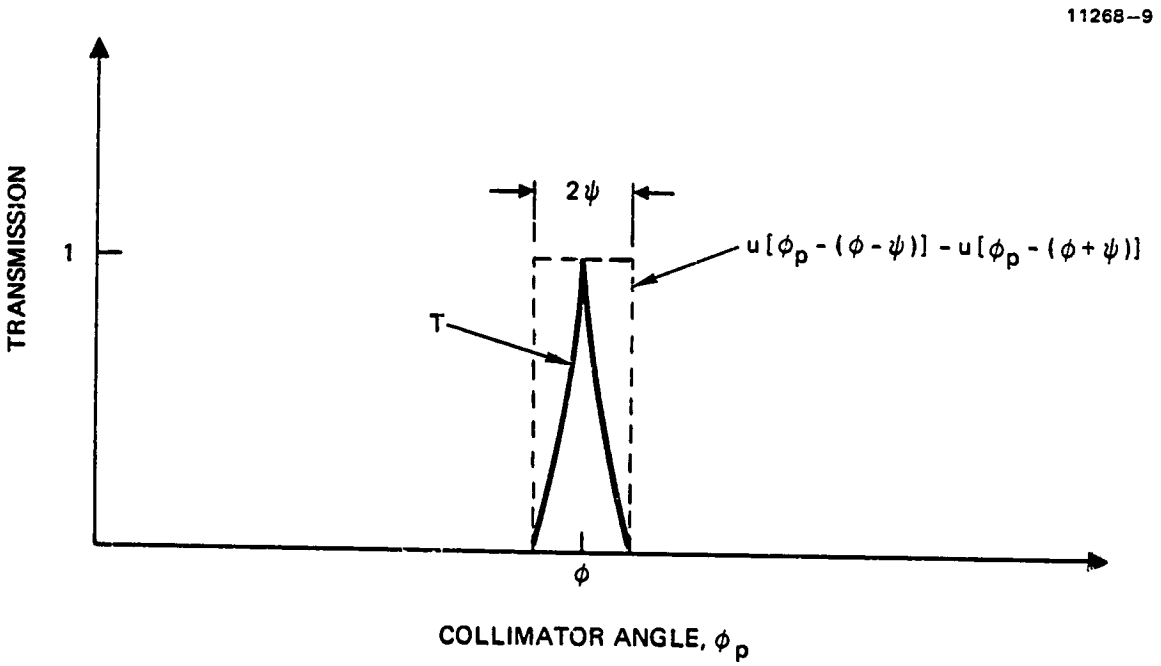

Figure D.1. Transmission of a cylinderical collimator inclined at an angle ϕ. The step functions filter out all angles except those of bandwidth 2ψ centered at ϕ. The function T is the transmission of cylindrical apertures viewing a parallel beam inclined at an angle ϕ.

where J is the current density and Ω is the solid angle subtended by the collimator. Reference to Figure D-2 shows that the solid angle Ω is given by

$$\Omega = \frac{A_p}{\ell^2} , \tag{D-4}$$

where the aperture area A_p is given by

$$A_p \cong \ell^2 \psi^2 . \tag{D-5}$$

where we have used the approximation $\tan \psi = \psi$. The differential solid angle $d\omega$ is given by

$$d\omega = \frac{dA_p}{\ell^2}, \tag{D-6}$$

$$= \frac{2\pi R dR}{\ell^2} . \tag{D-7}$$

For small angles $R = \ell\varepsilon$ and the expression above can be written as

$$d\omega = 2\pi\varepsilon d\varepsilon . \tag{D-8}$$

Combining Eqs. D-2, D-3, D-4, D-5 and D-8, and performing the integration over dA_p, gives

$$i_n(r,\phi_p) = \frac{2J_n(r,\phi_p)A_p}{\psi^2} \int_0^{\psi} \varepsilon T d\varepsilon , \tag{D-9}$$

which can be solved for the current density J_n

11268-10

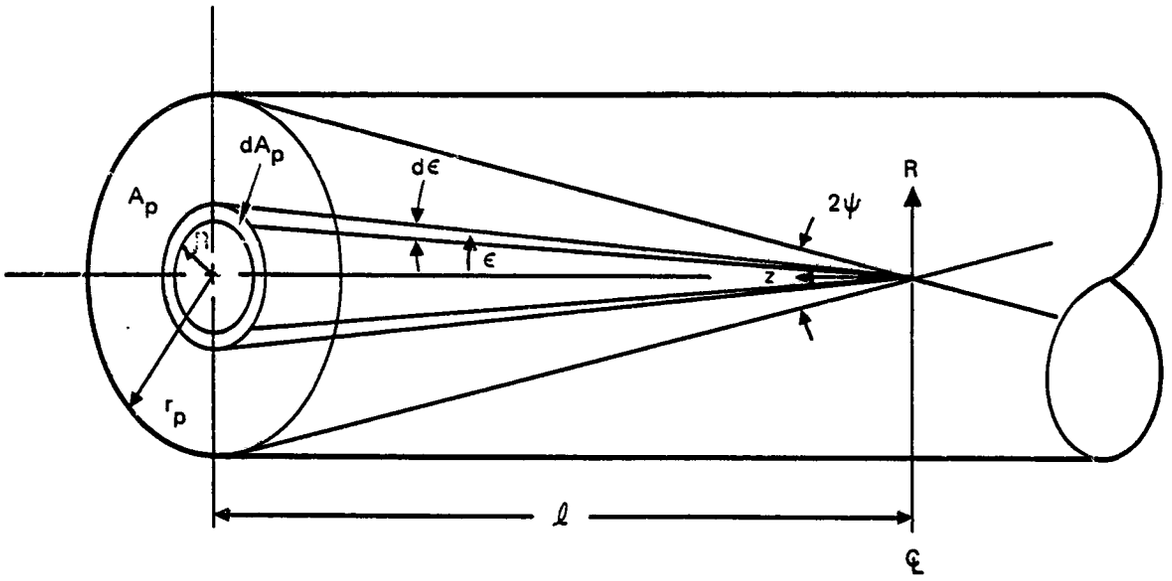

Figure D.2. Definition of variables used in analysis of the response of a cylindrical collimator of length 2ℓ.

$$J_n(r,\phi_p) = \frac{\psi^2}{2\int_0^{\psi} \varepsilon T d\varepsilon} \quad \frac{i_n(r,\phi_p)}{A_p} \qquad \text{(D-10)}$$

The transmission* of the cylindrical collimator is given by

$$T = 1 - \frac{2}{\pi}\left\{\frac{1+s}{2}\left[1 - \left(\frac{1+s}{2}\right)^2\right]^{1/2} + \sin^{-1}\left(\frac{1+s}{2}\right)\right\} , \qquad \text{(D-11)}$$

where, from Figure D-3,

$$\frac{1+s}{2} = \frac{\ell \sin \phi_p}{r_p} \qquad \text{(D-12)}$$

Equations D-11 and D-12 give the transmission of a cylindrical collimator inclined at an angle ϕ_p with respect to a parallel beam. In our case, we are interested in the response of the collimator to a superposition of beams (the isotropic and homogeneous assumption) which are inclined at an angle ε with respect to the probe axis (the angle ε varies from 0 to ψ). Therefore, the appropriate angle to use in the transmission function is ε, and for small angles the equation above reduces to

$$\frac{1+s}{2} = \frac{\ell \varepsilon}{r_p} , \qquad \text{(D-13)}$$

where

$$\frac{\ell}{r_p} = \frac{1}{\psi} . \qquad \text{(D-14)}$$

The transmission represents the fractional overlap of the circular areas of the entrance and exit apertures (as shown in Figure D-3) and, therefore, represents the response of the collimator to a parallel beam. Combining Eqs. D-11, D-13, and D-14 gives

$$T = 1 - \frac{2}{\pi}\left\{\frac{\varepsilon}{\psi}\left[1 - \left(\frac{\varepsilon}{\psi}\right)^2\right]^{1/2} + \sin^{-1}\left(\frac{\varepsilon}{\psi}\right)\right\} . \qquad \text{(D-15)}$$

---

*This expression is taken from Ref. D-2. An error in the equation appearing in the reference has been corrected.

11268-11

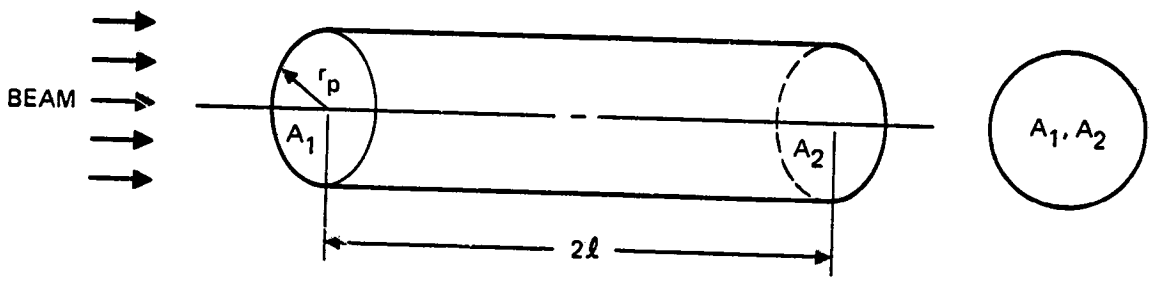

A. COLLIMATOR ARRANGED PARALLEL TO BEAM (T = 1)

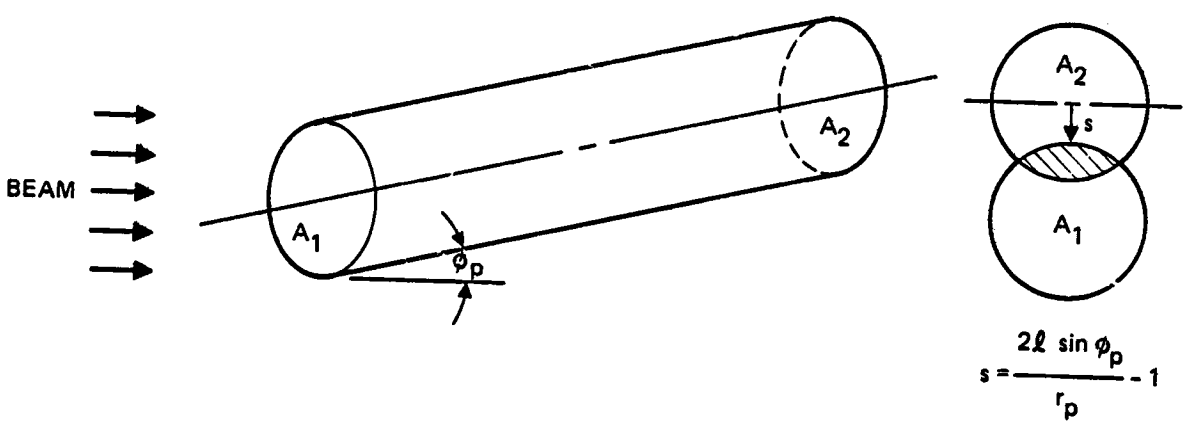

B. COLLIMATOR INCLINED AT AN ANGLE ϕ_p WITH RESPECT TO BEAM ($0 \leq T \leq 1$)

Figure D.3. Definition of variables used in determining the transmission of a cylindrical collimator.

Evaluation of the integral appearing in Eq. D-10 is simplifed by making the substitution

$$x = \frac{\varepsilon}{\psi} . \qquad \text{(D-16)}$$

which gives

$$\int_0^{\psi} \varepsilon T(\varepsilon) d\varepsilon = \psi^2 \int_0^1 x - \frac{2}{\pi}\left[x^2\sqrt{1-x^2} + x \sin^{-1}x\right] dx . \qquad \text{(D-17)}$$

The integration can be performed using standard techniques to evaluate the following integrals:

$$\int_0^1 x dx = \frac{1}{2} , \qquad \text{(D-18)}$$

$$\int_0^1 x^2\sqrt{1-x^2}\, dx = \frac{\pi}{16} , \qquad \text{(D-19)}$$

$$\int_0^1 x \sin^{-1}x dx = \frac{\pi}{8} . \qquad \text{(D-20)}$$

Substituting these results into Eq. D-17 gives

$$\int_0^{\psi} \varepsilon T(\varepsilon) d\varepsilon = \psi^2\left[\frac{1}{2} - \frac{2}{\pi}\left(\frac{\pi}{16} + \frac{\pi}{8}\right)\right]$$

$$= \frac{\psi^2}{8} . \qquad \text{(D-21)}$$

Combining Eqs. D-10 and D-21 gives the relationship between the current density at the probe aperture and the collector current

$$J_n(r,\phi_p) = 4\,\frac{i_n(r,\phi_p)}{A_p} . \qquad \text{(D-22)}$$

The relationship between the current density at the accel electrode and the collector current can be derived using the geometric variables defined in Figure D-4. The small area A_o of the accelerator electrode is "viewed" from different angles ϕ_p, resulting in a current-density dispersion profile similar to the one shown. This profile represents the current density* at the measurement plane due to ion flow from the area A_o. The total current from A_o is obtained by integrating this current density over the measurement plane

$$I_n = \int \vec{J}_n \cdot \hat{n} \, dA \, , \tag{D-23}$$

where the scalar product is given by

$$\vec{J} \cdot \hat{n} = J \cos \varphi_p \, . \tag{D-24}$$

The area element dA is given by the expression

$$dA = \frac{dA_\perp}{\cos \phi_o} \, , \tag{D-25}$$

which is obtained by projecting the area element dA onto a plane normal to the direction defined by the angle ϕ_o corresponding to the peak of the current-density distribution. In this plane, the current density is assumed symmetrical about the radii defined by the angles ϕ_{min} and ϕ_{max} of Figure D-4. Under this assumption, the area element $dA_\perp$ is given by

$$dA_\perp = \pi R dR \, , \tag{D-26}$$

---

*Note that the current density J is not necessarily the total current density at the measurement plane, since the collimator restricts the probe viewing area to A_o. For this reason, the total current from the accelerator system cannot be found by integrating the current density at the measurement plane.

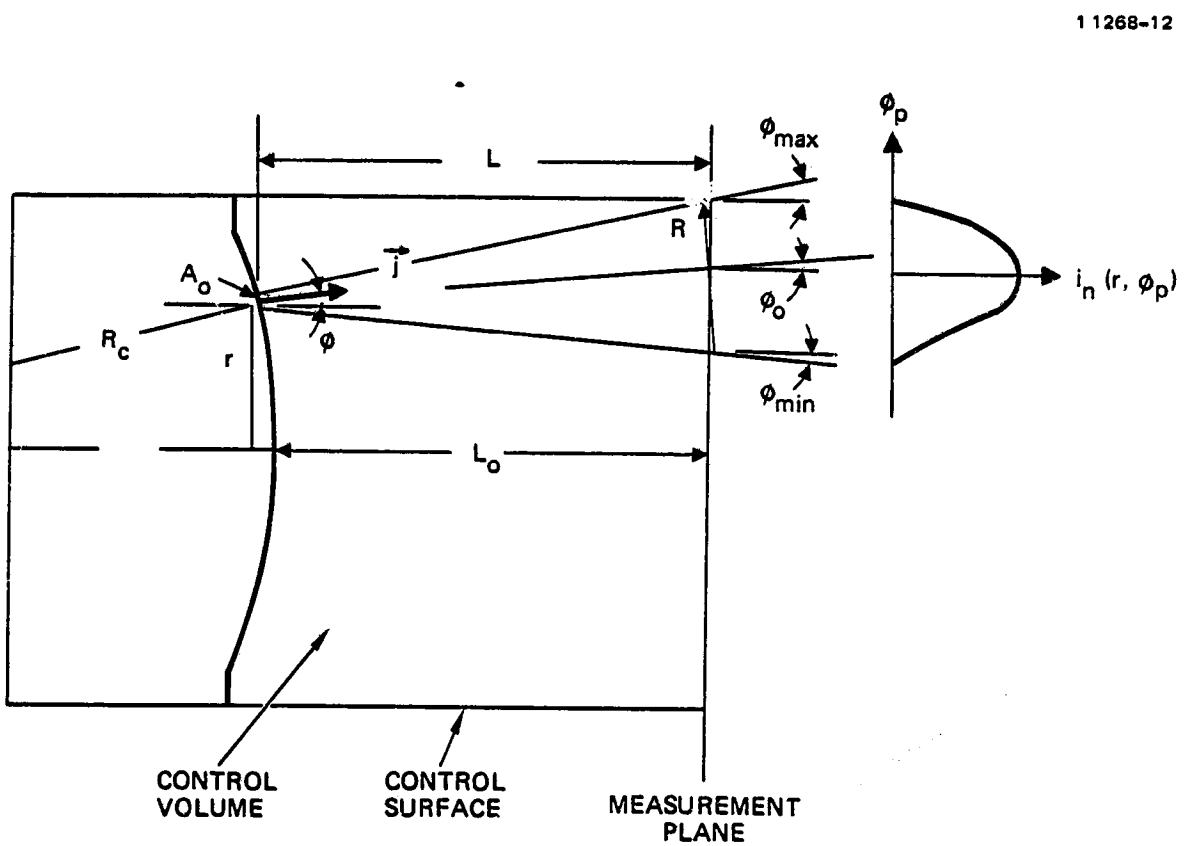

Figure D.4. Definition of variables used in analysis of probe-collector current.

where the coordinate R is given by

$$R = L \sec \phi_o \tan (\phi_p - \phi_o) , \qquad \text{(D-27)}$$

and

$$dR = L \sec \phi_o \sec^2 (\phi_p - \phi_o) d\phi_p . \qquad \text{(D-28)}$$

Note that the area element $dA_\perp$ is a half-ring element of length πR and width dR, which is consistent with the symmetry assumption.
The distance L from the measurement plane to the accelerator grid is given by

$$L = L_o + R_c(1 - \cos \gamma) , \qquad \text{(D-29)}$$

where L_o is the distance from the probe to the accelerator electrode on the thruster axis, and R_c is the radius of curvature of the electrodes (as shown, R_c is positive for electrodes dished outward). The angle γ is given by

$$\gamma = \sin^{-1} \left(\frac{r}{R_c} \right) . \qquad \text{(D-30)}$$

Combining Eqs. D-22 through D-28 gives the desired expression for the current through the measurement plane

$$I_n = \frac{4\pi L^2 \sec^3 \phi_o}{A_p} \int_{\phi_{min}}^{\phi_{max}} i_n \cos \phi_p \sec^2 (\phi_p - \phi_o) |\tan (\phi_p - \phi_o)| d\phi_p . \qquad \text{(D-31)}$$

This is also the current through the area A_o of the accelerator grid, which can be written as

$$I_n = j_n \cos (\gamma - \phi) A_o , \qquad \text{(D-32)}$$

where j_n is the current density at the accelerator electrode. Combining Eqs. D-31 and D-32 gives the desired expression relating the current density at the electrodes to the probe current

$$j_n(r) = \frac{4\pi L^2 \sec^3\phi_o}{A_o A_p \cos(\gamma-\phi)} \int_{\phi_{min}}^{\phi_{max}} i_n(r,\phi_p)\cos\phi_p \sec^2(\phi_p-\phi_o)\,|\tan(\phi_p-\phi_o)|\,d\phi_p \quad . \quad \text{(D-33)}$$

An expression for the angle ϕ can be derived by applying the momentum equation to the control volumes of Figure D-4. Using the measurement plane as the control surface, the net thrust* is given by

$$F_{net}(r) = \frac{mv_+}{e} \int \left[J_+(r,\phi_p) + \frac{\sqrt{2}}{2} J_{++}(r,\phi_p)\right] \cos^2 \phi_p \, dA \quad . \quad \text{(D-34)}$$

Using the accelerator electrode as the control surface, the net thrust is given by

$$F_{net}(r) = \frac{mv_+}{e} \left[j_+(r) + \frac{\sqrt{2}}{2} j_{++}(r)\right] \cos(\gamma - \phi) \cos\phi \, A_o \quad \text{(D-35)}$$

Equating the two expressions for net thrust and solving for the angle ϕ gives

$$\phi(r) = \cos^{-1}\left[\frac{\int \left[J_+(r,\phi_p) + \frac{\sqrt{2}}{2} J_{++}(r,\phi_p)\right] \cos^2 \phi_p \, dA}{\left[j_+(r) + \frac{\sqrt{2}}{2} j_{++}(r)\right] \cos(\gamma - \phi) A_o}\right] \quad . \quad \text{(D-36)}$$

Substituting Eqs. D-22, D-25 through D-28, and D-33 into Eq. D-36 gives the desired expression for the angle ϕ

*The thrust equation is derived in Appendix C, (Eq. C-8).

$$\phi = \cos^{-1}\left[\frac{\int_{\phi_{min}}^{\phi_{max}} \left[i_{+} + \frac{\sqrt{2}}{2} i_{++}\right] \cos^2 \phi_p \sec^2 (\phi_p - \phi_o) |\tan (\phi_p - \phi_o)| d\phi_p}{\int_{\phi_{min}}^{\phi_{max}} \left[i_{+} + \frac{\sqrt{2}}{2} i_{++}\right] \cos \phi_p \sec^2 (\phi_p - \phi_o) |\tan (\phi_p - \phi_o)| d\phi_p}\right] \quad \text{(D-37)}$$